TÉCNICO LISBOA

UNIVERSIDADE DE LISBOA

INSTITUTO SUPERIOR TÉCNICO

Development of hybrid FRP composites for strengthening concrete columns through confinement

Filipe Jorge Teixeira Ribeiro

Supervisor: **Doctor Fernando José Forte Garrido Branco**

Co-Supervisors: **Doctor José Manuel de Sena Cruz**

Doctor Eduardo Nuno Brito Santos Júlio

Thesis approved in public session to obtain the PhD Degree in

Civil Engineering

Jury final classification: **Pass with Distinction and Honour**

2019

TÉCNICO LISBOA

UNIVERSIDADE DE LISBOA

INSTITUTO SUPERIOR TÉCNICO

Development of hybrid FRP composites for strengthening concrete columns through confinement

Filipe Jorge Teixeira Ribeiro

Supervisor: **Doctor Fernando José Forte Garrido Branco**

Co-Supervisors: **Doctor José Manuel de Sena Cruz**

Doctor Eduardo Nuno Brito Santos Júlio

Thesis approved in public session to obtain the PhD Degree in

Civil Engineering

Jury final classification: **Pass with Distinction and Honour**

Jury

***Chairperson*:**

Doctor Fernando António Baptista Branco, *Instituto Superior Técnico, Universidade de Lisboa*

***Members of the Committee*:**

Doctor Joaquim António de Oliveira Barros, *Escola de Engenharia, Universidade do Minho*

Doctor João Pedro Ramôa Ribeiro Correia, *Instituto Superior Técnico, Universidade de Lisboa*

Doctor João Carlos de Oliveira Fernandes de Almeida, *Instituto Superior Técnico, Universidade de Lisboa*

Doctor Luís Filipe Pereira Juvandes, *Faculdade de Engenharia, Universidade do Porto*

Doctor José Manuel de Sena Cruz, *Escola de Engenharia, Universidade do Minho*

Doctor António José da Silva Costa, *Instituto Superior Técnico, Universidade de Lisboa*

Funding Institution

FUNDAÇÃO PARA A CIÊNCIA E A TECNOLOGIA

2019

Chaos is merely order waiting to be deciphered.

The Book of Contraries – José Saramago

To my family that I love so much

ABSTRACT

Concrete in compression expands radially leading to internal cracking. The confinement, first, delays cracking and, then, prevents concrete disaggregation, thus allowing concrete to reach higher compressive strength and higher ultimate axial and lateral strains. Although the performance of fibre reinforced polymer (FRP)-confined concrete is well studied, it still exhibits two relevant drawbacks. Firstly, FRP-confined concrete submitted to pure compression fails suddenly, being this behaviour dominated by FRP failure. Secondly, the ultimate tensile strain of conventional FRP jackets is lower than that observed in uniaxial tensile tests of laminates of the same material, revealing a decrease of efficiency.

The main objective and motivation of the present work was to study the possibility of improving the performance of FRP-confined concrete columns. For this purpose, an innovative confining hybrid FRP jacket was developed, in which two reinforcing materials, synthetic (carbon and glass) or natural (basalt), were combined in the same matrix. This type of solution has proved to be very interesting, because it can promote synergies between the involved reinforcing materials, conducting, for instance, to: (i) pseudo-ductile responses, characterized by fragmentation of the low strain material and dispersed delamination of the low strain material fragments from the undamaged high strain material; and (ii) an increase (until 50%) of the apparent strain at failure of low strain fibres, known as 'hybrid effect'.

In the first phase of the work, specific attention has been paid to developing hybrid FRP composites at the material level. Different interlayer (layer-by-layer) combinations of the following dry unidirectional fabric materials were investigated using experimental testing and analytical modelling: high-modulus carbon (CHM), standard-modulus carbon (C), E-glass (G), and basalt (B). The composites were produced by hand lay-up method, using an epoxy-based resin as matrix.

An experimental study on the tensile stress–strain curves of hybrid FRP composites was conducted aiming at evaluating the hybrid effect and pseudo-ductility. A maximum hybrid effect of circa 45% was achieved, by combining CHM with C. It was also concluded that combining CHM with G, CHM with B, or CHM with C can lead to pseudo-ductile tensile behaviour. An existing analytical model in the literature was satisfactorily adopted to predict the tensile stress-strain curve of these hybrid composites. Besides, it was demonstrated that elastic modulus and tensile strength can be predicted following simple models as the linear rule of mixtures and the bilinear rule of mixtures, respectively.

Then, tensile tests on single fibres were performed in order to determine their Weibull strength distribution parameters (shape and scale). The described factors were used as inputs to assess the performance of a progressive damage model on the prediction of hybrid effect. Comparisons of analytical predictions with experimental test results showed reasonably accuracy.

In the second phase of the work, the performance of the different hybrid combinations (previously tested in tension) was assessed in the confinement of small-scale plain concrete columns, exploiting the demonstrated hybrid effect and pseudo-ductility of this confining material. From the obtained results it is demonstrated that hybridisation can effectively contribute to maximize the lateral strain efficiency of low strain fibres. Furthermore, it is also demonstrated that pseudo-ductile responses are obtained, contributing to the elimination of the brittle failure of system. An existing analysis-oriented confinement model in the literature for non-hybrid FRP was satisfactorily modified to predict both: (i) dilation behaviour and (ii) compressive stress-strain behaviour of hybrid FRP-confined concrete.

Finally, a three-dimensional finite element model using ABAQUS was developed to predict the compressive behaviour of hybrid FRP-confined concrete. This was achieved through the modification of the concrete damaged plasticity model available in the adopted software. It was demonstrated that, by turning both the yield function and the flow rule dependent on the confining pressure, it is possible to use the referred to model and obtain accurate results.

In summary, it has been found that the application of unidirectional hybrid FRP systems in confinement of concrete can lead to improved mechanical performance. It has been shown that abrupt failure can be avoided; since the hybrid FRP, if materialized for this purpose, may exhibit a pseudo-ductile tensile behaviour, due to the fragmentation of low strain material. In this way, the confining system maintains its integrity even after reaching its tensile strength. Besides, it has been shown that it is possible to increase the efficiency of the low strain material.

These potentialities were first explored, in the context of civil engineering, in the present work. The study carried out allowed the calibration and development of analytical and numerical models to predict different properties of both the hybrid FRP system itself and its application in confinement. Thus, this thesis aimed to be a first and decisive step in the exploration of pseudo-ductility and hybrid effect in the referred to context. It is hoped that this work promotes the further development of hybrid FRP systems and their application not only in the confinement but also in the strengthening of different structural elements or new construction.

Keywords: Confined concrete; Hybrid FRP composites; Fragmentation; Experimental testing; Analytical modelling; Numerical modelling

RESUMO

O betão em compressão expande lateralmente o que conduz à sua fendilhação. O confinamento atrasa o processo de fissuração e previne que o betão se desagregue, o que leva a que seja possível atingir maiores valores de resistência à compressão e extensões axial e lateral. Embora o desempenho do betão confinado através de sistemas de polímeros reforçados com fibras (FRP – *fiber reinforced polymer*) seja um tema já estudado, apresenta ainda duas desvantagens relevantes. Em primeiro lugar, o betão confinado com um sistema de FRP, quando submetido a esforços de compressão uniaxial, colapsa abruptamente, sendo a rotura condicionada pelo sistema de FRP. Em segundo lugar, os sistemas de confinamento materializados com FRP tradicionais apresentam uma extensão de rotura menor do que aquela que é obtida em ensaios de tração uniaxial, revelando uma redução de eficiência.

O presente trabalho teve como principal objetivo e motivação estudar a possibilidade de melhorar o desempenho do betão confinado recorrendo aos sistemas de FRP referidos. Neste sentido, desenvolveu-se um sistema de FRP híbrido inovador, no qual se combinam, na mesma matriz polimérica, dois materiais de reforço, sintéticos (carbono e vidro) ou naturais (basalto). Este tipo de solução revela-se bastante interessante, na medida em que promove sinergias entre os materiais constituintes, conduzindo, por exemplo, a: (i) comportamentos em tração pseudo-dúcteis, que se caracterizam pela fragmentação do material com menor extensão última e pela delaminação dispersa entre os fragmentos do material de menor extensão última e o material de maior extensão última; e (ii) um aumento da extensão última aparente do material de menor extensão última (até 50%), sendo este aumento conhecido por 'efeito híbrido'.

Numa primeira fase do trabalho, deu-se ênfase ao desenvolvimento, ao nível material, dos sistemas FRP híbridos. Na produção destes sistemas, recorreu-se a mantas secas de carbono de alto módulo de elasticidade (CHM), carbono de módulo *standard* (C), vidro do tipo *E-Glass* (G) e basalto (B). Como matriz, utilizou-se uma resina epoxídica. Os compósitos foram produzidos camada-a-camada, por meio de laminagem manual.

Os sistemas de FRP híbridos foram submetidos a ensaios de tração uniaxial, com o intuito de avaliar o efeito híbrido e a pseudo-ducitlidade. Registou-se um efeito híbrido máximo de cerca de 45%, combinando fibras de CHM e de C. Concluiu-se que a combinação de CHM e G, CHM e B ou CHM e C pode conduzir a comportamento pseudo-dúctil à tração. Deve-se destacar que foi possível prever adequadamente todas as curvas tensão-extensão dos FRP híbridos ensaiados e todos os modos de rotura observados. Para tal, calibrou-se um modelo específico existente na bibliografia. Para além disso, verificou-se que modelos analíticos simples, como sejam a 'regra das misturas linear' e a 'regra das misturas bilinear', permitem prever de forma adequada o módulo de elasticidade e a resistência em tração, respetivamente.

Seguidamente, com o intuito de caraterizar a distribuição estatística da resistência das fibras, um grande número de fibras foi aleatoriamente retirado de cada manta e cada fibra foi testada isoladamente à tração. Desta forma, foi possível definir uma distribuição de probabilidade de

Weibull. Os parâmetros que caraterizam a distribuição anterior foram introduzidos num modelo de dano progressivo e, consecutivamente, o efeito híbrido foi estimado. Verificou-se que, de acordo com a metodologia adotada, o efeito referido pode ser razoavelmente previsto.

Numa segunda fase do trabalho, avaliou-se o desempenho de todas as combinações híbridas (estudadas previamente à tração) no confinamento de provetes circulares em betão, submetidos a compressão uniaxial. Verificou-se que a opção por um confinamento híbrido, em detrimento dos sistemas tradicionais, pode levar a um ganho de eficiência na utilização das fibras de ambos os tipos de carbono, promovido pelo aparecimento do efeito híbrido. Foi possível observar que o comportamento pseudo-dúctil de algumas combinações híbridas promoveu a rotura não abrupta do betão confinado. Um modelo analítico, anteriormente desenvolvido para prever o comportamento do betão confinado com sistemas FRP não híbridos, foi modificado de forma a torná-lo capaz de prever: (i) a curva extensão axial-extensão lateral e (ii) a curva tensão-extensão do betão confinado com sistemas FRP híbridos.

Por fim, procedeu-se à simulação numérica do comportamento experimental observado com recurso ao *software* de elementos finitos ABAQUS e ao modelo constitutivo *damage-plasticity*. Foi necessário a alteração do modelo em causa, tornando a função de cedência e de escoamento dependentes da tensão de confinamento. O modelo desenvolvido demonstrou ser capaz de prever, de forma adequada, o comportamento observado experimentalmente.

Em suma, verificou-se que a aplicação de sistemas FRP híbridos unidirecionais no confinamento do betão pode conduzir a um desempenho mecânico melhorado. Foi possível demonstrar que é possível evitar roturas abruptas; uma vez que o FRP híbrido, caso seja materializado com essa finalidade, é capaz de assegurar um modo de rotura à tração pseudo-dúctil, devido à fragmentação do material de menor extensão última. Desta forma, o sistema de confinamento mantem a sua integridade mesmo após ser atingida a sua resistência à tração. Para além disso, demonstrou-se que é possível aumentar a eficácia do material de menor extensão última.

Estas potencialidades foram pela primeira vez exploradas, no contexto da engenharia civil, no presente trabalho. O estudo efetuado permitiu a calibração e desenvolvimento de modelos analíticos e numéricos com capacidade de previsão de diferentes propriedades, tanto do sistema FRP híbrido em si como da sua aplicação no confinamento. Assim, esta tese afigura-se como um primeiro e decisivo passo na exploração da pseudo-ductilidade e efeito híbrido no contexto citado. Espera-se que este trabalho promova a continuação do desenvolvimento/aplicação de soluções de FRP híbridos, não só no campo do confinamento, mas também no reforço de diferentes elementos estruturais ou construção nova.

Palavras-chave: Betão confinado; Sistemas FRP híbridos; Fragmentação; Ensaios experimentais; Modelação analítica; Modelação numérica

ACKNOWLEDGMENTS

I would like to thank Doctor José Sena-Cruz for his support and friendship, for having taught me the true sense of ethics, integrity, rigor and responsibility. I am very grateful to him for having welcomed me so well and allowing myself to grow as a professional and a human being. Besides the professional side, I have to highlight his human qualities, the care he takes in dealing with each person he meets, and the attention he gives to all his students. I thank him for having taught me that everything comes with time and hard work.

I am also grateful for the unique opportunity to deal with Professor Eduardo Júlio. I would like to thank him for having welcomed me, for the support, for his knowledge and experience, for the precious time that he spent with me, and for all the effort that he has made to ensure that this work ends successfully. I am grateful for his valuable and intelligent contributions and for the fruitful discussions.

I would like to thank Doctor Fernando Garrido Branco for his contributions, for having known how to conduct his orientation, for giving me the necessary space, and for the time and effort put into this work.

I wish to thank the Portuguese Foundation for Science and Technology (FCT) and the 'Eco-Construction and Rehabilitation' (Eco-CoRe) Doctoral Program, for supporting the PhD grant (PD/BD/52660/2014).

I also would like to acknowledge the support of S&P Clever Reinforcement Ibérica Lda and the Dalla Betta Group Company.

I am very grateful to all my colleagues from University of Minho, Christoph de Sousa, Gonçalo Escusa, Jorge Rocha, José Granja, Luís Correia, Mário Coelho, Patrícia Silva, Pedro Fernandes, Ricardo Cruz, and Sérgio Soares, for their constant help and encouragement.

I would like to thank the staff of the Structural Laboratory of the University of Minho, especially the assistance provided by António Matos and Marco Peixoto.

I also would like to thank Doctor Sandra Nunes for her contributions and for having awakened my passion for scientific research.

I am very grateful to my parents and my sister for their love and support during all stages of my life.

I also would like to acknowledge all my friends for being always present. Without them, life would be much more difficult.

Last but not least, I would like to thank Ana for her love, friendship, patience, and support during all this work. I am grateful for her encouragement, for always believing in me, for the pride she has in me, and for making me always believe that better days will come.

TABLE OF CONTENTS

LIST OF TABLES

LIST OF FIGURES

NOTATIONS AND SYMBOLS

Latin upper-case letters

D^{e}_{ijkl} - initial elasticity matrix

E_c - elastic modulus of plain concrete

E_H - elastic modulus of the HS fibres

E_{hybrid} - elastic modulus of hybrid composites

G - Drucker-Prager hyperbolic function

G_F - fracture energy

G_{IIC} - mode II interlaminar fracture toughness of the interface between LS layers and HS layers

$\overline{I}_1$ - first effective stress invariant

$\overline{J}_2$ - second effective deviatoric stress invariant

K - strength ratio of concrete under equal biaxial compression to triaxial compression

S_L - reference strength of the LS material

V - volume of the specimen

Latin lower-case letters

d_a - maximum aggregate size

d_{ij} - damage tensor

$d\varepsilon^{p}_{ij}$ - flow rule

f_b - concrete strength under equal biaxial compression

f_c - compressive strength

$\overline{f}_c$ - effective principal compressive stress

f_{c0} - peak stress of unconfined concrete

f_{cc} - peak axial stress of confined concrete

f^{*}_{cc} - peak stress of actively confined concrete

$f_{c,res}$ - residual stress

f_{ij} - stress tensor

$\overline{f}_{ij}$ - effective stress tensor

f_l - confining pressure

$f_{l,1}$ - confining pressure in direction 1

$f_{l,2}$ - confining pressure in direction 2

$\overline{f}_{l,1}$ - effective principal lateral stress in direction 1

$\overline{f}_{l,2}$ - effective principal lateral stresses in direction 2

f_t - tensile strength of concrete

m_H - Weibull strength distribution modulus of the HS fibres

n - curve shape parameter

r - concrete brittleness

t_L- half thickness of the LS layers

t_H - half thickness of the HS layers

Greek letters

α - modulus ratios of the LS to HS fibres

β - thickness ratios of the LS to HS fibres

ε_c - axial strain of concrete

ε_{c0} - axial strain at the peak stress of the unconfined concrete

ε_{cc} - peak axial strain of confined concrete

ε_{cc}^* - peak strain of actively confined concrete

$\varepsilon_{c,i}$ - axial strain corresponding to the inflection point of the descending branch of stress-strain curve

$\varepsilon_{c,p}$ - axial plastic strain of concrete

ε_{ij} - strain tensor

ε_{ij}^{p} - plastic strain tensor

$\varepsilon_{l,p}$ - lateral plastic strain of concrete

$\tilde{\varepsilon}_{p,c}$ - compressive plastic strain

$\tilde{\varepsilon}_{p,t}$ - tensile plastic strain

$\varepsilon_{t,FRP}^{pl}$ - tensile plastic strain of hybrid composites

$\varepsilon_{t,hybrid}$ - total tensile strain of hybrid composites

$\sigma@LF$ - stress at which the first crack in the LS material occurs

$\sigma@del$ - stress at which delamination starts

$\sigma@HF$ - stress at which the HS material fails

$\overline{\sigma}_{cn}$ - effective compressive cohesion stress

σ_{hybrid} - tensile stress of hybrid composites

$\overline{\sigma}_{min}$ - minimum principal effective stress

σ_{to} - uniaxial tensile stress at failure

$\overline{\sigma}_{tn}$ - effective tensile cohesion stress

ν_i - initial Poisson's ratio of concrete

Ψ - plastic dilation angle

$\ni$ - eccentricity parameter

1. INTRODUCTION

1.1. Scope of the research

The importance of the global construction industry was US$10.8 trillion in 2017 [1] and it is set to grow to US$17.5 trillion by 2030 [2]. This will be largely motivated by Asia-Pacific region (namely by vast markets such as China, India and Japan), being responsible by the largest share of the overall construction industry. The United States of America (USA) will play as well an important role in global construction market growth in the next years. In fact, it is expected that China, USA and India together will account for 57% of all global growth in the construction and engineering market by 2030 [2]. In the case of European countries, compared with the pre-crisis period, the production has recovered and today transcends 2010 levels [3]. However, in the specific case of Southern European, although construction markets are recovering, production volumes in Portugal (52.5%), Greece (52.4%), Italy (68.0%), France (89.9%) and Spain (95.0%) have not yet reached 2010 levels [3].

Enclosed in the market described above, a significant growth for the rehabilitation subsector in the next years is expected. As it is known, advanced economies usually have relatively large infrastructure capital and face the challenge of maintaining, upgrading, and modernizing extensive transport, power, water, and telecommunications networks. For instance, only in the USA, a significant volume of infrastructure needs replacing, repairing and/or modernising (that will correspond to US$3.6 trillion of spending needs by 2020 [2]).

In the actual context, it can be stated that there is a global opportunity to apply innovative technologies and materials aiming at extending the service live of existing infrastructures and, simultaneously, could lead to the design and construction of highly durable new ones. Leveraged by the described above scenario, and taking into account that approximately one-third of construction cost is attributed to building materials [4], the need for the development and applying advanced building materials is critical.

In structural engineering, fibre reinforced polymer (FRP) composites, developed initially for the aerospace and defence industries, have become a very interesting alternative to conventional materials (concrete and steel) due to their versatility, no corrosiveness, lower maintenance, enhanced durability, high strength-to-weight ratio, accelerated construction feature, and cost-effectiveness. Over the last decades, there have been a myriad of successful applications of FRP composites for repairing and retrofitting existing infrastructure systems as well as for new construction. It is important to note that, in the current paradigm in which concerns regarding sustainability are highly valued, FRP composites have been characterized as environmentally favourable and substantial cost saver materials, with lower impact on users and society [5].

Despite the numerous advantages, ductility is a major problem for FRP applications, because these materials are stiff and strong, but brittle (with little or no warning before final failure). This means that higher safety factors, relative to more ductile materials, have to be applied in

the design of FRP materials [6]. Hybrid FRP composites (i.e. a composite material in which two or more different reinforcing materials are combined in the same polymeric matrix) have been seen as an interesting alternative to conventional FRP composites, because this solution can lead to the development of tensile pseudo-ductile failure process (characterized by the fragmentation of low strain material).

However, to achieve the referred to tensile behaviour is challenging and requires a thorough understanding of the failure mechanisms that occur during loading. Initiation and propagation of damage depend primarily on the strength, stiffness, volume fractions, stacking sequence, ply thickness of the low and high strain components, and mode II fracture toughness of the interface between the high and low strain materials [7]. Depending on the combination of these properties, failure can be either gradual or abrupt.

Although a significant amount of literature about the development of hybrid FRP composites for civil engineering applications have been published in the past, the exploitation of fragmentation in such applications is non-existent. The confinement of concrete columns is addressed herein. The application of hybrid FRP composites in this context would help to improve the performance of these applications and overcome their drawbacks.

1.2. Research objectives

The main objective of the work herein presented is (i) the development of hybrid FRP composites and (ii) their application to improvement of the performance of FRP-confined concrete columns. The hybrid FRP composites consists of combining two reinforcing materials, synthetic (carbon and glass) or natural (basalt), in the same matrix. The work was carried out in two phases. A first one, dedicated to the study of hybrid FRP composites at the material level, and a second, dedicated to assess the performance of different hybrid combinations in the confinement of small-scale plain concrete columns. The specific goals are listed next:

Phase I

i) To understand which properties of the constituent materials influence most the tensile response of hybrid FRP composites;
ii) To characterize the hybrid pseudo-ductile tensile behaviour;
iii) To validate the accuracy of different existing analytical models in predicting several tensile properties of hybrid FRP composites, namely elastic modulus, strength, hybrid effect, ‘yield’ stress and pseudo-ductile strain.

Phase II

i) To understand how the hybrid effect and pseudo-ductility can contribute to improve the performance of FRP-confined circular concrete columns;

ii) To develop analytical models to predict different properties of hybrid FRP-confined concrete, namely compressive strength, stress-strain curve, and dilation behaviour;
iii) To propose an accurate three-dimensional finite element model to simulate the compressive behaviour of hybrid FRP-confined concrete.

1.3. Chapter outline

This thesis is organized in seven chapters. Excluding the introduction and the conclusions chapters, each of the remaining five gave rise to a paper published (or submitted or under development for publication) in an international journal. Therefore, each chapter can be read independently. The overall research strategy is summarised in **Figure 1.1** and is briefly addressed in the next paragraphs.

In Chapter 2, a brief overview on suitability of FRP composites to current construction concerns is presented. Next, the main properties of hybrid FRP composites are resumed. Finally, a critical literature review on the development of hybrid FRP composites for construction is presented.

In Chapter 3, a literature review on the main properties of hybrid FRP composites is presented. Relevant information published between 1974 and 2016 is resumed. The tensile stress-strain response of 16 different UD interlayer (layer-by-layer) hybrid composite combinations, made through the hand lay-up method, of different commercial raw materials is experimentally investigated. The analysis of the obtained results is complemented using analytical modelling.

In Chapter 4, the hybrid effect is predicted using analytical modelling approach. The statistical strength scatter parameters of the fibres are determined experimentally through single fibre tests, to be used as inputs on the model. The evolution of hybrid properties (such as hybrid effect, 'yield' stress, pseudo-ductile strain, elastic modulus and strength) is investigated as function of the configuration of hybrid FRP composites.

In Chapter 5, the experimental study on the compressive stress-strain curves of small-scale plain circular concrete columns confined with hybrid FRP is reported. Two new simple design-oriented models developed in order to predict the compressive peak stress of compressed concrete columns confined with hybrid FRP jacketing are presented. Next, an existing analysis-oriented model developed for non-hybrid FRP-confined concrete adapted to also predict dilation and the compressive stress-strain curve of hybrid FRP-confined concrete are described.

In Chapter 6, an accurate three-dimensional finite element model to predict the compressive behaviour of hybrid FRP-confined concrete is proposed. This was achieved through the modification of the concrete damaged plasticity model available in ABAQUS software.

In Chapter 7, the main conclusions of this thesis are summarized, together with some suggestions for possible future research.

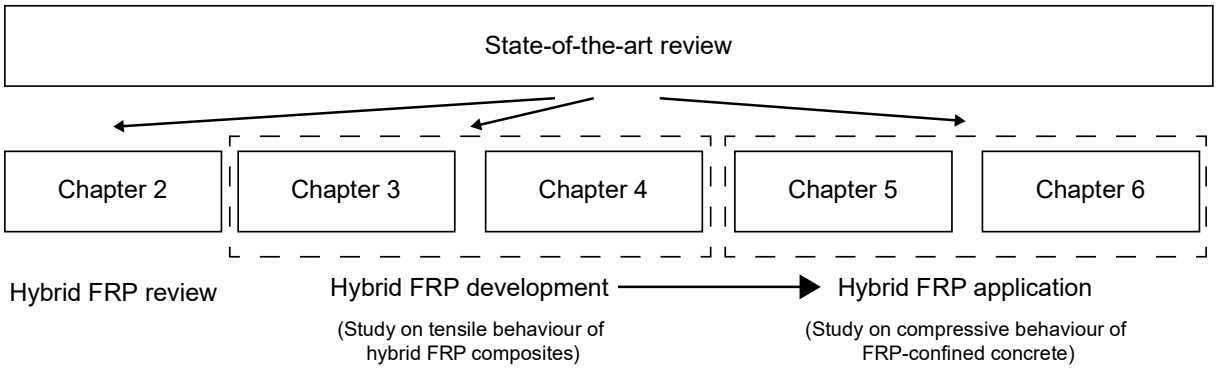

Figure 1.1 — Research strategy.

1.4. Outputs

The content presented in each main chapter of this thesis is directly related with a paper in an international journal. The reference to each paper and its correspondence to the chapter of this work is present in Section 1.4.1. Furthermore, the work developed in the framework of this thesis resulted also in several publications in conferences, as listed in sections 1.4.2 and 1.4.3.

1.4.1. Papers in international journals cited in ISI Web of Knowledge

1. (Chapter 2) Ribeiro, F.; Sena-Cruz, J.; Branco, F. G.; Júlio, E. – "Hybrid FRP composites for construction: A state-of-the-art review" – [Manuscript under final preparation to be submitted to Composites Part B: Engineering]

2. (Chapter 3) Ribeiro, F.; Sena-Cruz, J.; Branco, F. G.; Júlio, E. – "Hybrid effect and pseudo-ductile behaviour of unidirectional interlayer hybrid FRP composites for civil engineering applications" – Construction and Building Materials 171 (2018) 871–890. https://doi.org/10.1016/j.conbuildmat.2018.03.144

3. (Chapter 4) Ribeiro, F.; Sena-Cruz, J.; Branco, F. G.; Júlio, E. – "Hybrid effect prediction and evolution of the tensile response of hybrid FRP composites" – [Manuscript to be submitted soon to Journal of Composite Materials]

4. (Chapter 5) Ribeiro, F.; Sena-Cruz, J.; Branco, F. G.; Júlio, E. – "Hybrid FRP jacketing for enhanced confinement of circular concrete columns in compression" – Construction and Building Materials 184 (2018) 681–704. https://doi.org/10.1016/j.conbuildmat.2018.06.229

5. (Chapter 6) Ribeiro, F.; Sena-Cruz, J.; Branco, F. G.; Júlio, E. – "3D finite element model for hybrid FRP-confined concrete in compression using modified CDPM" – Engineering Structures [Manuscript submitted in 12/11/2018]

1.4.2. Papers in international conferences

1. Ribeiro, F.; Sena-Cruz, J.; Júlio, E.; Branco, F. G.; Castro, F. – "Evolution of the tensile response of unidirectional hybrid FRP fabricated by hand lay-up method: experimental and analytic assessment." – 9th International Conference on Fibre-Reinforced Polymer (FRP) Composites in Civil Engineering (CICE2018) – Paris 17-19 July, 2018, 8 pp.
2. Ribeiro, F.; Sena-Cruz, J.; Júlio, E.; Branco, F. G. – "Axial compressive behaviour of hybrid FRP-confined concrete." – 9th International Conference on Fibre-Reinforced Polymer (FRP) Composites in Civil Engineering (CICE2018) – Paris 17-19 July, 2018, 8 pp.

1.4.3. Papers in national conferences

1. Ribeiro, F.; Sena-Cruz, J.; Branco, F. G.; Júlio, E. – "Comportamento à compressão de pilares circulares de betão confinados por sistemas compósitos de FRP híbridos" – Encontro Nacional Betão Estrutural, 2018, 10 pp.
2. Ribeiro, F.; Sena-Cruz, J.; Nunes, S.; Branco, F. G.; Júlio, E. – "Resposta à tração uniaxial de sistemas FRP híbridos" – Encontro Nacional Betão Estrutural, 2016, 11 pp.

1.5. References

[1] Construction-Intelligence-Center. Global Construction Outlook to 2022: Q3 2018 Update. 2018.
[2] GCP-Global, Oxford-Economics. Global Construction 2030: A Global Forecast for the Construction Industry to 2030. Global/Oxford Economics, London. 2015.
[3] Deloite. European Construction Monitor 2017–2018: A looming new construction crisis? 2018.
[4] World-economic-forum. Shaping the Future of Construction: A Breakthrough in Mindset and Technology. 2016.
[5] Mara V, Haghani R, Harryson P. Bridge decks of fibre reinforced polymer (FRP): A sustainable solution. Construction and Building Materials. 2014;50:190-9.
[6] Swolfs Y, Verpoest I, Gorbatikh L. Recent advances in fibre-hybrid composites: materials selection, opportunities and applications. International Materials Reviews. 2018:1-35.
[7] Jalalvand M, Czél G, Wisnom MR. Parametric study of failure mechanisms and optimal configurations of pseudo-ductile thin-ply UD hybrid composites. Composites: Part A. 2015; 74:123–31.

2. HYBRID FRP COMPOSITES IN CIVIL ENGINEERING

2.1. Introduction

FRP composites materials have at least two constituents, typically a polymer (the matrix) and fibres (the reinforcing material). They can provide improved performance or new functions compared to each of their constituents alone.

In the 1950s and 1960s, the demanding requirements of the aerospace and defence industries triggered the development of these materials [1]. Today, although its use has spread to different industries, the main developments of composites have the original aims, namely to improve (high) performance and to reduce (light) weight, keeping the material strong enough to take high loads [2]. However, as knowledge of composites science and technology grows, a large amount of new opportunities, and applications emerge giving rise to the need for new developments.

Hybrid FRP composites (i.e. a composite material in which two or more different reinforcing materials are combined in the same matrix) is a paradigmatic example of the new opportunities/applications and needed developments above mentioned. This is a topic that has received much attention in the last five years. Although in the 1970s and 1980s this theme has already aroused scientific interest, e.g. [3-12] (resulting at least in the publication of three literature reviews: [3, 12, 13]), it seems it gained a new breath recently. At the moment, there are several ongoing research works in this area. This recent enthusiasm has resulted in a large number of publications, e.g. [14-34]. These studies have focused essentially on the mechanical behaviour of unidirectional (UD) layer-by-layer hybrid composites. However, some literature about the development of other hybrid composite configurations has been as well recently published, e.g. intermingled hybrid composites with aligned discontinuous fibres [28, 30].

In fact, the mechanical behaviour, particularly the tensile stress-strain response of UD hybrid composites is one of the most interesting characteristics of this type of materials. In this case, it was found that hybridisation promotes synergies between the reinforcing materials, conducting to ‘pseudo-ductile’ tensile response, characterized by fragmentation of the low strain (LS) material and dispersed delamination of the LS material fragments from the undamaged high strain (HS) material, and an increase of the apparent failure strain of LS material, known as ‘hybrid effect’. Nevertheless, in addition to synergetic effects for mechanical properties, the purpose of hybridisation may be of different nature: functional or environmental.

It should be noted that the main developments on hybrid composites have been essentially promoted in the areas of mechanics, aerospace, materials, and polymer engineering. However, given the relevance of the most recent findings, it is believed that today there are also opportunities for the study of this type of materials in the context of civil engineering. In fact, in the 1990s and 2000s there was already scientific interest in this topic. Essentially, this

resulted in the development of hybrid composite solutions for both the rehabilitation of existing concrete structures and the production of reinforcing bars for concrete structures. However, the work in this area is residual, not following the recent enthusiasm demonstrated by research groups from other areas.

Recently, Swolfs *et al*. [35] published a literature review about advances in hybrid composites. From this work, it is possible to understand that hybrid composites have been applied in different industries. However, the reasons that have been invoked to support their use are often vaguely scientific. Commercial advantages related with the implementation of a new material technology is sometimes more important than the real performance of the hybrid composites, especially in sport applications. In this work, it was identified that the production of wind turbine blades is an interesting field for hybrid composites because it is expected a market growth in the near future.

Swolfs *et al*. [35] do not make any reference to the developments achieved in construction/civil engineering context. The potential of the application of hybrid composites to this industry is not mentioned either. As it is justified in Section 2.2 of the present chapter, today there is a growing interest for the use of composite materials in construction industry. In fact, these materials can be efficiently used to correct deteriorated and functional deficient civil infrastructures. As it is known, this represents one of the most significant challenges that many developed countries have to face nowadays. Furthermore, FRP materials are increasingly used as well in new construction (sometimes in combination with other materials).

Taking into account the literature on development of hybrid composites for civil engineering, the present chapter aims to collect and critically review these works. For this, the main characteristics of these materials are discussed, up-to-date knowledge on this subject is exposed, and the challenges and future opportunities are identified. It should be noted that the word 'hybrid' has been used to mention different solutions, which may lead to some misunderstanding. Sometimes, solutions in which conventional FRP composites are joined to conventional structural concrete or steel elements are also named 'hybrid structural systems'. These applications are not addressed in the present chapter.

2.2. Suitability of FRP composites to current construction concerns: Brief overview

Aided by the growth in research and application projects funded by governments and industries around the world, FRP composites are now well accepted in the construction industry and their implementation has been growing up. Nowadays, 30% of all produced polymers (in generic terms) are utilised in the construction industry [36]. However, many years passed before these achievements. As it is known, the market of opportunities to use new materials in construction were rare because of the lack of investment in research and development over the three decades following Second World War [37]. Even today, the introduction of innovative materials is

difficult because this industry is highly conservative and initial cost-driven [38]. In this way, the major developments in FRP composites have always been driven by other industries, such as aerospace and automotive.

Gradually, the way of thinking is changing in construction industry. Today, there is increasing emphasis on sustainability, in the selection and performance of materials [39]. This entails a complex set of economic, environmental, and social factors. From the economic standpoint, the significance of costs associated to maintenance, rehabilitation, reconstruction, and replacement of construction has been increasingly seen as very important. In this way, it has been argued that these costs should be considered as part of the design process [38]. This means that the entire life-cycle costs should be analysed in order to provide a rational choice of materials.

FRP composites have been growing popularity in this context because, besides their superior mechanical strength advantage, they have better potential durability (despite the high initial costs) when compared with traditional materials, especially steel. For this reason, their use may provide more cost-effective solutions [38]. As it is known, corrosion and fatigue life are not major factors to consider in the design of composites [1], unlike steel.

However, durability issues relate with FRP employed in construction industry is a subject not entirely understood nowadays. This is due to the interaction between a significant number of factors that FRP can be subjected to during their service life, which leads to uncertainties regarding their long-term behaviour. These factors include atmospheric humidity, rain, solar (UV) radiations, large variations in temperature, freeze-thaw regimes, acid rain, sea-water, deicing chemicals, alkaline environment when in the proximity of Portland cement concrete, and sustained loads. FRP can also be accidentally exposed to extreme environments, such as fire, earthquake, and blasts. Obviously, the durability of FRP composites is a critical issue for safe and economical implementation of these materials. A great deal of recent research has been focused on this topic. More information about the latter can be found in several works, e.g. [40-53].

In parallel to economic benefits, the environmental issues have been increasingly valued by the construction industry. As it is known, the construction sector is one of the largest consumer of materials and producer of waste. In this way, there has been increasing pressure on this industry to reduce its environmental impact. Naturally, this has repercussions in research activity. The case of FRP, plant-based (e.g. hemp, flax, sisal, kenaf, jute, etc. [54-63]) or mineral-based (e.g. basalt [64-74]) fibres as alternatives to the conventional synthetic reinforcing materials (e.g. glass and carbon) have been investigated.

In particular, basalt fibres have been seen with special interest for their properties. These fibres are obtained from a basalt rock (composed by silica, alumina, and other oxide). The manufacturing process of basalt fibres is similar to that of glass fibres, but with less energy needs and no additives (which makes basalt fibres cheaper and more sustainable than glass or carbon fibres [73, 74]). Stiffness and strength properties of basalt fibres are also very similar to those of glass fibres. Furthermore, they have good thermal and chemical stability. Despite the

similarity in chemical composition with asbestos, basalt fibres have reduced health risks [75]. For these reasons, these fibres have been proposed as an appealing alternative to glass fibres.

In addition to natural fibres, bio-based polymers (synthesized from renewable resources) have been investigated as a viable alternative to traditional petroleum-based polymers [76, 77]. As it is known, thermosetting polymers are extensively used in FRP production. Among others, these group of polymers include vinyl ester, unsaturated polyesters, and epoxy resins (that represents around 70% of the thermosetting polymers market [78]). Usually, the monomer bisphenol A (BPA) is the chemical precursor of these group of resins. The use of BPA is associated with environmental (because it is obtained from fossil resources) and health concerns (being even classified as carcinogen mutagen and reprotoxic substance [78, 79]). Consequently, studies on alternative materials to BPA has been increasing [78-81]. However, the commercialization of the latter is far from being widespread.

Multifunctionality is as well a current research area on FRP field, i.e, the development of composites in which, besides the mechanical load-bearing capacity, other properties such as thermal stability, electrical conductivity, and/or wear resistance can be important. Multifunctionality can be achieved in FRP, using different types of polymer matrices and various nano and microsized fillers or reinforcements, see details in [82].

To conclude, it should be noted that for the past three decades FRP composites have been gradually accepted in the construction industry. More information can be found in a large set of books and review works dedicated to FRP composites for new civil infrastructures and rehabilitation of existing structures, e.g. [37, 83-91]. With the recent launching of new design codes/recommendations ([92-98]), it is expected that new high volume FRP composite markets will open up and existing markets will broaden further [99].

2.3. Hybrid FRP composites

2.3.1. Recent research trends

FRP composites are known by their freedom of design [35]. This means that there is an infinity of options to combine fibres with the matrix, which involves defining the constituent materials, the orientation of fibres, the stacking sequence of layers, and the final shape of the composite. Obviously, this freedom of choice have repercussions on performance of composites. Depending on the manner in which the constituents are combined, the properties of the FRP composite vary accordingly.

Hybridisation allows to further broaden the freedom of design of FRP composites, contributing to important mechanical or functional improvements, if the combination of fibres is properly materialized. However, hybridisation also contributes to turn design process more complex and, consequently, to make the performance of composites more difficult to predict. The hybridisation of fibres can be materialized on three different configurations [13]: (i) interlayer

or layer-by-layer, i.e., by mixing layers of different fibres, (ii) intralayer or yarn-by-yarn, i.e., by mixing the fibres within the layers, and (iii) intrayarn or fibre-by-fibre, i.e., by mixing the fibres completely at the yarn/tow level.

In the vast majority of new research works (referred to next in this paragraph), the mechanical performance of hybrid FRP composites has been the fundamental aspect of their study. In this set of works, hybridisation of commercially available UD thin-ply carbon fibres and standard ply glass fibres has received special interest, e.g. [16, 22-27, 100]. It has been proven that, in some cases, an optimised gradual tensile failure process can be achieved, thus avoiding catastrophic failure (this topic is further discussed in Section 2.3.2). The conclusions obtained in this set of works led to the recent lines of research dedicated to the study of multi-directional (specifically quasi-isotropic) hybrid composite laminates, e.g. [29, 101-103] and, at same time, intermingled hybrid composites with highly aligned discontinuous fibres [28, 30]. It should be noted that majority of these works are focused on tensile loading. More complex loading conditions, such as impact loading, received less attention and they still lack of a solid understanding [104].

To predict the mechanical behaviour of hybrid FRP composites, several analytical [21, 24, 31, 34] and numerical [17, 23, 31, 32, 105-107] models have been proposed. Swolfs *et al*. [35] classified into two categories, those that are intended to predict tensile behaviour: (i) models that take into account individual fibre breaks and how these develop into clusters of broken fibres until global failure, and (ii) ply level models which focus on predicting what happens when one or more plies have failed, without going into detail of damage development inside a single ply.

From the first category, the model of Swolfs *et al*. [17] is highlighted in this work [35] because the latter has been proven to be capable of providing reasonable quantitative results for the hybrid effect (see detailed definition in Section 2.3.2). The model uses finite element simulations to capture stress concentrations around a single broken fibre. This information is then expanded to the numerical simulation with thousands of fibres. However, this model is limited to predicting the failure strain of LS fibres and not the entire tensile stress-strain curve of hybrid FRP composite.

From the second category, the analytical model developed by Jalalvand *et al*. [24] is seen as an important milestone, since it is capable of predicting all possible damage modes of UD hybrids. Predictions from this model have been proven to be in good agreement with nonlinear tensile response of different hybrid configurations (see details in Section 2.3.2). Besides, the concept of ‘damage mode maps’ [25] was developed from this model. These maps have been proven to be a very efficient design tool for hybrid composites, since these allow studing the evolution of several tensile properties as function of absolute and relative thicknesses of the LS fibre layers. However, it should be highlighted that synergetic effects of hybridisation, such as the hybrid effect, is not included in the referred to model.

In addition to the most frequent combination of carbon with glass fibres, new polymer fibres have been explored in the development of hybrid solutions. Swolfs *et al*. [35] already referred to an interesting set of works in which the advantages of this hybridisation is highlighted. Polyarylate (PAR), polybenzobisoxazole (PBO), and ultrahigh molecular weight polyethylene (UHMWPE) are fibres that have been tested, combining these with traditional carbon fibres. It has been proven that the developed hybrid composites present improved impact performance (higher energy absorption and reduced damage area after impact), when compared with traditional ones. Furthermore, although less studied, functional improvements may as well be achieved with this new set of fibres because they offer improved thermal and fire performance.

As referred to in Section 2.2, natural fibres have been seen as promising materials, since environmental sustainability is increasingly valued nowadays. However, these fibres (especially those of plant origin) present some drawbacks, namely (i) low mechanical strength, and (ii) poor fibre/matrix adhesion. Hybridisation of natural fibres with synthetic ones has been reported in literature (once again mostly outside the context of civil engineering) as a way to improve the performance of these materials, both in environmental and mechanical terms. Simultaneously, these fibres can minimize the production costs of composites. In fact, much work has been published on this subject, e.g. [54, 55, 108-118]. However, it can be said that the development of these hybrid solutions is still taking the first steps. Given the large amount of natural fibre types, the potential to be explored is vast. From the studies carried out, the following main conclusion can be here highlighted:

- Velmurugan and Manikandan [108] studied the mechanical properties palmyra/glass hybrid composites. In this case, composites were prepared by varying both glass and palmyra fibres content, keeping the overall fibre content constant. As it was expected, mechanical properties mainly tensile, bending, shear and impact properties, increased due to hybridisation, when compared with the properties of all palmyra composites. It was concluded, as well, that moisture absorption decreases with the increase of glass fibres content. Again, this was expected because synthetic fibres are less sensitive to moisture;
- Ridzuan *et al*. [109] investigated the effect of moisture absorption on the mechanical degradation of hybrid pennisetum purpureum/glass composites. It was concluded that moisture absorption reduced with the increase of the glass fibre content. There was a reduction of 24% and 29% on tensile and flexural strength, respectively, in wet conditions, relatively to all glass composites, when the reinforcement was composed of 24% of pennisetum purpureum and 6% of glass fibres. All pennisetum purpureum composites, relatively to all glass composites, had a reduction on the tensile and flexural strength of approximately 50% and 47%, respectively;
- Ouarhim *et al*. [112] investigated the effect of alkaline treatment of rafia fibres on the thermal and mechanical properties of rafia/glass hybrid composites. The hybrid composites were made with 1 mm thick of glass fibres at faces, and treated or untreated rafia fibres of a thickness 2 mm at the core. It was concluded that the alkali treatment of

raffia fibres allowed to improve all analysed properties. Namely, flexural bending modulus (5.9%), shear strength of composite (32.1%) , shear strength between raffia fibres and matrix (38%), and thermal conductivity (7.0%). The referred to improvements are due to better interfacial adhesion between the fibres and the matrix, in the case of treated fibres. The treatment consisted of the following steps: (i) a solution of NaOH at a concentration of 8.0% (1.6 mol/L sodium hydroxide aqueous solution) was applied for 8 h at room temperature then, (ii) acetic acid (100 mL) was applied to neutralize the remaining hydroxide, and, (iii) finally the fibres were washed with distilled water for several times. The fibres were air-dried for 12 h before further use;

- Hawileh *et al*. [118] investigated the performance of basalt/carbon composites at elevated temperatures. It was shown that the degradation on the mechanical properties (elastic modulus and tensile strength) of hybrid composites subject to high temperature was lower than what was observed in all carbon composites. At 250 ºC degradation of elastic modulus and tensile strength of all carbon composite, when compared with test results obtained at 25ºC, was 90.9% and 80.5%, respectively. In the case of hybrid composites this degradation varied between 30.1% and 84.3%, for the elastic modulus, and between 24.9% and 79.8%, for the tensile strength. Analytical models, based on model proposed by Gibson *et al*. [119], were proposed to predict the variation in the elastic modulus and tensile strength with temperature. The error between experimental and analytical results varied between 2.0% and 3.7%, in the case of elastic modulus, and between 0.1% and 5.6%, in the case of tensile strength.

In addition to the above, it should be mentioned that the knowledge in metal fibres field have been evolving. These fibres present higher density than other fibres, but they have high toughness and ductility (in contrast with conventional synthetic fibres that are brittle). The use of metal fibres in composites is very scarce yet [35]. However, due to the potential of these fibres it is likely that their use will increase in the future. There are already examples of hybridisation of metal fibres with carbon fibres [120] and self-reinforced polypropylene tapes [121]. Furthermore, thin steel plies were hybridized with carbon fibres [122].

In the present section, it has presented the existing multitude of opportunities in the field of hybrid FRP composites. The great majority of recent works have been developed out of the context of civil engineering. Due to the exposed advantages, comparatively to conventional composites, it is believed that the application of hybrid FRP composites in construction industry could be very interesting and more attention should be paid to research and development of solutions to this end. Undoubtedly, the possibility of avoided tensile catastrophic failure on composites entirely composed by brittle materials is one of the great advantages of hybridisation. The same can greatly contribute to the increase of structural safety.

2.3.2. Mechanical properties

The mechanical behaviour of FRP composites has been continually studied. This is because, in most cases, the purpose of these materials is to be used in structural applications. As it is known, their mechanical response is governed by a complex set of different mechanisms (matrix cracking, delamination between plies, and debonding and subsequent pull-out between fibres and the matrix material [123]). Furthermore, it is usual to try to combine the latest developments of different individual materials in new composites. In this way, publications related with mechanical performance of composites continue to increase. Constantly, new modelling approaches are proposed, e.g. [32, 124-130]. This means that, even today, there is a lack of reliable predictive models for the simulation of the mechanical response of FRP composite materials, which is directly linked to an incomplete understanding of their failure mechanisms [131].

In particular case of tensile behaviour (the most studied topic), the development of proper models is dependent of two fundamental factors: (i) an accurate characterization of fibre strength and (ii) an understanding of the process of stress redistribution once a fibre is broken and the formation of clusters of broken fibres. It should be noted that fibre strength is a stochastic property that is dominated by a distribution of flaws (introduced during processing and handling of the fibres) [32].

Recently, Bunsell *et al*. [131] conducted a comparison between different models available in the literature to predict longitudinal tensile failure of FRP composites. It was concluded that there are significant discrepancies between the predictions of the different modelling approaches. In the same work, it is reminded that the micromechanics of longitudinal tensile failure of composites needs to be developed further.

In the present section, due to the importance that has been attributed to the tensile behaviour of FRP composites, the same is addressed in the context of hybrids. In this way, it is intended to provide the necessary basis for critically discussing the research conducted so far at civil engineering level (presented in Section 2.4).

As it is referred to in Section 2.3.1, hybrid FRP composites can be materialized in different configurations (interlayer, intralayer or intrayarn). Usually, it is tried to combine fibres with significantly different strain at the failure, in order to maximize synergistic effects. For this reason, the two fibre types (number of reinforcing materials that is typically used in hybrids) are distinguished as LS and HS fibres. The greater the difference between the strain at the failure of the two fibre types the greater the synergies. However, as explained in detail later, there are more factors that influence the tensile performance of hybrid FRP composites. It should be highlighted that if the hybrid configuration is not carefully designed, the hybrid composite may break suddenly and show a lower strength than the individual constituents.

2.3.2.1. Hybrid effect

The 'hybrid effect' is one of the important outcomes of hybrid FRP composites. Although in some works the same has been defined as the deviation of different tensile mechanical properties from the rule of mixtures, today it is unanimously understood as the increase of the apparent strain at the failure of LS material, see **Figure 2.1**. More precisely, the hybrid effect is defined as the ratio between the absolute variation of the strain at the failure of LS material (measured on UD non-hybrid and UD hybrid composites), $\Delta\varepsilon_L$, to the baseline strain at the failure of LS material (measured on UD non-hybrid composites), ε_L, according to the Equation (2.1):

$$Hybrid\ effect = \frac{\Delta\varepsilon_L}{\varepsilon_L} \times 100 \tag{2.1}$$

In the case of carbon/glass hybrid composites, the values for this effect are typically in the range of 10 to 50% [13, 132]. Generally, failure of UD composites is controlled by a critical cluster of weak fibres, and different fibres with higher strain at the failure can restrict the formation of the cluster, which explains the hybrid effect (among other factors little explored in bibliography) [13]. However, it is a matter of fact that there is some controversy about the best way to define the baseline strain at the failure of LS material. In standard tensile tests of UD non-hybrid composites, stress concentrations can arise where the load is applied leading to the reduction of the baseline strain [27]. It should be noted that, according to standards (e.g. EN 527-5 [133]) clamping system shall not cause premature facture at the grips. However, the information about the failure mode is not referred to in many works. This leads to difficulties in interpreting the results.

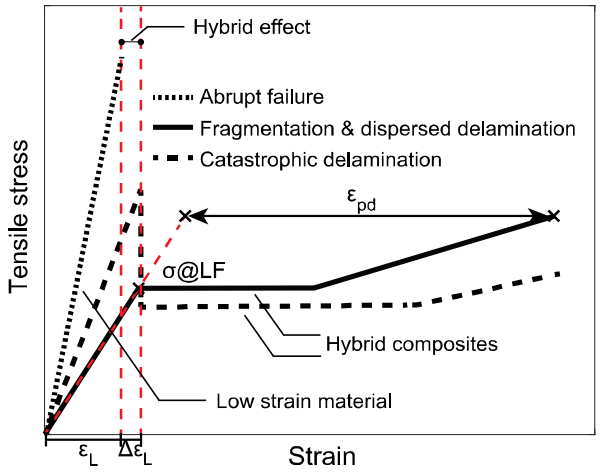

Figure 2.1 — Illustration of the hybrid effect definition and tensile nonlinear behaviour of hybrid FRP composites.

Wisnom *et al*. [27] have proposed a specimen geometry and test configuration to suppress the referred to stress concentrations. In this work carbon and glass were combined. It is indicated that hybrid effect only arises when the thickness of carbon plies varies between 0.029-0.058 mm (this means that thin carbon plies were used) and the thickness of glass plies is 0.310 mm (this means that standard thickness of glass plies were used). The modelling also presented in the work confirms the experimental results. However, hybrid composites were used to determine the strain at the failure of carbon fibres. Since the failure of composites is controlled by a critical cluster of weak fibres, and that different fibres with higher strain at the failure can restrict the formation of the cluster, the baseline strain definition of LS fibres can be somehow compromised by the referred to restriction, in opinion of the author of the present thesis.

In Chapter 5 of the present thesis, it is demonstrated that hybrid effect can actually arise in hybrid composites with carbon plies with 0.190-0.223 mm of thickness and glass or basalt plies with circa 0.310 mm of thickness (as long as the volume fraction of carbon remains below 60% of the reinforcing materials volume). Then hybrid composites were used to confine concrete cylinders. The failure strain of LS fibres in hybrid composites was measured in these cylinders, in which the gripping effects do not exist. However, in this case other sources of uncertainties can be pointed out. With particular emphasis on presence of (i) an overlap region in FRP jacket (which can conducted to stiffness variation in the jacket) and (ii) the fact that the jacket is subjected to a multiaxial stress state due to the curvature. In this way, the actual magnitude of the hybrid effect is as well conditioned by the measurement of the baseline strain in the referred to work. However, there is clear tendency of increasing the strain at the failure of carbon in hybrid composites with the decrease of the volume of the same.

An extensive work has been developed, using numerical and analytical models, to understand the hybrid effect [14-21]. In [20] and [21], it was demonstrated that the higher the scatter of LS fibres strength (usually described by Weibull distribution), the higher the hybrid effect. Furthermore, layer-by-layer hybrids are more efficient in delaying the failure development.

Based on the information collected and above summarized, it can be stated that the hybrid effect remains not thoroughly understood. There are still doubts about what it is best way to measure the strain at the failure of non-hybrid composites. For this reason, results of hybrid effect reported in bibliography should be critically interpreted.

2.3.2.2. Elastic modulus and strength

The longitudinal elastic modulus of the hybrid composites, E_{hybrid}, has been shown to follow the linear rule of mixtures (ROM) [13], considering the contributions of three constituents:

$$E_{hybrid} = V_L E_L + V_H E_H + V_M E_M \tag{2.2}$$

where V_L, V_H, V_M, E_L, E_H, and E_M are the volumetric fraction and elastic modulus of the LS fibres, HS fibres and matrix, respectively.

The tensile strength of the hybrid composites, σ_{hybrid}, follows a bilinear ROM (see Eq. (2.3)) [9, 12, 134]:

$$\sigma_{hybrid} = \begin{cases} V_L S_L + V_H E_H \varepsilon_L;\ V_H < V_{crit} \\ V_H S_H;\ V_H > V_{crit} \end{cases} \quad (2.3)$$

where S_L and S_H are the reference strengths of the LS and HS composites and ε_L is the strain at the failure of the non-hybrid LS composite.

Based on the last model, if V_H is lower than the critical value, V_{crit}, the hybrid composite would fail prematurely. On the contrary, if V_H is higher than V_{crit}, hybrid composites would keep their integrity up to the failure of HS fibres. V_{crit} is calculated by equating the two branches of equation (2.3):

$$V_{crit} = \frac{S_L}{S_L + S_H - E_H \varepsilon_L} \quad (2.4)$$

2.3.2.3. Stress-strain curve

Particular attention has been paid to UD interlayer hybrid configurations for two reasons: (i) this is the simplest and cheapest way for producing a hybrid composite, since the same consists of simply overlapping commercially available raw materials; and (ii) this is most efficient configuration to maximize the hybrid effect, as it was referred to in Section 2.3.2.1. In this way, the tensile behaviour of these materials is highlighted in the presented chapter. The analytical model of Jalalvand *et al*. [24] is briefly presented in this subsection.

In a UD hybrid FRP composite submitted to uniaxial tension, the first damage mode is always the failure of the LS fibres. However, the other damage modes depend on the properties and configuration of the composite reinforcing materials [25]. The analytical approach proposed by Jalalvand *et al.* [24] considers that four different damage modes may occur after LS fibres failure: (i) premature HS failure, (ii) unstable delamination, (iii) LS layer fragmentation, and (iv) LS fragmentation and stable delamination (see **Figure 2.2**). For each hybrid configuration, three stress levels can be computed [24]: (i) the stress at which the first crack in the LS material occurs, $\sigma@LF$, (ii) the stress at which delamination starts, $\sigma@del$, and (iii) the stress at which the HS material fails, $\sigma@HF$, in accordance with equations (2.5) to (2.7), respectively.

$$\sigma@LF = S_L \frac{\alpha\beta + 1}{\alpha(\beta + 1)} \quad (2.5)$$

$$\sigma@del = \frac{1}{1+\beta} \sqrt{\left(\frac{1+\alpha\beta}{\alpha\beta}\right)\left(\frac{2 G_{IIC} E_H}{t_H}\right)} \quad (2.6)$$

$$\sigma@HF = \frac{1}{(1+\beta)} \frac{S_H}{K_t \sqrt[m_H]{V}} \quad (2.7)$$

where S_L is the reference strength of the LS material, α and β are the modulus and thickness ratios of the LS to HS fibre, G_{IIC} is the mode II interlaminar fracture toughness of the interface between LS layers and HS layers of the hybrid composite, E_H is the elastic modulus of the HS

fibres, t_H is the half thickness of the HS fibre, m_H is the Weibull strength distribution modulus of the HS fibre, S_H is the reference strength of the HS material, K_t is the stress concentration factor in the HS material, and V is the volume of the specimen (free length × width × total fibre layer thickness).

Knowing the magnitude of all three possible stresses it is possible to assess their order of occurrence and, consecutively, the identification of the damage modes, according to **Table 2.1**. The details of the analytical approach presented in this work are fully discussed in [24].

After the determination of the damage modes, it is possible to plot the tensile stress–strain curve of hybrid FRP using the characteristic points given in **Table 2.2**. In this table, E_{sat} is the saturated modulus of the composite (according to equation (2.8)), ε_H is the failure strain of the HS fibres, and $\varepsilon_{@H\text{-}PS}$ is the strain in the composite at the post-saturation phase when the HS material fails (according equation (2.9)) [24].

$$E_{sat} = E_H \frac{\alpha\beta+1}{(\beta+1)(1+\frac{11}{18}\alpha\beta)} \tag{2.8}$$

$$\varepsilon_{@H-PS} = \frac{\varepsilon_H}{\frac{}{K_t}\sqrt[m_H]{V}} - \frac{7}{18}\frac{S_L\beta}{E_H} \tag{2.9}$$

In pseudo-ductile curves, the 'yield' stress is defined as the stress at the point that response deviates from the initial linear elastic line, i.e., equal to σ@LF and the pseudo-ductile strain is defined as the extra strain between the final failure strain and the strain on the extrapolated initial slope line at the failure stress of the stress-strain diagram (see **Figure 2.1**).

It should be noted that hybridisation of common synthetic fibres can promote the appearance of a flat-topped monotonic stress-strain curve, but the curve is not repeatable on subsequent unloadings/reloadings (similar to steel). Furthermore, this curve is dependent of fragmentation of LS material. For this reason, in FRP materials field this behaviour is known as 'pseudo-ductile'.

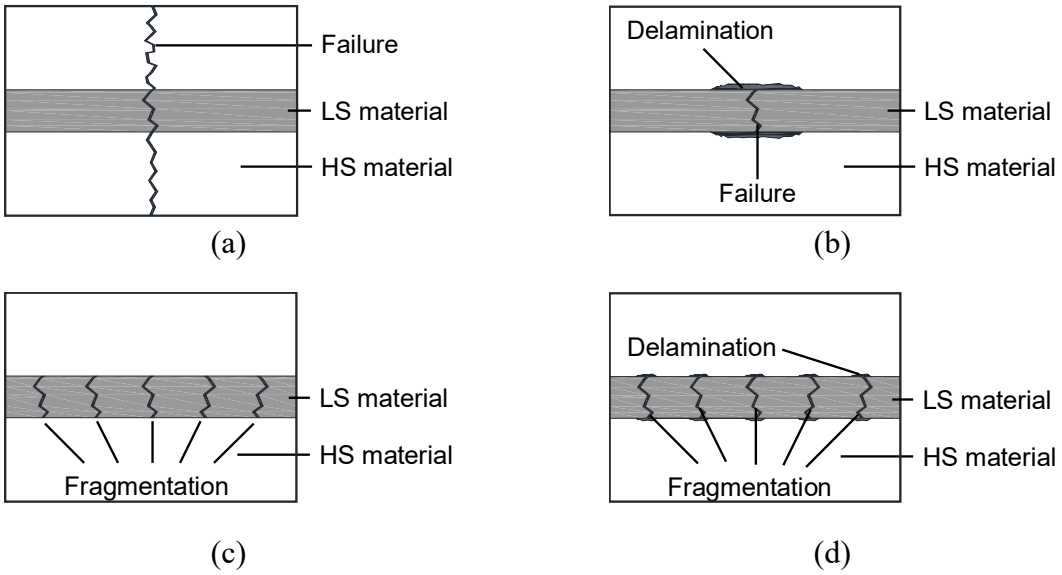

Figure 2.2 — Damage mode of longitudinal section: (a) premature HS failure; (b) unstable delamination; (c) LS layer fragmentation; (d) LS fragmentation and stable delamination.

Table 2.1 — Summary of different damage modes as function of stress level (adapted from [25]).

Damage mode	Stress level
Premature failure	$\sigma@HF \leq \sigma@LF \leq \sigma@del$
Catastrophic delamination	$\sigma@HF \leq \sigma@del \leq \sigma@LF$ $\sigma@del \leq \sigma@HF \leq \sigma@LF$ $\sigma@del \leq \sigma@LF \leq \sigma@HF$
Fragmentation	$\sigma@LF \leq \sigma@HF \leq \sigma@del$
Fragmentation & dispersed delamination	$\sigma@LF \leq \sigma@del \leq \sigma@HF$

Table 2.2 — Characteristic points of different damage processes on stress–strain graph (adapted from [24]).

Damage mode	Point 1	Point 2	Point 3	Point 4	Point 5
Premature failure	(0,0)	$(\varepsilon_L, \sigma@LF)$	--	--	--
Catastrophic delamination	(0,0)	$(\varepsilon_L, \sigma@LF)$	$(\varepsilon_L, \sigma@del)$	$\left(\frac{\sigma@del(1+\beta)}{E_H}, \sigma@del\right)$	$\left(\frac{\varepsilon_H}{K_t \sqrt[m_H]{V}}, \sigma@HF\right)$
Fragmentation	(0,0)	$(\varepsilon_L, \sigma@LF)$	$\left(\frac{\sigma@LF}{E_{sat}}, \sigma@LF\right)$	$(\varepsilon_{H-PS}, \sigma@HF)$	--
Fragmentation & dispersed delamination	(0,0)	$(\varepsilon_L, \sigma@LF)$	$\left(\frac{\sigma@LF}{E_{sat}}, \sigma@LF\right)$	$\left(\frac{\sigma@del(1+\beta)}{E_H}, \sigma@del\right)$	$\left(\frac{\varepsilon_H}{K_t \sqrt[m_H]{V}}, \sigma@HF\right)$

2.4. Hybrid FRP composites in the field of civil engineering

Research of hybrid FRP composites for civil engineering applications date back to the 1990s. At that time the research fundamentally focused in the development of three main systems: (i) reinforcing bars for reinforced concrete (RC) structures [135-147]; (ii) externally bonded strengthening for RC structures [148-166], and (iii) pultruded profiles for new structures [167-170]. More recently, some work has also been done on the development of cables for long-span bridges [171-174].

The main motivation for the development of such systems has been the interest by their mechanical performance, i.e., the search for non-abrupt failures. As it is known, large structural deformations and significant load-carrying capacity prior to ultimate failure are critical in civil engineering structures, in which weak failure modes should be avoided. This is import especially in the case of extreme event, where it is expected that structures give forewarning of failure and prevent total collapse. Close to ultimate load, some sections of the structure may reach their ultimate strength before others. In earthquake-resistant design, energy absorption by plastic hinges is necessary for ductile response of structures under seismic loads where load reversal and energy release occur [136].

Information about hybrid composites developed, between 1993 and 2018, by different authors is resumed in **Appendix I** (**Table 2.3**). The number of reinforcing materials (Nb. R.M.), relative volume between reinforcing materials, tensile strength (σ), elastic modulus (E) and strain at the failure (ε) of hybrid composites and respectively constituent materials, orientation of fibres, selected processing and fabrication, and final form of hybrid composite are presented in **Table 2.3**.

It is possible to observe that hybridisation of two reinforcing materials has been performed in most of the works. Besides, UD composites have been preferred over other solutions with fibres aligned in different directions. As it is referred to in Section 2.3.1, hybridisation promotes the complexity of composites, leading to increased difficulties in prediction of their mechanical performance. In this way, using a lower number of reinforcing materials and opting for UD composites helps to not increase the referred to complexity.

From **Table 2.3** it is also possible to observe that hand lay-up and pultrusion have been the most widely used production methods. Synthetic fibres as carbon, glass and aramid are the most frequently applied in hybridization. However, the combination of steel with synthetic fibres and resin has also been quite used, fundamentally in the development of reinforcing bars. As mentioned before, hybrid solutions with steel have been little explored in other industries. However, in the civil engineering context they have been explored, presenting a double advantage: (i) to enhance the elastic modulus of glass composites and (ii) to mitigate the corrosion problems of steel materials.

Despite much published works, it should be stated that the hybrid composites (developed for civil engineering) have been presented without a complete understanding about their behaviour

at material level. In **Table 2.3** is possible to observe that frequently tensile properties of hybrid composites are not quantified. Many times, experimental campaigns are executed without a single prediction based on the literature and existing models. In this way, all the potential of hybridisation has not been exploited. The concept of pseudo-ductility has been defined as the successive fractures of different reinforcing materials and not as a result of the previously described phenomena of fragmentation and controlled delamination of LS fibres. Besides, the hybrid effect has not been uniformly defined. In this section, it is presented a critical analysis about the most relevant work developed so far. All hybrid combinations studied in this set of works are detailed in **Table 2.3**.

2.4.1. Reinforcing bars

Somboonsong *et al*. [146] developed an innovative design methodology to produce a hybrid composite reinforcing bar named 'braidtrusion'. The same is a combination of two conventional composite manufacturing processes: (i) braiding and (ii) pultrusion. A brief overview about these two processes is presented next:

- Braiding, illustrated in **Figure 2.3**, is a textile process where multiple yarns are intertwined to form an interlocking pattern [175]. During the braiding process, the yarns are braided around a mandrel, which gives the braided preform shape. The mandrel is pulled forward while the braid is formed around it, and the relation of the rotational speed of the braid machine and the pulling speed impacts the resulting braid angle that is produced [175].
- Pultrusion, shown in **Figure 2.4**, is a manufacturing process used for producing continuous FRP structural shapes. The process involves pulling the raw materials through a heated steel-forming die using a continuous pulling device [176]. In this process, as the reinforcements are saturated with the resin (in the resin impregnator) and pulled through the die, the hardening of the resin is initiated by the heat from the die. In this way, a rigid cured profile is formed. A puller is used to move the composite through the process. The cured composite can then be cut to the desired length at the end of the line.

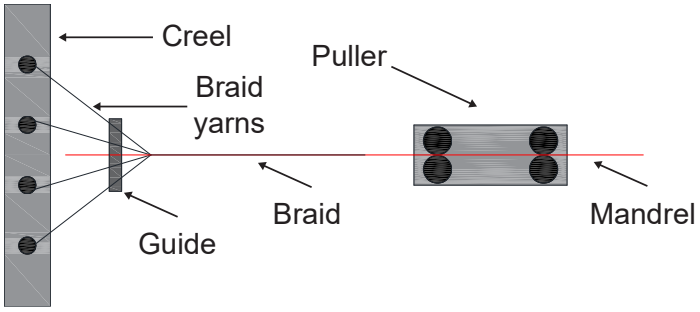

Figure 2.3 — Schematic of the braiding process (adapted from [175]).

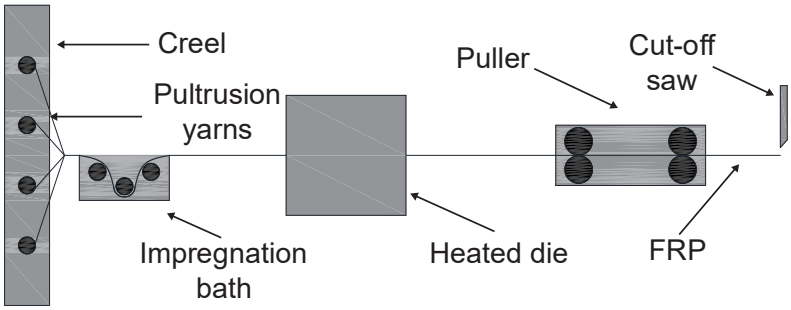

Figure 2.4 — Schematic of the pultrusion process (adapted from [175]).

In the work of Somboonsong *et al*. [146], innovative manufacturing process (see **Figure 2.5**) was used with the aim of developing a reinforcing bar that fails in a progressive manner. In this work, high modulus UD carbon fibres in the core were combined with a braided aramid fibre layer over top. The tensile stress-strain curve of the developed reinforcing bar presented several local peaks, which may indicate that carbon fragmentation occurred (although this phenomenon was not mentioned in that work). A typical pseudo-ductile behaviour is evident in experimental results. However, it is not clear from the same if the achieved pseudo-ductility derives from (i) the architecture of fibres (since the realignment of off-axis fibres can generate extra strain), (ii) the fragmentation of carbon, or (iii) a combination of both. The analytical model developed in the same work was not capable of producing stress–strain responses in a good agreement with the experimental data, i.e., the pseudo-ductile behaviour was not predicted.

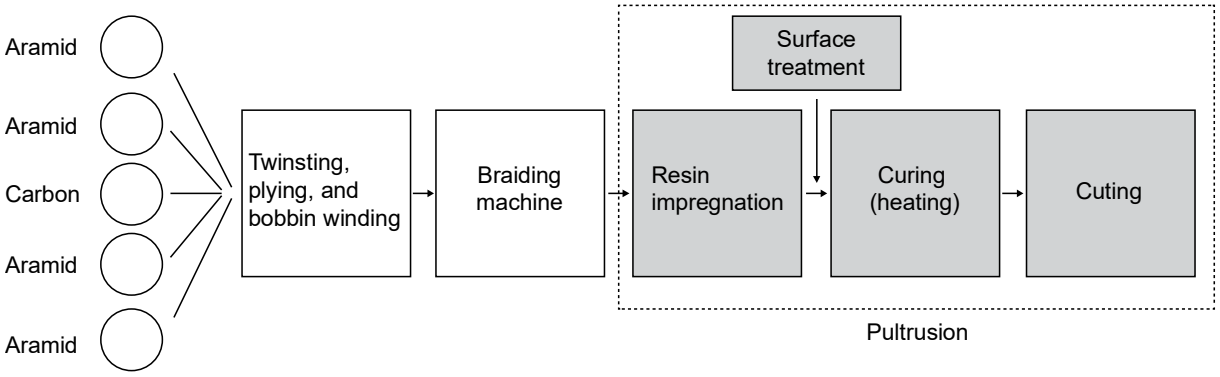

Figure 2.5 — Schematic of braidtrusion (adapted from **[136]**).

Won *et al*. [139] used braidtrusion process to produce three types of hybrid (listed in **Table 2.3**) and a glass FRP reinforcing bar. Tensile behaviour, fracture properties, and bond performance of carbon/aramid and carbon/glass combinations were evaluated. The hybrid FRP reinforcing bar have shown elastic behaviour up to a first local maximum, but had very irregular behaviour thereafter. It was observed that the fibres in braided cover of the hybrid FRP broken at very

irregular lengths. According to the bond test results, the hybrid FRP reinforcing bar specimens had greater bond strength than all glass FRP reinforcing bars.

Seo *et al*. [144] also used the braidtrusion process to produce several configurations of hybrid reinforcing bars consisting of steel and glass (GFRP), as listed in **Table 2.3** and illustrated in **Figure 2.6**. It should be highlighted that these reinforcing bars are not entirely made up of fibres. The objective of this work was to find the best solution to increase elastic modulus of all glass FRP reinforcing bars by using steel. It was concluded that the elastic modulus of hybrid FRP reinforcing bar increased up to 250% comparatively to the glass FRP bar, if configuration presented in **Figure 2.6** (c) is used.

Rana *et al*. [177] developed as well hybrid FRP reinforcing bars and characterized their strain sensing capability. A mixture of carbon and glass fibres was used in the core, which was surrounded by a braided cover of polyester fibres. The effect of carbon/glass weight ratio on both strain sensitivity and tensile properties were investigated. It was observed that the studied hybrid composites with lowest amount of carbon fibres (23%) led to the best strain sensitivity, i.e. the higher quotient between the change in electrical resistance and the initial resistance of the bar and the flexural strain of the latter, and higher tensile strength. The change of resistance in the hybrid composites was mainly attributed to strain-dependent change in the electrical contacts, either due to fibre separation or fibre alignment or both.

You *et al*. [145] carried out an experimental campaign on the tensile properties of several hybrid FRP reinforcing bars. Different dosages of carbon and glass fibres were used. Three different material architectures were as well considered for hybrid FRP rods (see **Figure 2.7**). It was concluded that differences in the tensile behaviour occurred according to the method adopted to arrange a given quantity of glass and carbon fibres. The tensile strength, elastic modulus, and ultimate strain of the specimens with carbon fibre arranged in the core was higher than the specimens with the carbon fibre arranged on the surface. Pseudo-ductile behaviour was not observed in this study.

Bakis *et al*. [137] developed a hybrid FRP reinforcing bar with capability to monitor strain. Different combinations of carbon, aramid, glass, and vinylon were evaluated. The electrical resistance of the hybrid reinforcing in function of their tensile strain was evaluated. It was concluded that the hybrid reinforcing bars with 6 and 13% of carbon dispersed in the section showed best early-warning of catastrophic failure.

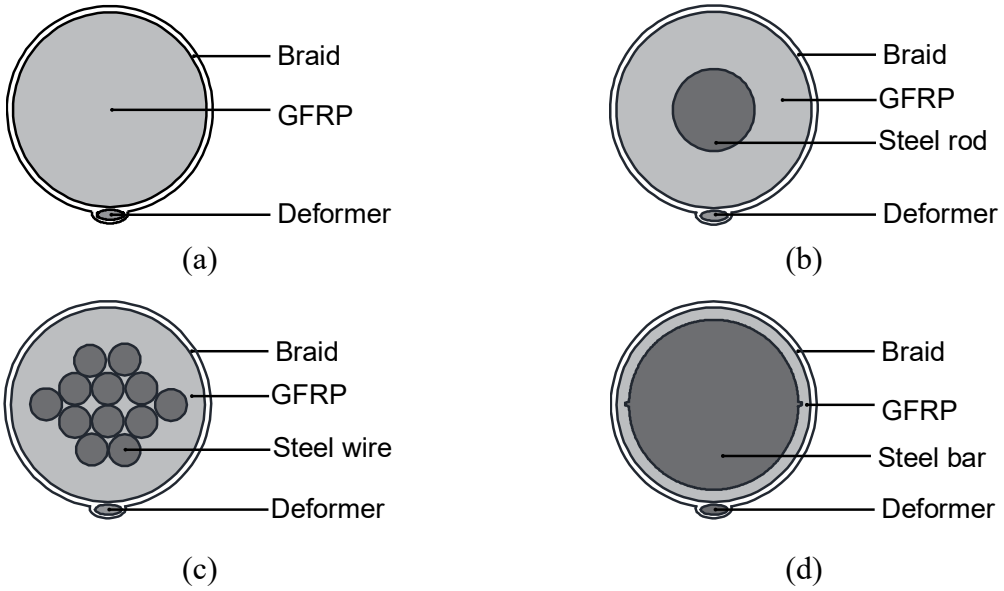

Figure 2.6 — Illustration of cross section types of hybrid bars (adapted from **[144]**).

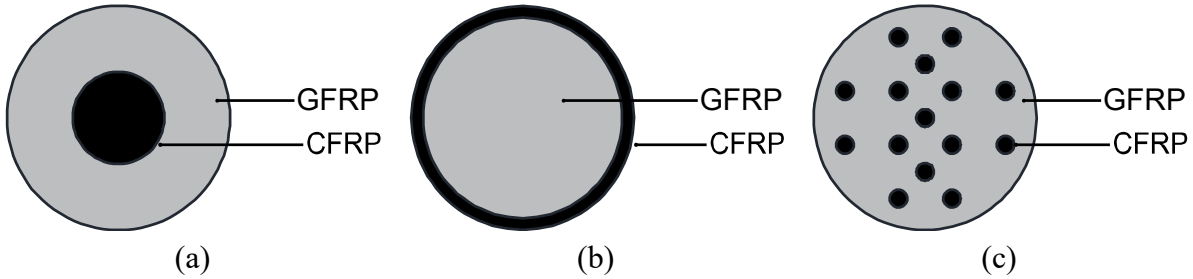

Figure 2.7 — Illustration of cross section of hybrid FRP rods (adapted from **[145]**).

2.4.2. Externally bonded strengthening

2.4.2.1. FRP-confined concrete

Wu *et al*. [157] studied the compressive behaviour of hybrid FRP-confined small-scale plain concrete columns. Ten hybrid combinations were contemplated. UD dry fabrics of standard-modulus carbon, high modulus carbon, aramid, glass, and PBO were used. In this work, neither the advantage of the hybrid effect nor the pseudo-ductility are evidenced. The combination of one layer of high modulus carbon and two layers of standard-modulus carbon in confining system lead to highest compressive strength (73.9 MPa). The combination of one layer of high modulus carbon and two layers of aramid in confining system lead to highest strain at the failure strength (3.94%). Based on the experimental data, an axial compressive stress - axial strain model was proposed. The relative errors varied between -19.0% and 17.8%, in the case of peak stress predictions, and between -29.8% and 16.7%, in the case of strain at the failure predictions.

Luca *et al*. [158] studied full-scale square and rectangular RC columns ([356-610]/[508-737]/3048 mm overall width/length/height, respectively) externally confined with all glass and basalt/glass FRP jackets. It was concluded that the contribution to column confinement of the hybrid FRP jackets was similar to that of the non-hybrid jackets. This was expected because the reinforcing materials used in hybrid combination have very similar mechanical properties. Different analytical models from other authors were used to predict the strength of concrete columns. According to this work, the model of Wang and Restrepo [178] lead to best predictions (with relative errors varying between 16.8% and 23.3%, in the case of square columns, and between 20.0% and 41.2%, in the case of rectangular columns).

Deng and Qu [166] carried out an experimental campaign on axial compression behaviour of ultra-high performance concrete filled hybrid FRP tubes. Carbon, aramid, basalt, and glass UD dry fabric were used as reinforcing materials, on combinations of two or three materials (see **Table 2.3**). The test results show that the local rupture of hybrid FRP tubes did not lead to abrupt failure of confined concrete. The combination of carbon with glass lead to highest increase of the confined concrete strength (3.14 times higher that plain concrete strength) and strain at the failure (7.07 times higher that strain at the failure of plain concrete). An analytical model was proposed to predict the compressive stress-strain curve of confined concrete. Experimental curves were reasonably predicted. In this work, none of the results evidenced pseudo-ductility.

Ispir *et al*. [165] conducted a similar study on compressive behaviour hybrid FRP-confined small-scale plain concrete columns. In this work, carbon, glass, polyethylene terephthalate (PET) fibres were combined. It was demonstrated that it is possible promote the appearance of flat-topped compressive curve of concrete confined with hybrid FRP jackets. It is stated that after the failure of LS material, the hybrid FRP-confined concrete could exhibit two different compressive stress-strain responses, which may be either characterized with an ascending range or horizontal plateau. It was observed that the use of carbon/PET combination promote the last. It was not validated if the horizontal plateau was due to carbon fragmentation. Different analytical models from other's works were used to predict the stress and strain confined concrete. It was verified that the model of Ilki and Kumbasar [179] can be used to predict stress values of the specimens confined with hybrid FRP composites (with errors varying between 8.0% and 9.7%), and Ilki et al. [180] (with errors around 19.7%), and energy balance method [165] (with errors between 33.0% and 37.0%) exhibit the best prediction strain performance for the first model.

2.4.2.2. Strengthening of concrete beams

Grace *et al*. [148] developed a UD fabric composed of two types of carbon fibres and one type of glass fibres. In this case, the pseudo-ductility of the composite was achieved through the combination of fibres with different strain at the failure, i.e., pseudo-ductility was defined as successive fractures of different reinforcing materials and the fragmentation of LS material was not explored. It was concluded that beams strengthened with hybrid composites have higher

increase in yield load than those strengthened with non-hybrid carbon composites. Beams strengthened with hybrid composite shown a yield plateau.

In [149], the latter authors further developed the initial concept by introducing fibres in the diagonal direction, thus enabling the use of the hybrid fabric for simultaneous flexural and shear strengthening of concrete beams. The last work resulted in one US patent [181]. It was concluded that the beams exhibited a yielding plateau and reached its shear capacity simultaneously with fabric yield.

Wu *et al*. [150] developed hybrid composites made of high-strength and high-modulus carbon sheets. The resulting solution was applied in the flexural strengthening of pre-cracked RC beams (with 150/200/2100 mm overall height/width/length, respectively). It was concluded that the hybrid composites allowed achieving the desired flexural stiffness, higher yielding strength (15-22% higher than the beam strengthened with high-strength carbon), and pseudo-ductility. In this work, both the hybrid effect and the pseudo-ductility are well explained, according to the most relevant bibliography on the subject.

Nikopour and Nehdi [156] investigated the behaviour of reinforced concrete (RC) beams (with 150/250/2438 mm overall height/width/length, respectively) strengthened by UD non hybrid and hybrid bidirectional FRP composites. The aim of this work was to increase the ultimate shear capacity of retrofitted beam. Hybrid FRP were applied at the beam extremities, wrapping it. According to this study, the use of bidirectional hybrid composites lead that fibres applied in transverse direction (aramid or glass) promote a confinement action at fibres applied in main direction (carbon), which allows the latter to approach its ultimate strain capacity. It was demonstrated that hybrid composites allowed an increase of 40% of ultimate shear capacity of strengthened beam, comparatively to the solution in which all carbon composites were used.

Attari *et al*. [151] studied the efficiency of carbon/glass hybrid combination in the flexural strengthening of reinforced concrete beams (with 160/100/1500 mm overall height/width/length, respectively). Different strengthening configurations were considered, using UD carbon and glass fabrics and bidirectional carbon/glass hybrid fabric. A strength capacity of 114% was obtained for the beam strengthened with glass carbon bidirectional hybrid composite, specimens in comparison with the reference control specimen of reinforced concrete. An analytical model to predict the flexural failure of strengthened concrete elements was also presented.

2.4.2.3. Other developments

Li *et al*. [162] developed a complex hybrid FRP to strengthen a concrete column–beam joint. For that purpose, they used simultaneously E-glass woven roving, plain carbon cloth and chopped strand mat, and glass tape. The results showed that retrofitting critical sections of concrete frames with hybrid FRP can provide significant strength and stiffeness to concrete frames and improve their behaviour under different types of loading.

Attari *et al*. [163] studied a reinforced concrete beam–column joint strengthened with hybrid FRP composite under cyclic loading. Hybrid FRP composites were made of carbon laminates and glass UD fabrics. It was observed that the combination of carbon with glass improves the shear resistance and the ductility of the RC joints, giving 44% and 23% of strength and ductile index gain, respectively, when compared with a specimen without any strengthening. The justification to the use of glass fabric was that it confined the concrete effectively and did not allow it to spall-off.

2.4.3. Pultruded profiles

Ranganathan and Mantena [167] studied the effects of hybridisation on the buckling characteristics of flat pultruded graphite/glass composite beams. Finite element models were developed with different beam dimensions and end constraint conditions to simulate different buckling conditions. Experiments were conducted to verify and validate the analytical and finite element results. Results showed that the critical buckling loads for hybrid composites lie in between the critical buckling loads of all glass and all graphite composites. Results from finite element modelling were in close agreement with experimental observations.

Hai *et al*. [170] developed an innovative hybrid FRP beam consisting of carbon/glass fibres and vinyl ester resin. The aim of the work was to investigate the optimum use of carbon and glass fibres in the flanges to maximize structural performance while reducing the overall cost by using only glass fibres in the web section. It was concluded that the failure strength and failure mode of hybrid FRP beams are dependent on the carbon volume content in the flanges. The optimum carbon volume content in the flanges for the best hybridisation of FRP beams was experimentally and numerically determined to be equal to 25–33%.

The effectiveness of utilizing hybridization to improve the local buckling capacity of pultruded wide flange I-beams loaded in bending was as well numerically studied by Ragheb [168]. In this work glass and carbon fibres were considered. A finite element model was built and a parametric study was conducted to investigate the effectiveness of different hybridization patterns in improving the local buckling capacity of the beam hybridisation. In this work were took into account (1) mat laminates that are made of randomly oriented chopped fibres in a form of a sheet and (2) roving laminates that contain continuous fibre yarns that are typically parallel to the longitudinal axis of the beam (see **Figure 2.8**). In this work, the following materials were considered: (i) a roving composed by 0.153 roving/mm of glass and 2.025 roving/mm of carbon (Roving A), (ii) a roving composed by 0.122 roving/mm of glass and 1.618 roving/mm of carbon (Roving B), (iii) a mat composed by 0.45 kg/m^2 of glass and 0.30 kg/m^2 of carbon (Mat A), and (iv) a mat composed by 0.60 kg/m^2 of glass and 0.45 kg/m^2 of carbon (Mat B). The beam considered was a wide flange I-beam that had a height of 203 mm, a flange width of 203 mm, and a thickness of 9.5 mm for both the web and the flanges. Results showed that significantly higher critical buckling loads (above 60% of increase) can be obtained if a proper hybridisation is employed.

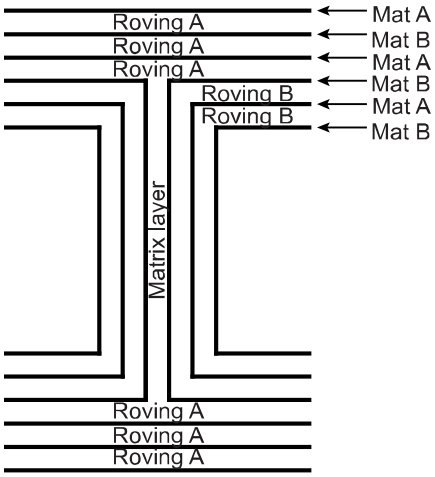

Figure 2.8 — Schematic of stacking sequence of a hybrid FRP pultruded I-beam (adapted from **[168]**).

Nunes *et al.* [169, 182] studied hybrid composite profiles of glass and carbon submitted to concentric compression. The main goal was to investigate the influence of introducing carbon layers reinforcement in glass composite pultruded columns. Three different lengths were considered in the production of profiles aiming at studying local and global buckling phenomena: (i) 0.60 m, (ii) 1.00 m, and (iii) 2.00 m. This work included experimental and numerical approaches. It was verified that even though small amounts of carbon (2.6% of the cross-section area) provided an increase in axial stiffness up to 17%. In long columns, the referred to stiffness increase promoted a higher global buckling critical load (10–17% above than the obtained on reference glass composite profile). In short and intermediate length hybrid columns, progressive delamination of the carbon mats led that the critical buckling load of those hybrid columns was lower (1–13%) than that of the reference series. Numerical prediction of the ultimate loads presented a reasonably good agreement with the experimental data (with a maximum error of 12.6%); the predicted failure modes were also consistent with those observed experimentally.

2.4.4. Cables

In the work of Wang *et al*. [172] two kinds of hybridisation: (i) basalt/carbon fibres and (ii) basalt fibres/steel-wire with 0.7 mm in diameter were adopted to develop FRP tendons. The fatigue strength of basalt/carbon combination was enhanced greatly in comparison to the obtained results with all basalt FRP solution. On the other hand, combining basalt fibres with steel-wires contributes to the fatigue behaviour enhancement of steel wires. In this work, the definition of hybrid effect is understood as on enhancing of mechanical of properties.

Yang *et al*. [171] studied the vibration characteristics and damping properties of a newly developed FRP cable with a self-damping function. In the materialization of the cable basalt fibres in the core and carbon/basalt combination in outer layer were used. Between the FRP materials was inserted a viscoelastic material (a silicone sealant). The idea is that relative motion between the two composite materials interact with viscoelastic. Because of the viscoelasticity and dissipation characteristics, viscoelastic materials can dissipate the vibration energy. It was concluded that hybrid FRP cables not only exhibit integrated advantages in static and dynamic behaviour for long-span cable-stayed bridges, but they also can provide superior vibration control ability as compared with conventional steel and all carbon FRP cables.

2.5. Summary and conclusions

The interest in FRP composite materials for both new construction and rehabilitation of existing structures has increased significantly over the last decades. This has been motivated especially by both higher strength and higher durability of FRP composites, when compared to traditional materials. As it is herein explained, these materials can respond to today's economic, environmental and social sustainability concerns of the construction industry.

Future trends for FRP composite materials will certainly involve the development of hybrid FRP composites. It is mentioned that the design of conventional FRP composites can be further extended with hybridisation, contributing to important mechanical and/or functional improvements. However, it is the mechanical characteristics of these materials that have attracted most interest and attention. This is because it has been proven that tensile gradual failure process (known as pseudo-ductile) and hybrid effects can be achieved, if hybrid combination is carefully designed. It should be highlighted that the possibility of avoiding tensile catastrophic failure with composites entirely constituted by brittle materials is one of the major advantages of hybridisation, since the latter can effectively contribute to increase structural safety.

Although knowledge in the field of hybrid composites has significantly evolved in recent years, there are still many open questions. Namely, the hybrid effect remains not thoroughly understood. There are doubts about what it is best way to measure the strain at the failure of non-hybrid composites. Today, models that are capable of predict the entire tensile stress-strain curve of hybrid FRP composite do not take account of the hybrid effect.

All the work on the development of hybrid FRP composites for civil engineering applications allows assuming these as very promising. The work has been fundamentally focused in the development of reinforcing bars for RC structures, externally bonded strengthening solutions for RC structures, pultruded profiles for new structures, and cables for long-span bridges. In spite of the significant amount of literature addressing this topic, the latter has been presented without a complete understanding about fundamental properties of hybrid FRP composites at material level, i.e., the adopted material combinations have not been substantiated with solid

scientific knowledge and the results have not been discussed with sufficient detail. Besides, fragmentation of LS material in developed hybrid composites has not been explored at all in civil engineering works. Recent lines of research dedicated to the study of intermingled hybrid composites with highly aligned discontinuous fibres or quasi-isotropic hybrid composite laminates have also never been explored.

Taking into account new fibre types, innovative architectural designs and emerging structural models, many opportunities of development are anticipated for hybrid FRP materials. However, it is expected that their adoption by the construction market will take time. As it is known, this industry is quite conservative, being subjected to strict rules and codes of practice. Therefore, the development of design guidelines is always the first step for any unconventional material to be widely accepted by the sector.

2.6. References

[1] Yi X-S, Du S, Zhang L. Composite Materials Engineering, Volume 1 - Fundamentals of Composite Materials.: Springer Singapore; 2018.
[2] Soutis C. 1 - Introduction: Engineering requirements for aerospace composite materials. In: Irving PE, Soutis C, editors. Polymer Composites in the Aerospace Industry: Woodhead Publishing; 2015. p. 1-18.
[3] Summerscales J, Short D. Carbon fibre and glass fibre hybrid reinforced plastics. Composites. 1978;9(3):157–66.
[4] Marron G, Fisher S, Tuler FR, Wagner HD. Hybrid effects in composites: conditions for positive or negative effects versus rule-of-mixtures behaviour Journal of Materials Science. 1978;13(7):1419–26.
[5] Phillips LN. Improving racing-car bodies. Composites. 1969;1:50-1.
[6] Zweben C. Tensile strength of hybrid composites. Journal of Materials Science 1977;12:1325-37.
[7] Kirk JN, Munro M, Beaumont PWR. The fracture energy of hybrid carbon and glass fibre composites. Journal of Materials Science. 1978:2197-204.
[8] Hancox NL, Wells H. Aluminum/Carbon Fiber Hybrid Composites. Polymer Engineering and Sience. 1979;19(13).
[9] Manders PW, Bader MG. The strength of hybrid glass/carbon fibre composites - Part 1. Journal of Materials Science. 1981;16:2233-45.
[10] Phillips MG. Composition parameters for hybrid composite materials. Composites. 1981;12(2):113-6.
[11] Harlow BG. Statistical Properties of Hybrid Composites. I. Recursion Analysis. Proc R Soc Lond A 1983;389:67-100.
[12] Kretsis G. A review of the tensile, compress,ve, flexural and shear properties of hybrid fibre reinforced plastics. Composites. 1987;18(1).
[13] Swolfs Y, Gorbatikh L, Verpoest I. Fibre hybridisation in polymer composites: a review. Composites Part A: Applied Science and Manufacturing. 2014;67:181-200.
[14] Swolfs Y, Gorbatikh L, Romanov V, Orlova S, Lomov SV, Verpoest I. Stress concentrations in an impregnated fibre bundle with random fibre packing. Composites Science and Technology. 2013;74:113–20.

[15] Swolfs Y, Gorbatikh L, Verpoest I. Stress concentrations in hybrid unidirectional fibre-reinforced composites with random fibre packings. Composites Science and Technology. 2013;85:10–6.
[16] Swolfs Y, Czél G, Jalalvand M, Wisnom M, Verpoest I, Gorbatikh L. Model validation of the hybrid effect in carbon/glass hybrid composites. 7th International Conference on Composites Testing and Model Identification, IMDEA, 2015. 2015.
[17] Swolfs Y, McMeeking RM, Verpoest I, Gorbatikh L. The effect of fibre dispersion on initial failure strain and cluster development in unidirectional carbon/glass hybrid composites. Composites: Part A 2015;69:279–87.
[18] Swolfs Y, McMeeking RM, Verpoest I, Gorbatikh L. Matrix cracks around fibre breaks and their effect on stress redistribution and failure development in unidirectional composites. Composites Science and Technology 2015;108:16–22.
[19] Swolfs Y, Verpoest I, Gorbatikh L. Issues in strength models for unidirectional fibre-reinforced composites related to Weibull distributions, fibre packings and boundary effects. Composites Science and Technology 2015;114:42–9.
[20] Swolfs Y, Verpoest I, Gorbatikh L. Maximising the hybrid effect in unidirectional hybrid composites. Materials and Design. 2016;93:39–45.
[21] Swolfs Y, McMeeking RM, Rajan VP, Zok FW, Verpoest I, Gorbatikh L. Global load-sharing model for unidirectional hybrid fibre-reinforced composites. Journal of the Mechanics and Physics of Solids. 2015;84:380–94.
[22] Czél G, Wisnom MR. Demonstration of pseudo-ductility in high performance glass/epoxy composites by hybridisation with thin-ply carbon prepreg. Composites: Part A: Applied Science and Manufacturing. 2013;52:23–30.
[23] Jalalvand M, Czél G, Wisnom MR. Numerical modelling of the damage modes in UD thin carbon/glass hybrid laminates. Composites Science and Technology. 2014;94:39–47.
[24] Jalalvand M, Czél G, Wisnom MR. Damage analysis of pseudo-ductile thin-ply UD hybrid composites – A new analytical method. Composites: Part A. 2015;69:83–93.
[25] Jalalvand M, Czél G, Wisnom MR. Parametric study of failure mechanisms and optimal configurations of pseudo-ductile thin-ply UD hybrid composites. Composites: Part A. 2015; 74:123–31.
[26] Czél G, Jalalvand M, Wisnom MR. Design and characterisation of advanced pseudo-ductile unidirectional thin-ply carbon/epoxy–glass/epoxy hybrid composites. Composite Structures. 2016;143:362–70.
[27] Wisnom MR, Czél G, Swolfs Y, Jalalvand M, Gorbatikh L, Verpoest I. Hybrid effects in thin ply carbon/glass unidirectional laminates: Accurate experimental determination and prediction. Composites: Part A. 2016;88:131–9.
[28] Yu H, Longana ML, Jalalvand M, Wisnom MR, Potter KD. Pseudo-ductility in intermingled carbon/glass hybrid composites with highly aligned discontinuous fibres. Composites: Part A 2015;73:35–44.
[29] Fotouhi M, Jalalvand M, Wisnom MR. High performance quasi-isotropic thin-ply carbon/glass hybrid composites with pseudo-ductile behaviour in all fibre orientations. Composites Science and Technology. 2017;152:101-10.
[30] Longana ML, Yu H, Jalavand M, Wisnom MR, Potter KD. Aligned discontinuous intermingled reclaimed/virgin carbon fibre composites for high performance and pseudo-ductile behaviour in interlaminated carbon-glass hybrids. Composites Science and Technology. 2017;143:13-21.
[31] Tavares RP, Melro AR, Bessa MA, Turon A, Liu WK, Camanho PP. Mechanics of hybrid polymer composites: analytical and computational study. Comput Mech DOI 101007/s00466-015-1252-0. 2016.

[32] Tavares RP, Otero F, Turon A, Camanho PP. Effective simulation of the mechanics of longitudinal tensile failure of unidirectional polymer composites. International Journal of Fracture. 2017;208(1-2):269-85.
[33] Selezneva M, Swolfs Y, Katalagarianakis A, Ichikawa T, Hirano N, Taketa I, et al. The brittle-to-ductile transition in tensile and impact behavior of hybrid carbon fibre/self-reinforced polypropylene composites. Composites Part A: Applied Science and Manufacturing. 2018;109:20-30.
[34] Guerrero JM, Mayugo JA, Costa J, Turon A. A 3D Progressive Failure Model for predicting pseudo-ductility in hybrid unidirectional composite materials under fibre tensile loading. Composites Part A: Applied Science and Manufacturing. 2018;107:579-91.
[35] Swolfs Y, Verpoest I, Gorbatikh L. Recent advances in fibre-hybrid composites: materials selection, opportunities and applications. International Materials Reviews. 2018:1-35.
[36] Hollaway LC. Chapter 50: Polymer fibre composites: an introduction. ICE manual of Construction Materials2009. p. 599-601.
[37] Hollaway LC. A review of the present and future utilisation of FRP composites in the civil infrastructure with reference to their important in-service properties. Construction and Building Materials. 2010;24(12):2419-45.
[38] Zhang C, Canning L. Application of non-conventional materials in construction. Proceedings of the Institution of Civil Engineers - Construction Materials. 2011;164(4):165-72.
[39] Hall C. Chapter 1: Fundamentals of materials. ICE manual of Construction Materials2009. p. 001-13.
[40] Guo F, Al-Saadi S, Singh Raman RK, Zhao XL. Durability of fiber reinforced polymer (FRP) in simulated seawater sea sand concrete (SWSSC) environment. Corrosion Science. 2018;141:1-13.
[41] Frigione M, Lettieri M. Durability Issues and Challenges for Material Advancements in FRP Employed in the Construction Industry. Polymers. 2018;10(3):247.
[42] Cabral-Fonseca S, Correia JR, Custódio J, Silva HM, Machado AM, Sousa J. Durability of FRP - concrete bonded joints in structural rehabilitation: A review. International Journal of Adhesion and Adhesives. 2018;83:153-67.
[43] Sethi S, Ray BC. Environmental effects on fibre reinforced polymeric composites: Evolving reasons and remarks on interfacial strength and stability. Advances in Colloid and Interface Science. 2015;217:43-67.
[44] Sen R. Developments in the durability of FRP-concrete bond. Construction and Building Materials. 2015;78:112-25.
[45] Silva MAG, da Fonseca BS, Biscaia H. On estimates of durability of FRP based on accelerated tests. Composite Structures. 2014;116:377-87.
[46] Ali AH, Mohamed HM, Benmokrane B, ElSafty A, Chaallal O. Durability performance and long-term prediction models of sand-coated basalt FRP bars. Composites Part B: Engineering. 2019;157:248-58.
[47] D'Antino T, Pisani MA. Influence of sustained stress on the durability of glass FRP reinforcing bars. Construction and Building Materials. 2018;187:474-86.
[48] Azzawi MA, Hopkins P, Mullins G, Sen R. FRP–Concrete Bond after 12-Year Exposure in Tidal Waters. Journal of Composites for Construction. 2018;22(5):04018031.
[49] Dong Z-Q, Wu G, Zhao X-L, Lian J-L. Long-Term Bond Durability of Fiber-Reinforced Polymer Bars Embedded in Seawater Sea-Sand Concrete under Ocean Environments. Journal of Composites for Construction. 2018;22(5):04018042.

[50] A. Gonilha J, R. Correia J, A. Branco F, Sena-Cruz J. Durability of GFRP-concrete adhesively bonded connections: Experimental and numerical studies. Engineering Structures. 2018;168:784-98.
[51] Fernandes P, Sena-Cruz J, Xavier J, Silva P, Pereira E, Cruz J. Durability of bond in NSM CFRP-concrete systems under different environmental conditions. Composites Part B: Engineering. 2018;138:19-34.
[52] Wang J, GangaRao H, Liang R, Liu W. Durability and prediction models of fiber-reinforced polymer composites under various environmental conditions: A critical review. Journal of Reinforced Plastics and Composites. 2016;35(3):179-211.
[53] Karbhari VM. Durability of Composites for Civil Structural Applications: Woodhead Publishing; 2007.
[54] Senthilkumar K, Saba N, Rajini N, Chandrasekar M, Jawaid M, Siengchin S, et al. Mechanical properties evaluation of sisal fibre reinforced polymer composites: A review. Construction and Building Materials. 2018;174:713-29.
[55] Alkbir MFM, Sapuan SM, Nuraini AA, Ishak MR. Fibre properties and crashworthiness parameters of natural fibre-reinforced composite structure: A literature review. Composite Structures. 2016;148:59-73.
[56] Ma G, Yan L, Shen W, Zhu D, Huang L, Kasal B. Effects of water, alkali solution and temperature ageing on water absorption, morphology and mechanical properties of natural FRP composites: Plant-based jute vs. mineral-based basalt. Composites Part B: Engineering. 2018;153:398-412.
[57] Chen J, Chouw N. Effect of the interface condition on the bond between flax FRP tube and coconut fibre reinforced concrete composites. Construction and Building Materials. 2018;167:597-604.
[58] Tan H, Yan L, Huang L, Wang Y, Li H, Chen J-y. Behavior of sisal fiber concrete cylinders externally wrapped with jute FRP. Polymer Composites. 2017;38(9):1910-7.
[59] Natural Fiber Composite Strengthening Solution for Structural Beam Component for Enhanced Flexural Strength, as Alternatives to CFRP and GFRP Strengthening Techniques. Handbook of Composites from Renewable Materials.
[60] Mahjoub R, Yatim JM, Mohd Sam AR, Hashemi SH. Tensile properties of kenaf fiber due to various conditions of chemical fiber surface modifications. Construction and Building Materials. 2014;55:103-13.
[61] Herrera-Franco PJ, Valadez-González A. Mechanical properties of continuous natural fibre-reinforced polymer composites. Composites Part A: Applied Science and Manufacturing. 2004;35(3):339-45.
[62] Ochi S. Mechanical properties of kenaf fibers and kenaf/PLA composites. Mechanics of Materials. 2008;40(4):446-52.
[63] Sapuan SM, Leenie A, Harimi M, Beng YK. Mechanical properties of woven banana fibre reinforced epoxy composites. Materials & Design. 2006;27(8):689-93.
[64] Wang X, Shi J, Wu G, Yang L, Wu Z. Effectiveness of basalt FRP tendons for strengthening of RC beams through the external prestressing technique. Engineering Structures. 2015;101:34-44.
[65] Wang Z, Yang Z, Yang Y, Xian G. Flexural fatigue behavior of a pultruded basalt fiber reinforced epoxy plate subjected to elevated temperatures exposure. Polymer Composites. 2018;39(5):1731-41.
[66] Lu Z, Xian G. Combined effects of sustained tensile loading and elevated temperatures on the mechanical properties of pultruded BFRP plates. Construction and Building Materials. 2017;150:310-20.

[67] Lu Z, Xian G, Li H. Effects of elevated temperatures on the mechanical properties of basalt fibers and BFRP plates. Construction and Building Materials. 2016;127:1029-36.
[68] Wu G, Dong Z-Q, Wang X, Zhu Y, Wu Z-S. Prediction of Long-Term Performance and Durability of BFRP Bars under the Combined Effect of Sustained Load and Corrosive Solutions. Journal of Composites for Construction. 2015;19(3):04014058.
[69] Wang H, Sun X, Peng G, Luo Y, Ying Q. Experimental study on bond behaviour between BFRP bar and engineered cementitious composite. Construction and Building Materials. 2015;95:448-56.
[70] Liu H-X, Liu G-J, Wang X-Z, Kong X-Q. Effect of cross-sectional aspect ratio and basalt fiber-reinforced polymer-confined number on axial compression behavior of short columns. Journal of Reinforced Plastics and Composites. 2015;34(10):782-94.
[71] Fiore V, Scalici T, Calabrese L, Valenza A, Proverbio E. Effect of external basalt layers on durability behaviour of flax reinforced composites. Composites Part B 2016;84:258-65.
[72] Jamshaid H, Mishra R. A green material from rock: basalt fiber – a review. The Journal of The Textile Institute. 2016;107(7):923-37.
[73] Fiore V, Scalici T, Di Bella G, Valenza A. A review on basalt fibre and its composites. Composites Part B: Engineering. 2015;74:74-94.
[74] Scalici T, Pitarresi G, Badagliacco D, Fiore V, Valenza A. Mechanical properties of basalt fiber reinforced composites manufactured with different vacuum assisted impregnation techniques. Composites Part B: Engineering. 2016;104:35-43.
[75] Kogan FM, Nikitina OV. Solubility of chrysotile asbestos and basalt fibers in relation to their fibrogenic and carcinogenic action. Environmental Health Perspectives. 1994;102(suppl 5):205-6.
[76] Uitterhaegen E, Parinet J, Labonne L, Mérian T, Ballas S, Véronèse T, et al. Performance, durability and recycling of thermoplastic biocomposites reinforced with coriander straw. Composites Part A: Applied Science and Manufacturing. 2018;113:254-63.
[77] McIsaac A, Fam A. The effect of bio-based content in resin blends on tensile properties of FRP wet layup systems. Construction and Building Materials. 2018;168:328-37.
[78] Ng F, Couture G, Philippe C, Boutevin B, Caillol S. Bio-Based Aromatic Epoxy Monomers for Thermoset Materials. Molecules. 2017;22(1):149.
[79] Baroncini EA, Kumar Yadav S, Palmese GR, Stanzione JF. Recent advances in bio-based epoxy resins and bio-based epoxy curing agents. Journal of Applied Polymer Science. 2016;133(45).
[80] Auvergne R, Caillol S, David G, Boutevin B, Pascault J-P. Biobased Thermosetting Epoxy: Present and Future. Chemical Reviews. 2014;114(2):1082-115.
[81] Ma S, Li T, Liu X, Zhu J. Research progress on bio-based thermosetting resins. Polymer International. 2016;65(2):164-73.
[82] Friedrich K. Chapter 1 - Routes for achieving multifunctionality in reinforced polymers and composite structures. In: Friedrich K, Breuer U, editors. Multifunctionality of Polymer Composites. Oxford: William Andrew Publishing; 2015. p. 3-41.
[83] Bakis CE, Bank LC, Brown VL, Cosenza E, Davalos JF, Lesko JJ, et al. Fiber-Reinforced Polymer Composites for Construction - State-of-the-Art Review. Journal of Composites for Construction. 2002;6(2):73-87.
[84] Bank L. Composites for Construction - Structural Design with FRP Materials. John Wiley & Sons, Inc. 2006.
[85] Jain R, Lee L. Fiber Reinforced Polymer (FRP) Composites for Infrastructure Applications. Focusing on Innovation, Technology Implementation and Sustainability Springer ISBN 978-94-007-2356-6. 2012.

[86] Bai J. Advanced fibrereinforced polymer (FRP) composites for structural applications. Woodhead Publishing Series in Civil and Structural Engineering ISBN 978-0-85709-418-6. 2013;46.
[87] Zoghi M. The International Handbook of FRP Composites in Civil Engineering. Taylor & Francis Group, LLC, CRC Press, ISBN-13: 978-1-4200-0374-1. 2014.
[88] Uddin N. Developments in Fiber-Reinforced Polymer (FRP) Composites for Civil Engineering.: Woodhead; 2013.
[89] Kim Y. Advanced Composites in Bridge Construction and Repair.: Woodhead; 2014.
[90] Rasheed HA. Strengthening Design of Reinforced Concrete with FRP.: CRC Press; 2014.
[91] Pellegrino C, Sena-Cruz J. Design Procedures for the Use of Composites in Strengthening of Reinforced Concrete Structures. State-of-the-Art Report of the RILEM Technical Committee 234-DUC, Springer, ISBN 978-94-017-7335-5. 2016.
[92] CNR-DT200. Guide for the Design and Construction of Externally Bonded FRP Systems for Strengthening Existing Structures. Advisory Committee on Techincal Recommendations for Construction, National Research Council, Rome, Italy. 2013.
[93] ACI. 440.2R-17: Guide for the Design and Construction of Externally Bonded FRP Systems for Strengthening Concrete Structures.2017.
[94] Oehlers D, Seracino R, Smith S. Design handbook for RC structures retrofitted with FRP and metal plates: beams and slabs.2008.
[95] Zilch K, Niedermeier R, Finckh W. DAfStb guideline. Strengthening of Concrete Structures with Adhesively Bonded Reinforcement2014.
[96] Motram T, Henderson J. CIRIA C779 - Fibre-reinforced polymer bridges - guidance for designers2018.
[97] ASCE. Pre-Standard for Load & Resistance Factor Design (LRFD) of Pultruded Fiber Reinforced Polymer (FRP) Structures. 2010.
[98] DNV. DNV-OS-C501 - Composite Components - Offshore standard. 2013.
[99] Liang R, Hota G. 16 - Fiber-reinforced polymer (FRP) composites in environmental engineering applications. In: Uddin N, editor. Developments in Fiber-Reinforced Polymer (FRP) Composites for Civil Engineering: Woodhead Publishing; 2013. p. 410-68.
[100] Fotouhi M, Suwarta P, Jalalvand M, Czel G, Wisnom MR. Detection of fibre fracture and ply fragmentation in thin-ply UD carbon/glass hybrid laminates using acoustic emission. Composites: Part A 2016;86:66–76.
[101] Jalalvand M, Fotouhi M, Wisnom MR. Orientation-dispersed pseudo-ductile hybrid composite laminates – A new lay-up concept to avoid free-edge delamination. Composites Science and Technology. 2017;153:232-40.
[102] Czél G, Rev T, Jalalvand M, Fotouhi M, Longana ML, Nixon-Pearson OJ, et al. Pseudo-ductility and reduced notch sensitivity in multi-directional all-carbon/epoxy thin-ply hybrid composites. Composites Part A: Applied Science and Manufacturing. 2018;104:151-64.
[103] Fotouhi M, Jalalvand M, Wisnom MR. Notch insensitive orientation-dispersed pseudo-ductile thin-ply carbon/glass hybrid laminates. Composites Part A: Applied Science and Manufacturing. 2018;110:29-44.
[104] Swolfs Y, Geboes Y, Gorbatikh L, Pinho ST. The importance of translaminar fracture toughness for the penetration impact behaviour of woven carbon/glass hybrid composites. Composites Part A: Applied Science and Manufacturing. 2017;103:1-8.
[105] Yang B, Wang Z, Zhou L, Zhang J, Liang W. Experimental and numerical investigation of interply hybrid composites based on woven fabrics and PCBT resin subjected to low-velocity impact. Composite Structures. 2015;132:464-76.
[106] Manikandan P, Chai GB. A layer-wise behavioral study of metal based interply hybrid composites under low velocity impact load. Composite Structures. 2014;117:17-31.

[107] Dai G, Mishnaevsky L. Fatigue of hybrid glass/carbon composites: 3D computational studies. Composites Science and Technology. 2014;94:71-9.
[108] Velmurugan R, Manikandan V. Mechanical properties of palmyra/glass fiber hybrid composites. Composites Part A: Applied Science and Manufacturing. 2007;38(10):2216-26.
[109] Ridzuan MJM, Abdul Majid MS, Afendi M, Azduwin K, Amin NAM, Zahri JM, et al. Moisture absorption and mechanical degradation of hybrid Pennisetum purpureum/glass–epoxy composites. Composite Structures. 2016;141:110-6.
[110] Ridzuan MJM, Majid MSA, Afendi M, Mazlee MN, Gibson AG. Thermal behaviour and dynamic mechanical analysis of Pennisetum purpureum/glass-reinforced epoxy hybrid composites. Composite Structures. 2016;152:850-9.
[111] Sarasini F, Fiore V. A systematic literature review on less common natural fibres and their biocomposites. Journal of Cleaner Production. 2018;195:240-67.
[112] Ouarhim W, Essabir H, Bensalah M-O, Zari N, Bouhfid R, Qaiss Aek. Structural laminated hybrid composites based on raffia and glass fibers: Effect of alkali treatment, mechanical and thermal properties. Composites Part B: Engineering. 2018;154:128-37.
[113] Hawileh RA, Abu-Obeidah A, Abdalla JA, Al-Tamimi A. Temperature effect on the mechanical properties of carbon, glass and carbon–glass FRP laminates. Construction and Building Materials 2015;75:342–8.
[114] Ferrante L, Tirillò J, Sarasini F, Touchard F, Ecault R, Vidal Urriza MA, et al. Behaviour of woven hybrid basalt-carbon/epoxy composites subjected to laser shock wave testing: Preliminary results. Composites Part B: Engineering. 2015;78:162-73.
[115] Najafi M, Mohammad S, Khalili R, Eslami-Farsani R. Hybridization effect of basalt and carbon fibers on impact and flexural properties of phenolic composites. Iranian Polymer Journal. 2014;23.
[116] Subagia IDGA, Kim Y, Tijing LD, Kim CS, Shon HK. Effect of stacking sequence on the flexural properties of hybrid composites reinforced with carbon and basalt fibers. Composites: Part B. 2014;58 251–8.
[117] Wu Z, Wang X, Iwashita K, Sasaki T, Hamaguchi Y. Tensile fatigue behaviour of FRP and hybrid FRP sheets. Composites Part B: Engineering. 2010;41(5):396-402.
[118] Hawileh RA, Abdalla JA, Hasan SS, Ziyada MB, Abu-Obeidah A. Models for predicting elastic modulus and tensile strength of carbon, basalt and hybrid carbon-basalt FRP laminates at elevated temperatures. Construction and Building Materials. 2016;114:364-73.
[119] Gibson AG, Wu YS, Evans JT, Mouritz AP. Laminate Theory Analysis of Composites under Load in Fire. Journal of Composite Materials. 2005;40(7):639-58.
[120] Fu H, Liao B, Qi F-j, Sun B-c, Liu A-p, Ren D-l. The application of PEEK in stainless steel fiber and carbon fiber reinforced composites. Composites Part B: Engineering. 2008;39(4):585-91.
[121] Swolfs Y, De Cuyper P, Callens MG, Verpoest I, Gorbatikh L. Hybridisation of two ductile materials – Steel fibre and self-reinforced polypropylene composites. Composites Part A: Applied Science and Manufacturing. 2017;100:48-54.
[122] Quagliato L, Jang C, Kim N. Manufacturing process and mechanical properties characterization for steel skin – Carbon fiber reinforced polymer core laminate structures. Composite Structures. 2019;209:1-12.
[123] Dávila CG, Remmers JJC, Pinho ST, Camanho PP. Mechanical Response of Composites: Springer; 2008.
[124] Turon A, Costa J, Maimí P, Trias D, Mayugo JA. A progressive damage model for unidirectional fibre-reinforced composites based on fibre fragmentation. Part I: Formulation. Composites Science and Technology. 2005;65 2039–48.

[125] Wehrkamp-Richter T, De Carvalho NV, Pinho ST. Predicting the non-linear mechanical response of triaxial braided composites. Composites Part A: Applied Science and Manufacturing. 2018;114:117-35.
[126] Chen BY, Tay TE, Pinho ST, Tan VBC. Modelling delamination migration in angle-ply laminates. Composites Science and Technology. 2017;142:145-55.
[127] Jalalvand M, Hosseini-Toudeshky H, Mohammadi B. Homogenization of diffuse delamination in composite laminates. Composite Structures. 2013;100:113-20.
[128] Bullegas G, Pinho ST, Pimenta S. Engineering the translaminar fracture behaviour of thin-ply composites. Composites Science and Technology. 2016;131:110-22.
[129] Xu X, Takeda S-i, Aoki Y, Hallett SR, Wisnom MR. Predicting notched tensile strength of full-scale composite structures from small coupons using fracture mechanics. Composite Structures. 2017;180:386-94.
[130] Xu X, Wisnom MR, Sun X, Rev T, Hallett SR. Experimental determination of Through-Thickness Compression (TTC) enhancement factor for Mode II fracture energy. Composites Science and Technology. 2018;165:66-73.
[131] Bunsell A, Gorbatikh L, Morton H, Pimenta S, Sinclair I, Spearing M, et al. Benchmarking of strength models for unidirectional composites under longitudinal tension. Composites Part A: Applied Science and Manufacturing. 2018;111:138-50.
[132] Ribeiro F, Sena-Cruz J, Branco FG, Júlio E. Hybrid effect and pseudo-ductile behaviour of unidirectional interlayer hybrid FRP composites for civil engineering applications. Construction and Building Materials. 2018;171:871-90.
[133] ISO. 527-5 Plastics — Determination of tensile properties; Part 5: Test conditions for unidirectional fibre-reinforced plastic composites. EUROPEAN COMMITTEE FOR STANDARDIZATION. 2009.
[134] Aveston J, Sillwood JM. Synergistic fibre strengthening in hybrid composites. Journal of Materials Science. 1976;11(1877-1883).
[135] Tamuzs V, Tepfers R. Ductility of non-metallic hybrid fiber composite reinforcement for concrete. Proceedings of the Second International RILEM Symposium,Ghent, Belgium August. 1996.
[136] Harris HG, Somboonsong W, Ko FK. New ductile Hybrid FRP reinforcing bar for concrete structures. J Compos Constr. 1998;2:28-37.
[137] Bakis CE, Terosky JA, Nanni A, Koehler SW. Self-monitoring, pseudo-ductile, hybrid FRP reinforcement rods for concrete applications. Composite Science Technology. 2001;61:815-23.
[138] Belarbi A, Watkins SE, Chandrashekhara K, Corra J, Konz1 B. Smart fiber-reinforced polymer rods featuring improved ductility and health monitoring capabilities. Smart Mater Struct. 2001;10 427–31.
[139] Won J-P, Chan-Gi Park, Jang C-I. Tensile Fracture and Bond Properties of Ductile Hybrid FRP Reinforcing Bars. Polymers & Polymer Composites. 2006;15(1).
[140] Cui Y-H, Tao J. A new type of ductile composite reinforcing bar with high tensile elastic modulus for use in reinforced concrete structures. Can J Civ Eng. 2008;36:672–5.
[141] Cheung MMS, Tsang TKC. Behaviour of Concrete Beams Reinforced with Hybrid FRP Composite Rebar. Advances in Structural Engineering. 2010;13.
[142] Behnam B, Eamon C. Resistance Factors for Ductile FRP-Reinforced Concrete Flexural Members. Journal of Composites for Construction doi:101061/(ASCE)CC1943-56140000363. 2013.
[143] Etman EE-S. Innovative Hybrid Reinforcement for Flexural Members. Journal of Composites for Construction. 2011;15(1):2-8.

[144] Seo D-W, Park K-T, You Y-J, Lee S-Y. Experimental Investigation for Tensile Performance of GFRP-Steel Hybridized Rebar. Advances in Materials Science and Engineering. 2016;2016:12.
[145] You Y-J, Park Y-H, Kim H-Y, Park J-S. Hybrid effect on tensile properties of FRP rods with various material compositions. Composite Structures. 2007;80(1):117-22.
[146] Somboonsong W, Ko FK, Harris HG. Ductile Hybrid Fiber Reinforced Plastic Reinforcing Bar for Concrete Structures: Design Methodology. Materials Journal. 1998;95(6).
[147] Nanni A, Henneke MJ, Okamoto T. Behaviour of concrete beams with hybrid reinforcement. Construction and Building Materials. 1993;8(2):89-95.
[148] Grace NF, Abdel-Sayed G, Ragheb WF. Strengthening of Concrete Beams Using Innovative Ductile Fiber-Reinforced Polymer Fabric. ACI Structural Journal. 2002;103(5)(99(5)):672–700.
[149] Grace NF, Ragheb WF, Abdel-Sayed G. Development and application of innovative triaxially braided ductile FRP fabric for strengthening concrete beams. Composite Structures 2004;64 521–30.
[150] Wu Z, Shao Y, Iwashita K, Sakamoto K. Strengthening of Preloaded RC Beams Using Hybrid Carbon Sheets. J Compos Constr. 2007;11:299-307.
[151] Attari N, Amziane S, Chemrouk M. Flexural strengthening of concrete beams using CFRP, GFRP and hybrid FRP sheets. Construction and Building Materials 2012;37 746–57.
[152] Hosny A, Shaheen H, Abdelrahman A, Elafandy T. Performance of reinforced concrete beams strengthened by hybrid FRP laminates. Cement & Concrete Composites. 2006;28:906–13.
[153] Hawileh RA, Rasheed HA, Abdalla JA, Al-Tamimi AK. Behavior of reinforced concrete beams strengthened with externally bonded hybrid fiber reinforced polymer systems. Materials and Design. 2014;53:972–82.
[154] Kang TH-K, Kim W, Ha S-S, Choi D-U. Hybrid Effects of Carbon-Glass FRP Sheets in Combination with or without Concrete Beams. International Journal of Concrete Structures and Materials Vol8, No1, pp27–41, March 2014 DOI 101007/s40069-013-0061-0. 2014.
[155] Zhang P, Zhu H, Wu G, Meng S, Wu Z. Flexural Performance of HFRP-RC Composite T-Beams with Different Interfaces. J Compos Constr, 04016101. 2016.
[156] Nikopour H, Nehdi M. Shear repair of RC beams using epoxy injection and hybrid external FRP. Materials and Structures. 2011;44:1865–187.
[157] Wu G, Wu ZS, Lu ZT, Ando YB. Structural Performance of Concrete Confined with Hybrid FRP Composites. Journal of reinforced plastics and composites. 2008;27(12).
[158] Luca AD, Nardone F, Matta F, Nanni A, Lignola GP, Prota A. Structural Evaluation of Full-Scale FRP-Confined Reinforced Concrete Columns. J Compos Constr. 2011;15:112-23.
[159] Xu S, Li L, Guo Y. Study on experimental behavior of concrete circular column confined by HFRP under axial compression. Advanced Materials Research. 2012;450-451:491-4.
[160] Li L-J, Xu S-D, Zeng L, Guo Y-C. Study on mechanical behavior of circular concrete columns confined by HFRP under axial compressive load. Research and Applications in Structural Engineering, Mechanics and Computation – Zingoni (Ed) Taylor & Francis Group, London, ISBN 978-1-138-00061-2. 2013.
[161] Li J, Samali B, Ye L, Bakoss S. Behaviour of concrete beam–column connections reinforced with hybrid FRP sheet. Composite Structures 2002;57:357–65.
[162] Li J, Bakoss SL, Samali B, Ye L. Reinforcement of concrete beam-column connections with hybrid FRP sheet. Composite Structures 1999;47:805-12.
[163] Attari N, Amziane S, Chemrouk M. Efficiency of Beam–Column Joint Strengthened by FRP Laminates. Advanced Composite Materials. 2010;19:171–83.

[164] Ribeiro F, Sena-Cruz J, Branco FG, Júlio E. Hybrid FRP jacketing for enhanced confinement of circular concrete columns in compression. Construction and Building Materials. 2018;184:681-704.
[165] Ispir M, Dalgic KD, Ilki A. Hybrid confinement of concrete through use of low and high rupture strain FRP. Composites Part B: Engineering. 2018;153:243-55.
[166] Deng Z-c, Qu J-l. The Experimental Studies on Behavior of Ultrahigh-Performance Concrete Confined by Hybrid Fiber-Reinforced Polymer Tubes. Advances in Materials Science and Engineering, Article ID 201289, 18 pages. 2015.
[167] Ranganathan S, Mantena PR. Axial Loading and Buckling Response Characteristics of Pultruded Hybrid Glass-Graphite/Epoxy Composite Beams. Journal of Reinforced Plastics and Composites. 2003;22(7).
[168] Ragheb WF. Hybridization Effectiveness in Improving Local Buckling Capacity of Pultruded I-Beams. Mechanics of Advanced Materials and Structures. 2010;17:448–57.
[169] Nunes F, Correia JR, Silvestre N. Structural behaviour of hybrid FRP pultruded columns. Part 1: Experimental study. Composite Structures. 2016;139:291–303.
[170] Hai ND, Mutsuyoshi H, Asamoto S, Matsui T. Structural behavior of hybrid FRP composite I-beam. Construction and Building Materials. 2009;24(6):956-69.
[171] Yang Y, Wang X, Wu Z. Damping Behavior of Hybrid Fiber-Reinforced Polymer Cable with Self-Damping for Long-Span Bridges. Journal of Bridge Engineering. 2017;22(7):05017005.
[172] Wang X, Wu Z, Wu G, Zhu H, Zen F. Enhancement of basalt FRP by hybridization for long-span cable-stayed bridge. Composites Part B: Engineering. 2013;44(1):184-92.
[173] Wang X, Wu Z. Modal damping evaluation of hybrid FRP cable with smart dampers for long-span cable-stayed bridges. Composite Structures. 2011;93(4):1231-8.
[174] Wang X, Wu Z. Evaluation of FRP and hybrid FRP cables for super long-span cable-stayed bridges. Composite Structures. 2010;92(10):2582-90.
[175] Ivey M, Ayranci C, Carey JP. 14 - Braidtrusion. In: Carey JP, editor. Handbook of Advances in Braided Composite Materials: Woodhead Publishing; 2017. p. 433-50.
[176] Park S-J. Carbon Fibers. Springer Series in Materials Science, Volume 210, ISBN 978-94-017-9477-0. 2015.
[177] Rana S, Zdraveva E, Pereira C, Fangueiro R, Correia AG. Development of Hybrid Braided Composite Rods for Reinforcement and Health Monitoring of Structures. The Scientific World Journal. 2014;2014:9.
[178] Yung CW, Jose IR. Investigation of Concentrically Loaded Reinforced Concrete Columns Confined with Glass Fiber-Reinforced Polymer Jackets. Structural Journal.98(3).
[179] Kumbasar N. COMPRESSIVE BEHAVIOUR OF CARBON FIBRE COMPOSITE JACKETED CONCRETE WITH CIRCULAR AND NON-CIRCULAR CROSS-SECTIONS AU - ILKI, ALPER. Journal of Earthquake Engineering. 2003;7(3):381-406.
[180] Ilki A, Kumbasar N, Koc V. Low strength concrete members externally confined with FRP sheets. Structural Engineering and Mechanics. 2004;18(2):167-94.
[181] Grace NF, Ragheb WF, Abdel-Sayed G. Ductile Hybrid Structural Fabric. Patent No: US 6,790,518 B2. 2002.
[182] Nunes F, Silvestre N, Correia JR. Structural behaviour of hybrid FRP pultruded columns. Part 2: Numerical study. Composite Structures. 2016;139:304-19.
[183] Liang Y, Sun C, Ansari F. Acoustic Emission Characterization of Damage in Hybrid Fiber-Reinforced Polymer Rods. Journal of Composites for Construction. 2004;8(1):70-8.
[184] Xiong GJ, Yang JZ, Ji ZB. Behavior of Reinforced Concrete Beams Strengthened with Externally Bonded Hybrid Carbon Fiber&-Glass Fiber Sheets. Journal of Composites for Construction. 2004;8(3):275-8.

[185] Bouchelaghem H, Bezazi A, Scarpa F. Compressive behaviour of concrete cylindrical FRP-confined columns subjected to a new sequential loading technique. Composites Part B: Engineering. 2011;42(7):1987-93.
[186] Wu G, Shi J-W, Jing W-J, Wu Z-S. Flexural Behavior of Concrete Beams Strengthened with New Prestressed Carbon-Basalt Hybrid Fiber Sheets. Journal Of Composites For Construction, 18 ISSN 1090-0268/04013053(10). 2014.
[187] Kang TH-K, Kim W, Ha S-S, Choi D-U. Hybrid Effects of Carbon-Glass FRP Sheets in Combination with or without Concrete Beams. International Journal of Concrete Structures and Materials. 2013;8(1):27–41.
[188] Long Y-L, Zhu J. Experimental Study on Concrete Columns with Various Sizes Confined by BFRP and hybrid FRP under Axial Compression. Advanced Materials Research. 2013;838-841:407-11.
[189] Ju M, Park G, Lee S, Park C. Bond performance of GFRP and deformed steel hybrid bar with sand coating to concrete. Journal of Reinforced Plastics and Composites. 2016;36(6):464-75.
[190] Padanattil A, Karingamanna J, K.M M. Novel hybrid composites based on glass and sisal fiber for retrofitting of reinforced concrete structures. Construction and Building Materials. 2017;133:146-53.

Appendix I

Table 2.3 — Hybrid composites developed for civil engineering by different authors.

Year	Ref.	Matrix	Nb. R.M.	Relative volume of reinforcing materials	Mechanical properties of hybrid composites			Mechanical properties of reinforcing materials				Orientation of fibres	Processing and fabrication	Final form of composite
					σ [MPa]	E [GPa]	ε [%]	Material	σ [MPa]	E [GPa]	ε [%]			
1993	[147]		2	Steel bar (66%) - aramid (34%)	733.0	--	--	Vinylon	429.0	5.0	2.9	Unidirectional	--	Reinforcing bar
				Steel bar (60%) - aramid (40%)	831.1	--	--	Steel bar	235.0	200.0	--			
				Steel bar (50%) - aramid (50%)	903.1	--	--	Aramid	1489.0	68.4	2.2			
				Steel bar (67%) - aramid (33%)	720.2	--	--							
				Steel bar (63%) - vinylon (37%)	332.4	--	--							
				Steel bar (56%) - vinylon (44%)	337.7	--	--							
				Steel bar 46%) - vinylon (54%)	311.5	--	--							
1998	[146]	Vinyl ester	2	Aramid (70%) - carbon 1 (30%)	--	--	--	Aramid	3600.0	124.0	2.5	Unidirectional (core) braid yarns (outside layer)	Pultrusion and braiding	Reinforcing bar
				Aramid (--%) - carbon 2 (--%)	--	--	--	Carbon 1	1896.0	379.3	0.5			
								Carbon 2	3654.0	231.0	1.4			

Table 2.3 — (Continued)

Year	Ref.	Matrix	Nb. R.M.	Relative volume of reinforcing materials	Mechanical properties of hybrid composites			Mechanical properties of reinforcing materials				Orientation of fibres	Processing and fabrication	Final form of composite
					σ [MPa]	E [GPa]	ε [%]	Material	σ [MPa]	E [GPa]	ε [%]			
1999	[162]	--	4	Glass woven roving (29%) - Glass chopped strand mat (13%) - glass tape (28%) - carbon cloth (29%)	--	--	--	Glass woven roving	--	--	--	Multi-directional	--	Beam–column joint
								Glass chopped strand mat	--	--	--			
								Glass tape	--	--	--			
								Carbon cloth	--	--	--			
2002	[148]	Epoxy	3	Glass (--%) - carbon 1 (--%) - carbon 2 (--%)	390.0	--	1.7	Glass	1034.0	48.0	2.1	Unidirectional	--	Laminate
				Glass (--%) – carbon 1 (--%) – carbon 2 (--%)	393.3	--	1.7	Carbon 1	1324.0	379.0	0.4	Triaxially braided fabric		
								Carbon 2	2413.0	231.0	0.9			

Table 2.3 — (Continued)

Year	Ref.	Matrix	Nb. R.M.	Relative volume of reinforcing materials	Mechanical properties of hybrid composites			Mechanical properties of reinforcing materials				Orientation of fibres	Processing and fabrication	Final form of composite
					σ [MPa]	E [GPa]	ε [%]	Material	σ [MPa]	E [GPa]	ε [%]			
2001	[137]	Unsaturated polyester	2	Glass (73%) carbon (27%)	706.0	57.2	1.2	Glass	2580.0	73.0	3.6	Unidirectional	Pultrusion	Reinforcing bar
				Glass (99%) - carbon (1%)	596.0	42.3	1.7	Carbon	3860.0	236.0	1.6			
				Glass (88%) - carbon (13%)	609.0	42.3	1.4	Vinyl alcohol	2010.0	45.0	4.9			
			3	Glass (43%) - vinyl alcohol (41%) - carbon (16%)	485.0	47.2	1.1	Aramid	3000.0	112.0	2.4			
				Vinyl alcohol (54%) - aramid (34%) - carbon (12%)	543.0	43.4	1.2	Steel bar	235.0	200.0	--			
		Vinyl ester		Vinyl alcohol (54%) - aramid (34%) - carbon (12%)	574.0	43.9	1.3	Aramid	1489.0	68.4	2.2			
2003	[167]	Epoxy	2	Glass (33%) - graphite (67%)	--	--	--	Glass	--	47.5	--	Unidirectional	Pultrusion	Pultruded beam
				Glass (50%) - graphite (50%)	--	--	--	Graphite	--	121.5	--			
				Glass (67%) - graphite (33%)	--	--	--							
				Glass (50%) - graphite (50%)	--	--	--							

Table 2.3 — (Continued)

Year	Ref.	Matrix	Nb. R.M.	Relative volume of reinforcing materials	Mechanical properties of hybrid composites			Mechanical properties of reinforcing materials				Orientation of fibres	Processing and fabrication	Final form of composite
					σ [MPa]	E [GPa]	ε [%]	Material	σ [MPa]	E [GPa]	ε [%]			
2004	[183]	Epoxy	2	Glass (79%) - carbon (21%)	--	--	--	Glass Carbon	4275.0 4930.0	89.6 230.3	5.0 4.9	Unidirectional	Pultrusion	Reinforcing bar
2004	[184]		2	Glass (56%) - carbon (44%)	1578.0	82.2	1.9	Glass Carbon	1703.0 1.5	49.1 122.6	3.5 1.2	--	--	Laminate
2006	[139]	Vinyl ester	2	Aramid (73%) - carbon(27%)	--	63.0	3.4	Glass	1890.0	75.0	2.6	Unidirectional (core) braid yarns (outside layer)	Pultrusion and braiding	Reinforcing bar
				Glass (81%) - carbon (19%)	--	43.0	3.4	Aramid	3100.0	77.0	4.6			
			3	Glass (52%) - aramid (35%) - carbon (14%)	--	37.0	3.4	Carbon	3500.0	244.0	1.2			
2007	[150]	Epoxy	2	High modulus carbon (44%) - high strength carbon (56%)	--	405.0	--	High modulus carbon	1900.0	540.0	0.4	Unidirectional	Hand lay-up	Laminate
				High modulus carbon (34%) - high strength carbon (66%)	--	373.0	--	High strength carbon	3400.0	230.0	1.5			
				High modulus carbon (28%) - high strength carbon (72%)	--	351.0	--							

Table 2.3 — (Continued)

Year	Ref.	Matrix	Nb. R.M.	Relative volume of reinforcing materials	Mechanical properties of hybrid composites			Mechanical properties of reinforcing materials				Orientation of fibres	Processing and fabrication	Final form of composite
					σ [MPa]	E [GPa]	ε [%]	Material	σ [MPa]	E [GPa]	ε [%]			
2007	[145]	Vinyl ester and unsaturated polyester	2	Glass (37%) - carbon (23%) - solution 1: carbon on core and vinyl ester matrix	1281.0	80.4	1.6	Glass	2410.0	79.0	3.0	Unidirectional	Pultrusion	Reinforcing bar
				Glass (37%) - carbon (23%) - solution 2: carbon in the core and polyester matrix	1331.0	83.1	1.6	Carbon	4900.0	230.0	2.1			
				Glass (37%) - carbon (23%) - solution 3: carbon on surfaceand vinyl ester matrix	1083.0	78.9	1.4							
				Glass (37%) - carbon (23%) - solution 4: carbon on surface and polyester matrix	1128.0	79.5	1.4							

Table 2.3 — (Continued)

Year	Ref.	Matrix	Nb. R.M.	Relative volume of reinforcing materials	Mechanical properties of hybrid composites			Mechanical properties of reinforcing materials				Orientation of fibres	Processing and fabrication	Final form of composite
					σ [MPa]	E [GPa]	ε [%]	Material	σ [MPa]	E [GPa]	ε [%]			
				Glass (37%) - carbon (23%) - solution 5: carbon dispersed and vinyl ester matrix	1045.0	62.4	1.7							
				Glass (37%) - carbon (23%) - solution 6: carbon dispersed and polyester matrix	1213.0	84.0	1.4							
2008	[140]	--	4	Glass (--%) - carbon (--%) - aramid (--%) - steel wire (--%)	--	--	--	Glass Carbon Aramid Steel wire		74.0 225.0 102.0 200.0	2.4 1.3 2.1 20.0	Unidirectional	Hand lay-up	Reinforcing bar
2010	[163]	Epoxy	2	Glass (--%) - carbon (--%)	--	--	--	Glass Carbon	2200.0 2800.0	76.0 165.0	2.8 1.7	Unidirectional	--	Beam–column joint
2011	[156]	Epoxy	2	Glass (--%) - carbon (--%)	--	--	--	Glass	--	--	--	Bidirectional	Hand lay-up	Laminate
				Aramid (--%) - carbon (--%)	--	--	--	Aramid Carbon	-- --	-- --	-- --			
2011	[185]	Polyester	2	Glass 1 (63%) - glass 2 (38%)	--	--	--	Glass 1 Glass2	-- --	-- --	-- --	Bidirectional	Hand lay-up	Jacket

Table 2.3 — (Continued)

Year	Ref.	Matrix	Nb. R.M.	Relative volume of reinforcing materials	Mechanical properties of hybrid composites			Mechanical properties of reinforcing materials				Orientation of fibres	Processing and fabrication	Final form of composite
					σ [MPa]	E [GPa]	ε [%]	Material	σ [MPa]	E [GPa]	ε [%]			
2008	[157]	Epoxy	2	High modulus carbon (54%) - high strength carbon (46%)	--	--	--	PBO	4158.2	240.0	1.6	Unidirectional	Hand lay-up	Jacket
				High modulus carbon (57%) - PBO (43%)	--	--	--	High modulus carbon	2543.5	540.0	0.5			
				High modulus carbon (37%) - aramid (63%)	--	--	--	High strength carbon	4233.8	230.0	1.7			
				High modulus carbon (32%) - glass (68%)	--	--	--	Glass	1793.7	73.0	2.2			
				High modulus carbon (37%) - high strength carbon (63%)	--	--	--	Aramid	2323.5	120.0	2.0			
				High modulus carbon (39%) - PBO (61%)	--	--	--							
				High modulus carbon (23%) - aramid (77%)	--	--	--							

Table 2.3 — (Continued)

Year	Ref.	Matrix	Nb. R.M.	Relative volume of reinforcing materials	Mechanical properties of hybrid composites			Mechanical properties of reinforcing materials				Orientation of fibres	Processing and fabrication	Final form of composite
					σ [MPa]	E [GPa]	ε [%]	Material	σ [MPa]	E [GPa]	ε [%]			
				High modulus carbon (26%) - glass (74%)	--	--	--							
			3	High modulus carbon (28%) - high strength carbon (24%) - aramid (48%)	--	--	--							
2009	[170]	Vinyl ester	2	Flange: Glass (48) - carbon (52%), web: glass (100%)	--	--	--	Glass	--	10.0	--	Unidirectional (carbon) multi-directional (glass)	Pultrusion	Pultruded beam
				Flange: Glass (67) - carbon (33%), web: glass (100%)	--	--	--	Carbon	--	113.0	--			
				Flange: Glass (86) - carbon (14%), web: glass (100%)	--	--	--							
2013	[172]	Vinyl ester	2	Basalt (75%) - carbon (25%)	1137.0	80.0	1.4	Basalt	1345.0	54.0	2.5	Unidirectional	Pultrusion	Cable for long-span cable-stayed bridges
				Basalt (50%) - carbon (50%)	1772.0	106.0	1.4	Carbon	1741.0	159.0	1.1			
				Basalt (80%) - 0.7 mm in diameter steel-wire (20%)	--	--	--	Steel wire	2500.0	200.0	>3.5			

Table 2.3 — (Continued)

Year	Ref.	Matrix	Nb. R.M.	Relative volume of reinforcing materials	Mechanical properties of hybrid composites			Mechanical properties of reinforcing materials				Orientation of fibres	Processing and fabrication	Final form of composite
					σ [MPa]	E [GPa]	ε [%]	Material	σ [MPa]	E [GPa]	ε [%]			
				Basalt (60%) - 0.7 mm in diameter steel-wire (40%)	--	--	--							
2010	[143]	Epoxy	2	Carbon (6%) - steel bar (94%)	445.0	150.0	--	Carbon	--	--	--	Unidirectional	Hand lay-up	Reinforcing bar
				Carbon (12%) - steel bar (88%)	415.0	89.0	--	Steel bar	365.0	200.0				
				Glass (1%) - steel bar (99%)	257.0	58.0	--	Aluminum bar	100.0	69.0				
				Glass (16%) - steel bar (84%)	160.0	66.0	--	Glass	--	--	--			
				Carbon (31%) - aluminum bar (69%)	420.0	120.0	--							
				Carbon (50%) - aluminum bar (50%)	188.0	101.0	--							
				Glass (39%) - aluminium bar (61%)	285.0	82.0	--							
			3	Glass (8%) - carbon (6%) - steel bar (86%)	460.0	156.0	--							

Table 2.3 — (Continued)

Year	Ref.	Matrix	Nb. R.M.	Relative volume of reinforcing materials	Mechanical properties of hybrid composites			Mechanical properties of reinforcing materials				Orientation of fibres	Processing and fabrication	Final form of composite
					σ [MPa]	E [GPa]	ε [%]	Material	σ [MPa]	E [GPa]	ε [%]			
				Glass (22%) - carbon (31%) - aluminum bar (41%)	420.0	87.0	--							
2011	[158]		2	Glass (33%) - basalt (67%)	3399-4840	76.9-88.9	3.15-4.7	Glass	3399.0	76.9	4.7	--	Hand lay-up	Jacket
								Basalt	3241.0	73.4	4.5			
2012	[159]		2	Glass (53%) - carbon (47%)	--	--	--	Glass	1863.0	72.0	2.2	--	Hand lay-up	Jacket
				Glass (36%) - carbon (64%)	--	--	--	Basalt	2130.0	93.0	2.0			
				Basalt (50%) - carbon (50%)	--	--	--	Carbon	4125.0	244.0	1.7			
				Basalt (33%) - carbon (67%)	--	--	--							
				Glass (53%) - basalt (47%)	--	--	--							
			3	Glass (34%) - basalt (35%) - carbon (31%)	--	--	--							
2012	[151]	Epoxy	2	Glass (58%) - carbon (42%)	--	--	--	Glass	--	--	--	Bidirectional	--	--
								Carbon	--	--	--			
2013	[186]	Epoxy (partial impregnation)	2	Basalt (70%) - carbon (30%)	--	--	0.9	Basalt	1825.0	70.8	2.6	Unidirectional	Hand lay-up	Laminate
				Basalt (60%) - carbon (40%)	--	--	0.8	Carbon	3400.0	230.0	1.5			

Table 2.3 — (Continued)

Year	Ref.	Matrix	Nb. R.M.	Relative volume of reinforcing materials	Mechanical properties of hybrid composites			Mechanical properties of reinforcing materials				Orientation of fibres	Processing and fabrication	Final form of composite
					σ [MPa]	E [GPa]	ε [%]	Material	σ [MPa]	E [GPa]	ε [%]			
				Basalt (70%) - carbon (30%)			0.8							
2013	[187]	Epoxy	2	Glass (50%) - carbon (50%)	2108.0	146.0	1.5	Glass	2900.0	72.4	4.0	Unidirectional	Hand lay-up	Laminate
				Glass (67%) - carbon (33%)	1657.0	126.0	1.5	Carbon	4900.0	230.0	2.1			
				Glass (75%) - carbon (25%)	1592.0	103.5	1.5							
				Glass (80%) - carbon (20%)	1818.0	99.1	1.8							
				Glass (84%) - carbon (16%)	1471.0	76.7	1.8							
				Glass (86%) - carbon (14%)	1535.0	82.2	1.9							
				Glass (88%) - carbon (12%)	1431.0	75.7	1.9							
				Glass (89%) - carbon (11%)	1476.0	79.0	1.9							
				Glass (90%) - carbon (10%)	1674.0	89.4	2.0							
				Glass (91%) - carbon (9%)	1479.0	79.8	1.9							
2013	[188]		2	Glass (50%) - carbon (50%)	--	--	--	Glass Carbon	-- --	105.0 210.0	2.2 1.9	--	Hand lay-up	Jacket

Table 2.3 — (Continued)

Year	Ref.	Matrix	Nb. R.M.	Relative volume of reinforcing materials	Mechanical properties of hybrid composites			Mechanical properties of reinforcing materials				Orientation of fibres	Processing and fabrication	Final form of composite
					σ [MPa]	E [GPa]	ε [%]	Material	σ [MPa]	E [GPa]	ε [%]			
2014	[177]	Polyester	2	Glass (77%) - carbon (23%)	766.7	78.5	1.4	Glass	3500.0	73.5	4.8	Unidirectional	Hand lay-up	Reinforcing bar
				Glass (53%) - carbon (47%)	740.4	74.5	1.2	Carbon	4300.0	240.0	1.8			
2014	[153]	Epoxy	2	Glass (50%) - carbon (50%)	1622.70	86.3	2.6	Glass	3400.0	72.0	4.5	Unidirectional	Hand lay-up	Laminate
				Glass (70%) - carbon (30%)	1186.90	65.3	2.8	Carbon	3450.0	230.0	1.5			
2015	[166]	Epoxy	2	Aramid (36%) - basalt (64%)	1079	23.9	4.5	Aramid	2000.0	125.0	1.6	Unidirectional	Hand lay-up	Jacket
				Basalt (44%) - glass (56%)	863	18.4	4.7	Basalt	3103.0	90.0	3.5			
				Carbon (33%) - basalt (67%)	1045	43.7	2.7	Glass	1800.0	55.0	3.3			
				Carbon (28%) - glass (72%)	1067	39.7	2.5	Carbon	3400.0	240.0	1.4			
			3	Carbon (35%) - aramid (20%) - glass (45%)	980	31.1	3.2							
				Carbon (21%) - aramid (24%) - glass (55%)	1010	33.7	3.0							
				Carbon (30%) - basalt (31%) - glass (39%)	791	27.5	2.9							

Table 2.3 — (Continued)

Year	Ref.	Matrix	Nb. R.M.	Relative volume of reinforcing materials	Mechanical properties of hybrid composites			Mechanical properties of reinforcing materials				Orientation of fibres	Processing and fabrication	Final form of composite
					σ [MPa]	E [GPa]	ε [%]	Material	σ [MPa]	E [GPa]	ε [%]			
2016	[144]	Unsaturated polyester	2	Glass (70%) - steel rod (30 %)	1269.7	94.9	--	Glass	2600.0	81.0		Unidirectional (core) braid yarns (outside layer)	Pultrusion and braiding	Reinforcing bar
				Glass (49%) - steel rod (51%)	1258.8	111.1	--	Steel rod	1180-1370	200.0				
				Glass (24%) - steel rod (76%)	833.9	148.2	--	Steel wire	1270-1470	200.0				
				Glass (90%) - steel rod (10%)	1150.3	62.6	--	Steel bar	400.0	200.0				
				Glass (68%) - steel wire (32%)	1245.4	99.8	--							
				Glass (43%) - steel wire (57%)	1323.2	126.9	--							
				Glass (30%) - steel wire (70%)	1156.4	157.3	--							
				Glass (43%) - steel wire (57%)	669.5	110.1								
				Glass (89%) - steel wire (11%)	1232.7	58.5	--							
				Glass (63%) - steel wire (37%)	1238.6	97.2	--							
				Glass (40%) - steel wire (60%)	1283.1	143.3	--							
				Glass (30%) - steel wire (70%)	1361.8	155.1	--							

Table 2.3 — (Continued)

Year	Ref.	Matrix	Nb. R.M.	Relative volume of reinforcing materials	Mechanical properties of hybrid composites			Mechanical properties of reinforcing materials				Orientation of fibres	Processing and fabrication	Final form of composite
					σ [MPa]	E [GPa]	ε [%]	Material	σ [MPa]	E [GPa]	ε [%]			
				Glass (63%) - steel bar (37%)	779.5	100.4	--							
				Glass (37%) - steel bar (63%)	596.5	146.8	--							
				Glass (75%) - steel bar (25%)	1217.9	90.8	--							
				Glass (56%) - steel bar (42%)	1197.2	123.2	--							
				Glass (34%) - steel bar (66%)	781.8	118.5	--							
				Glass 76%) - steel wire (24%)	899.6	88.8								
				Glass (54%) - steel wire (46%)	537.7	120.7								
				Glass (32%) - steel wire (68%)	466.6	148.2								
2016	[155]	Epoxy	2	Basalt (80%) - carbon (20%)	2053.0	118.0	1.8	Basalt	2120.0	82.0	2.6	Unidirectional	Hand lay-up	Laminate
				Basalt (84%) - carbon (16%)	1980.0	110.0	1.8	Carbon	4080.0	260.0	1.6			
				Basalt (87%) - carbon (13%)	1942.0	105.0	1.9							

Table 2.3 — (Continued)

Year	Ref.	Matrix	Nb. R.M.	Relative volume of reinforcing materials	Mechanical properties of hybrid composites			Mechanical properties of reinforcing materials				Orientation of fibres	Processing and fabrication	Final form of composite
					σ [MPa]	E [GPa]	ε [%]	Material	σ [MPa]	E [GPa]	ε [%]			
2017	[189]	Vinyl ester and epoxy	2	Glass (29%) - steel bar (71%)	--	--	--	Glass Steel bar	-- --	-- --	-- --	Unidirectional (core) braid yarns (outside layer)	Pultrusion	Reinforcing bar
2017	[190]	Epoxy	2	Glass (--%) - sisal (--%) 1 layer Glass (--%) - sisal (--%) 2 layers Glass (--%) - sisal (--%) 3 layers	233.2 368.4 441.0	11.8 12.4 13.4	1.6 1.9 2.3	Glass Sisal				Bidirectional	Hand lay-up	Jacket
2017	[171]	--	3	Basalt (--%) - viscolestatic material (--%) - hybrid composite (Basalt (50%)+Carbon (50%)) (--%)	--	--	--	Basalt Viscolestatic material Hybrid composite	1389.0 -- 1666.0	52.0 -- 103.0	2.7 -- 2.0	Unidirectional		Cable for long-span cable-stayed bridges

Table 2.3 — (Continued)

Year	Ref.	Matrix	Nb. R.M.	Relative volume of reinforcing materials	Mechanical properties of hybrid composites			Mechanical properties of reinforcing materials				Orientation of fibres	Processing and fabrication	Final form of composite
					σ [MPa]	E [GPa]	ε [%]	Material	σ [MPa]	E [GPa]	ε [%]			
2018	[164]	Epoxy	2	Basalt (29%) - high modulus carbon (71%)	1150.0	474.1	0.2	Basalt	1886.7	61.4	3.1	Unidirectional	Hand lay-up	Jacket
				Basalt (62%) - high modulus carbon (38%)	1328.0	97.4	2.0	Glass	2662.1	76.9	3.7			
				High modulus carbon (63%) - standard carbon (37%)	1352.5	489.6	0.3	Standard carbon	3920.7	214.0	1.4			
				High modulus carbon (30%) - standard carbon (70%)	1937.5	368.8	0.9	High modulus carbon	2934.2	558.1	0.5			
				Glass (26%) - standard carbon (74%)	2176.9	201.7	1.0							
				Glass (31%) - standard carbon (69%)	2216.0	202.4	1.1							
				Glass (51%) - standard carbon (49%)	1776.3	148.9	1.2							
				Glass (58%) - standard carbon (42%)	1856.0	146.7	1.3							

Table 2.3 — (Continued)

Year	Ref.	Matrix	Nb. R.M.	Relative volume of reinforcing materials	Mechanical properties of hybrid composites			Mechanical properties of reinforcing materials				Orientation of fibres	Processing and fabrication	Final form of composite
					σ [MPa]	E [GPa]	ε [%]	Material	σ [MPa]	E [GPa]	ε [%]			
				Glass (73%) - standard carbon (27%)	1244.4	110.8	1.2							
				Glass (29%) - high modulus carbon (71%)	1168.9	454.5	0.3							
				Glass (35%) - high modulus carbon (65%)	1053.5	439.2	1.9							
				Glass (55%) - high modulus carbon (45%)	1105.8	318.7	1.9							
				Glass (62%) - high modulus carbon (38%)	1054.7	252.0	1.9							
				Glass (76%) - high modulus carbon (24%)	1164.7	214.3	1.9							

Table 2.3 — (Continued)

Year	Ref.	Matrix	Nb. R.M.	Relative volume of reinforcing materials	Mechanical properties of hybrid composites			Mechanical properties of reinforcing materials				Orientation of fibres	Processing and fabrication	Final form of composite
					σ [MPa]	E [GPa]	ε [%]	Material	σ [MPa]	E [GPa]	ε [%]			
2018	[165]	Epoxy	2	PET (88%) - carbon(12%)	--	--	--	PET	740.0	10.0	10.0	Unidirectional	Hand lay-up	Jacket
				PET (94%) - carbon(6%)	--	--	--	Glass	1700.0	80.0	2.8			
				PET (96%) - carbon(4%)	--	--	--	Carbon	4900.0	230.0	2.1			
				PET (85%) - glass (15%)	--	--	--							
				Glass (73%) - carbon (27%)	--	--	--							
				Glass (89%) - carbon (11%)	--	--	--							

3. TENSILE BEHAVIOUR OF HYBRID FRP COMPOSITES

3.1. Introduction

Unidirectional (UD) FRP composites are brittle materials, exhibiting linear elastic behaviour up to failure. Therefore, structures made of these materials, although apparently without any problem, may fail abruptly [1]. This characteristic does not allow to take full advantage of FRP properties, namely the high tensile strength due to conservative design limits [2]. For this reason, to obtain composites with progressive failure behaviour ensuring safe, strain hardening, and meaningful ultimate tensile strain are seen as priority goal by different industries [2], including civil engineering.

Hybridisation, i.e., the incorporation of two or more types of fibres within the same polymeric matrix [3], is an established approach to deal with the above mentioned problem, since this strategy promotes synergies between the adopted reinforcing materials, lessening their intrinsic disadvantages [4]. For instance, when submitted to uniaxial tension, Low Strain (LS) fibres fail earlier than High Strain (HS) fibres and this fracture behaviour can be used as a warning sign before the ultimate failure of the hybrid FRP composite [1, 4]. Furthermore, it has been observed that hybridisation increases the apparent strain at LS fibres failure [5]. This phenomenon has been described as "hybrid effect" [6]. In the case of carbon/glass hybrid composites, the values for this effect are typically in the range of 10% to 50% [4]. Nowadays, however, there is some controversy about the hybrid effect definition because, in traditional uniaxial tensile testing configuration, stress concentration at the grips may cause premature composite failure, leading to an underestimation of the strain at the failure of the baseline LS material [7]. For this reason, these results should be critically interpreted.

Nevertheless, the most relevant advantage of hybrid composites is their gradual, and thus non-catastrophic, failure mode that has been registered in UD layer-by-layer configurations [2, 8], when both the configuration and materials combination are appropriately selected. This is due to the load transfer between LS and HS layers, fragmentation (a damage process where multiple fractures take place) of the formers, followed by the stable delamination of the LS layers from the HS layers, close to the LS layer fractures, ending with the failure of the latter [1]. This behaviour is known as pseudo-ductile [1, 4]. It should be stressed that the term 'pseudo-ductility' is used because it is possible to achieve a flat-topped stress-strain curve of monotonic tensile tests up to the failure of some unidirectional hybrid FRP composites but the tensile curve is not repeatable on subsequent unloadings/reloadings.

The topic of hybrid composites has become a highly active research area in the 1970's and 1980's [3, 5, 9-16]. Over the time, several literature reviews on this subject were published [3, 4, 16]. The study of hybrid composites was essentially motivated in the scope of the aerospace and automotive industries [3, 4, 17]. It has been demonstrated that hybrid composites have greater advantages over traditional composites. The vast majority of the works published generally reported mechanical tension test results of hybrid composites indicating: (i) a linear

increase of elastic modulus in respect to HS material (generally glass fibres) with the addition of LS material (in most part of cases, carbon fibres) [3], (ii) a load drop at the LS material fracture (in non-catastrophic cases), and (iii) a significant hybrid effect [2].

Swolfs *et al.* [18] explained that, in non-hybrid UD composites, when a fibre fails, it locally loses its load transfer capability. The surrounding matrix is loaded in shear and transfers the load carried out by the broken fibre to the surrounding ones, increasing their probability of break. When enough neighbouring fibres are broken, a critical cluster size is reached and catastrophic failure occurs. The restriction caused by HS fibres adjacent to a LS fibre broken, has been reported as the main factor contributing for the hybrid effect, since HS fibres inhibit the formation of critical clusters [4, 7]. However, other reasons for the hybrid effect have been pointed out, namely: (i) thermal residual stresses, i.e., residual shrinkage stresses due to differences in the thermal contraction of the two fibre types, and (ii) the modification, relatively to non-hybrid composites, of the temporary dynamic stress concentrations, due to stress wave travelling along each fibre when it fails [4]. The latter has received no attention at all in the past two decades and remains poorly investigated today [4].

Recently, Swolfs and his co-authors have carried out extensive work aiming at understanding the hybrid effect [18-25]. In [21], the effect of fibres dispersion on the initial strain at the failure and cluster development in UD carbon/glass hybrid composites was numerically studied. It was concluded that the strain at the failure of carbon fibre composites can be dramatically increased with a large fraction of well-dispersed glass fibres. However, random dispersion configurations are not the best option to achieve maximum hybrid effect. Layer-by-layer hybrids are more efficient in delaying the failure development. Furthermore, it was indicated that the hybrid effect gradually increases with the increase in volume fraction of HS fibres. In [24] and [25], it was demonstrated that the higher the scatter of LS fibres strength, the higher the hybrid effect.

Simultaneously, an exhaustive work to achieve pseudo-ductile tensile response with UD hybrid composites has been carried out at both the University of Bristol and the Budapest University of Technology and Economics [1, 7, 8, 26-29]. It has been demonstrated that for achieving pseudo-ductility in hybrid composites two damage mechanisms should take place simultaneously, namely: (i) the fragmentation of the LS material and (ii) the stable delamination of the LS material from the HS material layers close to the LS fractures. In carbon/glass hybrid composites made with prepreg plies, it was shown that, if the carbon layer is thin enough, catastrophic delamination propagation around the first carbon fracture is suppressed and, therefore, further fractures in the carbon layer may occur, introducing pseudo-ductility into the stress–strain curve [1, 27]. According to Jalalvand *et al*. [8], the fragmentation in the low strain material becomes saturated and stops when there is no longer any part of the low strain material with constant stress. The different failure mechanisms in carbon/glass hybrid composites were found to be dependent on the ratio of carbon to glass thickness and also the absolute thickness of the carbon [26]. As explained in detail by Jalalvand *et al*. [27], the control of the two mentioned factors can lead to four possible tensile damage modes of UD hybrid composites, as described in Section 3.2.5.3.

An important milestone achieved by Jalalvand *et al*. [8] was the development of an analytical model to predict all possible damage modes of thin-layer UD hybrids. Predictions of this model proved to be in good agreement with nonlinear tensile response of different UD layer-by-layer hybrid configurations. Damage mode maps were generated to study the effects of absolute and relative thicknesses of the carbon layers; these maps have proven to be a very efficient design tool for hybrid composites [27, 28].

In civil engineering context there are already several examples of applying the hybrid composite concept, mainly in the research and development of three main systems: (i) reinforcing bars for reinforced concrete (RC) structures [30-37]; (ii) externally bonded strengthening for RC structures [17, 38-52], and (iii) pultruded profiles for new structures [53-55]. In a general way, experimental results have shown that a significant ductile response, similar or even better, than that of a steel-reinforced concrete member can be achieved with hybrid composites [31, 36]. In addition to gradual failure mode, hybrid composites have the benefit of eliminating the corrosion problems of steel materials [35, 37].

Cui and Tao [35] and Cheung and Tsang [36] conducted works on the development of hybrid composite reinforcing bars. In the design of these solutions four different reinforcing materials, namely carbon, aramid, glass, and steel, were simultaneously used. The resulting hybrid bars demonstrated pseudo-ductile behaviour, with a tensile strength of 644 MPa, a modulus of 140 GPa and an ultimate strain of circa 3%. A series of concrete beams reinforced with the proposed solution were tested and it was demonstrated that the beams had the ability to undergo large inelastic deformations. Pseudo-ductility was found to be similar to that of conventional steel-reinforced beams.

Grace *et al*. [38] develop a UD fabric composed of two types of carbon fibres and one type of glass fibres. In this case, the pseudo-ductility of the composite was achieved through the combination of the different ultimate strain of each of the adopted types of fibres. In [39], the same authors further developed the initial concept by introducing fibres in the diagonal direction, thus enabling the use of the hybrid fabric for simultaneous flexural and shear strengthening of concrete beams. The last work resulted in one US patent [56].

Wu *et al*. [17] developed hybrid composites made of high-strength and high-modulus carbon sheets. The resulting solution was applied in the upgrading of pre-cracked RC beams. It was concluded that the hybrid composites allowed achieving the desired flexural stiffness, ‘yielding’ strength, and pseudo-ductility.

Several of these attempts (in the field of civil engineering) have been developed/applied without a complete understanding about the behaviour of hybrid composites at material level. In most works, the concept of pseudo-ductility was defined as the successive fractures of different (more than two) reinforcing materials and not as a result of the previously described phenomena of fragmentation and controlled delamination of LS fibres. Moreover, with some exceptions [17, 44, 48, 57, 58], the hybrid effect has been ignored in this set of works and the factors that controlled the damage mode of the hybrid composites have not been clearly explained.

Nowadays, it is very common to apply composites made in-situ through the hand lay-up method, i.e., forming the composite on the surface of the structural member to be strengthened, using flexible dry fibre fabrics or sheets and liquid adhesives. This has proved to be a cost effective method and, in addition, the composite can adopt versatile shapes and sizes using simple tools. Despite its advantages, the hand lay-up method is dependent on the skill of the worker, and thus quality control plays a major role to ensure that defects and voids are avoided. According to the best practices suggested in the guidelines, e.g. [59], hand lay-up system shall be referred to the area of dry fibres only because, in this case, the final thickness of the composite cannot be deterministically estimated [59].

Due to the above reasons, it is important to study the performance of hybrid composites produced through the hand lay-up method for civil engineering applications. In the context of analytical modelling, Jalalvand *et al*. [8] have proposed a model to predict with proper accuracy the tensile response of hybrid composites made of prepreg systems, cured at controlled conditions of pressure and temperature. In retrofitting and strengthening, resins are usually impregnated by hand into dry fabrics with curing times being governed by the environmental conditions. In fact, this is one of the most widely used processes for manufacturing FRP composites for structural engineering [60]. In this way, the availability of an analytical model to predict the tensile behaviour of hybrid composites, produced by hand lay-up method, is seen as a very important tool for the design of UD hybrid composites in civil engineering context.

The aim of this chapter is to investigate the tensile stress–strain responses of 16 different UD interlayer (layer-by-layer) hybrid composite combinations, made through the hand lay-up method, of different commercially available raw materials (fibres' packages + resin). Four dry UD fabric materials were used combined with epoxy resin, namely (i) high-modulus carbon, (ii) standard-modulus carbon (also known as 'high-strength carbon'), (iii) E-glass and (iv) basalt, in order to evaluate the hybrid effect and to achieve pseudo-ductility, fully exploiting the benefits of hybridisation. The hybrid effects and the information of the fibres used in other authors' works, published between 1974 and 2016, were collected with the objective of carrying out a statistical analysis. In this way, the data collection of Manders and Bader [13] and Swolfs *et al*. [4] was updated in this chapter. The analysis of the obtained experimental results was complemented with analytical modelling based on the approach developed by Jalalvand *et al.* [8] for hybrid composites.

3.2. Experimental program

3.2.1. Objectives

The main objective of the present chapter is to contribute to the knowledge on the performance of UD hybrid composites produced by the hand lay-up method. The following specific goals are envisaged:

i. To determine the influence of LS fibres relative volume (vol%) on the hybrid effect of different layer-by-layer hybrid composite combinations made through hand lay-up method;
ii. To understand which non-hybrid properties of the constituent materials influence most the hybrid effect, identifying the correlation between intrinsic mechanical properties of fibres and the obtained response (in the present chapter, according to general practice [4], failure strains of non-hybrid composite, obtained in tensile tests, were used as the baseline tensile failure strain to compute the hybrid effect);
iii. To evaluate the accuracy of the rule of mixtures (ROM) and of the bilinear ROM to predict respectively the elastic modulus and the tensile strength of the hybrid composites;
iv. To characterize the hybrid pseudo-ductile tensile behaviour;
v. To extend the analytical approach developed by Jalalvand *et al.* [8] to the present experimental program.

3.2.2. Materials

In the present chapter, commercial dry UD fabrics with similar areal mass of 400 g/m^2 were used. The materials used for the experiments were the UD HM carbon (S&P C-Sheet 640) [61], ST carbon (S&P C-Sheet 240) [62], E-glass (S&P G-sheet E 90/10) [63], and basalt (Dalla Betta Group U400B-40-50-03) [64] fabrics.

In **Table 3.1** the density, areal mass, fibre layer thickness (areal mass density divided by the volumetric mass density) and the basic tensile properties of the mentioned materials are presented. The tensile properties of the fibres were determined according to ASTM D3379-75 [65]. For each dry fabric, a large number of single fibres (see the details in **Table 3.1**) were randomly taken from the dry fabrics and tested in tension. The tests were carried out in a Hounsfield H100KS universal testing machine with a maximum load cell capacity of 2.5 N (with an accuracy of ± 0.2% of applied force across load cell force range). Fibres were individually assembled in the tensile jig by means of a work template with a fixed gauge length of 20 mm. Fibre ends were glued to the work template by an ethyl cyanoacrylate-based adhesive. Then the tab ends were gripped in the jaws of the machine. The work template was cut across, so that just the fibre was fixed as a continuous length within the jig, before starting the tensile tests. The measurements were performed at a rate of 1.5 mm/min, until breakage occurred. For each fibre, records of applied load against extension were taken, and using an average mean diameter, determined through the analysis of microscopy images of fibres obtained with Scanning Electronic Microscopy (SEM), the data were converted to stress against strain.

An epoxy-based material (S&P Resin Epoxy 55) was used as matrix for laminating the studied composites, as recommend by the supplier of three dry fabrics (high-modulus carbon, standard-modulus carbon and E-glass). Relatively to basalt fabric, the same resin was used since the

corresponding supplier does not provide a package of fibres and resin. According to the supplier, this epoxy has the following main properties [66]: (i) a tensile strength of 35.8 MPa; (ii) a strain at the failure of 2.3%; and, (iii) an elastic modulus of 2.6 GPa.

Each reinforcing material was labelled according to the information included in **Table 3.1**. In the present chapter, in case of composite materials, numbers placed after letters are used for indicating number of layers. The order that letters appear indicate the stacking sequence of the reinforcing materials.

3.2.3. Specimen manufacturing and test setup

The hybrid composite laminates were manufactured by hand lay-up method, following the best practices suggested in the guidelines [59]. Prior to the manufacturing, dry fabrics were cut into 250 mm × 80 mm pieces. A Teflon film was used to avoid the adhesion of the produced composite laminate to the rigid base. The following protocol was used to obtain the laminates: (i) application of a layer of epoxy over the Teflon film with a brush; (ii) saturation of the fabric layer with epoxy resin; (iii) placement of the fabric over last layer, adjusting it manually; (iv) pressure application by means of a ribbed rigid roller, in order to expel both the epoxy resin excess and air in the composite, and also stretching the latter; and (iv) repetition of steps ii to iv for subsequent layers. The top of the laminate was left rough, simulating real applications. All the samples were then cured at room temperature (20 ± 0.5ºC) for 40 days.

The four specimens of each series were obtained from the laminates produced according to the protocol previously described, using a diamond tipped wheel cutter. Tensile tests were performed according to ISO 527-5:2009 standard [67]. Specimen dimensions were 250/150/15/[0.7-3.5]/[0.5-1.0] mm overall length/free length/width/total thickness/fibre layer thickness, respectively.

Aluminium tabs of 50 × 15 mm^2 were used at each end of the specimen to try to minimise gripping effects. A clip gauge with a gauge length of 100 mm (with a linear error, including hysteresis of 0.25%) was used.

Tensile tests were carried out at room temperature on a universal testing machine (UTM) equipped with a 200 kN load cell (with a linear error less than 0.05% of full scale) and hydraulic grips, as shown in **Figure 3.1**. The specimens were held between grips of the UTM and extended (at a rate of 1 mm/min) up to failure.

3.2.4. Material combinations

In the present chapter, it was decided to perform single-factor experiments with several levels of LS fibres vol%. Symmetric specimens were adopted to test the hybrid combinations, in order to minimize load eccentricity and differential thermal contraction during the cure of the epoxy resin, ultimately leading to bending-stretching coupling, and thus causing undesirable warping

[3]. Furthermore, in a way to try to restrict the stress concentrations at the grips, LS layers were whenever possible sandwiched between HS layers, according to Wisnom *et al.* [7] conclusions.

All possible hybrid composite combinations until 5 layers were studied. In total, 16 series were considered: 10 combinations with 3 reinforcing material layers, and 6 combinations with 5 reinforcing material layers. Since each series was composed of 4 specimens, a total of 64 tests were performed. The combinations of 3 symmetrical layers allowed to analyse the following approximate levels of LS fibres vol%: 0%, 33%, 66% and 100%. In addition, combinations with 5 layers allowed to analyse the following approximate levels of LS fibres vol%: 20%, 40% and 60%. It should be noted that specimens with 5 layers were only tested on 2 hybrid combinations: HM carbon/glass and ST carbon/glass. As previously mentioned, the UD fabrics had slightly different nominal thicknesses and, for this reason, the relative volume of LS fibres (*Vol% LS*) was computed in the next sections, according to Equation (3.1):

$$Vol\%\ LS = \frac{t_L}{t_L + t_H} \times 100 \tag{3.1}$$

where t_L is the half thickness of the LS layers and t_H is the half thickness of the HS layers.

In **Table 3.2** the layer ratio and the stacking sequence of the studied hybrid composite combinations are summarized. In addition to hybrid series, 8 series of non-hybrid composites were produced: half with a single layer of reinforcing material and other half with 3 layers of reinforcing material. Each series was composed of 4 specimens, totalling 32 specimens tested.

In the present chapter, the exact volume of resin was not directly controlled during the application and cross-sectional area of the composite was computed considering only the thickness of the dry fabrics, according to the recommendation suggested in the guideline [59]. In this way, mechanical proprieties of impregnated composite (elastic modulus and tensile stress) were computed considering the wet lay-up system similar to an equivalent system of only dry fabrics. However, in order to present an idea of geometric properties, all the composites were measured with a digital calliper (see **Figure 3.1**).

Table 3.1 — Properties of the dry fabrics and tensile properties of fibres.

Material ID	Properties of the dry fabric, as reporter by the manufacturer			Properties of the fibres (tested according to ASTM D3379)				
	Density [g/m^3]	Areal mass [g/m^2]	Fibre layer thickness [mm/layer]	N. of samples	Fibre diameter [μm] (CoV [%])	Elastic modulus [GPa] (CoV [%])	Tensile strength [MPa] (CoV [%])	Strain at the failure [%] (CoV [%])
Basalt (B)	2.67	420	0.157	50	18.14 (3.56)	61.41 (31.14)	1886.70 (40.79)	3.10 (27.73)
E-glass (G)	2.60	400	0.154	50	14.98 (16.25)	76.92 (27.97)	2662.06 (33.88)	3.72 (20.45)
ST carbon (C)	1.79	400	0.223	36	7.88 (5.15)	213.95 (43.36)	3920.67 (39.37)	1.38 (17.37)
HM carbon (CHM)	2.10	400	0.190	26	11.03 (6.66)	558.07 (24.67)	2934.24 (19.16)	0.53 (18.99)

Table 3.2 — Layer ratio and stacking sequence of the tested hybrid composites.

Designation	Layer ratio (LS/HS fibres) [%]	Stacking sequence
1LS/1HS/1LS	66/33	□■□
1HS/3LS/1HS	60/40	■□□□■
1HS/1LS/1HS/1LS/1HS	40/60	■□■□■
1HS/1LS/1HS	33/66	■□■
2HS/1LS/2HS	20/80	■■□■■

Notes: ■ – HS fibres layer; □ – LS fibres layer.

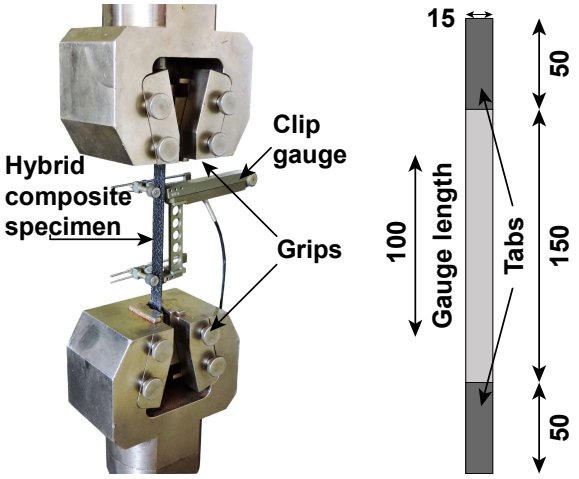

(a) (b)

Figure 3.1 — Tensile test: (a) illustration of the test and (b) geometry of specimen (dimensions in mm).

3.2.5. Analytical models for hybrid composites

3.2.5.1. Elastic modulus

The longitudinal elastic modulus of the hybrid composites has been shown to follow the linear rule of mixtures (ROM) [4]. According to this model, the elastic modulus of the hybrid composite, E_{hybrid}, can be predicted as the sum of the contributions of the three constituents, given by equation (3.2):

$$E_{hybrid} = V_L E_L + V_H E_H + V_M E_M \tag{3.2}$$

where V_L, V_H, V_M, E_L, E_H, and E_M are the volumetric fraction and elastic modulus of the LS fibres, HS fibres and matrix, respectively.

Phillips [14] and Kretsis [16] pointed that some deviations in the predictions of elastic modulus of hybrid composites by using ROM can only be explained by an incorrect use of this rule, namely due to an incorrect input of the volume fraction of reinforcing materials.

In the present chapter, the linear ROM was used to predict the elastic modulus of hybrid composites in order to check the volume and alignment of the reinforcing materials. To achieve this, the mechanical properties experimentally characterized of non-hybrid composites were used as input variables. The exact volume of resin was not directly controlled during the application and cross-sectional area of the composite was computed considering only the thickness of the dry fabrics, according to the usual practice of the hand lay-up method [59]. In this way, E_L and E_H were considered the elastic modulus of LS and HS one layer composites, respectively. Therefore, the contribution of $V_M E_M$ was contemplated in $V_L E_L$ and $V_H E_H$ terms, leading to $V_L + V_H = 1$ and $V_M E_M = 0$.

3.2.5.2. Tensile strength

The tensile strength of the hybrid composites does not follow linear ROM, e.g. [4, 13, 16, 68, 69] because if the volume fraction of HS fibres is appropriate when LS fibres fail, the load can be transferred to HS fibres until their final failure. Otherwise, the composite would fail prematurely. For this reason, some authors [13, 16, 70] have proposed a bilinear ROM (see Eq. (3.3)) to predict the tensile strength of hybrid composites, σ_{hybrid}.

$$\sigma_{hybrid} = \begin{cases} V_L S_L + V_H E_H \varepsilon_L;\ V_H < V_{crit} \\ V_H S_H;\ V_H > V_{crit} \end{cases} \tag{3.3}$$

where S_L and S_H are the reference strengths of the LS and HS one layer composites and ε_L is the strain at the failure of the non-hybrid LS composite.

Based on this model, if V_H is lower than the critical value, V_{crit}, the hybrid composite would fail prematurely. On the contrary, if V_H is higher than V_{crit}, hybrid composites would keep their integrity up to the failure of HS fibres.

In the present chapter, the bilinear ROM model was used to evaluate the magnitude of predictions' errors. V_{crit} was calculated by equating the two branches of equation (3.3), taking into account that $V_L + V_H = 1$, i.e., V_L is equal to 1-V_H:

$$V_{crit} = \frac{S_L}{S_L + S_H - E_H \varepsilon_L} \tag{3.4}$$

3.2.5.3. Stress-strain curve

In an UD hybrid composite under uniaxial tension loading conditions, the first damage mode is always the failure of the LS fibres; however, the other following damage modes depend on the properties and configuration of reinforcing materials of the composite [27]. The analytical approach proposed by Jalalvand *et al.* [8] considers that four different damage modes may occur after the LS fibres failure: (i) premature HS failure, (ii) unstable delamination, (iii) LS layer fragmentation and (iv) LS fragmentation and stable delamination. For each hybrid configuration, three stress levels could be computed [8]: (i) the stress at which the first crack in the LS material occurs, *σ@LF*, (ii) the stress level at which delamination development occurs, *σ@del,* and (iii) the stress when the high strain material fails, *σ@HF*, in accordance with the equations (3.5) to (3.7), respectively.

$$\sigma@LF = S_L \frac{\alpha\beta + 1}{\alpha(\beta + 1)} \tag{3.5}$$

$$\sigma@del = \frac{1}{1+\beta} \sqrt{\left(\frac{1+\alpha\beta}{\alpha\beta}\right)\left(\frac{2 G_{IIC} E_H}{t_H}\right)} \tag{3.6}$$

$$\sigma@HF = \frac{1}{(1+\beta)} \frac{S_H}{K_t \sqrt[m_H]{V}} \tag{3.7}$$

where α and β are the modulus and thickness ratios of the LS to HS fibres, G_{IIC} is the mode II interlaminar fracture toughness of the interface between LS layers and HS layers of the hybrid

composite, m_H is the Weibull strength distribution modulus of the HS fibres, K_t is the stress concentration factor in the high strain material and V is the volume of the specimen (free length × width × total fibre layer thickness).

Knowing the magnitude of all three possible stresses allows assessing their order of occurrence and, consecutively, the identification of the damage modes, according to **Table 3.4**. The details of the analytical approach are fully discussed in [8].

After the determination of the damage modes, it is possible to plot the stress–strain curve using the characteristic points given in **Table 3.5**. In the latter, E_{sat} is the saturated modulus of the composite (according to equation (3.8)), ε_H is the strain at the failure of the HS fibres and $\varepsilon_{@H\text{-}PS}$ is the strain in the composite at the post-saturation phase when the high strain material fails (according equation (3.9)).

$$E_{sat} = E_H \frac{\alpha\beta+1}{(\beta+1)(1+\frac{11}{18}\alpha\beta)} \tag{3.8}$$

$$\varepsilon_{@H-PS} = \frac{\varepsilon_H}{\frac{m_H\sqrt{V}}{K_t}} - \frac{7}{18}\frac{S_L\beta}{E_H} \tag{3.9}$$

Since the model by Jalalvand *et al.* [8] does not consider the hybrid effect, the strain at the failure of LS materials in hybrid combination was assumed to be equal to the obtained experimental values (according to the method developed by the author), and S_L was computed according to Hooke's law. In the present chapter, the definitions of 'yield' stress and pseudo-ductile strain suggested by Jalalvand *et al*. [27] were considered: the 'yield' stress is the stress at the point that response deviates from the initial linear elastic line, i.e., equal to σ@LF and the pseudo-ductile strain is defined as the extra strain between the final failure strain and the strain on the extrapolated initial slope line at the failure stress of the stress-strain diagram (see **Figure 3.2**).

Table 3.3 — Geometric properties of specimens.

Material combination	**Series ID**	**Total thickness** [mm] (CoV [%])	**Fibre layer thickness** [mm]	**HS layer thickness** [mm]	**LS layer thickness** [mm]	**Fibre volume fraction** [%]
Non-hybrid	1B	1.01 (18.43)	0.157	--	--	15.57
	3B	1.90 (11.89)	0.471	--	--	24.80
	1G	0.66 (12.74)	0.154	--	--	23.27
	3G	1.87 (3.42)	0.462	--	--	24.67
	1C	1.22 (11.30)	0.223	--	--	18.27
	3C	2.46 (0.85)	0.669	--	--	27.16
	1CHM	1.31 (7.93)	0.190	--	--	14.49
	3CHM	2.95 (9.82)	0.570	--	--	19.34
C/B	1C/1B/1C	2.62 (4.82)	0.603	0.157	0.446	23.01
	1B/1C/1B	2.07 (6.02)	0.537	0.314	0.223	25.92
CHM/B	1CHM/1B/1CHM	2.37 (7.99)	0.537	0.157	0.380	22.71
	1B/1CHM/1B	2.28 (7.96)	0.504	0.314	0.190	22.09
CHM/C	1CHM/1C/1CHM	2.56 (5.55)	0.603	0.223	0.380	23.55
	1C/1CHM/1C	2.55 (4.36)	0.636	0.446	0.190	24.98
C/G	1C/1G/1C	2.85 (7.61)	0.600	0.154	0.446	21.04
	1G/3C/1G	3.24 (6.27)	0.977	0.308	0.669	30.19
	1G/1C/1G/1C/1G	3.05 (3.52)	0.908	0.462	0.446	29.73
	1G/1C/1G	2.05 (4.74)	0.531	0.308	0.223	25.87
	2G/1C/2G	2.91 (3.47)	0.839	0.616	0.223	28.88
CHM/G	1CHM/1G/1CHM	2.66 (5.94)	0.534	0.154	0.380	20.11
	1G/3CHM/1G	3.48 (3.69)	0.878	0.308	0.570	25.25
	1G/1CHM/1G/1CHM/1G	3.36 (2.59)	0.842	0.462	0.380	25.10
	1G/1CHM/1G	2.13 (3.29)	0.498	0.308	0.190	23.40
	2G/1CHM/2G	3.02 (4.00)	0.806	0.616	0.190	26.65

Table 3.4 — Summary of different damage modes in function of stress level (adapted from [27]).

Damage mode	Stress level
Premature failure	$\sigma@HF \leq \sigma@LF \leq \sigma@del$
Catastrophic delamination	$\sigma@HF \leq \sigma@del \leq \sigma@LF$ $\sigma@del \leq \sigma@HF \leq \sigma@LF$ $\sigma@del \leq \sigma@LF \leq \sigma@HF$
Fragmentation	$\sigma@LF \leq \sigma@HF \leq \sigma@del$
Fragmentation & dispersed delamination	$\sigma@LF \leq \sigma@del \leq \sigma@HF$

Table 3.5 — Characteristic points of different damage processes on stress–strain graph (adapted from [8]).

Damage mode	Point 1	Point 2	Point 3	Point 4	Point 5
Premature failure	(0,0)	$(\varepsilon_L, \sigma@LF)$	--	--	--
Catastrophic delamination	(0,0)	$(\varepsilon_L, \sigma@LF)$	$(\varepsilon_L, \sigma@del)$	$\left(\frac{\sigma@del(1+\beta)}{E_H}, \sigma@del\right)$	$\left(\frac{\varepsilon_H}{K_t \sqrt[m_H]{V}}, \sigma@HF\right)$
Fragmentation	(0,0)	$(\varepsilon_L, \sigma@LF)$	$\left(\frac{\sigma@LF}{E_{sat}}, \sigma@LF\right)$	$(\varepsilon_{H-PS}, \sigma@HF)$	--
Fragmentation & dispersed delamination	(0,0)	$(\varepsilon_L, \sigma@LF)$	$\left(\frac{\sigma@LF}{E_{sat}}, \sigma@LF\right)$	$\left(\frac{\sigma@del(1+\beta)}{E_H}, \sigma@del\right)$	$\left(\frac{\varepsilon_H}{K_t \sqrt[m_H]{V}}, \sigma@HF\right)$

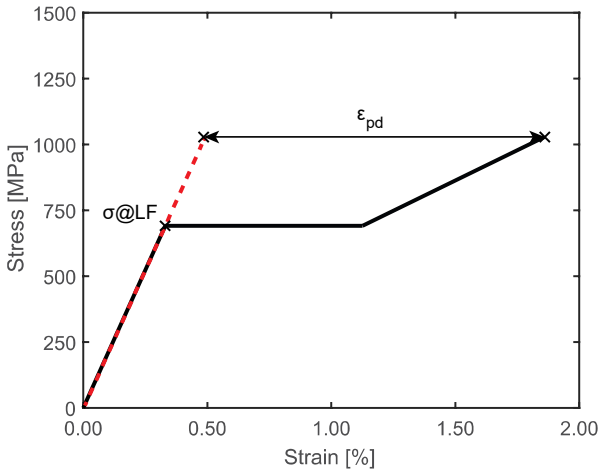

Figure 3.2 — Illustration of nonlinear pseudo-ductile behaviour and definition of 'yield' stress and pseudo-ductile strain (adapted from [2]).

3.3. Results and discussion

3.3.1. Tensile properties of non-hybrid composites

In **Figure 3.3**, the dispersion of the obtained results and their mean values are plotted. It can be concluded that, in all cases, the change from 1 to 3 layers of reinforcing material promotes a

reduction of the magnitude of the elastic modulus, tensile strength, and tensile strain at failure. The mean values of the tensile properties and their coefficient of variation (CoV) are presented in **Table 3.6**, for each series. For each reinforcing material, the *t* statistical test (*t*-test) was used to assess whether the mean values of two groups of tensile properties are statistically different from each other, with a significant level of 5%. The mean values that were significantly different are underlined in **Table 3.6**. The highest decreases were founded in glass and HM carbon composites: tensile strength and strain at the failure decreases 416.4 MPa (24.9%) and 675.5 MPa (38.6%) and 0.31% (13.4%) and 0.09% (33.3%), respectively. These decreases can be explained by two factors: (i) for one hand, it is well known that there is a size effect in tensile properties of reinforcing fibre due to the higher probability of finding a cluster of weaker fibre in a larger volume of material [7]; (ii) for other hand, in tensile tests, stress concentrations can be more predominate where the load is introduced. As expected, in the elastic modulus non-significant variations were registered in all cases.

In **Table 3.6** it is even possible to observe that tensile strength, and consequently the elastic modulus, of cured composites are higher than the obtained values for single fibres. This is due to the fact that, in case of composites, the tensile properties were evaluated considering only the dry fabric thickness which conducted to overestimation of these properties. On the other hand, the strain at failure of composites is lower than the one obtained for single fibres. This was expected because in UD composites fibres break as soon as the weakest link is overloaded. Broken fibre sheds load to the nearby fibres, subjecting them to stress concentrations. Stress concentrations increase the failure probability of the nearby fibres that will lead to the development of fibre break clusters and cause final composite failure [71]. Furthermore, in glass and basalt series the mechanical properties of epoxy could be predominant in the composite failure because the strain of the resin at failure is lower than the strain of fibres at failure.

In **Table 3.6** the obtained failures modes of all specimens are also identified. Each failure mode was labelled according to the information included in ASTM D 3039/D 3039M standard [72]. Numbers placed after letters are used for indicating the number of specimens in which the same failure mode was obtained. As referred before, stress concentrations may be responsible for the variability observed in failure modes and lowering both the average strength and strain. Furthermore, layer overlap, in case of specimens with 3 layers, can lead to the occurrence of more emphasized size effects and different failure modes, such as delamination, that would cause more scatter. Therefore, an accurate way of measuring the strain at failure of non-hybrid composites should be further investigated. For this reason, a hypothetic increase on baseline strain of LS material would lead to a decrease on the values of hybrid effects obtained in the present chapter. Nevertheless, from **Table 3.6** it is possible to observe that, for series 1C and 1CHM, 3 out of the 4 tested specimens have failed at gage length.

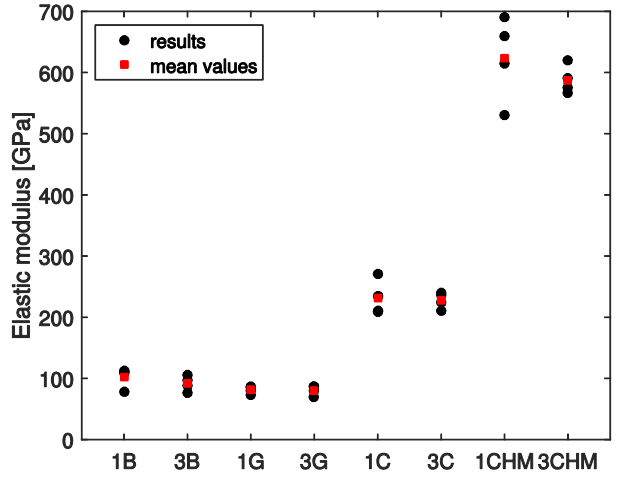

(a)

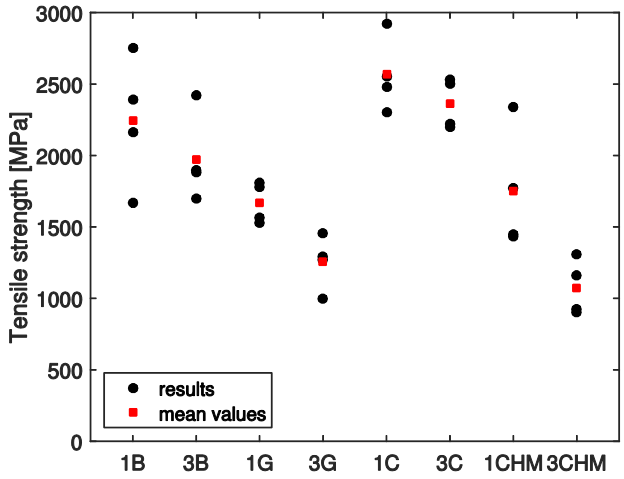

(b)

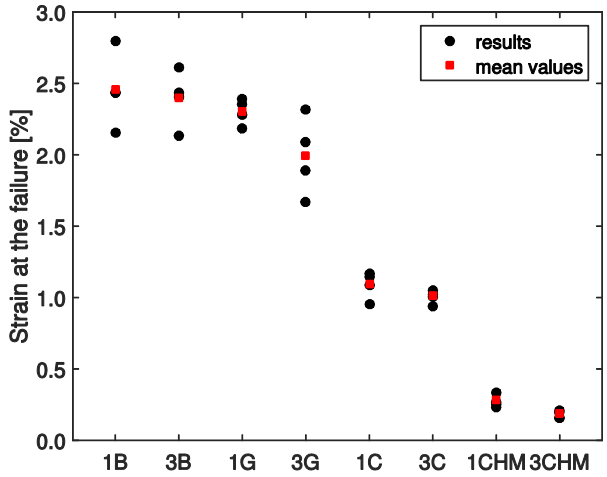

(c)

Figure 3.3 — Scatter diagrams and mean values of the non-hybrid composites tensile properties: (a) elastic modulus; (b) tensile strength and (c) strain at the failure.

Table 3.6 — Tensile properties obtained with non-hybrid composites.

Series ID	**Elastic modulus** [GPa] (CoV [%])	**Tensile strength** [MPa] (CoV [%])	**Strain at the failure** [%] (CoV [%])	**Failure modes, according to ASTM D3039** [72]
1B	102.5 (15.46)	2244.2 (20.17)	2.46 (10.61)	LIT(1) OGM(3)
3B	92.6 (13.55)	1974.6 (15.76)	2.40 (8.26)	OGM(4)
1G	81.6 (7.39)	1671.2 (8.59)	2.31 (3.78)	LGM(2)
3G	80.6 (10.10)	1254.8 (15.05)	2.00 (13.95)	LAT(1) LGM(2) AGM(1)
1C	231.3 (12.50)	2565.9 (10.18)	1.09 (8.81)	OGM(1) LGM(3)
3C	227.6 (5.80)	2363.2 (7.44)	1.02 (6.02)	LAB(1) LGM(1) LIT(1) LAT(1)
1CHM	624.1 (11.13)	1749.4 (24.39)	0.27 (19.61)	LGM(3) SGM(1)
3CHM	588.2 (3.97)	1073.9 (18.27)	0.18 (15.84)	LAB(3) LIT(1)

Note: the pair mean values underlined are significantly different from each other (according to t-test); L – lateral; S – longitudinal splitting; O – other; I – inside grip; G – gage; A – at grip; T – top; M – middle; B – bottom; numbers placed after letters are used for indicating the number of specimens in which the same failure mode was obtained.

3.3.2. Tensile tests of hybrid composites

3.3.2.1. Elastic modulus and tensile strength

A summary of the tensile properties obtained for the hybrid composites is presented in **Table 3.7**. Volumes of reinforcing materials were computed as a function of their density and areal mass. The tensile strength was defined as the maximum value observed in the stress–strain curve. The results of 1 layer non-hybrid composites were used to serve as reference in the comparisons with the analytical predictions.

Figure 3.4 shows the evolution of the elastic modulus with the LS fibre vol% of the tested specimens, as well as the mean and their 95% Fisher level of confidence intervals overlapped with ROM curves. As previously mentioned, the elastic modulus increases linearly with the increase of LS fibres vol%. As expected, the largest elastic modulus increases were found in the combinations of reinforcing materials in which this property differed the most: HM carbon/glass (**Figure 3.4** (a)) and HM carbon/basalt (**Figure 3.4** (c)). Relatively to the ST carbon/glass (**Figure 3.4** (b)), ST carbon/basalt (**Figure 3.4** (d)), and HM carbon/ST carbon (**Figure 3.4** (e)) combinations, the elastic modulus increases were softer.

Relatively to ROM, predictions showed a good agreement with the experimental results. The obtained relative errors varied between -14.5% and 9.6%. This magnitude of the error values is acceptable and it is in agreement with the bibliography [16]. For this reason, it is believed that in the present case there was not a significant deviation in fibres alignment. Therefore, it can be

stated that ROM is a model that can be used as a quality control tool for hand lay-up hybrid composites, since it allows checking the volume and the alignment of the reinforcing materials used in this type of composites.

Figure 3.5 presents the experimental results for the case of the tensile strength. As in the previous case, the scatter diagrams of tensile strength results, their mean results, and their 95% Fisher level of confidence intervals were overlapped with bilinear ROM curves. In general, it is possible to distinguish between two types of behaviour: (i) in the combinations that included HM carbon fibres, a small tensile strength variation with increasing LS fibres vol% was registered, and (ii) in the combinations that included ST carbon fibres, a clear tensile strength increase with the increase in LS fibres vol% was observed. This is understandable, since HM carbon exhibits a low tensile strength and, therefore, it is not expectable to observe improvements in the tensile strength by increasing the volume of this material. An opposite behaviour is observed when ST carbon is used.

In the case of bilinear ROM predictions, deviations from the experimental results were also found, varying between -15.7% and 16.9%. In this way, the relative errors were higher than those obtained with ROM. These results were expected, since, as previously explained, the bilinear ROM does not consider delamination and hybrid effect phenomena [8, 69]. In **Figure 3.5** it is also possible to observe that there were 5 combinations located in the multiple facture zone: 2G/1CHM/2G, 1G/1CHM/1G, 1G/1CHM/1G/1CHM/1G, 1B/1CHM/1B and 1C/1CHM/1C. All these combinations had in common the use of the HM carbon fibres as LS fibres. In these cases, catastrophic failures were avoided. In the remaining cases, a catastrophic failure of the HS fibres occurred at the moment of LS fibres failure. In this way, the bilinear ROM was capable of predicting satisfactorily the occurrence of multiple fractures. This topic is further discussed in Section 3.3.2.3.

3.3.2.2. Hybrid effect

The hybrid effect was computed relatively to 1 layer non-hybrid composite results, according to the Equation (3.10):

$$Hybrid\ effect = \frac{\Delta\varepsilon_L}{\varepsilon_L} \times 100 \tag{3.10}$$

where $\Delta\varepsilon_L$ is absolute variation of the strain at the failure of LS material obtained in hybrid and non-hybrid composites.

As previously mentioned, volumes of reinforcing materials were adjusted in accordance with their density and areal mass. **Figure 3.6** shows the scatter diagrams of the obtained hybrid effects, their mean results and their 95% Fisher level of confidence intervals.

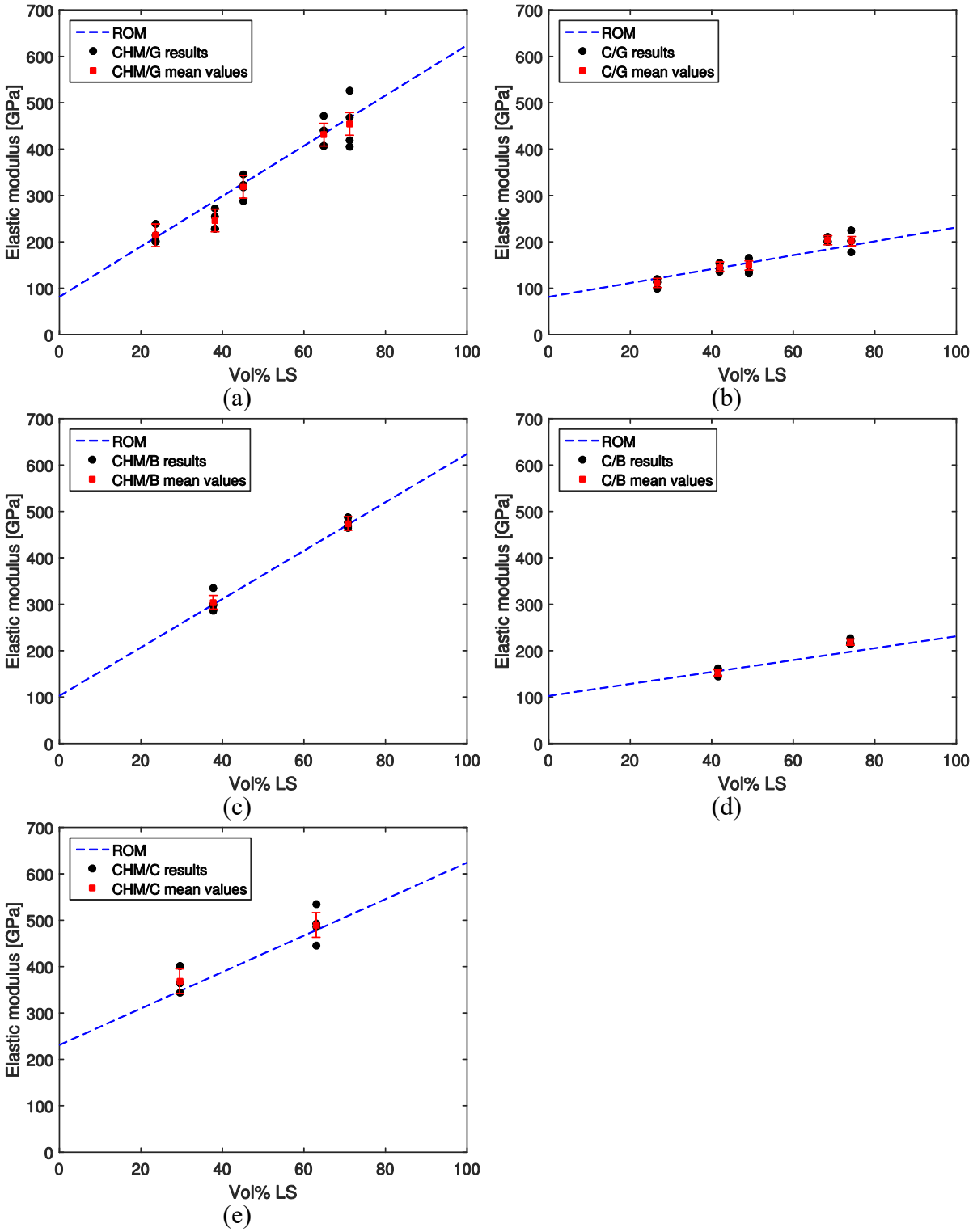

Figure 3.4 — Elastic modulus as function of the LS fibres vol% of the: HM carbon/glass; (b) ST carbon/glass; (c) HM carbon/basalt; (d) ST carbon/basalt and (e) HM carbon/ST carbon.

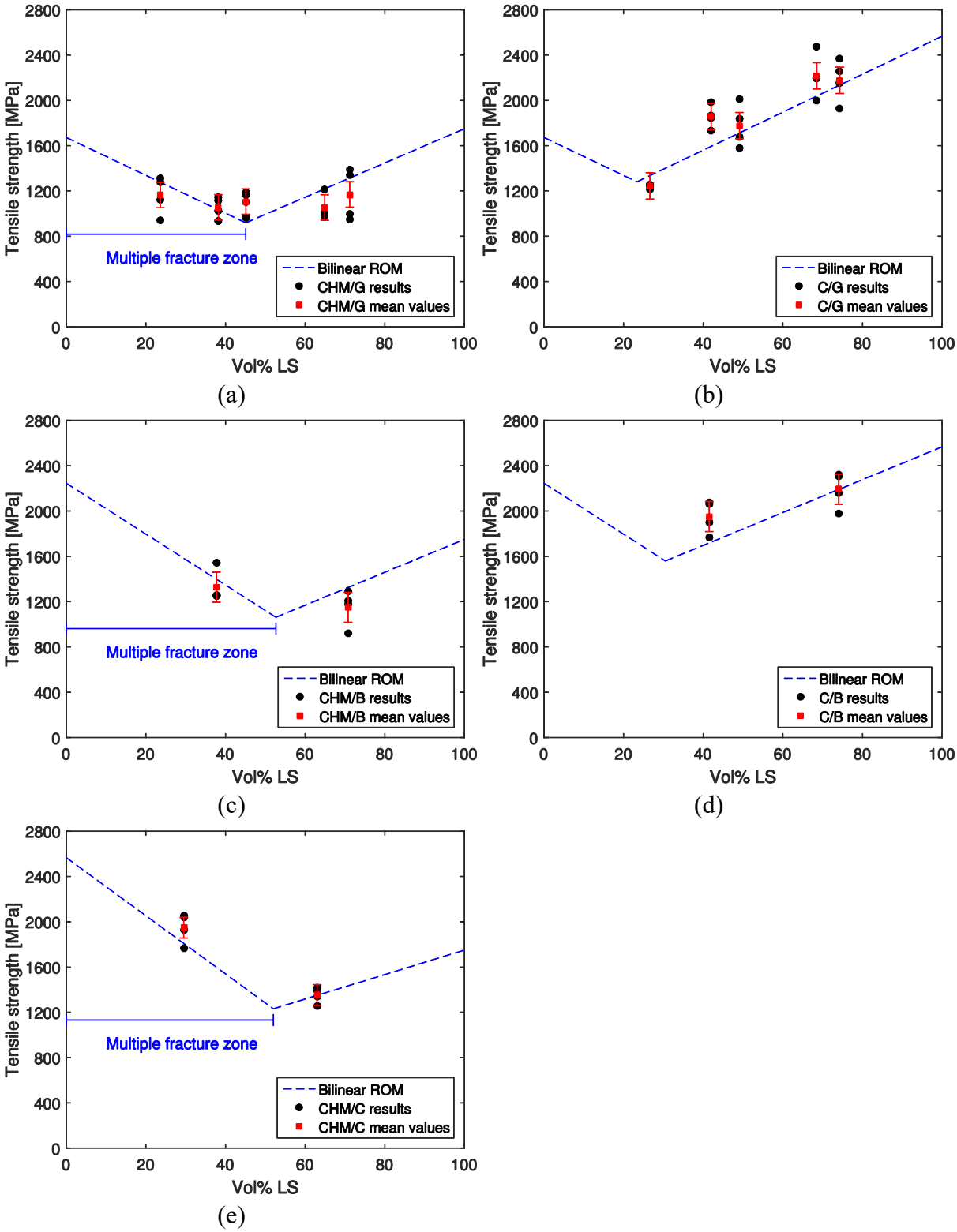

Figure 3.5 — Tensile strength as function of the LS fibres vol% of the: (a) HM carbon/glass; (b) ST carbon/glass; (c) HM carbon/basalt; (d) ST carbon/basalt and (e) HM carbon/ST carbon composites.

As expected, it was possible to observe that the reduction of the LS fibres vol% leads to a clear increase of the hybrid effect. In general, the hybrid effect varied between -14.1% and 44.5%. However, the hybrid effect increase was not linear. In all cases, it was possible to observe that above 60% of relative volume of LS fibres the hybrid effect was close to zero or even negative. As presented above, in non-hybrid composites the use of more layers of the same material caused the reduction of all the analysed tensile properties. The hybrid effect was negative in cases where 2 or 3 layers of LS fibres were used. It should be noted that, since failure strains of 1 layer non-hybrid composite were used as the baseline tensile failure strain to compute the hybrid effect, negative hybrid effects are possible. In fact, it was confirmed that negative hybrid effects never arise when comparisons are made with the results obtained with the 3-layer non-hybrid composites.

Several *t*-tests at a significance level of 5% were performed to compare all pairs of hybrid effect mean values. Relative to HM carbon/glass case, differences between the 3 initial levels of LS fibres vol% hybrid effect mean values were not significant. The same could be concluded for the last 2 levels. The analysis of the carbon/glass series results led to the same conclusion. Since in the remaining combinations of materials only two levels of LS fibres vol% were analysed, the previous conclusion was not refuted for these combinations either.

In order to understand if there were significant variations due to the replacement of glass with basalt material, *t*-tests were performed to compare the pairs of hybrid effect mean values between the combinations of HM carbon/glass, HM carbon/basalt, ST carbon/glass, and ST carbon/basalt. It can be concluded that the changes referred to did not conduct to significant differences in hybrid effect results, as it is shown in **Figure 3.7**. However, with 38.2% of HM carbon fibres relative volume (1G/1CHM/1G), a significant difference was achieved. From the analysis of **Table 3.7** it can be seen that for the 1G/1CHM/1G combination the worst prediction of elastic modulus was achieved by ROM, indicating that the mentioned difference was probably promoted by some misalignment of the fibres.

The hybrid effects and the information of the fibres used in other authors' works, published between 1974 and 2016, were contemplated in the present chapter (see **Table 3.8**). Although the data collection was mainly focused on the interlayer configurations, the information of intralayer configurations presented by Chamis *et al*. [73] was also included, since it is one of the few works in which the hybrid effect with more than 70% of LS fibres relative volume was studied.

Associations between hybrid effect and material factors (such as S_L, S_H, E_L, E_H, ε_L and ε_H) were analysed by a Spearman's rank test using SPSS version 23 (IBM, New York). Additionally, the hybrid effect was also analysed as function of S_L/S_H, E_L/E_H and $\varepsilon_L/\varepsilon_H$ ratios, S_L-S_H, E_L-E_H and ε_L-ε_H differences and a non-dimensional stiffness parameter, E_{ND}, defined by equation (3.11). The E_{ND} was first introduced by Swolfs *et al*. [25], who indicated that the hybrid effect depends on this parameter.

$$E_{ND} = \frac{V_L E_L}{V_H E_H} \tag{3.11}$$

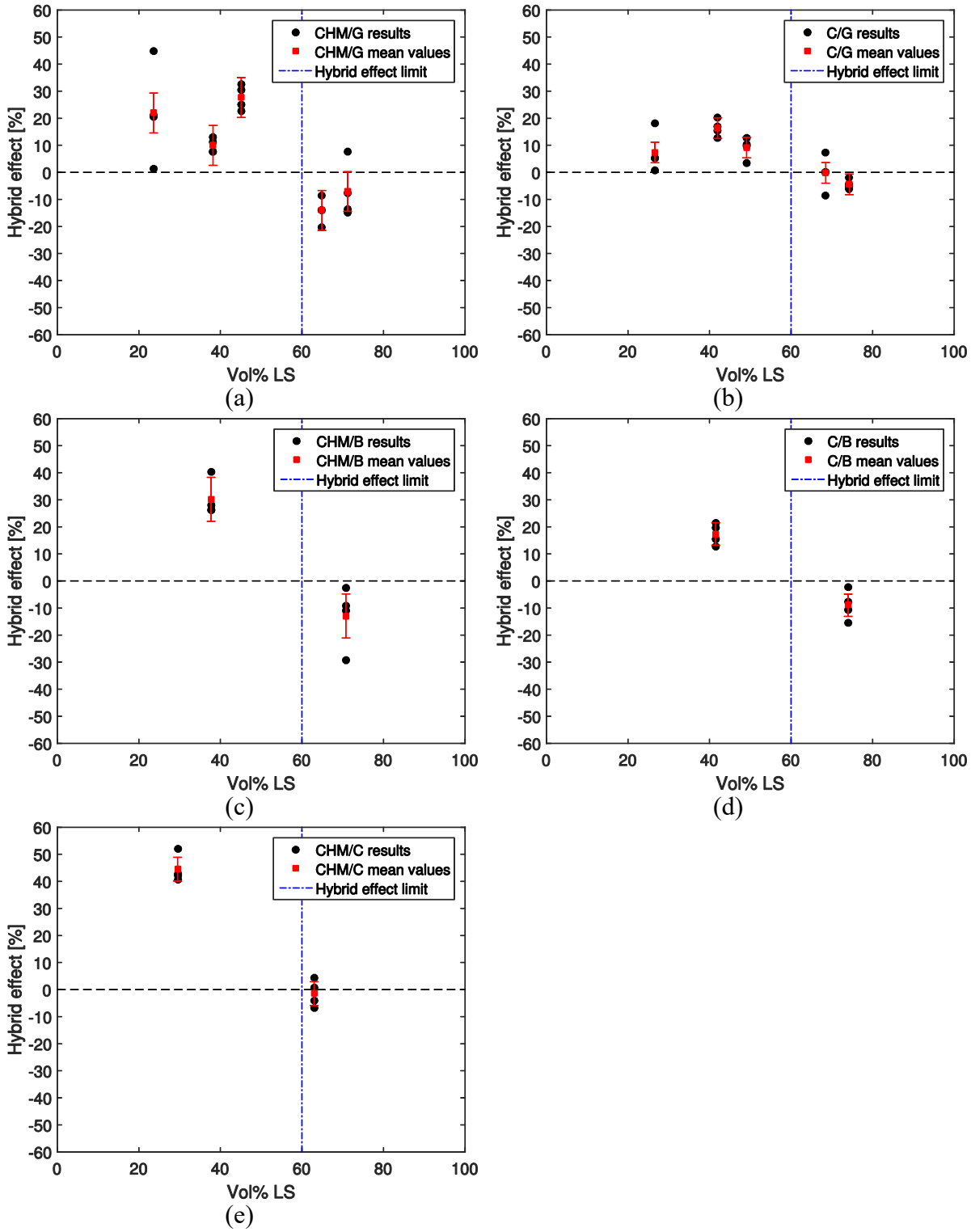

Figure 3.6 — Hybrid effect in function of the LS fibres volume fraction fo the: (a) HM carbon/glass; (b) ST carbon/glass; (c) HM carbon/basalt; (d) ST carbon/basalt and (e) HM carbon/ST carbon composites.

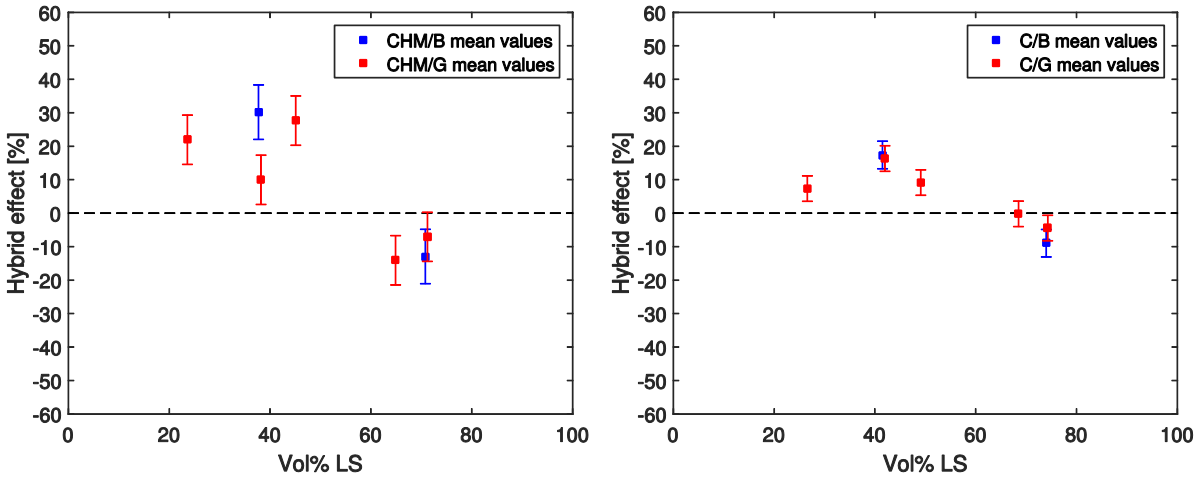

(a) (b)

Figure 3.7 — Differences in hybrid effect caused by replacing glass with basalt: (a) HM carbon series and (b) ST carbon series.

Table 3.7 — Tensile properties obtained with the hybrid composites and ROM and bilinear ROM predictions.

Material combination	Series ID	Volume of LS fibres [%]	Elastic modulus			Tensile strength			Strain at the failure of LS fibres [%] (CoV [%])	Hybrid effect [%]	Failure modes, according ASTM D3039 [72]
			Experimental [GPa] (CoV [%])	ROM [GPa]	Relative error [%]	Experimental [MPa] (CoV [%])	Bilinear ROM [MPa]	Relative error [%]			
C/B	1C/1B/1C	74.0	218.4 (2.84)	197.7	9.5	2191.4 (7.28)	2189.3	0.1	0.99 (5.76)	-8.99	LAT(4)
	1B/1C/1B	41.5	152.5 (5.93)	155.9	-2.2	1950.2 (7.51)	1718.4	11.9	1.28 (3.46)	17.37	OGM(4)
CHM/B	1CHM/1B/1CHM	70.8	474.1 (2.25)	471.6	0.5	1150.0 (14.10)	1325.4	-15.3	0.24 (11.19)	-12.95	LAT(3) LGM(1)
	1B/1CHM/1B	37.7	297.4 (9.29)	299.1	-0.6	1328.0 (10.74)	1398.1	-5	0.36 (5.77)	30.19	fragmentation
CHM/C	1CHM/1C/1CHM	63.0	489.6 (7.39)	478.8	2.2	1352.5 (5.10)	1350.3	0.2	0.27 (5.55)	-1.50	LGM(1) LAB(1) LAT(2)
	1C/1CHM/1C	29.5	368.8 (6.43)	348.6	5.5	1937.5 (6.79)	1809.0	7	0.39 (3.59)	44.52	fragmentation
C/G	1C/1G/1C	74.3	201.7 (9.63)	192.8	4.4	2176.9 (8.55)	2135.1	1.9	1.04 (1.92)	-4.44	LAB(3) LAT(1)
	1G/3C/1G	68.5	202.4 (2.64)	184.0	9.6	2216.0 (8.77)	2037.8	8.0	1.08 (6.26)	-0.20	LAB(2) LIT(1) LGM(1)
	1G/1C/1G/1C/1G	49.1	148.9 (11.75)	155.1	-4.1	1776.3 (10.55)	1712.6	3.6	1.19 (3.68)	9.15	LAT(1) LGM(2) LAB(1)
	1G/1C/1G	42.0	146.7 (5.92)	144.4	1.6	1856.0 (5.67)	1593.6	14.1	1.27 (2.72)	16.33	LGM(4)
	2G/1C/2G	26.6	110.8 (10.21)	121.4	-9.5	1244.4 (1.74)	1335.4	-7.3	1.18 (8.27)	7.33	LAT(2) LAB(1) LGM(1)
CHM/G	1CHM/1G/1CHM	71.2	454.5 (11.95)	457.7	-2.9	1168.9 (19.49)	1313.7	-12.4	0.25 (11.66)	-7.07	LAT(2) LAB(1) LGM(1)
	1G/3CHM/1G	64.9	439.2 (7.35)	433.8	-0.6	1053.5 (10.14)	1218.4	-15.7	0.23 (6.43)	-14.09	LGM(1) LAT(2) LAB(1)
	1G/1CHM/1G/1CHM/1G	45.1	318.7 (7.33)	326.4	-2.4	1105.8 (9.18)	918.9	16.9	0.35 (5.02)	27.66	LGM(2) LAT(2)
	1G/1CHM/1G	38.2	252.0 (8.55)	288.6	-14.5	1054.7 (9.11)	1032.8	2.0	0.30 (2.39)	9.97	fragmentation
	2G/1CHM/2G	23.6	214.3 (8.45)	209.5	2.2	1164.7 (14.47)	1276.8	-10.0	0.33 (14.65)	21.94	fragmentation

Notes: L – lateral; S – longitudinal splitting; O – other; I – inside grip; G – gage; A – at grip; T – top; M – middle; B – bottom; numbers placed after letters are used for indicating the number of specimens in which the same failure mode was obtained.

Table 3.8 — Resume of tensile properties of different hybrid combinations obtained by different authors.

Year	Ref.	Matrix	Stacking sequence	Tensile strength [MPa]	Elastic modulus [GPa]	Strain at the failure [%]	S_L [MPa]	E_L [GPa]	ε_L [%]	S_H [MPa]	E_H [GPa]	ε_H [%]	Vol% LS [%]	Hybrid effect [%]
1974	[13]	Epoxy	1G/2C/1G	300	89	0.37	400.00	142.00	0.26	520.00	41.00	1.25	50.0	42.0
1974		Epoxy	1G/1C/1G	340	72	0.48	400.00	142.00	0.26	520.00	41.00	1.25	33.0	85.0
1976		Vinylester	4G/1C	660	56	1.18	1130.00	115.00	0.98	730.00	40.00	2.00	20.0	20.0
1976		Vinylester	3G/1C	690	60	1.15	1130.00	115.00	0.98	730.00	40.00	2.00	25.0	17.0
1976		Vinylester	2G/1C	720	65	1.11	1130.00	115.00	0.98	730.00	40.00	2.00	33.0	13.0
1976		Vinylester	1G/1C	750	75	1.00	1130.00	115.00	0.98	730.00	40.00	2.00	50.0	2.0
1977		Epoxy	1C/1G						1.80			1.04	50.0	3.8
1978		Epoxy	1C/1G	850	61	1.39	1200.00	97.00	1.23	700.00	25.00	2.80	50.0	13.0
1979		Epoxy	2C/2G	830	61	1.36	1200.00	97.00	1.23	700.00	25.00	2.80	50.0	11.0
1980		Epoxy	5C/5G	800	62	1.29	1200.00	97.00	1.23	700.00	25.00	2.80	50.0	5.0
1981		Epoxy	1G/1CHS/1G	1040	83	1.25	1520.00	135.00	1.12	1200.00	39.00	3.00	33.0	39.0
1981		Epoxy	2G/1CHS/2G	920	65	1.42	1520.00	135.00	1.12	1200.00	39.00	3.00	20.0	57.0
1981		Epoxy	3G/1CHS/3G	870	59	1.48	1520.00	135.00	1.12	1200.00	39.00	3.00	14.0	67.0
1981		Epoxy	4G/1CHS/4G	900	60	1.49	1520.00	135.00	1.12	1200.00	39.00	3.00	11.0	74.0
1981		Epoxy	6G/1CHS/6G	820	55	1.5	1520.00	135.00	1.12	1200.00	39.00	3.00	8.0	82.0
1981		Epoxy	9G/1CHS/9G	760	49	1.55	1520.00	135.00	1.12	1200.00	39.00	3.00	5.0	88.0
1981		Epoxy	2G/2CHS/2G	1030	76	1.35	1520.00	135.00	1.12	1200.00	39.00	3.00	33.0	40.0
1981		Epoxy	3G/2CHS/3G	970	72	1.35	1520.00	135.00	1.12	1200.00	39.00	3.00	25.0	50.0
1981		Epoxy	1G/3CHS/1G	1430	104	1.37	1520.00	135.00	1.12	1200.00	39.00	3.00	60.0	18.0

Table 3.8 — (Continued)

Year	Ref.	Matrix	Stacking sequence	Tensile strength [MPa]	Elastic modulus [GPa]	Strain at the failure [%]	S_L [MPa]	E_L [GPa]	ε_L [%]	S_H [MPa]	E_H [GPa]	ε_H [%]	Vol% LS [%]	Hybrid effect [%]
1981	[13]	Epoxy	3G/3CHS/3G	1040	77	1.36	1520.00	135.00	1.12	1200.00	39.00	3.00	33.0	40.0
1981		Epoxy	8G/3CHS/8G	820	58	1.41	1520.00	135.00	1.12	1200.00	39.00	3.00	16.0	64.0
1981		Epoxy	3G/8CHS/3G	1380	102	1.36	1520.00	135.00	1.12	1200.00	39.00	3.00	57.0	19.0
1981		Epoxy	1G/9CHS/1G	1400	109	1.29	1520.00	135.00	1.12	1200.00	39.00	3.00	82.0	7.0
1981		Epoxy	8G/9CHS/8G	1030	81	1.27	1520.00	135.00	1.12	1200.00	39.00	3.00	36.0	36.0
1981		Epoxy	1G/1CHM/1G	750	95	0.79	1330.00	192.00	0.69	1200.00	39.00	3.00	33.0	15.0
1981		Epoxy	2G/2CHM/2G	830	99	0.84	1330.00	192.00	0.69	1200.00	39.00	3.00	33.0	22.0
1981		Epoxy	3G/3CHM/3G	750	89	0.84	1330.00	192.00	0.69	1200.00	39.00	3.00	33.0	22.0
1981		Epoxy	6G/7CHM/6G	820	100	0.82	1330.00	192.00	0.69	1200.00	39.00	3.00	37.0	19.0
1981		Epoxy	8G/3CHM/8G	550	65	0.84	1330.00	192.00	0.69	1200.00	39.00	3.00	16.0	22.0
1981		Epoxy	9G/1CHM/9G	510	50	1.01	1330.00	192.00	0.69	1200.00	39.00	3.00	5.0	46.0
1981	[73]	Epoxy	Intralayer	265	20	1.30	1467.57	125.40	1.12	1322.88	47.89	2.84	90	16.1
1981		Epoxy	Intralayer	191	17.8	1.06	1467.57	125.40	1.12	1322.88	47.89	2.84	80	-5.4
1981		Epoxy	Intralayer	84.7	30.4	0.38	1051.41	185.69	0.54	1324.95	47.89	2.84	90	-29.0
1981		Epoxy	Intralayer	81.3	29.6	0.31	1051.41	185.69	0.54	1324.95	47.89	2.84	80	-42.1
1981		Epoxy	Intralayer	109	24.1	0.45	1051.41	185.69	0.54	1324.95	47.89	2.84	70	-15.9
1981		Epoxy	Intralayer	196	18.5	0.38	1472.39	125.40	1.12	1281.54	77.17	1.73	90	-66.1
1981		Epoxy	Intralayer	204	17.8	1.13	1472.39	125.40	1.12	1281.54	77.17	1.73	80	0.9
1981		Epoxy	Intralayer	205	16.8	1.01	1472.39	125.40	1.12	1281.54	77.17	1.73	70	-9.8

Table 3.8 — (Continued)

Year	Ref.	Matrix	Stacking sequence	Tensile strength [MPa]	Elastic modulus [GPa]	Strain at the failure [%]	S_L [MPa]	E_L [GPa]	ε_L [%]	S_H [MPa]	E_H [GPa]	ε_H [%]	Vol% LS [%]	Hybrid effect [%]
1981	[73]	Epoxy	Intralayer	103	26.8	0.37	1051.41	182.59	0.54	1281.54	77.17	1.73	90	-30.8
1981		Epoxy	Intralayer	105	26.9	0.38	1051.41	182.59	0.54	1281.54	77.17	1.73	80	-29.0
1981		Epoxy	Intralayer	110	25.9	0.43	1051.41	182.59	0.54	1281.54	77.17	1.73	70	-19.6
2007	[17]	Epoxy	1C/1G	3305	162.0	2.04	4214.00	242.00	1.74	2121.00	87.00	2.45	48.5	17.2
2007		Epoxy	1C/1B	2271	166.0	1.67	4214.00	242.00	1.74	2332.00	87.00	2.56	50	-4.0
2010	[74]	Polypropylene	2SRPP/1C/2SRPP	219	15.4	1.27	644.00	50.70	1.19	149.00	2.80	21.70	17.0	7.0
2010		Polypropylene	1C/2SRPP/1C	398	26.3	1.41	644.00	50.70	1.19	149.00	2.80	21.70	33.0	18.0
2010		Polypropylene	1SRPP/1C/1SRPP /1C/1SRPP	347	22.8	1.31	644.00	50.70	1.19	149.00	2.80	21.70	28.0	10.0
2011	[75]	Epoxy	3G/4C/3G	436	27.0	2.59	511.00	39	1.36	322.00	12.5	4.25	47.0	90.4
2011		Epoxy	2C/6G/2C	421	27.5	1.86	511.00	39	1.36	322.00	12.5	4.25	47.0	36.8
2011	[76]	Epoxy	1C/1B	2409	142.0	1.74	4067.00	239.80	1.74	2145.00	81.50	2.76	41.57	0.0
2011		Epoxy	1C/2B	2186	125.0	1.84	4067.00	239.80	1.74	2145.00	81.50	2.76	26.24	5.7
2013	[77]	Phenolic	1G/8F/1G		32.3	0.99		29.04	0.85		51.22	1.41	86.0	16.5
2013		Phenolic	1G/2F/1G/2F/1G/ 2F/1G		36.4	1.12		29.04	0.85		51.22	1.41	69.0	31.8
2013		Phenolic	1G/1F/1G/1F/2G/ 1F/1G/1F/1G		40.9	1.25		29.04	0.85		51.22	1.41	50.0	47.1
2013		Phenolic	3G/1F/2G/1F/3G		45.0	1.37		29.04	0.85		51.22	1.41	27.0	61.2
2013	[1]	Epoxy	2G/1C/2G	967	44.0	2.20	1962.00	101.70	1.50	1548.00	38.70	3.40	4.9	18.4

Table 3.8 — (Continued)

Year	Ref.	Matrix	Stacking sequence	Tensile strength [MPa]	Elastic modulus [GPa]	Strain at the failure [%]	S_L [MPa]	E_L [GPa]	ε_L [%]	S_H [MPa]	E_H [GPa]	ε_H [%]	Vol% LS [%]	Hybrid effect [%]
2013	[1]	Epoxy	2G/2C/2G	954	47.0	2.06	1962.00	101.70	1.50	1548.00	38.70	3.40	9.4	10.9
2013		Epoxy	2G/3C/2G	965	49.0	1.92	1962.00	101.70	1.50	1548.00	38.70	3.40	13.4	3.3
2013		Epoxy	2G/4C/2G	985	51.0	1.93	1962.00	101.70	1.50	1548.00	38.70	3.40	17.2	3.9
2014	[78]	Epoxy	1B/1C	2482	145.0	1.74	4067.00	239.80	1.74	2077.00	80.20	2.68	41.6	0.0
2014		Epoxy	2B/1C	2213	124.0	1.84	4067.00	239.80	1.74	2077.00	80.20	2.68	26.2	5.7
2014	[79]	Epoxy	4C/1B/5C	630	60.0	1.07	687.00	65.00	1.06	402.00	18.00	2.20	92.2	0.8
2014		Epoxy	4C/2B/4C	602	55.0	1.10	687.00	65.00	1.06	402.00	18.00	2.20	84.0	3.1
2014		Epoxy	3C/3B/4C	558	50.0	1.10	687.00	65.00	1.06	402.00	18.00	2.20	75.4	3.6
2014		Epoxy	3C/4B/3C	536	45.0	1.14	687.00	65.00	1.06	402.00	18.00	2.20	66.4	7.3
2014		Epoxy	2C/5B/3C	502	40.0	1.20	687.00	65.00	1.06	402.00	18.00	2.20	56.8	13.0
2014		Epoxy	2B/6C/2B	571	49.5	1.15	687.00	65.00	1.06	402.00	18.00	2.20	66.4	8.3
2014		Epoxy	2C/2B/2C/2B/2C	556	47.5	1.17	687.00	65.00	1.06	402.00	18.00	2.20	66.4	10.2
2016	[80]	Epoxy	1C/1G/1C/1G	1034	57.0	2.01	4400.00	235.00	1.70	1838.00	73.10	4.51	56.0	18.2
2016	[28]	Epoxy	1G/1C/1G			2.17	1962.00	101.00	1.50	2138.00	45.70	4.51	8.6	16.6
2016		Epoxy	1G/2C/1G			1.96	1962.00	101.00	1.50	2138.00	45.70	4.51	15.8	5.7
2016		Epoxy	1G/3C/1G			1.84	1962.00	101.00	1.50	2138.00	45.70	4.51	21.9	-1.0
2016		Epoxy	2G/4C/2G			1.88	1962.00	101.00	1.50	2138.00	45.70	4.51	15.8	1.0

Notes: CHS – high-tensile carbon; SRPP – self-reinforced polypropylene; F – flax.

Spearman's correlation coefficient, r, is a statistical measure of the "strength" of a monotonic relationship between paired data. In the present chapter, spearman's rank of data revealed that statistically significant correlations, at a significance level of 5% between the hybrid effect and mentioned variables, were achieved for the cases of S_H, Vol% LS fibres and E_{ND}. There was a weak negative correlation between hybrid effect and S_H (r = - 0.311). On the other hand, moderately strong negative correlations exist between hybrid effect and Vol% LS fibres (r = - 0.526) and E_{ND} (r = - 0.515).

The moderate relationships previously mentioned are plotted in **Figure 3.8**. The dispersion of results and the low Spearman's correlation coefficients obtained do not allow the suggestion of an appropriate model to describe the results. However, no linear trends are clearly observable in the presented diagrams. It is possible to see in **Figure 3.8** that the results obtained in the present chapter are in agreement with those in the literature.

3.3.2.3. Failure modes

As mentioned before, multiple fractures were achieved in some hybrid configurations, according to bilinear ROM predictions (see **Figure 3.5**). Usually, multiple fractures in hybrid composites are characterized by 2 successive failures: the LS fibres fail firstly followed by the HS fibres. However, in 4 situations in this work, pseudo-ductile tensile responses with multiple fractures were observed with some combinations that included HM carbon, as it is shown in **Figure 3.9**. Two outlier results obtained in 1G/1CHM/1G and 1B/1CHM/1B combinations were ignored.

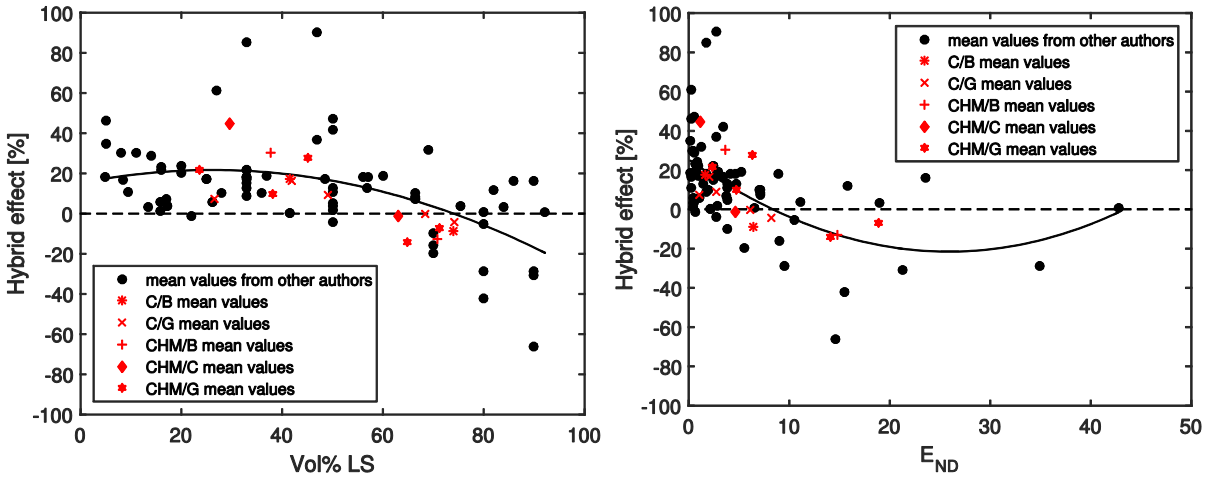

(a) (b)

Figure 3.8 — Scatter diagrams of hybrid effect mean results obtained in this work compared against mean results from other authors: (a) as function of LS fibres vol% and (b) as function of E_{ND}.

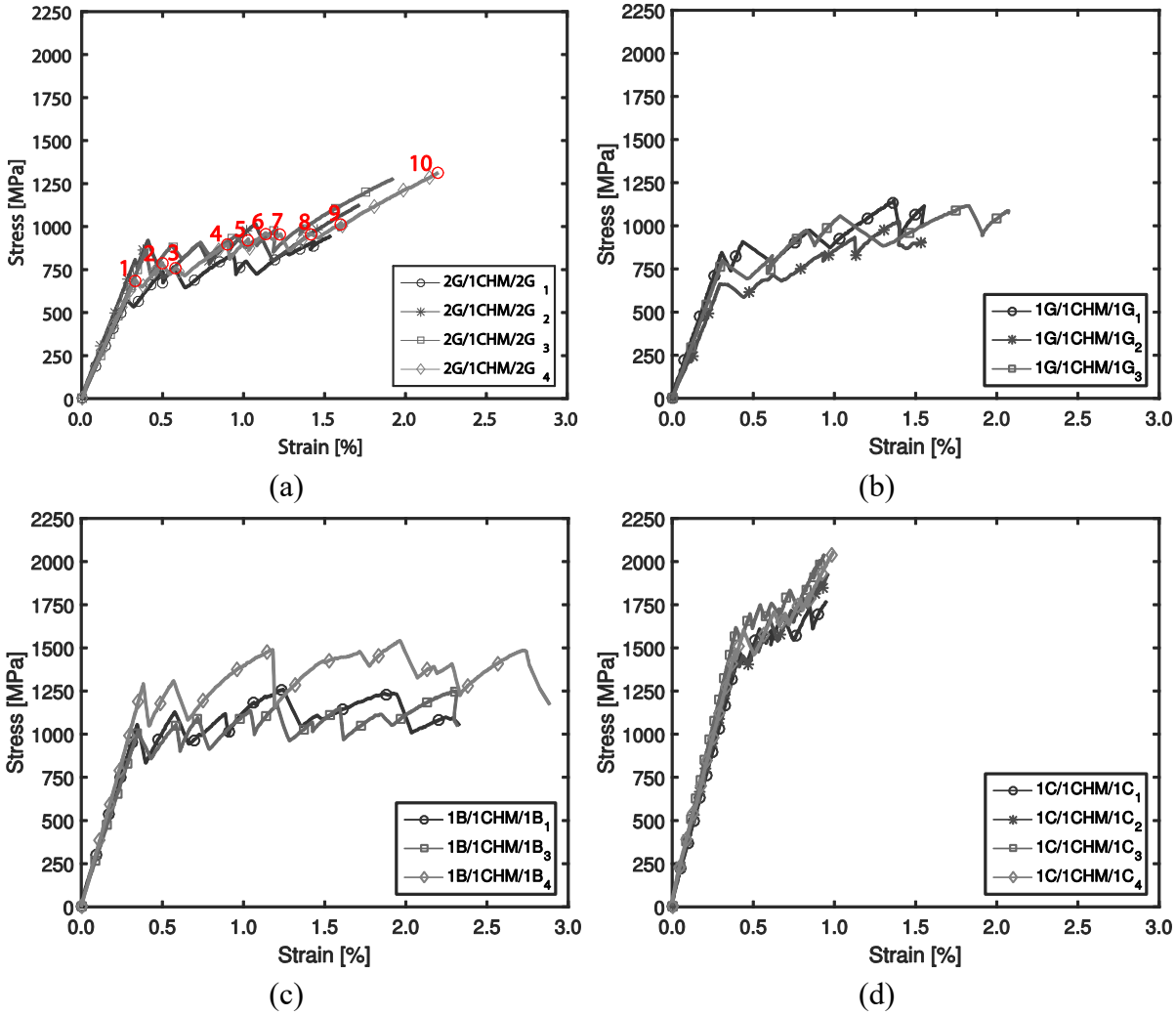

Figure 3.9 — Pseudo-ductile tensile responses: (a) 2G/1CHM/2G; (b) 1G/1CHM/1G; (c) 1B/1CHM/1B and (d) 1C/1CHM/1C series.

In the case of 2G/1CHM/2G, a mean 'yield' stress of 732.6 MPa and a mean pseudo-ductile strain of 1.4% were registered (see **Figure 3.9** (a)). In 1C/1CHM/1C combination a mean 'yield' stress of 1504.5 MPa and a mean pseudo-ductile strain of 0.4% were observed (see **Figure 3.9** (d)). The replacement of glass by basalt resulted in slightly different behaviours (see **Figure 3.9** (b) and **Figure 3.9** (c)): with basalt, higher pseudo-ductile strain and 'yield' stress were obtained. The combination with basalt led to a mean 'yield' stress of 1120.7 MPa and a mean pseudo-ductile strain of 2.0%, whereas the combination with glass yielded a mean 'yield' stress of 768.2 MPa and a mean pseudo-ductile strain of 1.2%. Furthermore, two different behaviours were observed: one with (see **Figure 3.9** (a) and (d)) a clear hardening branch in the end of the pseudo-ductile strain, and another without (see **Figure 3.9** (b) and (c)) the latter.

It should be noted that, since the strain of the epoxy at failure is lower than the strain of glass and basalt fibres at failure, if a resin with higher ultimate strain had been used, larger pseudo-

ductile strains may have been reached in 2G/1CHM/2G, 1G/1CHM/1G and 1B/1CHM/1B combinations. Further studies to confirm these hypotheses are deemed necessary.

In the HM carbon/glass combinations the fragmentation of the HM carbon and delamination could be observed visually during the tensile test due to the translucence of the glass. The specimens were initially black due to the HM carbon natural colour but, after fragmentation and delamination, light was reflected from the interface, and the specimens looked white. **Figure 3.10** shows an example of the aspect of specimen in consecutive phases of the tensile test. The fragmentation of HM carbon is evident. Furthermore, it is possible to observe localised delamination around the carbon layer fractures that developed stably during test until saturation. It is noticed that each stress-strain curve peak, as it is identified in **Figure 3.9** (a), corresponds to a crack of the HM carbon and localised delamination.

3.3.3. Prediction of stress–strain curves

In this section, the predicted stress-strain curves of all hybrid configurations studied in the present chapter, obtained with the model proposed by Jalalvand *et al*. [8], are compared with the corresponding experimental curves. One layer non-hybrid composite results were used as input variables. Since the model of Jalalvand *et al*. [8] is not able to predict the hybrid effect, the ε_L of the different material combinations was assumed to be equal to the experimental values obtained and S_L was computed according to Hooke's law, a similar procedure was used in [8]. As it was demonstrated, the hybrid effect can increase substantially the strain at failure of LS fibres. For this reason, to turn the model capable of predicting the mechanical behaviour of new configurations, a way to predict the hybrid effect should be incorporated. The length and width of all specimens for prediction of high strain material failure were assumed to be equal to L = 150 mm and W = 15 mm, respectively. The interlaminar toughness, G_{IIC}, for the different hybrid interfaces and the value of the stress concentration factor, K_t, were not experimentally assessed. They were computed in a way that, in combinations with pseudo-ductile behaviour, the fragmentation and dispersed delamination damage mode, indicated in **Table 3.4**, was analytical achieved. The G_{IIC} was assumed to be constant for the same material combinations. Weibull modulus was assumed to be equal to the value used by Jalalvand *et al*. [8], i.e., m_H = 29.3. The value of the stress concentration factor was assumed constant for all of the specimens, K_t = 0.97. This value is slightly lower than the one used by Jalalvand *et al*. [8] but allowed the best predictions. All input data is shown in **Table 3.9**.

As it can be seen in **Figure 3.11** to **Figure 3.15**, there is a good agreement between predictions and experiments. Analysing the curves, three groups of behaviours can be identified: (i) pseudo-ductile behaviours (the same that were discussed in Section 3.3.2.3), (ii) failure with two peaks (**Figure 3.11** (c), **Figure 3.11** (d) and **Figure 3.14** (a)), and (iii) premature and abrupt failure of HS fibres (in the remaining cases). The chosen way to estimate the G_{IIC} parameter (considering only configurations in which fragmentation and dispersed delamination damage mode occurred) allowed to estimate with good accuracy the remaining cases.

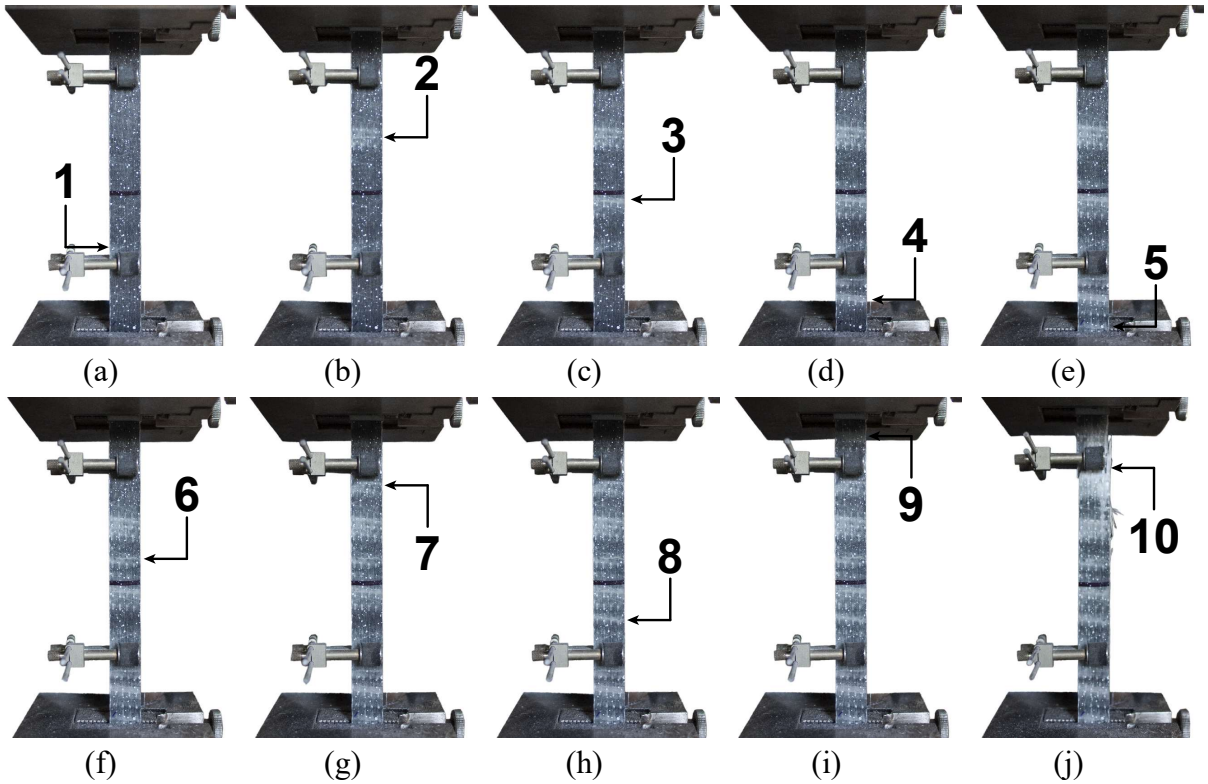

Figure 3.10 — Example of localised delamination around multiple cracked HM carbon-layer that occurred until the final rupture in 2G/1CHM/2G 4th specimen: (a) 1st peak; (b) 2nd peak; (c) 3rd peak; (d) 4th peak; (e) 5th peak; (f) 6th peak; (g) 7th peak; (h) 8th peak; (i) 9th peak and (j) final rupture.

It is also possible to observe that, in the combinations with pseudo-ductile behaviours, the model was not capable of capturing the peaks in the 'flat-topped stress strain curve', since it considers that the fragmentation and delamination occurred consecutively and not simultaneously. In the 1C/1CHM/1C series, the predicted stress-strain curves was somehow conservative. This occurred because S_L and S_H input properties were probably underestimated because these properties were assumed equal to the experimental values obtained with non-hybrid specimens and there is always some variability in the constituents.

In the 1G/1CHM/1G/1CHM/1G and 1G/3CHM/1G series, the model predicted well the catastrophic delamination damage mode, but the prediction of the delamination branch was much higher than the one observed experimentally. This lack of precision is probably related to some overestimation of G_{IIC} in these cases.

In the case of 1B/1C/1B series, the volume proportion of the constituent materials was between premature failure of HS fibres and catastrophic delamination damage mode. For this reason, the model was not capable of predicting the complete tensile response. A 20% increase in ST carbon thickness, keeping the same volume proportion between the reinforcing materials, was enough to get a correct prediction from the model.

Table 3.9 — Analytical model input data.

Material combination	Series ID	G_{IIC} [kN/m]	E_H [GPa]	E_L [GPa]	S_H [MPa]	S_L [MPa]	ε_H [%]	ε_L [%]	K_t	W [mm]	L [mm]	m_H	t_H [mm]	t_L [mm]
C/B	1C/1B/1C	1.90	102.5	231.3	2244.2	2289.9	2.46	0.99	0.97	15	150	29.3	0.0785	0.2230
	1B/1C/1B	1.90	102.5	231.3	2244.2	2960.6	2.46	1.28	0.97	15	150	29.3	0.1570	0.1115
CHM/B	1CHM/1B/1CHM	1.90	102.5	624.1	2244.2	1497.8	2.46	0.24	0.97	15	150	29.3	0.0785	0.1900
	1B/1CHM/1B	1.90	102.5	624.1	2244.2	2246.8	2.46	0.36	0.97	15	150	29.3	0.1570	0.0950
CHM/C	1CHM/1C/1CHM	1.25	231.3	624.1	2565.9	1684.8	1.09	0.27	0.97	15	150	29.3	0.1115	0.1900
	1C/1CHM/1C	1.25	231.3	624.1	2565.9	2434.0	1.09	0.39	0.97	15	150	29.3	0.223	0.0950
C/G	1C/1G/1C	1.90	81.6	231.3	1671.2	2405.0	2.31	1.04	0.97	15	150	29.3	0.0770	0.2230
	1G/3C/1G	1.90	81.6	231.3	1671.2	2521.2	2.31	1.09	0.97	15	150	29.3	0.1540	0.3345
	1G/1C/1G/1C/1G	1.90	81.6	231.3	1671.2	2752.5	2.31	1.19	0.97	15	150	29.3	0.2310	0.2230
	1G/1C/1G	1.90	81.6	231.3	1671.2	2937.5	2.31	1.27	0.97	15	150	29.3	0.1540	0.1115
	2G/1C/2G	1.90	81.6	231.3	1671.2	2706.2	2.31	1.18	0.97	15	150	29.3	0.3080	0.1115
CHM/G	1CHM/1G/1CHM	1.46	81.6	624.1	1671.2	1560.3	2.31	0.25	0.97	15	150	29.3	0.0770	0.1900
	1G/3CHM/1G	1.46	81.6	624.1	1671.2	1435.4	2.31	0.23	0.97	15	150	29.3	0.1540	0.2850
	1G/1CHM/1G/1CHM/1G	1.46	81.6	624.1	1671.2	2184.4	2.31	0.35	0.97	15	150	29.3	0.2310	0.1900
	1G/1CHM/1G	1.46	81.6	624.1	1671.2	1872.0	2.31	0.30	0.97	15	150	29.3	0.154	0.0950
	2G/1CHM/2G	1.46	81.6	624.1	1671.2	2059.5	2.31	0.33	0.97	15	150	29.3	0.3080	0.0950

Notes: t_H – half thickness of the high strain material; t_L – half thickness of the low strain material.

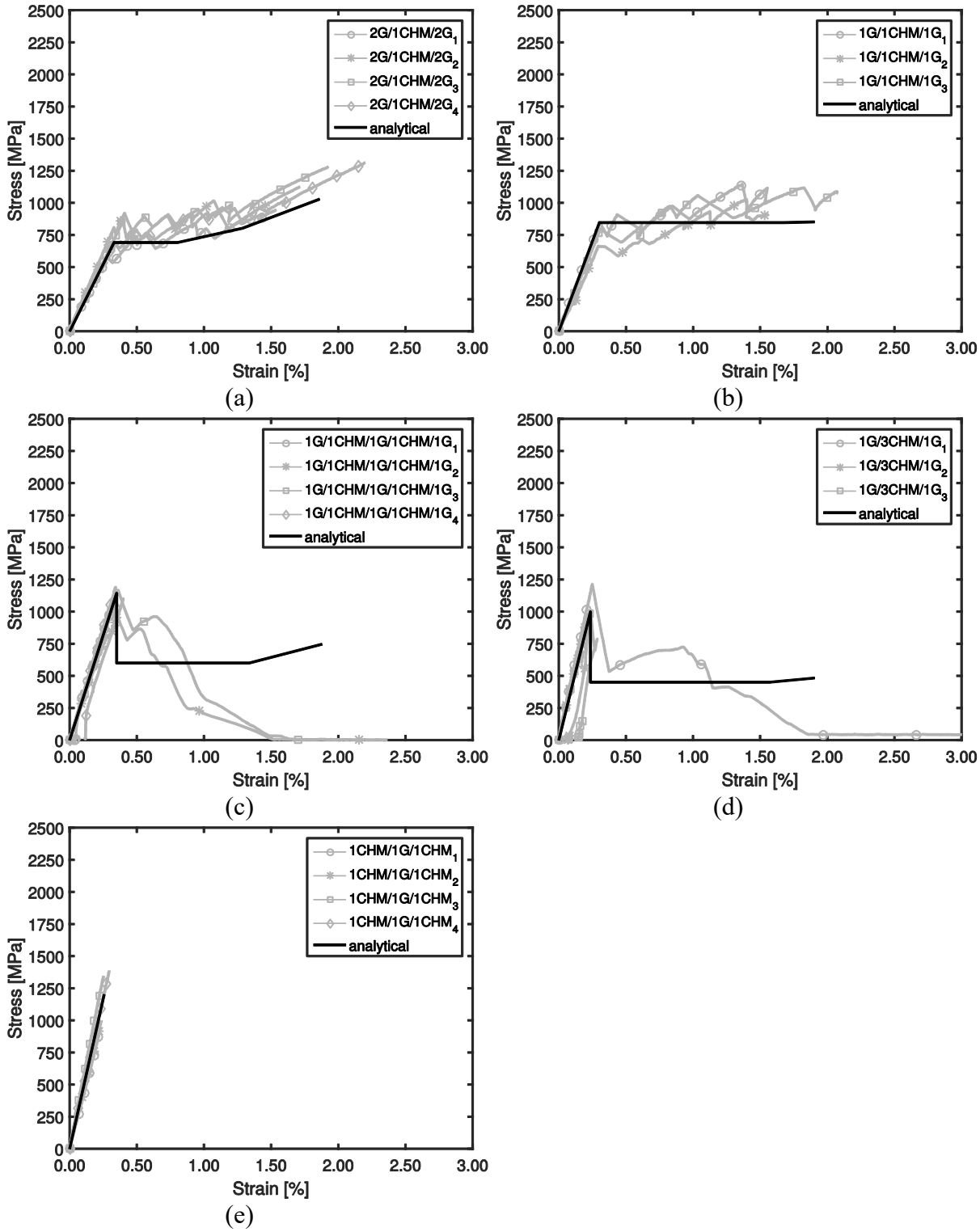

Figure 3.11 — Stress–strain curves of CHM/G combinations: experimental versus predicted values.

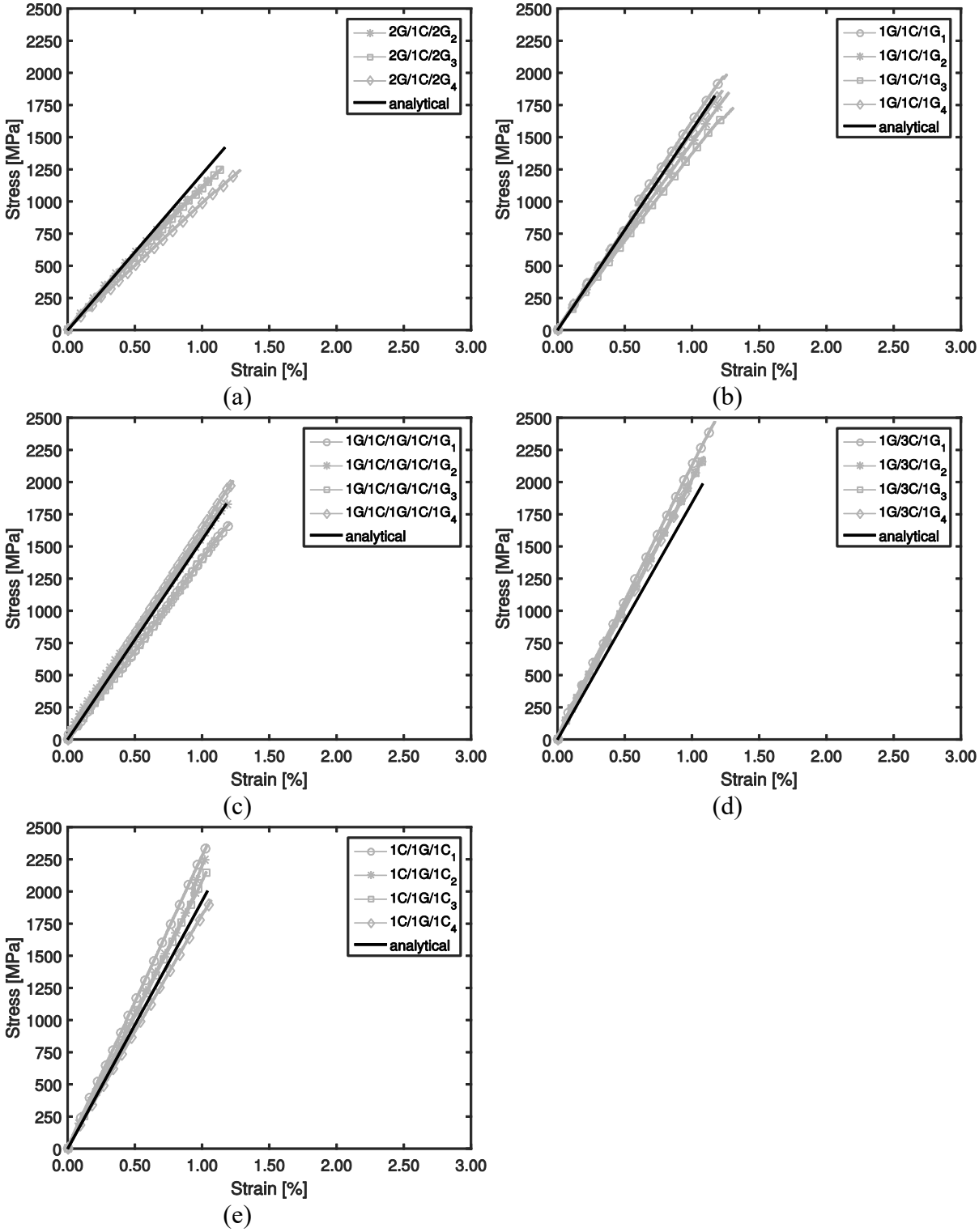

Figure 3.12 — Stress–strain curves of C/G combinations: experimental *versus* predicted values.

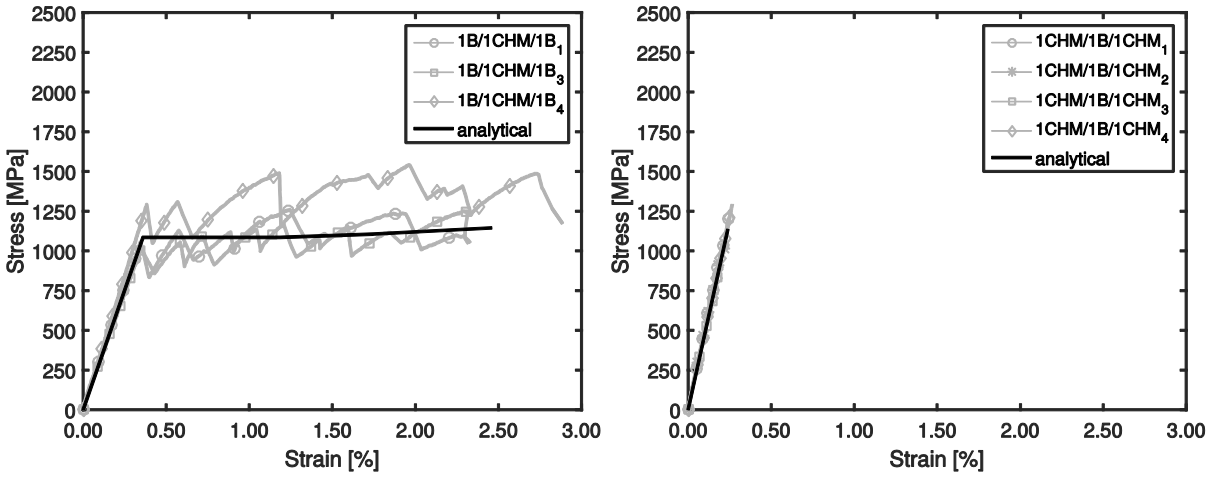

(a) (b)

Figure 3.13 — Stress–strain curves of CHM/B combinations: experimental *versus* predicted values.

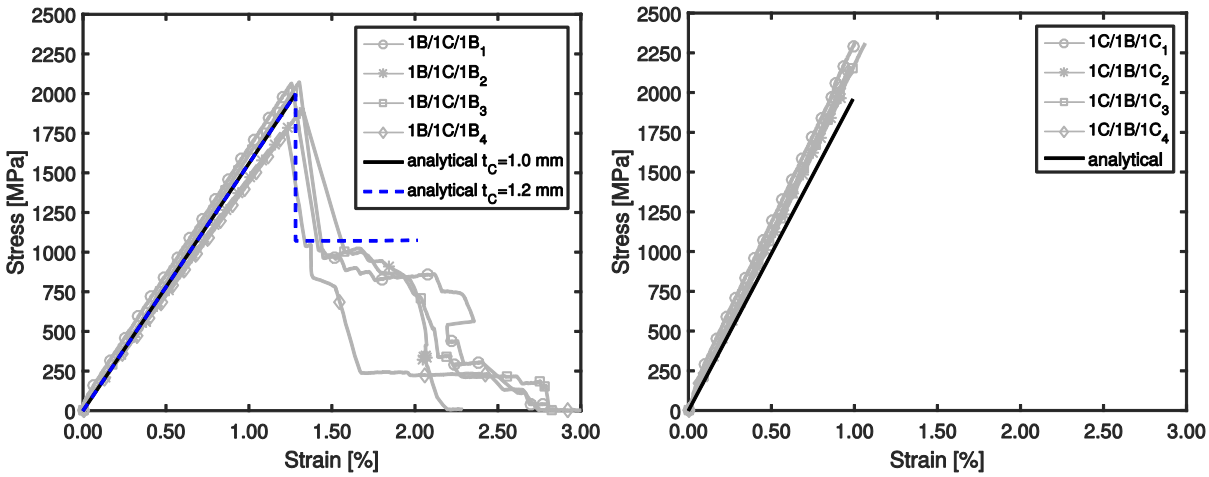

(a) (b)

Figure 3.14 — Stress–strain curves of C/B combinations: experimental *versus* predicted values.

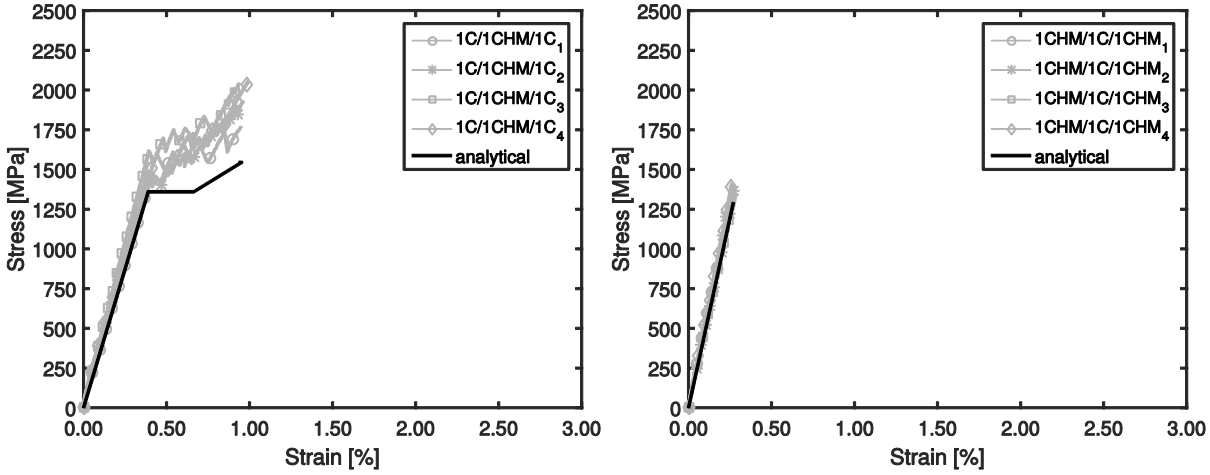

(a) (b)

Figure 3.15 — Stress–strain curves of CHM/C combinations: experimental *versus* predicted values.

3.4. Conclusions

The tensile behaviour of several layer-by-layer hybrid combinations has been investigated using experimental testing and analytical modelling. All the composites were made through the hand lamination of four different commercially available dry UD fabrics: high-modulus carbon (CHM), standard-modulus carbon (C), E-glass (G), and basalt (B). The following main observations and conclusions were drawn.

It was verified that hybrid effect depends not only on the vol% of LS fibres but also on the non-dimensional stiffness parameter (E_{ND}), and the elastic modulus of the hybrid composite (E_{hybrid}). According to the Spearman's rank test carried out, moderately strong negative correlations between hybrid effect and Vol% LS fibres (r = -0.526) and E_{ND} (r = -0.515) were found. The hybrid effect varied between -14.1% and 44.5%. The maximum hybrid effect was obtained combining CHM with C, in combination 1C/1CHM/1C, and the minimum was obtained combining CHM with G, in combination 1G/3CHM/1G. In all analysed cases, it was possible to observe that above 60% of LS fibres relative volume, the hybrid effects were nearly zero or negative. It is believed that the latter results are due to the size effect, since in the present chapter hybrid effects were computed in respect to 1 layer non-hybrid composite results, and in the cases in which the negative hybrid effect were obtained 2 or 3 layers of LS fibres were used. In this way, the magnitude of the hybrid effect potentially depends on the ply thickness of the LS fibres and this subject should be further studied.

Elastic modulus was well-predicted using the rule of mixtures (ROM). The obtained relative errors were acceptable, varying between -14.5% and 9.6%. In the case of the tensile strength, the relative errors between the bilinear ROM prediction and experimental results varied

between -15.7% and 16.9%. In this case, larger errors were expected comparatively with elastic modulus predictions, since bilinear ROM does not account for the hybrid effect and size effect. However, the bilinear ROM was capable of predicting satisfactorily for the cases where multiple fractures occurred.

In the four tested hybrid combinations, that included HM carbon as LS material (2G/1CHM/G, 1G/1CHM/1G, 1B/1CHM1B, and 1C/1CHM/1C), pseudo-ductile tensile responses with fragmentation and dispersed delamination were achieved. In these combinations, the mean 'yield' stress varied between 732.6 and 1504.5 MPa and the pseudo-ductile strain between 0.4 and 2.0%.

The analytical approach developed by Jalalvand *et al*. [8] allowed to predict all the failure modes successfully. In this way, the presented chapter validated the developed approach for the set of materials and fabrication method used. However, since the hybrid effect can increase substantially the strain at failure of LS fibres, it is recommend to incorporate a way of predicting the hybrid effect into the model in the future.

3.5. References

[1] Czél G, Wisnom MR. Demonstration of pseudo-ductility in high performance glass/epoxy composites by hybridisation with thin-ply carbon prepreg. Composites: Part A: Applied Science and Manufacturing. 2013;52:23–30.
[2] Czél G, Jalalvand M, Wisnom MR, Czigány T. Design and characterisation of high performance, pseudo-ductile all-carbon/epoxy unidirectional hybrid composites. Composites Part B. 2017;111 348-56.
[3] Summerscales J, Short D. Carbon fibre and glass fibre hybrid reinforced plastics. Composites. 1978;9(3):157–66.
[4] Swolfs Y, Gorbatikh L, Verpoest I. Fibre hybridisation in polymer composites: a review. Composites Part A: Applied Science and Manufacturing. 2014;67:181-200.
[5] Marron G, Fisher S, Tuler FR, Wagner HD. Hybrid effects in composites: conditions for positive or negative effects versus rule-of-mixtures behaviour Journal of Materials Science. 1978;13(7):1419–26.
[6] Hayashi T. On the improvement of mechanical properties of composites by hybrid composition. Proc 8th Intl Reinforced Plastics Conference. 1972:149-52.
[7] Wisnom MR, Czél G, Swolfs Y, Jalalvand M, Gorbatikh L, Verpoest I. Hybrid effects in thin ply carbon/glass unidirectional laminates: Accurate experimental determination and prediction. Composites: Part A. 2016;88:131–9.
[8] Jalalvand M, Czél G, Wisnom MR. Damage analysis of pseudo-ductile thin-ply UD hybrid composites – A new analytical method. Composites: Part A. 2015;69:83–93.
[9] Phillips LN. Improving racing-car bodies. Composites. 1969;1:50-1.
[10] Zweben C. Tensile strength of hybrid composites. Journal of Materials Science 1977;12:1325-37.
[11] Kirk JN, Munro M, Beaumont PWR. The fracture energy of hybrid carbon and glass fibre composites. Journal of Materials Science. 1978:2197-204.

[12] Hancox NL, Wells H. Aluminum/Carbon Fiber Hybrid Composites. Polymer Engineering and Sience. 1979;19(13).
[13] Manders PW, Bader MG. The strength of hybrid glass/carbon fibre composites - Part 1. Journal of Materials Science. 1981;16:2233-45.
[14] Phillips MG. Composition parameters for hybrid composite materials. Composites. 1981;12(2):113-6.
[15] Harlow BG. Statistical Properties of Hybrid Composites. I. Recursion Analysis. Proc R Soc Lond A 1983;389:67-100.
[16] Kretsis G. A review of the tensile, compress,ve, flexural and shear properties of hybrid fibre reinforced plastics. Composites. 1987;18(1).
[17] Wu Z, Shao Y, Iwashita K, Sakamoto K. Strengthening of Preloaded RC Beams Using Hybrid Carbon Sheets. J Compos Constr. 2007;11:299-307.
[18] Swolfs Y, Gorbatikh L, Romanov V, Orlova S, Lomov SV, Verpoest I. Stress concentrations in an impregnated fibre bundle with random fibre packing. Composites Science and Technology. 2013;74:113–20.
[19] Swolfs Y, Gorbatikh L, Verpoest I. Stress concentrations in hybrid unidirectional fibre-reinforced composites with random fibre packings. Composites Science and Technology. 2013;85:10–6.
[20] Swolfs Y, Czél G, Jalalvand M, Wisnom M, Verpoest I, Gorbatikh L. Model validation of the hybrid effect in carbon/glass hybrid composites. 7th International Conference on Composites Testing and Model Identification, IMDEA, 2015. 2015.
[21] Swolfs Y, McMeeking RM, Verpoest I, Gorbatikh L. The effect of fibre dispersion on initial failure strain and cluster development in unidirectional carbon/glass hybrid composites. Composites: Part A 2015;69:279–87.
[22] Swolfs Y, McMeeking RM, Verpoest I, Gorbatikh L. Matrix cracks around fibre breaks and their effect on stress redistribution and failure development in unidirectional composites. Composites Science and Technology 2015;108:16–22.
[23] Swolfs Y, Verpoest I, Gorbatikh L. Issues in strength models for unidirectional fibre-reinforced composites related to Weibull distributions, fibre packings and boundary effects. Composites Science and Technology 2015;114:42–9.
[24] Swolfs Y, Verpoest I, Gorbatikh L. Maximising the hybrid effect in unidirectional hybrid composites. Materials and Design. 2016;93:39–45.
[25] Swolfs Y, McMeeking RM, Rajan VP, Zok FW, Verpoest I, Gorbatikh L. Global load-sharing model for unidirectional hybrid fibre-reinforced composites. Journal of the Mechanics and Physics of Solids. 2015;84:380–94.
[26] Jalalvand M, Czél G, Wisnom MR. Numerical modelling of the damage modes in UD thin carbon/glass hybrid laminates. Composites Science and Technology. 2014;94:39–47.
[27] Jalalvand M, Czél G, Wisnom MR. Parametric study of failure mechanisms and optimal configurations of pseudo-ductile thin-ply UD hybrid composites. Composites: Part A. 2015; 74:123–31.
[28] Czél G, Jalalvand M, Wisnom MR. Design and characterisation of advanced pseudo-ductile unidirectional thin-ply carbon/epoxy–glass/epoxy hybrid composites. Composite Structures. 2016;143:362–70.
[29] Yu H, Longana ML, Jalalvand M, Wisnom MR, Potter KD. Pseudo-ductility in intermingled carbon/glass hybrid composites with highly aligned discontinuous fibres. Composites: Part A 2015;73:35–44.

[30] Tamuzs V, Tepfers R. Ductility of non-metallic hybrid fiber composite reinforcement for concrete. Proceedings of the Second International RILEM Symposium,Ghent, Belgium August. 1996.
[31] Harris HG, Somboonsong W, Ko FK. New ductile Hybrid FRP reinforcing bar for concrete structures. J Compos Constr. 1998;2:28-37.
[32] Bakis CE, Terosky JA, Nanni A, Koehler SW. Self-monitoring, pseudo-ductile, hybrid FRP reinforcement rods for concrete applications. Composite Science Technology. 2001;61:815-23.
[33] Belarbi A, Watkins SE, Chandrashekhara K, Corra J, Konz1 B. Smart fiber-reinforced polymer rods featuring improved ductility and health monitoring capabilities. Smart Mater Struct. 2001;10 427–31.
[34] Won J-P, Chan-Gi Park, Jang C-I. Tensile Fracture and Bond Properties of Ductile Hybrid FRP Reinforcing Bars. Polymers & Polymer Composites. 2006;15(1).
[35] Cui Y-H, Tao J. A new type of ductile composite reinforcing bar with high tensile elastic modulus for use in reinforced concrete structures. Can J Civ Eng. 2008;36:672–5.
[36] Cheung MMS, Tsang TKC. Behaviour of Concrete Beams Reinforced with Hybrid FRP Composite Rebar. Advances in Structural Engineering. 2010;13.
[37] Behnam B, Eamon C. Resistance Factors for Ductile FRP-Reinforced Concrete Flexural Members. Journal of Composites for Construction doi:101061/(ASCE)CC1943-56140000363. 2013.
[38] Grace NF, Abdel-Sayed G, Ragheb WF. Strengthening of Concrete Beams Using Innovative Ductile Fiber-Reinforced Polymer Fabric. ACI Structural Journal. 2002;103(5)(99(5)):672–700.
[39] Grace NF, Ragheb WF, Abdel-Sayed G. Development and application of innovative triaxially braided ductile FRP fabric for strengthening concrete beams. Composite Structures 2004;64 521–30.
[40] Attari N, Amziane S, Chemrouk M. Flexural strengthening of concrete beams using CFRP, GFRP and hybrid FRP sheets. Construction and Building Materials 2012;37 746–57.
[41] Hosny A, Shaheen H, Abdelrahman A, Elafandy T. Performance of reinforced concrete beams strengthened by hybrid FRP laminates. Cement & Concrete Composites. 2006;28:906–13.
[42] Hawileh RA, Rasheed HA, Abdalla JA, Al-Tamimi AK. Behavior of reinforced concrete beams strengthened with externally bonded hybrid fiber reinforced polymer systems. Materials and Design. 2014;53:972–82.
[43] Kang TH-K, Kim W, Ha S-S, Choi D-U. Hybrid Effects of Carbon-Glass FRP Sheets in Combination with or without Concrete Beams. International Journal of Concrete Structures and Materials Vol8, No1, pp27–41, March 2014 DOI 101007/s40069-013-0061-0. 2014.
[44] Zhang P, Zhu H, Wu G, Meng S, Wu Z. Flexural Performance of HFRP-RC Composite T-Beams with Different Interfaces. J Compos Constr, 04016101. 2016.
[45] Nikopour H, Nehdi M. Shear repair of RC beams using epoxy injection and hybrid external FRP. Materials and Structures. 2011;44:1865–187.
[46] Wu G, Wu ZS, Lu ZT, Ando YB. Structural Performance of Concrete Confined with Hybrid FRP Composites. Journal of reinforced plastics and composites. 2008;27(12).
[47] Luca AD, Nardone F, Matta F, Nanni A, Lignola GP, Prota A. Structural Evaluation of Full-Scale FRP-Confined Reinforced Concrete Columns. J Compos Constr. 2011;15:112-23.
[48] Xu S, Li L, Guo Y. Study on experimental behavior of concrete circular column confined by HFRP under axial compression. Advanced Materials Research. 2012;450-451:491-4.

[49] Li L-J, Xu S-D, Zeng L, Guo Y-C. Study on mechanical behavior of circular concrete columns confined by HFRP under axial compressive load. Research and Applications in Structural Engineering, Mechanics and Computation – Zingoni (Ed) Taylor & Francis Group, London, ISBN 978-1-138-00061-2. 2013.
[50] Li J, Samali B, Ye L, Bakoss S. Behaviour of concrete beam–column connections reinforced with hybrid FRP sheet. Composite Structures 2002;57:357–65.
[51] Li J, Bakoss SL, Samali B, Ye L. Reinforcement of concrete beam-column connections with hybrid FRP sheet. Composite Structures 1999;47:805-12.
[52] Attari N, Amziane S, Chemrouk M. Efficiency of Beam–Column Joint Strengthened by FRP Laminates. Advanced Composite Materials. 2010;19:171–83.
[53] Ranganathan S, Mantena PR. Axial Loading and Buckling Response Characteristics of Pultruded Hybrid Glass-Graphite/Epoxy Composite Beams. Journal of Reinforced Plastics and Composites. 2003;22(7).
[54] Ragheb WF. Hybridization Effectiveness in Improving Local Buckling Capacity of Pultruded I-Beams. Mechanics of Advanced Materials and Structures. 2010;17:448–57.
[55] Nunes F, Correia JR, Silvestre N. Structural behaviour of hybrid FRP pultruded columns. Part 1: Experimental study. Composite Structures. 2016;139:291–303.
[56] Grace NF, Ragheb WF, Abdel-Sayed G. Ductile Hybrid Structural Fabric. Patent No: US 6,790,518 B2. 2002.
[57] Kang TH-K, Kim W, Ha S-S, Choi D-U. Hybrid Effects of Carbon-Glass FRP Sheets in Combination with or without Concrete Beams. International Journal of Concrete Structures and Materials. 2013;8(1):27–41.
[58] Wu G, Shi J-W, Jing W-J, Wu Z-S. Flexural Behavior of Concrete Beams Strengthened with New Prestressed Carbon-Basalt Hybrid Fiber Sheets. Journal Of Composites For Construction, 18 ISSN 1090-0268/04013053(10). 2014.
[59] CNR-DT200. Guide for the Design and Construction of Externally Bonded FRP Systems for Strengthening Existing Structures. Advisory Committee on Techincal Recommendations for Construction, National Research Council, Rome, Italy. 2013.
[60] Bank L. Composites for Construction - Structural Design with FRP Materials. John Wiley & Sons, Inc. 2006.
[61] S&P. Technical Data Sheet S&P C-Sheet 640. 2015.
[62] S&P. Technical Data Sheet S&P C-Sheet 240. 2015.
[63] S&P. Technical Data Sheet S&P G-Sheet E or AR 90/10, typA. 2015.
[64] Dalla-Betta-group. Catalogue 2015. 2015.
[65] ASTM. D 3379 – 75 - Standard Test Method for Tensile Strength and Young's Modulus for High-Modulus Single-Filament Materials. 1989.
[66] S&P. Technical Data Sheet S&P Resin 55. 2015.
[67] ISO. 527-5 Plastics — Determination of tensile properties; Part 5: Test conditions for unidirectional fibre-reinforced plastic composites. EUROPEAN COMMITTEE FOR STANDARDIZATION. 2009.
[68] Pan N, Postle R. The tensile strength of hybrid fibre composites: a probabilist analysis of hybrid effects. Phil Trans R Soc Lond A. 1996;354:1875-97.
[69] Shan Y, Liao K. Environmental fatigue behavior and life prediction of unidirectional glass–carbon/epoxy hybrid composites. International Journal of Fatigue. 2002;24:847–59.
[70] Aveston J, Sillwood JM. Synergistic fibre strengthening in hybrid composites. Journal of Materials Science. 1976;11(1877-1883).

[71] Swolfs Y, Verpoest I, Gorbatikh L. A review of input data and modelling assumptions in longitudinal strength models for unidirectional fibre-reinforced composites. Composite Structures. 2016;150:153–72.
[72] ASTM. D 3039/D 3039M Standard Test Method for Tensile Properties of Polymer Matrix Composite Materials. 2002.
[73] Chamis CC, Lark RF, Sinclair JH. Mechanical property characterization of intraply hybrid composites. NASA Technical Memorandum 79306. 1979.
[74] Taketa I, Ustarroz J, Gorbatikh L, Lomov SV, Verpoest I. Interply hybrid composites with carbon fiber reinforced polypropylene and self-reinforced polypropylene. Composites: Part A. 2010;41:927–32.
[75] Pandya KS, Veerraju C, Naik NK. Hybrid composites made of carbon and glass woven fabrics under quasi-static loading. Materials and Design. 2011;32:4094–9.
[76] Shi J, Zhu H, Wu Z, Wu G. Durability of BFRP and hybrid FRP sheets under Freeze-Thaw Cycling. Advanced Materials Research. 2011;163-167 3297-300.
[77] Zhang Y, Li Y, Ma H, Yu T. Tensile and interfacial properties of unidirectional flax/glass fiber reinforced hybrid composites. Composites Science and Technology. 2013;88:172–7.
[78] Shi J-W, Zhu H, Wu G, Wu Z-S. Tensile behavior of FRP and hybrid FRP sheets in freeze–thaw cycling environments. Composites: Part B. 2014; 60:239–47.
[79] Subagia IDGA, Kim Y, Tijing LD, Kim CS, Shon HK. Effect of stacking sequence on the flexural properties of hybrid composites reinforced with carbon and basalt fibers. Composites: Part B. 2014;58 251–8.
[80] Ikbal MH, Ahmed A, Qingtao W, Shuai Z, Wei L. Hybrid composites made of unidirectional T600S carbon and E-glass fabrics under quasi-static loading. Journal of Industrial Textiles 2016;0(00):1–25.

4. HYBRID EFFECT PREDICTION AND EVOLUTION OF THE TENSILE RESPONSE

4.1. Introduction

The linear elastic behaviour up to the point of sudden brittle failure, without sufficient warning and residual integrity of the traditional unidirectional (UD) FRP composite materials, leads to limitations in the fully exploitation of their great inherent mechanical advantages, namely the high tensile strength, due to conservative safety design limits [1, 2]. For this reason, the unfavourable failure characteristic of these materials restricts the spread of their application. In this way, the possibility to promote a gradual failure to the composites, improving their safety and maintaining their mechanical virtues simultaneously, has a tremendous interest for different industries, in particular for civil engineering, in which ductile materials are required in several applications.

Hybridisation, defined as the incorporation of two fibre types with different strain failures, usually designated as Low Strain (LS) and High Strain (HS) fibres, within the same polymeric matrix [3], allows overcoming the previously pointed out drawback. With this innovative solution, it is possible to achieve a mechanical non-linear and non-catastrophic behaviour characterized by presenting a flat-topped stress-strain curve in monotonic tensile tests. This desired behaviour is reached by selecting appropriate relative thickness of the involved materials (i.e. proportion of the LS to HS material layers) and absolute thickness of the LS material layers. It is important to note that achieving non-catastrophic behaviour is possible with some configuration of UD hybrid FRP composites, but the tensile curve is not repeatable on subsequent unloadings/reloadings. In this context, this behaviour is known as pseudo-ductile [4, 5].

In addition to the potential to introduce pseudo-ductility to the UD composite materials, hybridisation promotes synergies between the involved reinforcing materials, leading, for instance, to the increase (until 50% [5, 6]) of the apparent failure strain of LS fibres. This phenomenon has been described as “hybrid effect” and it was reported, for the first time, in 1972, by Hayashi [7]. Today, there is some controversy about the best way to define the baseline tensile failure strain of a UD non-hybrid composite against which the strain at failure of the hybrid composite is compared in the determination of the hybrid effect. In standard tensile tests of UD non-hybrid composites, stress concentrations can arise where the load is applied [8]. This effect can lead to premature failures, and may be responsible for some of the variability observed in tensile results. A potential specimen type to suppress premature failures is presented in [8]. However, the proposed specimen type is not yet widely widespread.

Swolfs *et al*. [5] pointed out changes in 3 main mechanisms, that occur in UD hybrid composites relatively to non-hybrid ones, that induces the emergence of the hybrid effect: (1) residual thermal stresses, (2) fracture propagation effects and (3) dynamic stress concentrations. Relatively to the first change, in a more recent work, Sowlfs *et al*. [9] state that using

representative thermal expansion coefficients and longitudinal elastic modulus of fibres, the influence of residual thermal stresses in hybrid effect is small for carbon/glass hybrid composites. Wisnom *et al*. [8] supported the previous view, mentioning that a low effect of thermal residual stresses would be expected in UD hybrid composites, where stresses are driven by the difference in fibre expansion coefficients rather than by matrix contraction. Relatively to the second change, it is possible to understand that hybridisation can modify the stress concentrations and stress recovery at a broken fibre due to the presence of neighbouring fibres with different stiffness [10]. In fact, it is believed that substantial increase in strain of the LS material is caused by the restraint from the adjacent HS material, which inhibits the formation of broken clusters of LS fibres [8]. Relatively to the third change, it has been poorly investigated and it has received no attention at all in the past two decades [5, 8]. Finally, in addition to the 3 main changes cited before, the size effect has also been shown to influence the hybrid effect [6, 8, 9]. This fact is understandable because, for a constant sample size, the number of LS fibres is reduced by the hybridisation, leading to lower probability of finding a flaw and, consequently, to superior strains at the failure of LS fibres in hybrid composites. Nevertheless, the magnitude of the size effect is not quantified [9].

Over time, different analytical models to predict the mechanical response of UD hybrid composites have been developed. Zweben [11], in 1977, extended a previous developed shear lag model for UD non-hybrid composites (that assumes that fibres carry all the axial load and the matrix only the shear load) by introducing a strain concentration factor, that increases the stress in the HS fibre next to a single LS broken fibre, and by defining an ineffective length, assuming that a broken LS fibre locally loses its load transfer capacity over a certain length. Later, Fukuda [12], in 1983, improved Zweben's model, introducing more accurate stress concentration and ineffective lengths factors and turning the model independent to the ratio of failure strains between fibres. One of the most relevant disadvantages of the models of Zweben [11] and Fukuda [12] is that they consider a fixed ratio of LS over HS fibres, which means that it is not possible to check the influence of the variation of LS fibres relative volume fraction (vol%) with these models. This parameter is a crucial factor on mechanical hybrid response [6, 9, 13].

In last years, Global Load Sharing (GLS) theory, developed by Curtin [14, 15] and expanded by Hui *et al*. [16] for UD non-hybrid composites, has been adapted for UD hybrid composites [9, 17, 18]. GLS incorporates the mechanics and statistics of fibre fragmentation and assumes that the stress dropped by a broken fibre is redistributed equally to all other fibres in the plane of the break [17]. Analytical models based on GLS theory, sometimes referred to as Progressive Damage Models (PDMs) [19], should be able to reproduce the on-axis non-linear behaviour of a UD composites, where the mechanical properties are fibre-dominated. Although the GLS theory omits many real phenomena, such as fragmentation, local load sharing (stress concentrations), size effects, delamination between composite layers and fibre dispersion, it remains a very useful tool for exploring the effect of constituent properties on the composite performance [17]. In fact, if the shear yield strength of the matrix is sufficiently low, then the

local stress concentrations cannot be too large and the stress must be redistributed over a large number of fibres [15]. Given the analytical nature of the model, there is the advantage of exploring rapidly the hybrid tensile response of different combinations. An extensive revision about GLS theory can be found in [15, 17, 19].

Swolfs *et al*. [9] applied GLS theory in a parametric study of hybrid effect. The developed model allowed the prediction of the hybrid effect of carbon/glass combination. The influence of several factors on the hybrid effect was evaluated, namely the Weibull modulus (see the definition in section 4.2.1.1) of carbon fibres and glass fibres, the failure strain ratio, the stiffness ratio and the strength ratio between the involved fibres. It was concluded that hybrid effect is mainly affected by two of the referred to factors: the Weibull modulus of carbon fibres and the stiffness ratio between the fibres. Furthermore, in terms of the strength predictions, it was concluded that the GLS model essentially follows the bilinear rule-of-mixtures (as defined in [5, 20-23]). Rajan and Curtin [17] used as well GLS model to study the tensile response of different UD hybrid combinations of continuous or discontinuous fibres. The analytical model predictions were supported by experimental results obtained in [24]. They concluded that using discontinuous LS fibres improves hybrid composite performance, because such fibres fragment more gracefully over a wide range of strain. However, quantitative comparisons with experimental results were not presented. Tavares *et al*. [18] extended a Progressive Damage Model (PDM), initially developed by Turon *et al*. [19] for UD non-hybrid composites, to UD hybrid composites field. An analytical parametric study was performed analysing essentially the influence of the vol% of the constituent materials (3 carbon types and 1 AR glass) on the tensile response of the resulting hybrid composite combinations. Through two different models (one that takes into account only the statistical strength distribution of fibre and another that, in addition, considers the influence of the shear yield strength of the matrix) it was possible to conclude that the matrix–fibre interface leads to significant differences in the tensile response. However, a proper justification to this phenomenon (or the identification of pattern) was not reported in the work.

Despite great progress achieved in last studies with GLS models in hybrid composite field, an experimental quantitative validation of fitness of the hybrid effect prediction was still not carried out [17]. The first main goal of the present chapter is to evaluate the performance of the analytical approach developed recently by Tavares *et al*. [18]. This was assessed using the experimental results published in [6]. The statistical strength scatter parameters of the fibres were determined experimentally, through the single fibre tests, to be used as inputs of the model. The UD composites were produced with materials designed for civil engineering industry, through the hand lay-up method. As it is well known, this is a very common manufacturing method of composites in strengthening of reinforced concrete structures. For this reason, analytical models developed to hybrid composites must be validated in this context.

Secondly, the model of Jalalvand et al. [13] was modified to take into account the hybrid effect predictions obtained with the model of Tavares et al. [18]. The evolution of hybrid properties (such as hybrid effect, ‘yield’ stress, pseudo-ductile strain, elastic modulus and strength) was

investigated as function of the configuration of UD hybrid composites by means of novel Damage Mode Maps (DMMs) presented in [25].

4.2. Modelling assumptions

4.2.1. Progressive damage model for hybrid composites

The PDM of Tavares et al. [18] aims at establishing the degradation of the tensile mechanical properties of the UD hybrid composites resulting from fibre fragmentation that leads to the stiffness-loss simulation of the two constituent reinforcing materials. Traditional brittle fibres used in composites are characterized by their strength scatter due to the presence of flaws introduced during processing and handling. In this way, strength distribution is contemplated in cited PDM, considering the two parameters of Weibull cumulative failure probability distribution, as described in next sections.

4.2.1.1. Weibull fibre strength distribution (input data)

Fibres are characterized by breaking as soon as the weakest link is overloaded [26]. As most part of physical systems, successive observations of the strength do not produce exactly the same result. In this way, strength of a single fibre cannot be accurate modelled with one single average value. Usually, the strength variable of fibres is described by the Weibull distribution [27]:

$$P(\sigma) = 1 - exp\left(-\left(\frac{L}{L_0}\right)\left(\frac{\sigma}{\sigma_0}\right)^m\right) \tag{4.1}$$

where L is the characteristic gauge length, L_0 the reference gauge length, σ the fibre strength, σ_0 the Weibull scale parameter and m the Weibull modulus. The Weibull modulus m varies with the scatter around the average value: a large Weibull modulus indicates little scatter in the fibre strength. The reference length L_0 is usually introduced just for convenience, because then L/L_0 becomes a non-dimensional quantity, and the Weibull scale parameter has the dimension of stress. The choice of L and L_0 implies modification of σ_0 parameter value.

The Weibull distribution parameters are usually determined by testing individual fibres, as described in section 4.3.2. However, tensile tests of single fibres could be associated to some sources of error, such as specimen alignment with respect to the load direction (that leads to bending stresses in the fibre) and premature fibre failure within the adhesive or at the tabs [28]. Furthermore, the extraction of fibres from a bundle may cause the weakest ones to fracture in the process, thus effectively censoring the fibre sample that undergoes the test [28]. Today, there is a discussion about the best number of tests and the gauge length of specimen, that may influence the estimation of Weibull parameters [26]. However, researchers have not yet agreed on the best testing practices.

In this work, the Weibull distribution parameters from single fibre tests, described in section 4.3.2, were determined by the maximum likelihood method (MLM) [29], which is believed to

be more accurate than least squares regression [26, 29]. However, these values can be seen as susceptible of being altered, according to the sources of error previously reported. The chi-square goodness-of-fit test was used to check distributional assumptions.

4.2.1.2. Model description

The analytical approach proposed by Tavares *et al*. [18] is an adaptation for UD hybrid composites of the model developed by Turon *et al*. [19]. Essentially, this approach assumes that the multiple fragmentation phenomena of single fibre fragmentation tests (a test in which a single fibre embedded in the matrix is loaded and the number of fibre breaks as a function of the applied load is monitored) has the same nature of the stiffness loss of the UD non-hybrid composite due to fibre breakage. In this way, exactly the same model could be used to predict both behaviours. A synopsis of the model and the underlying assumptions are described as follows.

Ideally, the model considers the behaviour of a single brittle fibre embedded along the centre line of a dog-bone-shaped matrix specimen, in which the matrix has a much larger cross-sectional area and larger strain to failure than the fibre material. As the strain is increased, the fibre fails progressively at randomly positioned flaws producing an increasing number of shorter fragments. The apparent stiffness of the system, matrix and fibre, decreases with the number of fibre breaks, due to their loss of ability to carry the load. Assuming that the influence of other damage modes is neglected, the number of breaks at a given stress could be related to the apparent axial stiffness of the composite. Equation (4.1) gives the relationship between the mean number of breaks in a fibre, $\langle N \rangle$, and the length L under a defined σ:

$$\langle N \rangle = \frac{L}{L_0}\left(\frac{\sigma}{\sigma_0}\right)^m \tag{4.2}$$

From the statistic laws, it can be shown that the distance between the two consecutive breaks, x, will follow an exponential law (see the details in [19]):

$$f(x) = \Lambda e^{-\Lambda x} \tag{4.3}$$

where Λ is the number of breaks in a fibre per unit length:

$$\Lambda = \frac{\langle N \rangle}{L} = \frac{1}{L_0}\left(\frac{\sigma}{\sigma_0}\right)^m \tag{4.4}$$

When a fibre breaks, the load carried by the fibre drops down to zero at the position of the break, and the load is transferred by shear between the fibre and the matrix. This causes a stress redistribution near fibre break. The model assumes a linear increase of the axial stress from a fibre break, until a total recovery occurs at a certain distance from it. The length of this load recovery region, l_{ex}, is defined as:

$$l_{ex} = \frac{R_f}{\tau}\frac{E_f \varepsilon}{2} \tag{4.5}$$

where R_f is the fibre radius, E_f is the elastic modulus of fibres, τ the matrix–fibre interfacial shear strength and ε the applied strain.

The average fibre stress along the fibre, σ_m, can be computed by integrating the axial stress over all of the fibre fragments along the fibre length, resulting, after some simplifications (please see the details in [19]), in the following closed-form analytical solution:

$$\sigma_m(\varepsilon) = \left(\frac{1-e^{-2l_{ex}\Lambda}}{2l_{ex}\Lambda} + \Lambda l_{ex} e^{-L\Lambda}\right) E_f \varepsilon \tag{4.6}$$

In case of hybrid composites, the developed model assumes that there are two 'sub-composites' in parallel, one for each reinforcing material, subjected to the same applied axial strain. The model defines how a fibre failure affects the stresses in the remaining intact fibres and assemble the mechanical behaviour of the constituents in the composite material. Given the tensile responses for the two pure composites using GLS (equation (4.6)), the stress-strain response for the hybrid composite can be described simply by considering the contribution of two materials, taking into account the vol% of the constituents. Damage in the matrix is not considered, since the tensile failure of composite materials is mainly a fibre dominated process [18]:

$$\sigma(\varepsilon) = \left(\left(\frac{1-e^{-2l_{ex,L}\Lambda_L}}{2l_{ex,L}\Lambda_L} + l_{ex,L}\Lambda_L e^{-L\Lambda_L}\right) E_{L,f} \frac{t_L}{t_L+t_H} + \left(\frac{1-e^{-2l_{ex,H}\Lambda_H}}{2l_{ex,H}\Lambda_H} + l_{ex,H}\Lambda_H e^{-L\Lambda_H}\right) E_{H,f} \frac{t_H}{t_L+t_H}\right) \varepsilon V_f \tag{4.7}$$

where $l_{ex,L}$, Λ_L, $E_{L,f}$ and t_L are the length load recovery region, the number of breaks in a fibre per unit length, the elastic modulus and the half thickness of a layer of the LS fibres and $l_{ex,H}$, Λ_H, $E_{H,f}$ and t_H are the length load recovery region, the number of breaks in a fibre per unit length, the elastic modulus and the half thickness of a layer of the HS fibres. V_f is the volume of fibres.

In the present chapter, the PDM was used to estimate the hybrid effect, defined here as apparent failure strain enhancement of the LS fibre in a hybrid composite compared to the failure strain of a LS fibre-reinforced non-hybrid composite. The failure strain of the LS fibres was considered as the strain at first local maximum point of the stress-strain diagram, see **Figure 4.1**. However, in some cases, especially in combination with low vol% of LS fibres, a clear local maximum point was impossible to achieve, since the analytical stress-strain diagrams presented only a global maximum point due to statistical issues. This fact is illustrated in the example of **Figure 4.2**: contrary to the case with 50% of HM carbon fibres, in which it is possible to distinguish clearly two local maxima, in the case of 10% of LS fibres, only a global maximum is totally observable. The lower the volume of LS fibres, the less distinguishable is the first local maximum. This occurs because the contribution of LS fibres to the tensile response of the composite gradually decreases. Although imperceptible in analytical stress-strain diagrams, it is plausible that hybrid effect exists in combinations with very low vol% of LS fibres, because the most important factor that influences the hybrid effect is the restraint of clusters formation of break LS fibres due to the adjacent HS material. In this way, when it was

not possible to detect a local maximum corresponding to the failure of the LS fibres, a constant hybrid effect (equal to the achieved with lowest possible vol% of LS fibres) was considered.

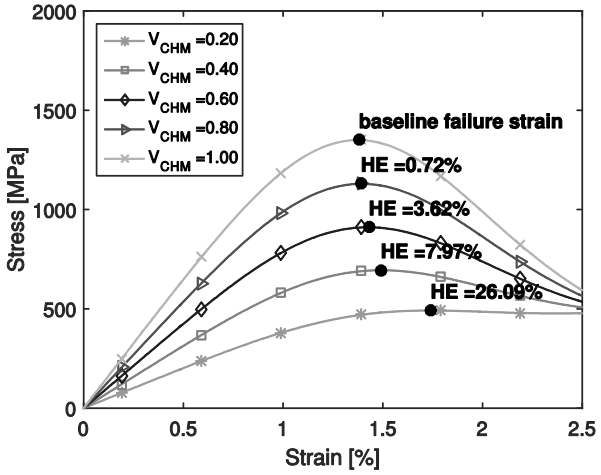

Figure 4.1 — PDM predictions: zoomed stress–strain curves of HM carbon/glass combination and identification of hybrid effect (HE).

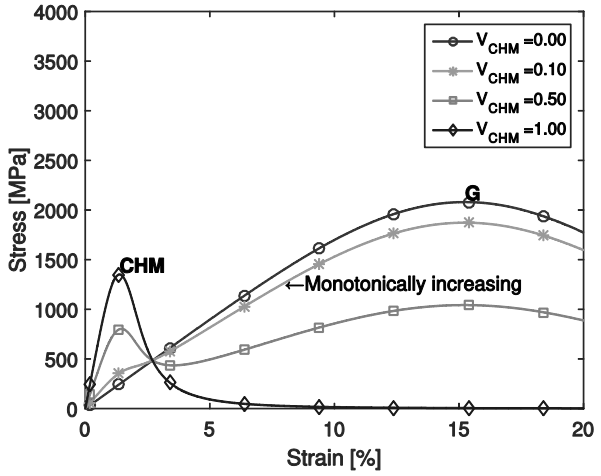

Figure 4.2 — PDM predictions: identification of stress–strain curve with monotonic increase.

4.2.2. Evolution of hybrid properties (damage mode maps)

The effect of the configuration (geometric and material parameters) of hybrid composites on different responses of UD hybrid composites can be clearly interpreted using a novel representation of the damage modes, known as damage mode maps (DMMs), recently developed by Jalalvand *et al*. [25]. The DMMs are a very interesting graphical construction that facilitates interpretation and allows subsequent analysis and better visualization of the evolution of hybrid responses. DMMs have been used [1, 2, 25, 30] to analyse the evolution (through colormaps) of pseudo-ductile strain, defined as the strain between the final failure strain and

the strain on the extrapolated initial slope line at the failure stress of the stress-strain diagram, and 'yield' stress, defined as the stress at first local maximum point of stress-strain diagram, of hybrid combinations (see **Figure 4.3**). In the cited works, the focus was to study the LS layer fragmentation and LS fragmentation and stable delamination damages modes in order to maximize the pseudo-ductile and 'yield' stress. In this way, the DMMs can easily be used as a design tool to achieve optimal hybrid composites with desired damage modes [2]. DMMs divide all possible configurations of a UD hybrid composite into four possible damage modes:

1. Premature HS failure, in which the whole hybrid specimen fails at first LS fracture;
2. Unstable delamination, in which delamination occurs at first LS fracture;
3. LS layer fragmentation, in which the energy released at first LS layer is not enough to drive unstable delamination, allowing that other fractures take place in the LS layer until saturation;
4. LS fragmentation and stable delamination in which the fragmented LS segments are pulled-out stably from the HS layers.

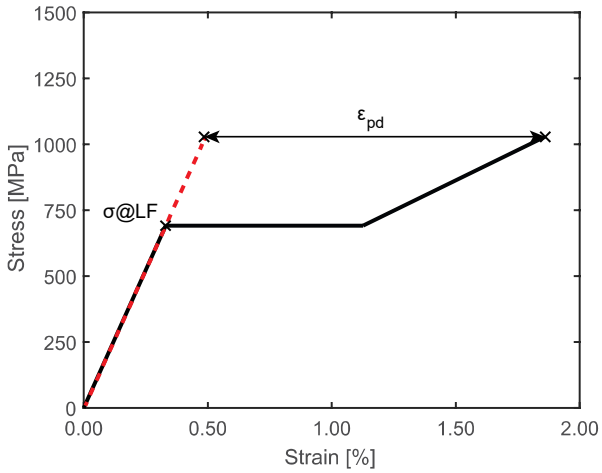

Figure 4.3 — Illustration of nonlinear pseudo-ductile behaviour and definitions of 'yield' stress and pseudo-ductile strain (adapted from [1]).

In DMMs, the horizontal axis is the ratio between the thickness of the two fibre type layers and the vertical is the absolute thickness of the LS layer. The boundaries between different zones can be determined by equating any two of the three stress levels described in [13]: (i) the stress level at which the first crack in the LS material occurs, $\sigma@LF$, (ii) the stress level at which delamination development occurs, $\sigma@del$, and (iii) stress level at which the high strain material fails, $\sigma@HF$, in accordance with the equations (4.8) to (4.10), respectively.

$$\sigma@LF = S_L \frac{\alpha\beta+1}{\alpha(\beta+1)} \tag{4.8}$$

$$\sigma@del = \frac{1}{1+\beta}\sqrt{\left(\frac{1+\alpha\beta}{\alpha\beta}\right)\left(\frac{2G_{IIC}E_H}{t_H}\right)} \tag{4.9}$$

$$\sigma@HF = \frac{1}{(1+\beta)} \frac{S_H}{K_t \sqrt[m_H]{V}} \tag{4.10}$$

where S_L and S_H are the reference strength of the LS and HS materials, α and β are the modulus and thickness ratios of the LS to HS fibre layers, G_{IIC} is the mode II interlaminar fracture toughness of the interface between LS layers and HS layers of the hybrid composite, E_H the elastic modulus of the HS fibres, m_H is the Weibull strength distribution modulus of the HS fibre, S_H is the reference strength of the HS material, K_t is the stress concentration factor in the high strain material and V is the volume of the specimen (free length × width × total fibre layer thickness).

Hybrid configurations in which fragmentation in the LS material initiates before delamination should satisfy the $\sigma@LF < \sigma@del$ condition, resulting after some simplifications in the following inequality:

$$t_L < \frac{2G_{IIC}E_H}{{S_L}^2} \frac{\alpha(1-\gamma)}{(\alpha\gamma+1-\gamma)} \tag{4.11}$$

where γ is defined as:

$$\gamma = \frac{t_L}{t_L+t_H} = \frac{\beta}{1+\beta} \tag{4.12}$$

Hybrid configurations in which LS material fragmentation takes place before failure in the HS material should satisfy $\sigma@LF < \sigma@HF$ condition, resulting after some simplifications in the following inequality:

$$\sqrt[m]{t_L} < \frac{S_H}{K_t S_L} \left(\frac{\alpha}{\alpha\beta+1}\right) \sqrt[m_H]{\frac{\beta}{2WL}} \tag{4.13}$$

where W is the width and L is the free length of specimens.

Hybrid configurations in which the HS material delamination stress failure stress, $\sigma@HF > \sigma@del$, delamination propagation is expected before final failure, satisfying the next inequality:

$${t_L}^{\left(\frac{1}{2}-\frac{1}{m_H}\right)} > \beta^{-\frac{1}{m_H}} \frac{K_t}{S_H} \sqrt[m_H]{2WL} \sqrt{2G_{IIC}E_H} \sqrt{\frac{1+\alpha\beta}{\alpha}} \tag{4.14}$$

In all last models, S_L is assumed as a constant mean value, not taking into account the hybrid effect variation as function of the vol% of LS fibres, which would greatly contribute to 'yield' stress and pseudo-ductile strain of hybrid composites. In the present chapter, an actual strength of the LS material, $S_{L,a}$, was considered assuming the hybrid effect (computed according to the PDM described in section 4.2.1.2).

$$S_{L,a} = S_L + (S_L \times HE(vol\%\ of\ LS\ fibres)) \tag{4.15}$$

where HE is the hybrid effect a function of vol% of LS fibres.

DMMs were used to analyse the evolution and to identify the trade-offs between different responses in all damages modes, namely hybrid effect, 'yield' stress, pseudo-ductile strain,

strength and elastic modulus. All the responses, with the exception of the elastic modulus (E_{hybrid}), were predicted with Jalalvand et al. model, taking into account equation (4.15). E_{hybrid} was predicted according to the rule of mixtures (see equation (4.16)) that has been proven to accurately estimate this property [6].

$$E_{hybrid} = V_L E_L + V_H E_H + V_M E_M \quad (4.16)$$

where V_L, V_H, V_M, E_L, E_H, and E_M are the volume and elastic modulus of the LS fibre, HS fibre and matrix, respectively.

In the present chapter, the mechanical properties experimentally characterized of UD non-hybrid composites were used as input variables of model (4.16) (see **Table 4.1**). The exact volume of resin was not directly controlled during the application. Cross-sectional area of the composite was computed considering only the thickness of the dry fabrics, according to the usual practice of the hand lay-up method [31]. In this way, E_L and E_H were considered the elastic modulus of LS and HS one layer composites, respectively. Therefore, the contribution of $V_M E_M$ was contemplated in $V_L E_L$ and $V_H E_H$ terms, leading to $V_L + V_H = 1$ and $V_M E_M = 0$.

4.3. Experimental procedure

4.3.1. Materials

Commercial dry UD fabrics available for civil engineering applications, with a similar areal mass of 400 g/m^2, were used in this work, namely UD HM carbon (S&P C-Sheet 640), ST carbon (S&P C-Sheet 240), E-glass (S&P G-sheet E 90/10) and basalt (Dalla Betta Group U400B-40-50-03). An epoxy-based material (S&P Resin Epoxy 55) was used as matrix for laminating the studied composites. According to the supplier, this epoxy has the following main properties [32]: (i) a tensile strength of 35.8 MPa; (ii) a strain at the failure of 2.3%; and, (iii) an elastic modulus of 2.6 GPa.

In **Table 4.1** the density, areal mass, and fibre layer thickness (areal mass density divided by the volumetric mass density) of UD fabrics are presented.

4.3.2. Tensile single fibre test

For each dry fabric, a reasonable number of single fibres (see **Table 4.1**) were randomly taken from the dry fabrics and tested. The method used follows the guidelines laid down in ASTM D3379-75 [33] for the tensile testing of fibres. The measurements were performed in a Hounsfield H100KS universal testing machine with a load cell with 2.5 N maximum capacity (with an accuracy of ± 0.2% of applied force across load cell force range). In total, 200 fibres were individually mounted in the jig by means of a work template with a fixed gauge length of 20 mm, see **Figure 4.4**. Fibre ends were bonded to the work template by an ethyl cyanoacrylate-based adhesive. Then the tab ends were gripped in the jaws of the machine. Before the tensile

tests were started, the work template was cut across, so that just the fibre was fixed as a continuous length within the jig. The measurements were performed at a rate of 1.5 mm/min, until breakage occurred. For each fibre, records of applied load against extension were taken, and using an average mean diameter, determined through the analysis of microscopy images of fibres obtained with Scanning Electron Microscopy (SEM) (see **Figure 4.5**), the data registered were converted to stress-strain relationship.

In **Table 4.1** it is possible to observe that elastic modulus of single fibres is lower than the elastic modulus of cured composites. This is due to the fact that, in case of composites, the tensile properties were evaluated ignoring the contribution of the resin. This means that tensile strength was computed considering only the dry fabric thickness, which conducted to overestimation of the tensile strength and, consequently, large elastic modulus.

Table 4.1 — Properties of the dry fabrics, fibres and cured composite materials determined experimentally.

Material ID	**Properties of the dry fabric, as reporter by the manufacturer**			**Properties of the fibres (tested according to ASTM D3379)**					**Properties of 1 ply composites [6]***		
	Density [g/m^3]	**Areal mass** [g/m^2]	**Fibre layer thickness** [mm/layer]	**N. of samples**	**Fibre diameter** [μm] (CoV [%])	**Elastic modulus** [GPa] (CoV [%])	**Tensile strength** [MPa] (CoV [%])	**Strain at the failure** [%] (CoV [%])	**Elastic modulus** [GPa] (CoV [%])	**Tensile strength** [MPa] (CoV [%])	**Strain at the strain** [%] (CoV [%])
Basalt (B)	2.67	420	0.157	50	18.14	61.41	1886.70	3.10	102.5	2244.2	2.46
					(3.56)	(31.14)	(40.79)	(27.73)	(15.46)	(20.17)	(10.61)
E-glass (G)	2.60	400	0.154	50	14.98	76.92	2662.06	3.72	81.6	1671.2	2.31
					(16.25)	(27.97)	(33.88)	(20.45)	(7.39)	(8.59)	(3.78)
ST carbon (C)	1.79	400	0.223	36	7.88	213.95	3920.67	1.38	231.3	2565.9	1.09
					(5.15)	(43.36)	(39.37)	(17.37)	(12.50)	(10.18)	(8.81)
HM carbon (CHM)	2.10	400	0.190	26	11.03	558.07	2934.24	0.53	624.1	1749.4	0.27
					(6.66)	(24.67)	(19.16)	(18.99)	(11.13)	(24.39)	(19.61)

Note: *The tensile properties were computed considering only the thickness of the dry fabrics, according the recommendation suggested in the guidelines [31].

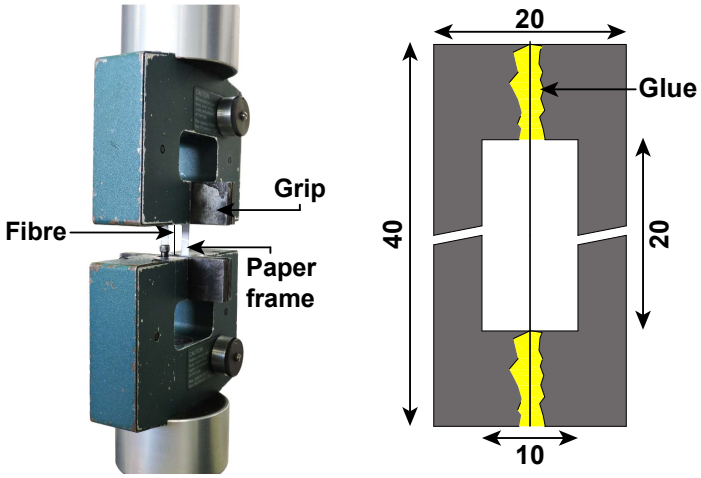

(a) (b)

Figure 4.4 — Tensile fibre test: (a) illustration of the test and (b) geometry of specimen (dimensions in mm).

4.3.3. Hybrid composite combinations

Hybrid composite combinations of HM carbon/glass, ST carbon/glass, HM carbon/basalt, ST carbon/basalt and HM carbon/ST carbon up to 5 layers were studied. In total, 16 series of hybrid composite combinations results were compared with PDM predictions: 12 combinations with 3 reinforcing material layers and 6 combinations with 5 reinforcing material layers. The combinations of 3 symmetrical layers allowed to analyse the following approximate levels of LS fibre vol%: 0%, 33%, 66% and 100%. In addition, combinations with 5 layers allowed to analyse the following approximate levels of LS fibre vol%: 20%, 40% and 60%. Specimens with 5 layers were only tested on 2 hybrid combinations: HM carbon/glass and ST carbon/glass. Since each series was composed of 4 specimens, a total of 64 tests was carried out. It should be noted that the UD fabrics had slightly different thicknesses and, for this reason, the vol% before mentioned were corrected in the next sections, according to the corresponding thickness layer, assuming that vol% = $t_L/(t_L + t_H) \times 100$.

The hybrid composite laminates were manufactured by hand lay-up method, according to the best practices suggested in the guidelines [31], following this protocol: (i) dry fabrics were cut into pieces with 250 mm at parallel direction of fibres and 80 mm at perpendicular direction of fibres; (ii) a layer of epoxy was applied over a teflon film and in the first fabric layer with a brush; (iii) the fabric layer was adjusted manually, and then a ribbed rigid roller was used to apply pressure, in order to force excess resin and air out of the composite; (iv) the above mentioned steps were repeated for further layers. The top of the laminate was left rough, in order to simulate real applications. All the samples were then cured at room temperature (20 ± 0.5ºC) for 40 days.

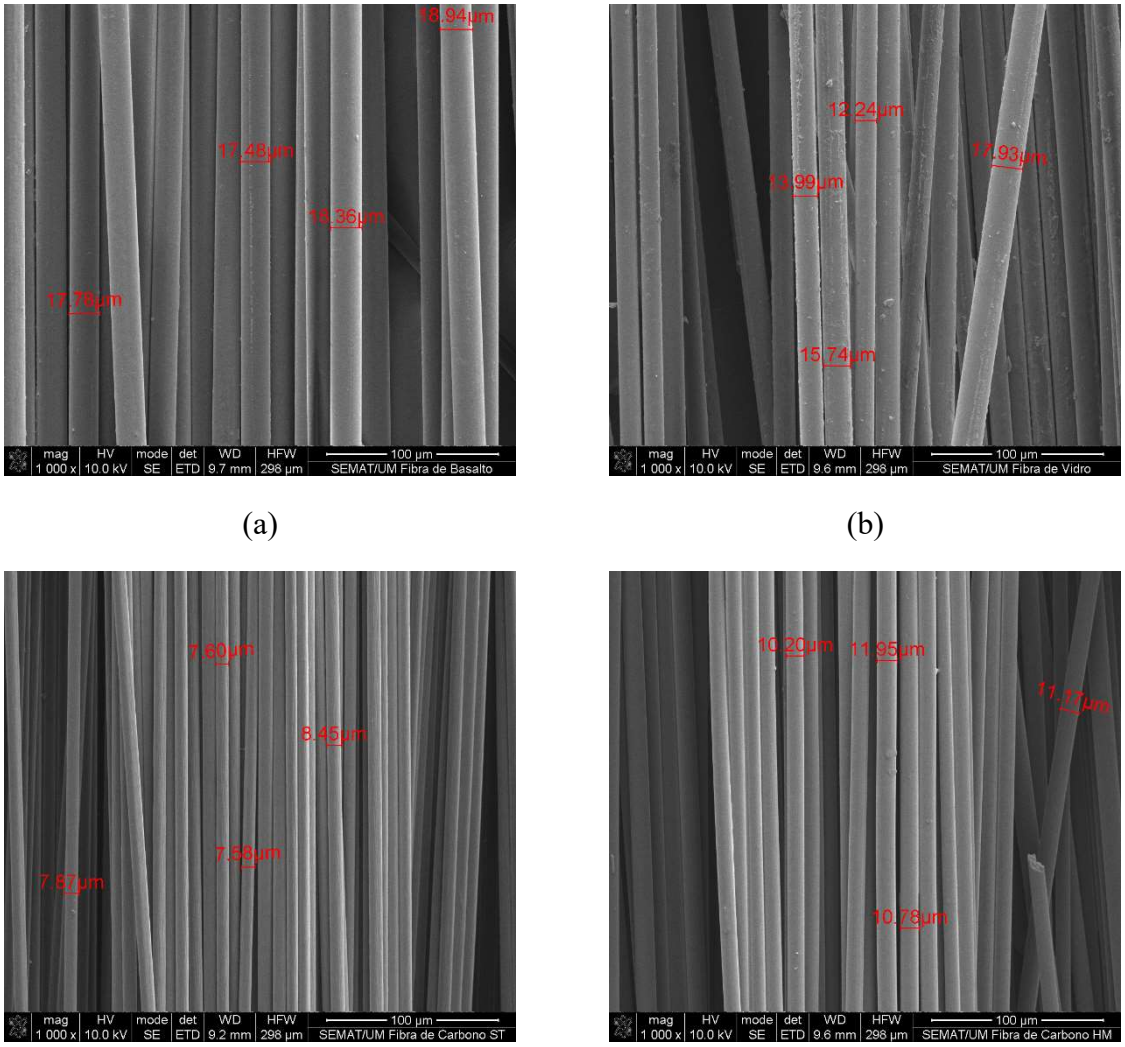

Figure 4.5 — SEM images of the surface and diameter indication of: (a) glass fibres; (b) basalt fibres; (c) ST carbon and (d) HM carbon.

The specimens of each series were obtained from the laminates using a diamond tipped wheel cutter. Tensile tests were performed according to ISO 527-5:2009 standard [34]. Specimen dimensions were 250/150/15/[0.7-3.5]/[0.5-1.0] mm overall length/free length/width/total thickness/fibre layer thickness, respectively. Aluminium tabs of 50 × 15 mm^2 were used at each end of the specimen to avoid gripping effects. A clip gauge with a gauge length of 100 mm (with a linear error, including hysteresis of 0.25%) was used.

Tensile tests were carried out at room temperature on a universal testing machine (UTM) equipped with a 200 kN load cell (with a linear error less than 0.05% of full scale) and hydraulic grips. The specimens were held between grips of the UTM and extended (at a rate of 1 mm/min) up to failure.

As stated before, cross-sectional area of the composite was computed considering only the thickness of the dry fabrics, according the recommendation suggested in the guidelines [31]. In this way, mechanical properties of impregnated composite (elastic modulus and tensile stress) were computed considering the wet lay-up system similar to an equivalent system of only dry fabrics. However, all the composites were measured with a digital calliper, which allowed to determine a fibre mean volume (Vf) of 23.4%, taking into account the fibre layer thickness reported by the manufacturer.

4.4. Results and discussion

4.4.1. Single fibre strength distributions

The strength distribution obtained by testing single fibres in tension is shown in **Figure 4.6** together with the Weibull model plotted by solid lines, considering L_0=20 mm and L=150 mm. The MLM was used to determine the Weibull parameters (shape and scale). The followed procedure is based in application of fitdist function available in Mathworks' Matlab R2015b [35]. The failure probabilities were estimated using the equation (4.17) (which is often used in the literature, e.g. [28, 29]) in order to allow the visualisation of the data, although it was not used to compute the distribution parameters, because MLM does not use such estimators [29].

$$P = \frac{i-0.3}{n+0.4} \tag{4.17}$$

where i is the i-th number in ascendingly ordered strength data and n is the sample size.

Visual examination of the diagrams indicates that the experimental data are reasonably well approximated by the chosen model. However, in the case of ST carbon fibres (**Figure 4.6** (c)) there was some discrepancy between experimental results and fitted model, essentially due to the contribution of the strongest fibres. As it was shown (in **Figure 4.5**), this type of fibres present the lowest diameter and for this reason they are more sensible to large stress deviations. It should be noticed that all stress results were computed considering an average fibre cross-sectional area for converting load into stress.

The overall adequacy of the Weibull distribution was evaluated according to the chi-square goodness-of-fit test. This test depends on the number and the size of the classes of equal probabilities in which the data are grouped. For this reason, this approach maintains a certain degree of arbitrariness. The test result can be reported through the p-value approach [36] to state that the null hypothesis (described below) was or was not rejected at a specified level of significance. P-value varies between 0 and 1 and it is the smallest level of significance that would lead to rejection of the null hypothesis. In its turn, the level of significance is the probability wrongly reject the null hypothesis when it is true. For example a p-value lower or equal to 0.01 leads to the rejection of the null hypothesis with significant level of 1%.

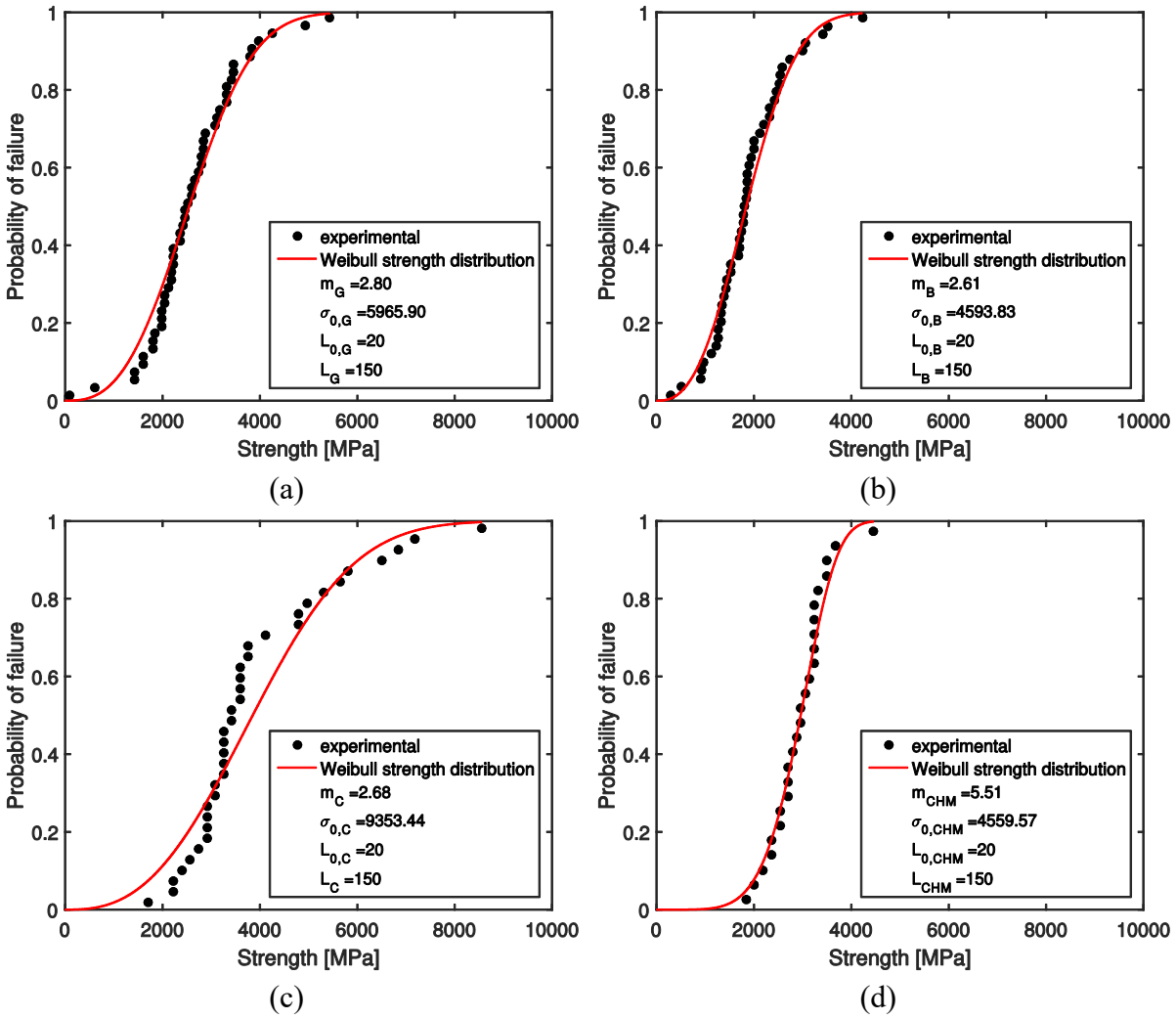

Figure 4.6 — Cumulative Weibull fibre strength distribution for: (a) glass fibres; (b) basalt fibres; (c) ST carbon; (d) HM carbon.

The null hypothesis is defined as: the strength follows a Weibull distribution. The obtained *p*-values for the series tested are summarized in **Table 4.2**. It is possible to observe that all of the *p*-values for these goodness-of-fit statistics are larger than 0.01, implying that the null hypothesis cannot be reject with significant level >1%. The *p*-value obtained in basalt and E-glass cases is clearly superior to the obtained with the 2 types of carbon. Relatively to the ST carbon, the low *p*-value indicates the worst agreement of the experimental results with the Weibull distribution. However, the obtained *p*-value is high enough to avoid the rejection of null hypothesis. For this reason, the obtained parameters for the Weibull distributions were all accepted.

During the preparation of tests, mainly during the extraction of fibres, it was impossible to prevent some fibres from breaking, particularly the HM carbon ones. This is understandable, since the mean breaking force of all fibre types was very low, varying between 0.2 and 0.5 N. The elimination of the weakest fibres causes deviations from Weibull distribution and underestimates the scatter of strength (which means higher values of *m*). The *m* value of HM

carbon is higher than in other cases. The experience gained in the execution of tests lead the authors of this work to believe that this value is not correct, since it was not possible to test a large number of weak fibres. As it is evident in Section 4.4.2, assuming an *m* value equal to the average of the 3 other types of fibres, i.e., *m*=2.70 leads to much better adjustment of the hybrid effect predictions. An algorithm that changes σ_0 of CHM fibres while maintaining either the same strength was implemented, this means that failure strain of CHM was changed. The parameters that define this hypothetical distribution are as well exposed in **Table 4.2**.

Table 4.2 — Weibull distribution parameters.

Material ID	L_0 [mm]	L [mm]	σ_0 [MPa]	m	p-value
B	20	150	4593.83	2.61	0.5496
G	20	150	5965.90	2.80	0.1455
C	20	150	9353.44	2.68	0.0267
CHM	20	150	4559.57	5.51	0.0547
(Hypothetical) CHM*	20	150	2874.00	2.70	--

Note: *m value was assumed equal to the mean of the 3 other types of fibres because the elimination of the weakest fibres underestimates the strength scatter.

4.4.2. Tensile strength and hybrid effect predictions of hybrid composites

The variation of vol% of LS fibres greatly modifies the hybrid tensile response. The PDM, equation (4.7), is obviously sensitive to this variation. An example of the evolution of the stress–strain analytical relationships of the CHM/G combination as the vol% of LS fibres increases are plotted in Figure 4.2. It is possible to observe that when the vol% of HM carbon fibres increases, the strength of the hybrid composite is no longer dominated by glass fibres and depends on the contribution of the two types of fibres. This behaviour essentially follows the bilinear rule of mixtures (ROM):

$$\sigma_{hybrid} = \begin{cases} V_L S_L + V_H E_H \varepsilon_L;\ V_H < V_{crit} \\ V_H S_H;\ V_H > V_{crit} \end{cases} \tag{4.18}$$

where σ_{hybrid} is tensile strength of hybrid composites and ε_L is the ultimate strain of the LS composite.

Based on this model, if the V_H is lower than a critical value, $V_{crit,}$ the hybrid composite would fail prematurely. On the other hand, if the V_H is higher than V_{crit}, hybrid composites would keep their integrity until the failure of HS fibre.

As shown in **Figure 4.7**, the strength predictions follow completely the bilinear ROM. The input parameters used to define the bilinear ROM derived from PDM model: the reference HM carbon composite has a strength of 1350 MPa, an elastic modulus of 100.0 GPa and a failure strain of 1.35%, while the reference glass composite has a strength of 2080 MPa, an elastic modulus of 13.6 GPa and a failure strain of 15.24%. V_{crit} was calculated by equating the two branches of equation (4.18) and it was determined equal to 41.6%. The predicted failure strains of the composites exceed a lot the experimental values (see **Table 4.1**), which lead to very low values of elastic modulus. In this way, the PDM cannot be considered a good model to predict the failure strains. Swolfs *et al*. [9] obtained the same conclusion and they believe that this is due to the fact the GLS models neglect the stress concentrations. In the work of Turon *et al*. [19], it was referred that failure prediction is out of the scope of the present model.

The two different sets of Weibull parameters were used as inputs of PDM in CHM fibres case: (i) the m=5.51 and σ_0= 4559.57 MPa, pair computed according to the experimental tensile CHM fibres strength distribution, and (ii) the m=2.70 and σ_0=2874.00 MPa pair, hypothetical suggested. It is possible to observe in **Figure 4.7** and **Figure 4.8** that the suggested change had no impact in the strength predictions, but had a great influence in the hybrid effect predictions, improving reasonably the predictions of this property.

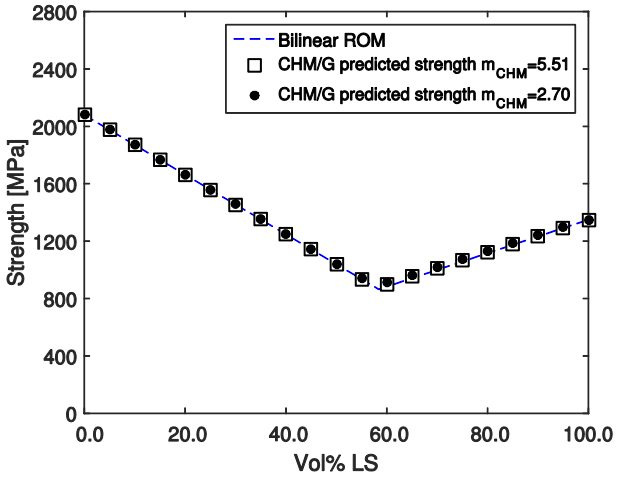

Figure 4.7 —PDM strength predictions compared with the bilinear rule-of-mixtures as function of Weibull modulus and relative volume of HM carbon fibres.

In **Figure 4.8** the mean (and the 95% Fisher level of confidence intervals) of hybrid effect are compared against the PDM predictions. As it is shown, the predictions are, in general, in good agreement with the obtained experimental results. Quantitative comparisons between analytical and experimental results are presented in **Table 4.3**.

It can be seen that apparently very high relative errors (between -251.7% and 2597.5%) were registered. However, it is possible to observe that very high relative errors were registered in

cases in which experimental hybrid effects were negative. Experimental negative hybrid effects only make sense because the number of layers of LS material is not the same in all hybrid combinations. It is well-known that there is a size effect in tensile properties of reinforcing fibre due to the higher probability of finding a cluster of weaker fibre in a larger volume of material [8]. In cases where the hybrid effect was negative, 2 or 3 layers of LS fibre were used. Since the hybrid effect was computed relatively to the 1 layer non-hybrid composite results, negative hybrid effects are understandable. The influence of size effect on the hybrid effect has not yet been investigated in the literature [8]. In any case, in combinations in which the hybrid effect was negative, the predictions are very close to zero, which would be a plausible prediction if the size effect did not exist. With the exception of 2 combinations (1G/1CHM/1G/1CHM/1G and 2G/1C/2G), the positive hybrid effects were predicted satisfactorily, with relative errors varying between -20.4% and 31.1%.

Analytical hybrid effects were used to compute $S_{L,a}$ (according to equation (4.15)). The results are exposed in **Table 4.3**. It is possible to observe that $S_{L,a}$ was predicted satisfactorily, with relative errors varying between -25.4% and 14.7%

In view of the above, PDM is a simple model that, if used with care, can predict reasonably the hybrid effect. However, some limitations should be considered, for instance: (i) it does not take into account the real number of fibres, leading to size effects being ignored. Furthermore, (ii) it ignores the dispersion of fibres, which has been shown to be a very important parameter affecting the hybrid effect [37].

4.4.3. Damage mode maps

In this section, the influence of the geometric and reinforcing material combinations in different characteristics of the hybrid stress–strain response, such as hybrid effect, ‘yield’ stress, pseudo-ductile strain, strength and elastic modulus of the hybrid composites is investigated. The main objective of this part of the work is to better understand the potential of the hybridization of the studied materials, and to identify which combinations maximize the tensile response.

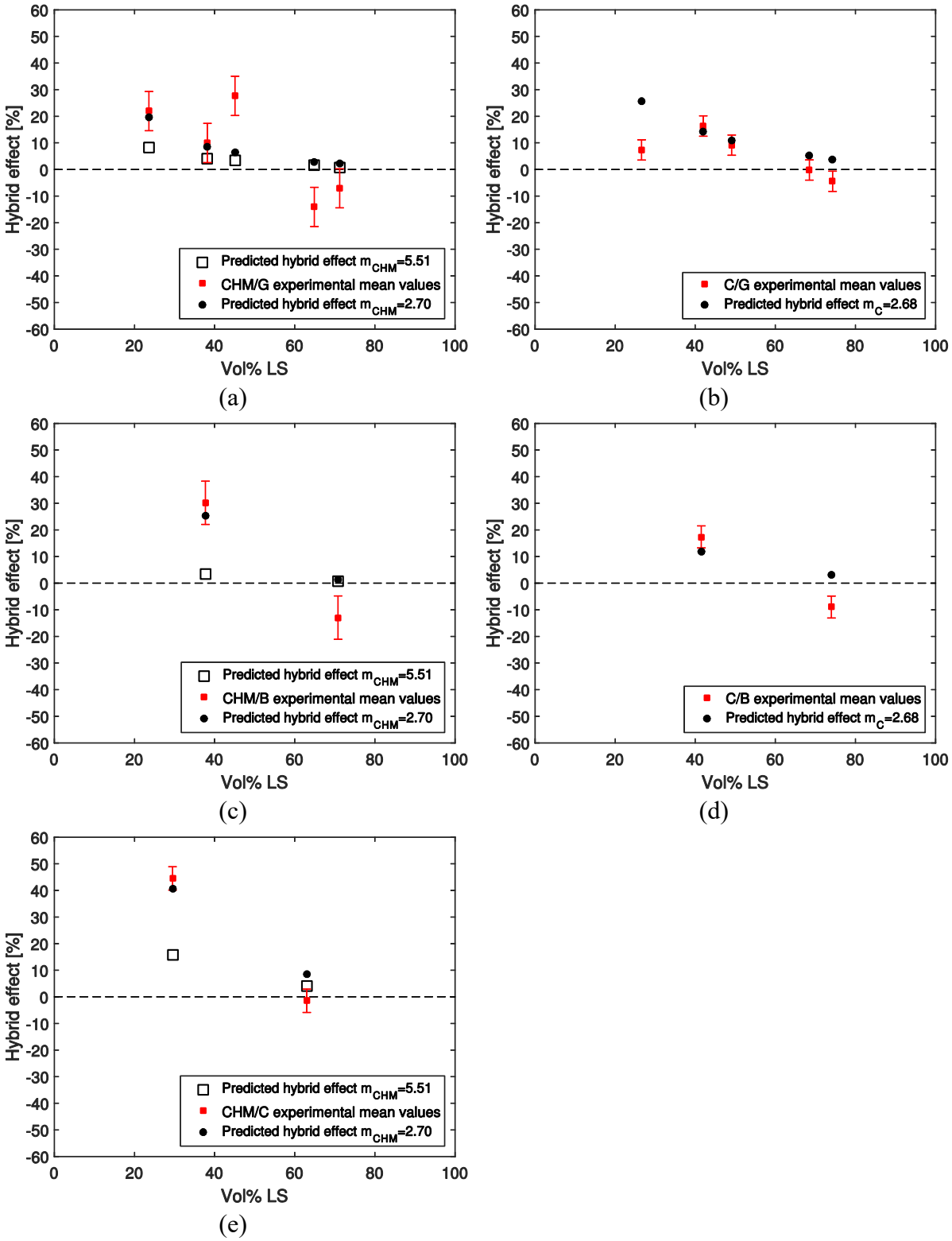

Figure 4.8 — Experimental mean hybrid effect results compared with analytical predictions.

Table 4.3 — Comparison between experimental and analytical results.

Combinations	Series ID	Volume of LS fibre [%]	Hybrid effect			$S_{L,a}$ [MPa]			Tensile streng			Pseudo-ductile strain		
			Experimental [%] **[6]**	PDM prediction [%]	Error [%]	Experimental [MPa] **[6]**	Based on predicted HE [MPa]	Error [%]	Experimental [MPa] **[6]**	Analytical [MPa]	Error [%]	Experimental [%] **[6]**	Analytical [%]	Error [%]
C/B	1C/1B/1C	74.0	-8.99	3.21	135.7[a]	2289.9	2648.3	-15.65	2191.4 (7.28)	2264.6	-3.3	--	--	--
	1B/1C/1B	41.5	17.37	11.97	31.1	2960.6	2873.0	2.96	1950.2 (7.51)	1938.2	0.6	--	--	--
CHM/B	1CHM/1B/1CHM	70.8	-12.95	1.44	111.2[a]	1497.8	1774.6	-18.48	1150.0 (14.10)	1341.0	-16.6	--	--	--
	1B/1CHM/1B	37.7	30.19	25.36	16.0	2246.8	2193.0	2.39	1328.0 (10.74)	1125.3	15.3	2.04 (8.84)	1.80	11.8
CHM/C	1CHM/1C/1CHM	63.0	-1.50	8.69	680.1[a]	1684.8	1901.4	-12.84	1352.5 (5.10)	1458.8	-7.9	--	--	--
	1C/1CHM/1C	29.5	44.52	40.58	8.9	2434.0	2459.3	-1.04	1937.5 (6.79)	1431.0	26.1	0.44 (9.57)	0.64	-45.5
C/G	1C/1G/1C	74.3	-4.44	3.85	186.6[a]	2405.0	2664.7	-10.77	2176.9 (8.55)	2222.0	-2.1	--	--	--
	1G/3C/1G	68.5	-0.20	5.13	2597.5[a]	2521.2	2697.5	-7.00	2216.0 (8.77)	2143.7	3.3	--	--	--
	1G/1C/1G/1C/1G	49.1	9.15	11.01	-20.4	2752.5	2848.4	-3.49	1776.3 (10.55)	1910.4	-7.5	--	--	--
	1G/1C/1G	42.0	16.33	14.22	12.9	2937.5	2930.8	0.23	1856.0 (5.67)	1830.6	1.3	--	--	--
	2G/1C/2G	26.6	7.33	25.77	-251.7	2706.2	3227.1	-19.25	1244.4 (1.74)	1693.6	-36.1	--	--	--
CHM/G	1CHM/1G/1CHM	71.2	-7.07	2.17	130.7[a]	1560.3	1787.4	-14.56	1168.9 (19.49)	1339.3	-14.6	--	--	--
	1G/3CHM/1G	64.9	-14.09	2.89	120.6[a]	1435.4	1800.0	-25.40	1053.5 (10.14)	1251.1	-18.8	--	--	--
	1G/1CHM/1G/1CHM/1G	45.1	27.66	6.52	76.4	2184.4	1863.5	14.69	1105.8 (9.18)	974.7	11.9	--	--	--
	1G/1CHM/1G	38.2	9.97	8.69	12.8	1872.0	1901.4	-1.56	1054.7 (9.11)	879.1	16.6	1.21 (23.32)	1.73	-43.0
	2G/1CHM/2G	23.6	21.94	19.57	10.8	2059.5	2091.8	-1.56	1164.7 (14.47)	1004.6	13.7	1.4 (15.20)	1.66	-18.6

Note: [a]apparently very high relative errors were registered in cases that hybrid effect was negative.

4.4.3.1. Hybrid effect

The evolution of the hybrid effect for the different reinforcing material combinations is presented in **Figure 4.9**. The presentation of the results for hybrid effect is based on DMMs described in Section 4.2.2. Each DMM locates four zones that divide all possible expected tensile damage modes of UD hybrid composites. The horizontal axis of DMMs shows the ratio between LS and HS material thickness and the vertical axis shows the absolute thickness of LS material. The border lines are defined for each material combination according to the equations (4.11), (4.13) and (4.14). In innovative way, the evolution of S_L was contemplated according to the predictions of hybrid effect, assuming $S_L = S_{L,a}$. This means that mean values presented in the **Table 4.1** and the corresponding computed hybrid effect were updated as function of the ratio between the thicknesses of the reinforcing materials. This option had influence in the definition of the boundaries that depend on S_L, namely those which are defined in equations (4.11) and (4.13) .The length and width of specimens were assumed equal to L = 150 mm and W = 15 mm, respectively. The interlaminar toughness, G_{IIC}, for the different hybrid interfaces was not experimentally measured and it was arbitrated in way that, in combination with experimental pseudo-ductile behaviour, the fragmentation & dispersed delamination damage mode was analytically achieved (see the details in [6]). Weibull modulus of HS fibres was assumed constant and equal to the value used by Jalalvand *et al*. [13], m_H = 29.3. This value is significantly higher than that obtained experimentally in this work (and higher than those usually reported in bibliography, e.g. [26]). However, it was proved by the authors' model [13] that this value allowed the best predictions. In practice, this implies that a lower variability of HS fibres strength is being considered. The value of the stress concentration factor was assumed constant for all of the specimens, K_t = 0.97.

In general terms, observing the **Figure 4.9**, it is possible to conclude that the combination of HM carbon with ST carbon allowed to achieve the maximum hybrid effect (at least close to 50%). For all the combinations the maximum hybrid effect was achieved with the occurrence of fragmentation or fragmentation & delamination.

In **Figure 4.10** the DMMs of different reinforcing material combinations are presented in conjugation with the localization of experimental configurations and indication of vol% of LS fibres. The border lines defined with the contemplation of a mean experimental $S_{L,a}$ and analytical $S_{L,a}$ are compared. The mean experimental $S_{L,a}$ was computed assuming the mean value obtained for all series within the material combination. It is possible to observe that the contemplation of analytical $S_{L,a}$ reduced the fragmentation and fragmentation & delamination zones. In this way, the premature failure and catastrophic delamination damages modes occur much more frequently. Anyway, in both cases the boundaries in **Figure 4.10** separate the studied configuration in absolute accordance with registered damage modes exposed in [6]. However, in the case of HM carbon/glass combination, the configuration with 38.2% of LS fibres is located very close to the border line. This point is even slightly outside of fragmentation & delamination zone, considering boundaries with analytical $S_{L,a}$ contemplation. In this case,

the $S_{L,a}$ are a little overestimated. In the remaining cases, all the points that correspond to combinations in which the pseudo-ductile was achieved are located in fragmentation and stable delamination zone. This happened essentially with some combinations that included HM carbon as the LS material. For other hand, configuration in which the ST carbon is considered the LS material, it is possible to observe that the fragmentation and fragmentation & delamination zones are very reduced, indicating that it is almost impossible to get these types of damage modes in practice. For instance, the abscissa point of the apex of the boundary lines of ST carbon/glass combination is 0.1548. A layer of ST carbon has a thickness of 0.223 mm (see **Table 4.1**), this means that in the referred point, the thickness of the glass is 1.505 mm, which corresponds approximately to 9.77 layers. The best practices suggested in the guidelines [31] advise to use no more than 5 layers.

4.4.3.2. 'Yield' stress and pseudo-ductile strain

DMMs presented in **Figure 4.11** allow to observe that the highest value of 'yield' stress, if it exists, can be achieved close to LS fragmentation/HS failure boundary. This means that this property increases with the amount of the LS fibres. 'Yield' stress was computed according to equation (4.8), for the damages modes 3 and 4 described in Section 4.2.2, i.e., the white zones in DMMs correspond to configurations in which damage modes 1 and 2 take place. S_L was assumed equal to analytical $S_{L,a}$. The maximum 'yield' stress was achieved for the combination of ST carbon with basalt. However, in this material combination, the reduced areas of the fragmentation and fragmentation & delamination zones leads almost to the impossibly of achieving this damage mode in practice. In this way, the combination of HM carbon with ST carbon is the best plausible choice to reach the highest 'yield' stress.

The predicted pseudo-ductile strains for all material combinations are present in **Figure 4.12**. As in the previous case, the coloured regions of the maps indicate the existence of pseudo-ductility. The white regions show either premature HS material failure or catastrophic delamination. It is possible to observe that the highest value of pseudo-ductile strain can be achieved close to the intersection of the boundaries within fragmentation & delamination zones. This is understandable because delamination promotes extra extension to the composite, when compared to the case in which only fragmentation takes place. The highest values of pseudo-ductile strain were achieved in the combination of HM carbon with basalt. On the other hand, the combination of HM carbon with ST carbon resulted in the worst response. Again, the pseudo-ductile strain in the combination of ST carbon with glass or basalt are very difficult to achieve experimentally. The predicted pseudo-ductile strains are presented in **Table 4.3** and they are compared with experimental results. Although, the relative errors are very high, absolute values are close. Comparing very low values generates situations where small variations lead to very high relative errors. For this reason, this type of errors should be carefully analysed.

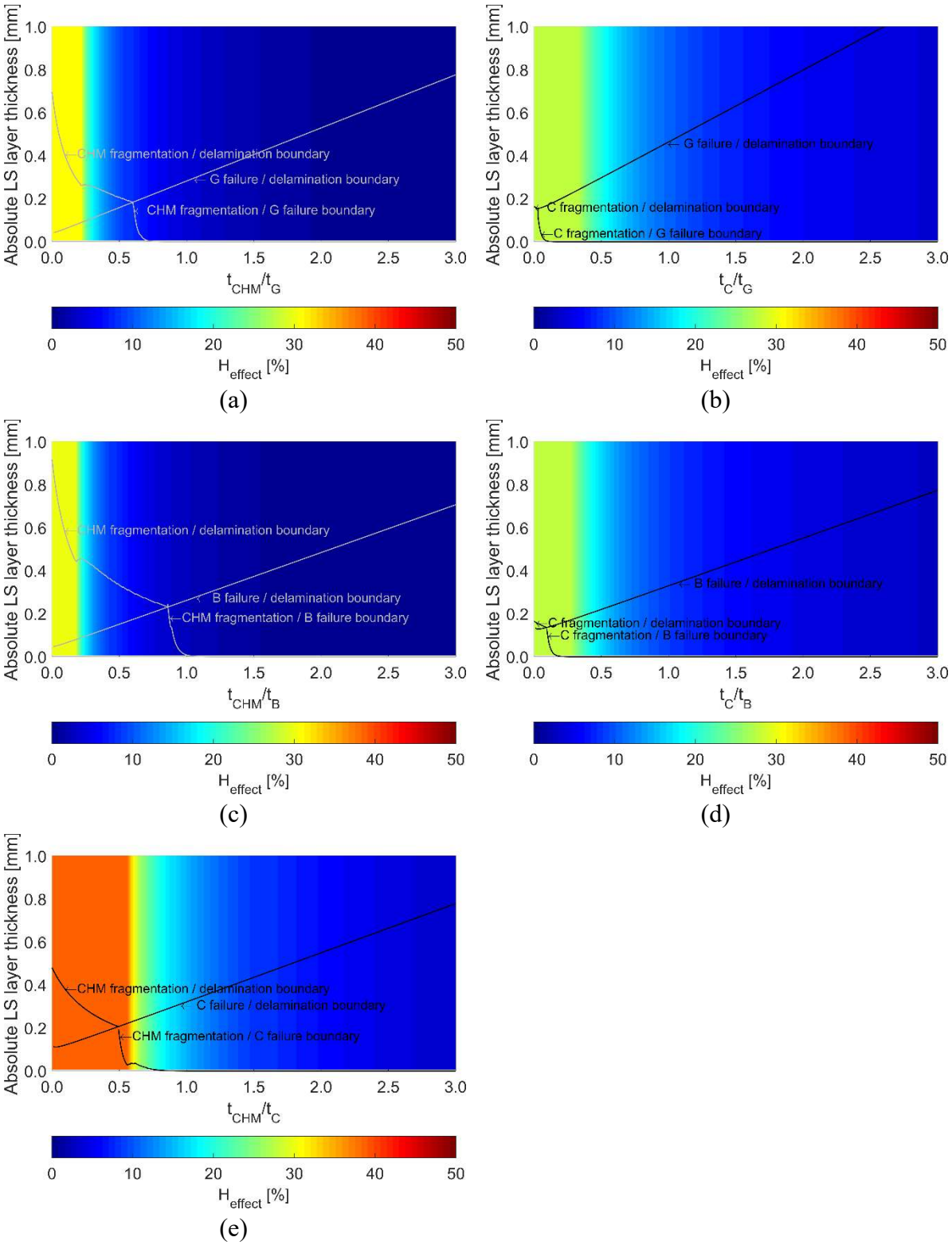

Figure 4.9 — Damage mode map and distribution of hybrid effect of: (a) HM carbon/glass; (b) ST carbon/glass; (c) HM carbon/basalt; (d) ST carbon/basalt and (e) HM carbon/ST carbon hybrid composites.

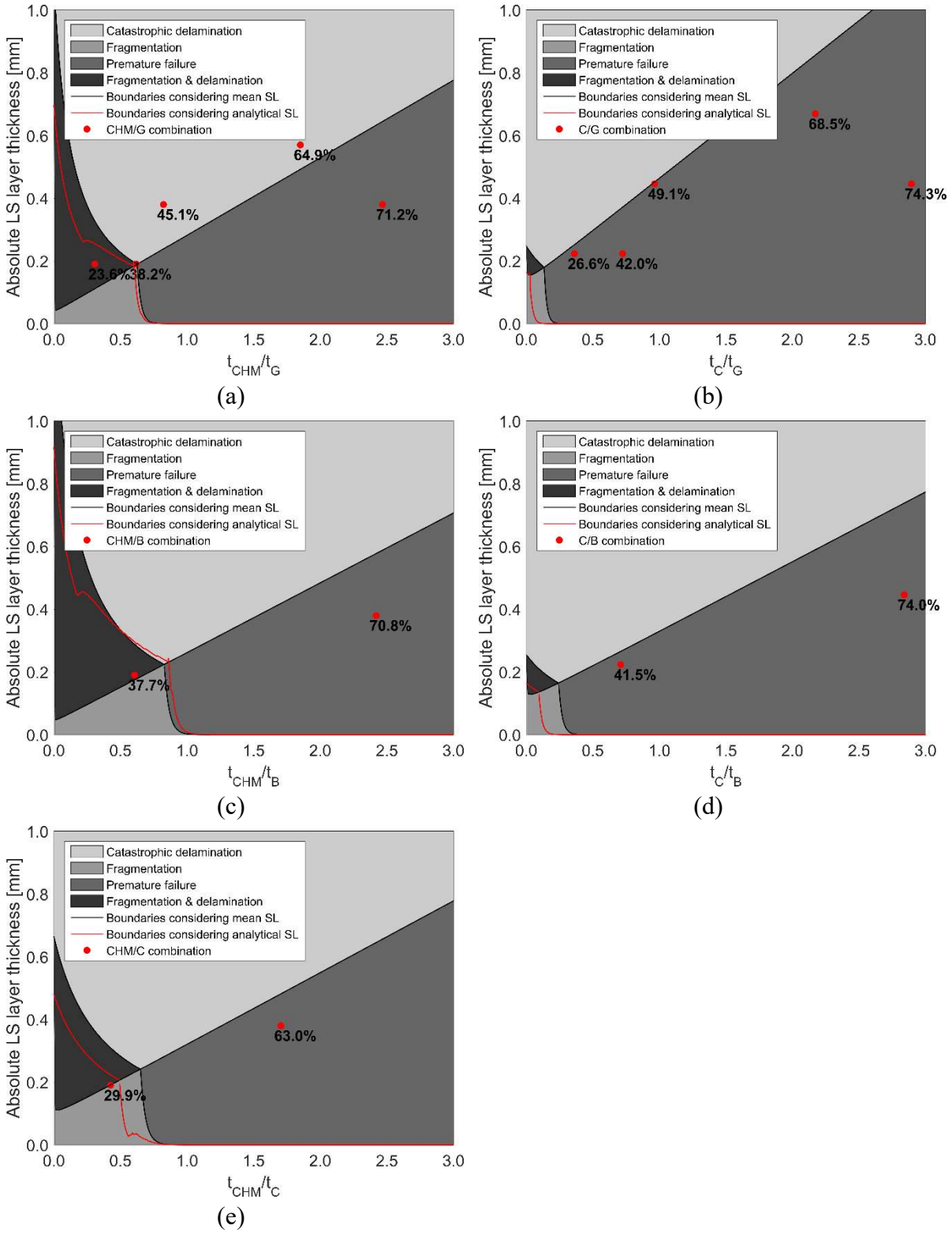

Figure 4.10 — Predicted damage mode maps with the experimental configurations of: (a) HM carbon/glass; (b) ST carbon/glass; (c) HM carbon/basalt; (d) ST carbon/basalt and (e) HM carbon/ST carbon composites.

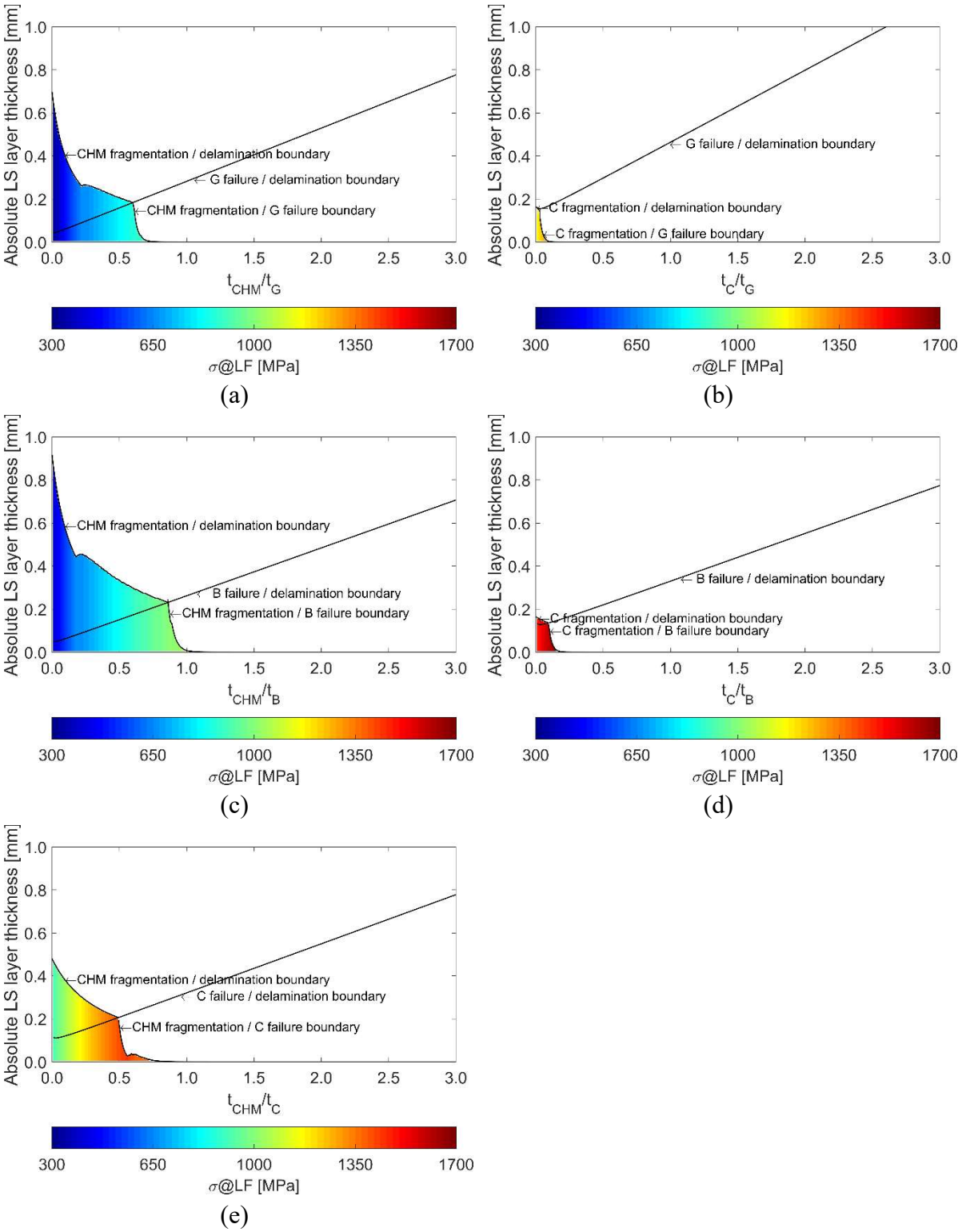

Figure 4.11 — Damage mode map and distribution of 'yield' stress of: (a) HM carbon/glass; (b) ST carbon/glass; (c) HM carbon/basalt; (d) ST carbon/basalt and (e) HM carbon/ST carbon hybrid composites.

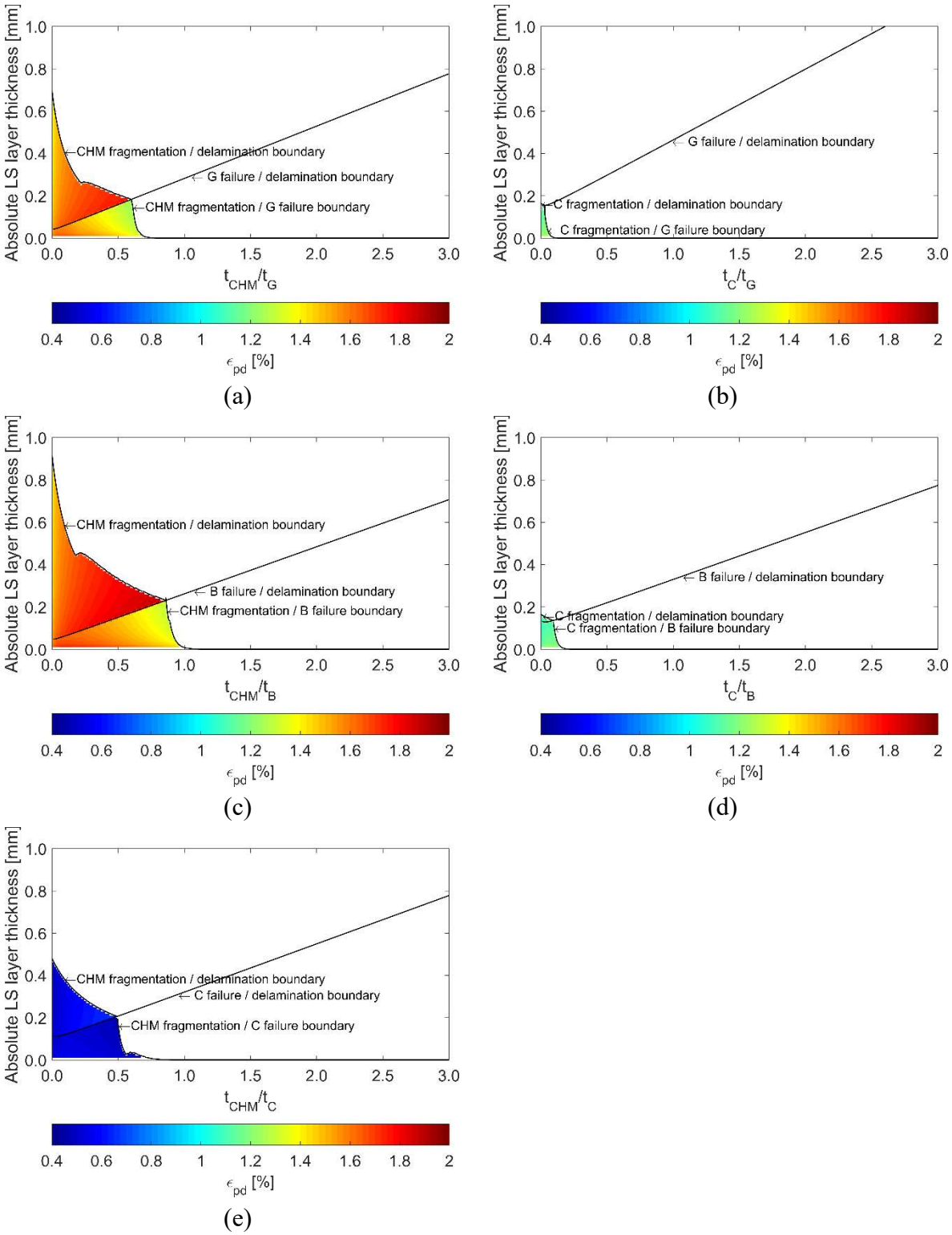

Figure 4.12 — Damage mode map and distribution of pseudo-ductile strain of: (a) HM carbon/glass; (b) ST carbon/glass; (c) HM carbon/basalt; (d) ST carbon/basalt and (e) HM carbon/ST carbon hybrid composites.

4.4.3.3. Strength and elastic modulus

The strength was predicted according to equations (4.8) and (4.9). For each configuration, the maximum between *σ@LF* and *σ@HF* was assumed as the strength. The evolution of the strength for studied hybrid combinations is presented in **Figure 4.13**. It is possible to observe that, in all cases, the minimum strength was achieved in LS fragmentation/delamination boundary. The evolution of strength follows basically the conclusions obtained with bilinear ROM. The highest strength was achieved with the combination of ST carbon with basalt. Since HM carbon is one of the materials with lower tensile strength, in combination with this material, the increase of volume of HM carbon would not lead to significant improvements in tensile strength. Experimental and analytical strengths are presented in **Table 4.3**. It is possible to observe that strength was reasonably predicted, with relative errors varying between -36.1% and 26.1%.

Figure 4.14 presents the evolution of elastic modulus of the 5 material combinations referred before. This property was evaluated according to equation (4.16). As expected, the elasticity modulus increases with the thickness increase of LS fibres in all the combinations. It is possible to observe that the property under review varies only with thickness ratio between the reinforcing materials, i.e. the absolute LS layer thickness has no influence in the response. Combinations that include HM carbon are the ones that allow reaching higher elasticity modulus. According to the DMMs shown in **Figure 4.14**, the combination of HM carbon with ST carbon results in the highest elastic modulus and the combination of carbon with glass in the lowest values.

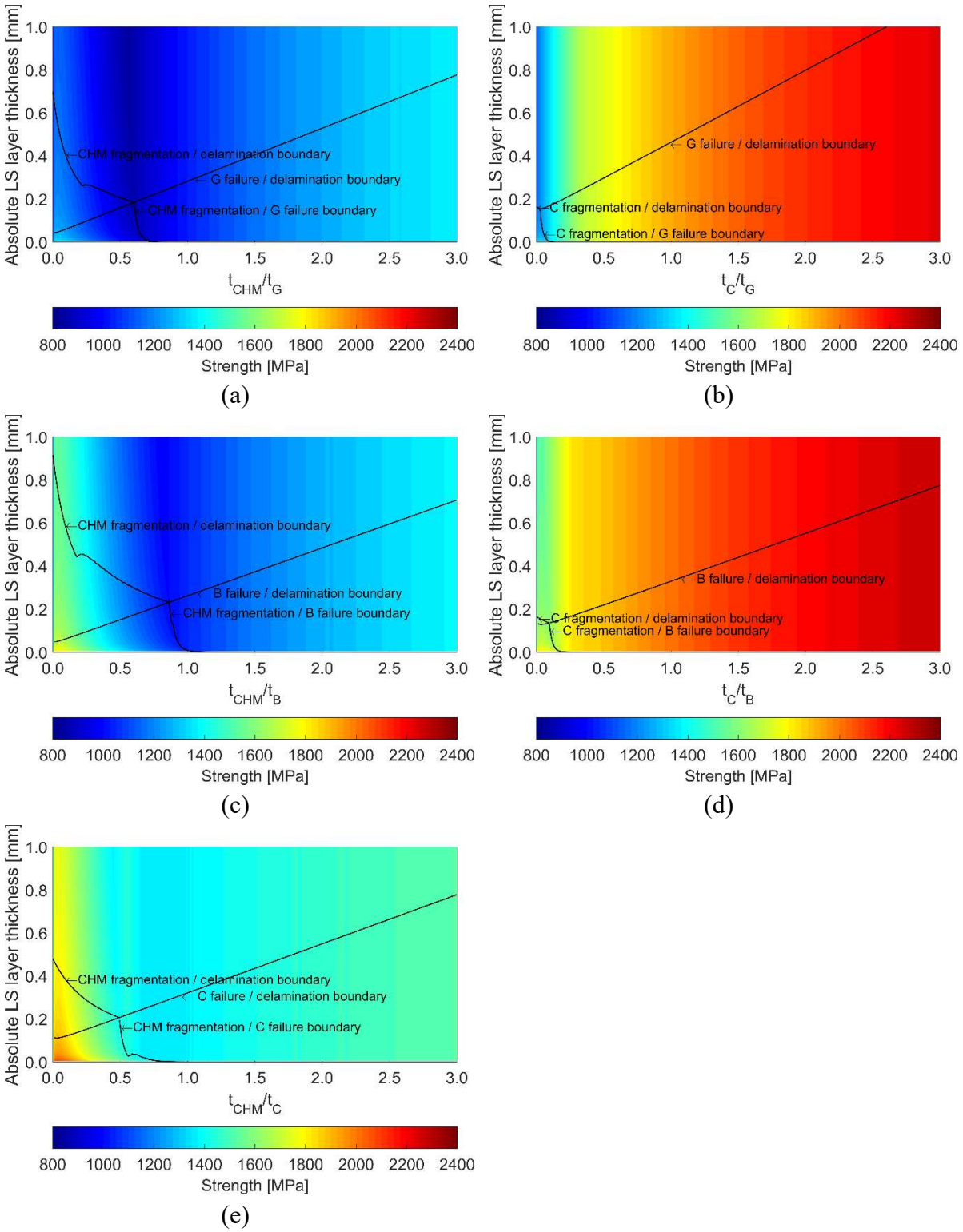

Figure 4.13 — Damage mode map and distribution of strength of: (a) HM carbon/glass; (b) ST carbon/glass; (c) HM carbon/basalt; (d) ST carbon/basalt and (e) HM carbon/ST carbon hybrid composites.

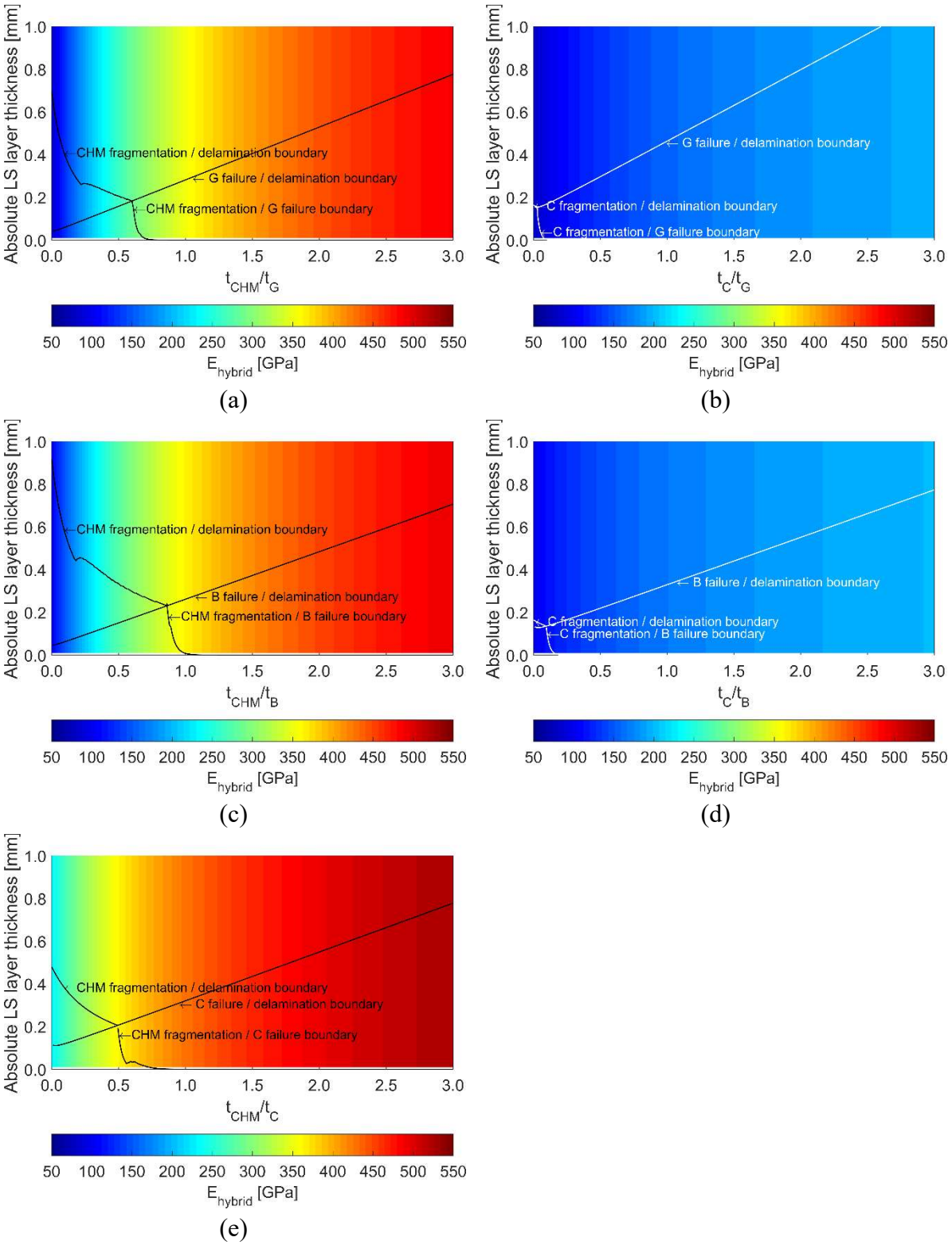

Figure 4.14 — Damage mode map and distribution of elastic modulus of: (a) HM carbon/glass; (b) ST carbon/glass; (c) HM carbon/basalt; (d) ST carbon/basalt and (e) HM carbon/ST carbon hybrid composites.

4.5. Conclusions

In the present chapter, it was concluded that PDM, if used with care, can predict reasonably the hybrid effect. However, there are some limitations, because the method does not take into account scale effects or the dispersion of fibres. Furthermore, Weibull parameters, which are used as inputs of the PDM, are susceptible to several error sources and they are dependent of the number of tests and the gauge length of specimens. Having said that, quantitative comparisons between analytical and experimental results revealed that positive hybrid effects were predicted with relative errors varying between -20.4% and 31.1%. It was explained that negative hybrid effects appear probably due to the size effect in tensile properties of reinforcing fibre due to the higher probability of finding a cluster of weaker fibre in a larger volume of material. It should be highlighted that it is not possible, in combination with low vol% of LS fibres, to achieve a clear local maximum point at stress-strain diagram predicted with PDM, corresponding to strain to failure of LS fibres. In these cases, the hybrid effect was considered equal to the achieved with lowest possible vol% of LS fibres.

Analytical hybrid effects were used to compute the reference strength of LS fibres and it was demonstrated that this property was reasonably predicted, with relative errors varying between -25.4% and 14.7%. Furthermore, analytical hybrid effects were considered to modify the model of Jalalvand et al. [13] and, in this way, to predict pseudo-ductile strain and strength. It was demonstrated that the magnitude of the two cited properties is close to the experimental results.

DMMs of different reinforcing material combinations were presented. The border lines were defined with the contemplation of the hybrid effect. It was possible to observe that this contemplation reduced the fragmentation and fragmentation & delamination zones. DMMs allowed as well to observe that the highest value of 'yield' stress can be achieved if the coordinates of a given hybrid configuration are close to LS fragmentation\HS failure boundary. In configurations where C was considered as the LS material, it was possible to observe that the fragmentation and fragmentation & delamination zones were very reduced, indicating that it is almost impossible to get these types of damage modes in practice. In this way, the combination of CHM with C is the best plausible choice to reach the highest 'yield' stress.

It was also possible to observe that the highest value of pseudo-ductile strain can be achieved close to the intersection of the boundaries within fragmentation & delamination zone. The highest values of pseudo-ductile were achieved in the combination of CHM with B.

It was also possible to observe that in all cases the minimum strength was achieved in LS fragmentation/ delamination boundary. The highest strength was achieved with the combination of C with B.

As expected, the elasticity modulus increases with the increase of thickness of LS fibres in all the combinations. The combination of CHM with C resulted in the highest elastic modulus.

4.6. References

[1] Czél G, Jalalvand M, Wisnom MR, Czigány T. Design and characterisation of high performance, pseudo-ductile all-carbon/epoxy unidirectional hybrid composites. Composites Part B. 2017;111 348-56.
[2] Czél G, Jalalvand M, Wisnom MR. Design and characterisation of advanced pseudo-ductile unidirectional thin-ply carbon/epoxy–glass/epoxy hybrid composites. Composite Structures. 2016;143:362–70.
[3] Summerscales J, Short D. Carbon fibre and glass fibre hybrid reinforced plastics. Composites. 1978;9(3):157–66.
[4] Czél G, Wisnom MR. Demonstration of pseudo-ductility in high performance glass/epoxy composites by hybridisation with thin-ply carbon prepreg. Composites: Part A: Applied Science and Manufacturing. 2013;52:23–30.
[5] Swolfs Y, Gorbatikh L, Verpoest I. Fibre hybridisation in polymer composites: a review. Composites Part A: Applied Science and Manufacturing. 2014;67:181-200.
[6] Ribeiro F, Sena-Cruz J, Branco FG, Júlio E. Hybrid effect and pseudo-ductile behaviour of unidirectional interlayer hybrid FRP composites for civil engineering applications. Construction and Building Materials. 2018;171:871-90.
[7] Hayashi T. On the improvement of mechanical properties of composites by hybrid composition. Proc 8th Intl Reinforced Plastics Conference. 1972:149-52.
[8] Wisnom MR, Czél G, Swolfs Y, Jalalvand M, Gorbatikh L, Verpoest I. Hybrid effects in thin ply carbon/glass unidirectional laminates: Accurate experimental determination and prediction. Composites: Part A. 2016;88:131–9.
[9] Swolfs Y, McMeeking RM, Rajan VP, Zok FW, Verpoest I, Gorbatikh L. Global load-sharing model for unidirectional hybrid fibre-reinforced composites. Journal of the Mechanics and Physics of Solids. 2015;84:380–94.
[10] Swolfs Y, Gorbatikh L, Verpoest I. Stress concentrations in hybrid unidirectional fibre-reinforced composites with random fibre packings. Composites Science and Technology. 2013;85:10–6.
[11] Zweben C. Tensile strength of hybrid composites. Journal of Materials Science 1977;12:1325-37.
[12] Fukuda H. An advanced theory of the strength of hybrid composites. . Journal of Materials Science. 1983;19:974-82.
[13] Jalalvand M, Czél G, Wisnom MR. Damage analysis of pseudo-ductile thin-ply UD hybrid composites – A new analytical method. Composites: Part A. 2015;69:83–93.
[14] Curtin WA. Theory of Mechanical Properties of Ceramic-Matrix Composites. J Am Ceram Soc. 1991;74(11):2837-45
[15] Curtin WA. Stochastic Damage Evolution and Failure in Fiber-Reinforced Composites. Advances in Applied Mechanics Volume. 1998;36:163-253.
[16] Hui C-Y, Phoenix SL, Ibnabdeljalil M, Smiths RL. An exact closed form solution for fragmentation of Weibull fibers in a single filament composite with applications to fiberreinforced ceramics. J Mech Phys Solids. 1991;43(10):1551-85.
[17] Rajan VP, Curtin WA. Rational design of fiber-reinforced hybrid composites: A global load sharing analysis. Composites Science and Technology 2015;117:199-207.
[18] Tavares RP, Melro AR, Bessa MA, Turon A, Liu WK, Camanho PP. Mechanics of hybrid polymer composites: analytical and computational study. Comput Mech DOI 101007/s00466-015-1252-0. 2016.

[19] Turon A, Costa J, Maimí P, Trias D, Mayugo JA. A progressive damage model for unidirectional fibre-reinforced composites based on fibre fragmentation. Part I: Formulation. Composites Science and Technology. 2005;65 2039–48.
[20] Pan N, Postle R. The tensile strength of hybrid fibre composites: a probabilist analysis of hybrid effects. Phil Trans R Soc Lond A. 1996;354:1875-97.
[21] Manders PW, Bader MG. The strength of hybrid glass/carbon fibre composites - Part 1. Journal of Materials Science. 1981;16:2233-45.
[22] Kretsis G. A review of the tensile, compress,ve, flexural and shear properties of hybrid fibre reinforced plastics. Composites. 1987;18(1).
[23] Shan Y, Liao K. Environmental fatigue behavior and life prediction of unidirectional glass–carbon/epoxy hybrid composites. International Journal of Fatigue. 2002;24:847–59.
[24] Yu H, Longana ML, Jalalvand M, Wisnom MR, Potter KD. Pseudo-ductility in intermingled carbon/glass hybrid composites with highly aligned discontinuous fibres. Composites: Part A 2015;73:35–44.
[25] Jalalvand M, Czél G, Wisnom MR. Parametric study of failure mechanisms and optimal configurations of pseudo-ductile thin-ply UD hybrid composites. Composites: Part A. 2015; 74:123–31.
[26] Swolfs Y, Verpoest I, Gorbatikh L. A review of input data and modelling assumptions in longitudinal strength models for unidirectional fibre-reinforced composites. Composite Structures. 2016;150:153–72.
[27] Weibull W. A Statistical Distribution Function of Wide Applicability. 1951:293-7.
[28] Andersons J, Joffe R, Hojo M, Ochiai S. Glass fibre strength distribution determined by common experimental methods. Composites Science and Technology 2002;62:131–45.
[29] Ambrožič M, Gorjan L. Reliability of a Weibull analysis using the maximum-likelihood method. Journal of materials science. 2011;46(6):1862-9.
[30] Fotouhi M, Suwarta P, Jalalvand M, Czel G, Wisnom MR. Detection of fibre fracture and ply fragmentation in thin-ply UD carbon/glass hybrid laminates using acoustic emission. Composites: Part A 2016;86:66–76.
[31] CNR-DT200. Guide for the Design and Construction of Externally Bonded FRP Systems for Strengthening Existing Structures. Advisory Committee on Techincal Recommendations for Construction, National Research Council, Rome, Italy. 2013.
[32] S&P. Technical Data Sheet S&P Resin 55. 2015.
[33] ASTM. D 3379 – 75 - Standard Test Method for Tensile Strength and Young's Modulus for High-Modulus Single-Filament Materials. 1989.
[34] ISO. 527-5 Plastics — Determination of tensile properties; Part 5: Test conditions for unidirectional fibre-reinforced plastic composites. EUROPEAN COMMITTEE FOR STANDARDIZATION. 2009.
[35] MATLAB Release 2015b, The MathWorks, Inc., Natick, Massachusetts, United States.
[36] Montgomery DC, Runger GC. Applied Statistics and Probability for Engineers. John Wiley & Sons, Inc ISBN-13 9781118539712. 2014.
[37] Swolfs Y, McMeeking RM, Verpoest I, Gorbatikh L. The effect of fibre dispersion on initial failure strain and cluster development in unidirectional carbon/glass hybrid composites. Composites: Part A 2015;69:279–87.

5. HYBRID FRP-CONFINED CONCRETE: EXPERIMENTAL AND ANALYTICAL STUDY

5.1. Introduction

FRP composites have been effectively used as passive jacket of concrete columns in the last three decades. It is known that concrete in compression expands radially leading to internal cracking [1]. The confinement, first, delays cracking and, then, prevents the relative displacement of disaggregated concrete pieces, thus allowing concrete to reach higher compressive strength and higher ultimate axial and lateral strains [2]. FRP jackets are typically produced through the wet lay-up method [2]. These systems have been implemented mainly in two situations: (i) in rehabilitation of existing concrete structures, being columns retrofitted through FRP wrapping (positioning the fibres transversely oriented, relatively to the longitudinal axis of the member) and (ii) in new construction, adopting composite columns made of concrete-filled FRP tubes (CFFTs) [3-5].

Confinement of concrete columns is more effective in the case of circular cross-sections, than in the case of square/rectangular cross-sections because, in the former situation, concrete is uniformly confined. For this reason, as addressed in [6], the behaviour of FRP-confined concrete in circular cross-sections has been widely studied since the mid-1980s. A database built from an extensive literature review covering 1063 test results is published in [7, 8]. The behaviour of FRP-confined concrete in square/rectangular cross-sections has received relatively less attention. Thus, in a similar database, published in [9], it was possible to assemble 484 test results.

Although the performance of FRP-confined concrete is well studied, it can be improved. For instance, results in bibliography have shown that the ultimate tensile strain of conventional FRP jackets is lower than that observed in tensile tests of laminates of non-hybrid FRP of the same material [10-12]. This phenomenon has been designated as lateral strain efficiency of FRP jackets. A several number of factors has been reported as cause of lower efficiency in FRP jackets [10]. These factors include differences between FRP jackets and laminate specimens in variables such as the form, the methods of measurement and testing, the quality of workmanship, the geometric imperfections, the presence of an overlap region in the jacket, and the curvature and multiaxial stress state of the FRP jacket. Lim and Ozbakkaloglu [10] have presented the results of an analytical study that closely examined factors influencing the lateral rupture strains and axial strains in FRP-confined concrete. It has been concluded that ultimate tensile strain of non-hybrid FRP jackets are significantly affected by (i) concrete strength, and (ii) type of FRP material. It has been demonstrated that the FRP lateral strain at failure decreases with an increase in the unconfined concrete strength and elastic modulus of fibres. In addition, conventional FRP materials are brittle, exhibiting a linear elastic behaviour up to failure. For this reason, when submitted to pure compression, the compressive stress of the confined

concrete continuously increases with the strain up to FRP failure. Since the confinement material is brittle, failure is abrupt, even explosive, dominated by FRP failure.

In the present chapter, an innovative solution to overcome these drawbacks is presented. The strategy passed by combining commercially available unidirectional dry fabrics of different materials in the same matrix obtained a hybrid composite that promotes synergies between the involved reinforcing materials, conducting, for instance, a pseudo-ductile tensile response (characterized by fragmentation in the low strain material and dispersed delamination, please see details in [13]), and an increase (until 50% [13, 24]) of the apparent failure strain of low strain fibres, known as 'hybrid effect'. The present research focus on the results of pure compression tests, performed on small-scale plain concrete columns confined with 16 unidirectional interlayer hybrid composite combinations, exploiting the demonstrated hybrid effect and pseudo-ductility of this confining material [14]. All the unidirectional hybrid composites used in the jacketing have been tensile characterized before in [14]. This work aims at demonstrating that the hybrid effect can maximize the efficiency of the FRP jackets and pseudo-ductility can avoid abrupt failures, and thus, improve safety. To the best of the author's knowledge, it is the first time that fragmentation of low strain material and dispersed delamination is explored in this type of applications. Moreover, it is intended to prove that the model of Jalalvand *et al*. [13] and the bilinear rule of mixtures (ROM) [14] can be used to predict satisfactorily the confining pressure of hybrid composites. A new design-oriented model to predict the ultimate condition of hybrid FRP-confined concrete is proposed in this work. Lastly, an analysis-oriented model for hybrid FRP-confined concrete, developed by modifying the calculation method of the confining pressure of Lim and Ozbakkaloglu [15, 16] model, is also presented.

5.1.1. Tensile behaviour of hybrid unidirectional composites

Aiming at achieving pseudo-ductile tensile response (so called to describe a mechanical non-linear behaviour characterized by presenting a flat-topped stress-strain curve in monotonic tensile tests), exhaustive work has been carried out with a combination of different unidirectional FRP composites [13, 14, 17-22]. This type of combination consist of two types of fibres, namely low strain (LS) and high strain (HS) fibres, within the same polymeric matrix. Please note that non-catastrophic tensile curve, achievable with some configuration of unidirectional hybrid FRP composites, is not repeatable on subsequent unloadings/reloadings [17, 23].

In addition to pseudo-ductility, as referred to above hybridisation also promotes the appearance of the 'hybrid effect', i.e., an increase of strain at the failure of LS material. This was reported, for the first time, in 1972, by Hayashi [24]. The restriction caused by HS fibres adjacent to a broken LS fibre has been reported as the main factor contributing for the hybrid effect, since HS fibres inhibit the formation of critical clusters [21, 23].

Ribeiro *et al*. [14] conducted an experimental study on the tensile stress–strain curves of interlayer (layer-by-layer) unidirectional hybrid FRP composites, aiming at evaluating the corresponding hybrid effect and pseudo-ductility of this innovative solution. A maximum hybrid effect of circa 45% was achieved, by combining unidirectional fabrics of high-modulus carbon with standard-modulus carbon. In four tested hybrid combinations, that included HM carbon as LS material, pseudo-ductile tensile responses with fragmentation and dispersed delamination of LS fibres were achieved. In these combinations, the mean 'yielding' stress varied between circa 730 and 1500 MPa and the pseudo-ductile strain between 0.4 and 2.0%.

At the present moment, although the documentation on hybrid solutions applied in the confinement of concrete columns is very scarce, the few studies already carried out allow assuming these as very promising [25-29]. Generally, experimental results have demonstrated that failure of hybrid composites does not lead to explosive failure of confined concrete. However, as emphasized in Ribeiro *et al*. [14], these attempts have been performed without a complete understanding of the material behaviour and the factors controlling the failure mode of the hybrid composites have not been clearly explained. Moreover, the pseudo-ductility concept, resulting from the fragmentation phenomena and controlled delamination of LS fibres, has not been explained either.

However, even with the above mentioned advantages of hybrid composites, it is important to be aware that, if the hybrid configuration is not carefully designed, the hybrid composite may not only break suddenly, but it may also show a strength lower than its constituents individually.

5.2. Analytical models for FRP-confined concrete

Over time a large number of models has been proposed to predict the behaviour of non-hybrid FRP-confined concrete [6]. These models can be classified into two categories [11]: (i) design-oriented models and (ii) analysis-oriented models.

Typically, design-oriented models are closed form equations developed through regression analyses from axial compression test results. These models allow to predict the ultimate conditions of confined concrete without capturing the confinement mechanisms [15]. In the work of Ozbakkaloglu *et al*. [6], an exhaustive critical review of 59 design-oriented models was performed. It was concluded that the models developed by Lam and Teng [11] and Tamuzs *et al*. [30] are the most accurate for predicting, respectively, the ultimate strength and the ultimate axial strain of confined concrete. The work of Ozbakkaloglu *et al*. [6] contemplated the prediction of 832 test results, leading to average errors of 11.8% for the first model and 26.3% for the second [7].

Analysis-oriented models are capable of establishing all the axial stress-strain behaviour of FRP-confined concrete, considering the interaction between the confining material and the concrete core. In these models, it is assumed that the axial stress and the axial strain of FRP-confined concrete are those of concrete actively confined with a constant confining pressure

(equal to that supplied by the FRP at every moment) [15]. This way, the accuracy of this type of models depends on two input parameters: (1) the lateral strain-to-axial strain relationship, and (2) the stress-strain base curves of the actively confined concrete [15].

Recently, Lim and Ozbakkaloglu [15] proposed a generic model to describe the lateral strain-to-axial strain relationship of confined concrete. This model emerged following an in-depth evaluation of previous models in the literature. The predictions of the proposed model are well above of previous models for both FRP-confined and actively confined concretes. The lateral strain-to-axial strain relationship of confined concrete is shown to be a function of the confining pressure, type of confining material and concrete strength. In [16], the same authors presented an analysis-oriented model to describe the stress-strain relationships of both actively confined concretes and FRP-confined concretes. It was proved that the model provides improved predictions compared to the previous models presented in the literature. For these reasons the models presented in [15] and [16] were used in present work. Since these models proved to be quite efficient, it is not expected to get improved predictions with other models.

5.2.1. Analysis-oriented model

Analysis-oriented models assume that, for a given confining pressure (f_l), an active confinement model for concrete can be used to evaluate the corresponding FRP-confined concrete compressive stress. This way, the complete stress-strain curve of FRP-confined concrete can be obtained by repeating the next incremental procedure until FRP failure:

i. Lateral strain (ε_l) is the input parameter to estimate the f_l of FRP-confined concrete (see section 5.2.1.1);
ii. ε_l and f_l are used to estimate the axial strain (ε_c) of FRP-confined concrete (see Section 5.2.1.2);
iii. Simultaneously, f_l is used to define the stress-strain model of actively confined concrete (see Section 5.2.1.3);
iv. The latter allows to determine the compressive stress (f_c) of FRP-confined concrete, assuming that it is equal to the compressive stress of actively confined concrete for the estimated ε_c.

5.2.1.1. Confining pressure modelling

Under concentric compression, the lateral tensile stress (or hoop tensile stress) from the FRP jacket in circular confined columns results in uniform f_l. The latter increases proportionally with the lateral expansion of concrete up to the failure of the system. Based on the deformation compatibility between the jacket and the concrete surface, the lateral confining pressure applied to concrete by the FRP jacket can be computed according to the following equation [6]:

$$f_l = \frac{2E_{frp}\varepsilon_l t_{frp}}{D} \tag{5.1}$$

where E_{frp} is the elastic modulus of FRP, t_{frp} is the total thickness of FRP and D is the diameter of the concrete specimen.

In the present chapter, the exact volume of the epoxy resin was not directly controlled during the application. For this reason, the total thickness of the FRP was computed considering only the thickness of the dry fabrics, according to the usual practice of the wet lay-up method and suggested by codes, e.g., [31].

In a unidirectional (UD) hybrid FRP submitted to uniaxial tension, the first damage mode is always the failure of the LS fibres. However, the other damage modes depend on the properties and configuration of the composite reinforcing materials [19]. The analytical approach proposed by Jalalvand *et al.* [13], validated in the scope of the present work in [14], considers that four different damage modes may occur after LS fibres failure: (i) premature HS failure, (ii) unstable delamination, (iii) LS layer fragmentation, and (iv) LS fragmentation and stable delamination. For each hybrid configuration, three stress levels can be computed [13]: (i) the stress at which the first crack in the LS material occurs, $\sigma@LF$, (ii) the stress at which delamination starts, $\sigma@del$, and (iii) the stress at which the HS material fails, $\sigma@HF$, in accordance with equations (5.2) to (5.4), respectively.

$$\sigma@LF = S_L \frac{\alpha\beta+1}{\alpha(\beta+1)} \tag{5.2}$$

$$\sigma@del = \frac{1}{1+\beta}\sqrt{\left(\frac{1+\alpha\beta}{\alpha\beta}\right)\left(\frac{2G_{IIC}E_H}{t_H}\right)} \tag{5.3}$$

$$\sigma@HF = \frac{1}{(1+\beta)}\frac{S_H}{K_t \sqrt[m_H]{V}} \tag{5.4}$$

where S_L is the reference strength of the LS material, α and β are the modulus and thickness ratios of the LS to HS fibre, G_{IIC} is the mode II interlaminar fracture toughness of the interface between LS layers and HS layers of the hybrid composite, E_H is the elastic modulus of the HS fibres, t_H is the half thickness of the HS fibre, m_H is the Weibull strength distribution modulus of the HS fibre, S_H is the reference strength of the HS material, K_t is the stress concentration factor in the high strain material, and V is the volume of the specimen (free length × width × total fibre layer thickness).

Knowing the magnitude of all three possible stresses allows assessing their order of occurrence and, consecutively, the identification of the damage modes, according to **Table 5.1**. The details of the adopted analytical approach are fully discussed in [13].

After the determination of the damage modes, it is possible to plot the tensile stress–strain curve of hybrid FRP using the characteristic points given in **Table 5.2**. In the latter, E_{sat} is the saturated modulus of the composite (according to equation (5.5)), ε_H is the failure strain of the HS fibres, and $\varepsilon_{@H\text{-}PS}$ is the strain in the composite at the post-saturation phase when the high strain material fails (according equation (5.6)) [13].

$$E_{sat} = E_H \frac{\alpha\beta+1}{(\beta+1)(1+\frac{11}{18}\alpha\beta)} \quad (5.5)$$

$$\varepsilon_{@H-PS} = \frac{\frac{\varepsilon_H}{K_t}}{m_H\sqrt{V}} - \frac{7}{18}\frac{S_L\beta}{E_H} \quad (5.6)$$

In the present chapter, the definitions of 'yield' stress and pseudo-ductile strain suggested by Jalalvand *et al.* [13] were considered. Thus, the 'yield' stress is the stress at the point where the response deviates from the initial linear elastic line, i.e., equal to σ@LF and the pseudo-ductile strain is defined as the extra strain between the final failure strain and the strain on the extrapolated initial slope line at the failure stress of the stress-strain diagram (see **Figure 5.1**).

In confining applications, FRP is essentially subjected to tensile stress. For this reason, in the present chapter, f_l of different hybrid combinations was computed assuming a modified equation (5.1):

$$f_l = \frac{2\sigma_{hybrid}t_{frp}}{D} \quad (5.7)$$

where σ_{hybrid} is the stress of hybrid FRP for a given tensile strain, assuming that the tensile strain is the same in all layers of the hybrid composites. The stress was computed according to the described stress-strain model of Jalalvand *et al.* [13]. The length and width of tensile specimens were assumed equal to L = 150 mm and W = 15 mm, respectively. The interlaminar toughness, G_{IIC}, for the different hybrid interfaces was estimated, assuming that for combinations with experimental pseudo-ductile behaviour, the fragmentation & dispersed delamination damage mode was analytically determined (see details in [14]). Weibull modulus of HS fibres was assumed constant and equal to the value used by Jalalvand *et al.* [13], m_H = 29.3. The value of the stress concentration factor was assumed constant, K_t = 0.97, for all of the specimens. This value is slightly lower than the one used by Jalalvand *et al.* [13] but it led to the best predictions.

Table 5.1 — Summary of different damage modes in function of stress level (adapted from [19]).

Damage mode	Stress level
Premature failure	$\sigma@HF \leq \sigma@LF \leq \sigma@del$
Catastrophic delamination	$\sigma@HF \leq \sigma@del \leq \sigma@LF$
	$\sigma@del \leq \sigma@HF \leq \sigma@LF$
	$\sigma@del \leq \sigma@LF \leq \sigma@HF$
Fragmentation	$\sigma@LF \leq \sigma@HF \leq \sigma@del$
Fragmentation & dispersed delamination	$\sigma@LF \leq \sigma@del \leq \sigma@HF$

Table 5.2 — Characteristic points of different damage processes on stress–strain graph (adapted from [13]).

Damage mode	Point 1	Point 2	Point 3	Point 4	Point 5
Premature failure	(0,0)	$(\varepsilon_L, \sigma@LF)$	--	--	--
Catastrophic delamination	(0,0)	$(\varepsilon_L, \sigma@LF)$	$(\varepsilon_L, \sigma@del)$	$\left(\frac{\sigma@del(1+\beta)}{E_H}, \sigma@del\right)$	$\left(\frac{\varepsilon_H}{K_t \sqrt[m_H]{V}}, \sigma@HF\right)$
Fragmentation	(0,0)	$(\varepsilon_L, \sigma@LF)$	$\left(\frac{\sigma@LF}{E_{sat}}, \sigma@LF\right)$	$(\varepsilon_{H-PS}, \sigma@HF)$	--
Fragmentation & dispersed delamination	(0,0)	$(\varepsilon_L, \sigma@LF)$	$\left(\frac{\sigma@LF}{E_{sat}}, \sigma@LF\right)$	$\left(\frac{\sigma@del(1+\beta)}{E_H}, \sigma@del\right)$	$\left(\frac{\varepsilon_H}{K_t \sqrt[m_H]{V}}, \sigma@HF\right)$

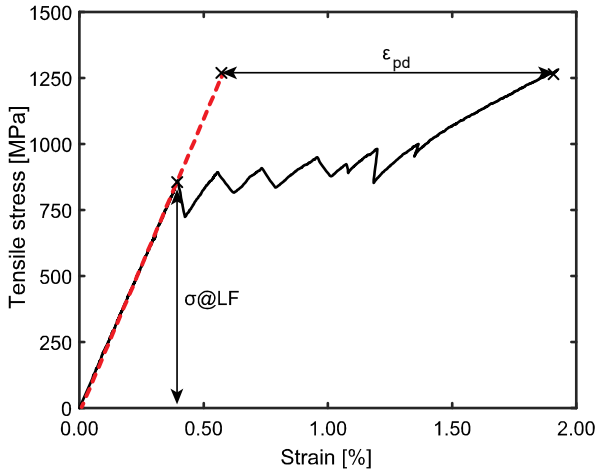

Figure 5.1 — Illustration of nonlinear pseudo-ductile tensile behaviour of hybrid composite and definition of 'yield' stress and pseudo-ductile strain.

5.2.1.2. Lateral strain-to-axial strain relationship

The prediction of ε_c based on f_l of the FRP-confined concrete is fundamental to estimate f_c. According to Lim and Ozbakkaloglu [15], lateral strains of actively confined and FRP-confined concrete match, for the same f_l. The use of FRP as passive jacket means that a specific f_l is reached for a certain ε_c. This assumption allows developing a model to describe the dilation behaviour of confined concrete, i.e., to describe the evolution of ε_c with ε_l, see equation (5.8) [15]:

$$\varepsilon_c = \frac{\varepsilon_l}{\nu_i\left[1+\left(\frac{\varepsilon_l}{\nu_i \varepsilon_{c0}}\right)^n\right]^{1/n}} + 0.04{\varepsilon_l}^{0.7}\left[1+21\left(\frac{f_l}{f_{c0}}\right)^{0.8}\right] \tag{5.8}$$

where ν_i is the initial Poisson's ratio of concrete ($\varepsilon_l/\varepsilon_c$) [32]:

$$\nu_i = 8\times10^{-6}{f_{c0}}^2 + 0.0002 f_{c0} + 0.138 \tag{5.9}$$

ε_{c0} is the axial strain at the peak stress (f_{c0}) of the unconfined concrete:

$$\varepsilon_{c0} = \left(-0.067{f_{c0}}^2 + 29.9f_{c0} + 1053\right) \times 10^{-6} \quad (5.10)$$

n is the curve shape parameter:

$$n = 1 + 0.03f_{c0} \quad (5.11)$$

This way, the trend of the lateral strain-to-axial strain relationship of confined concrete is shown to be a function of f_l, type of confining material, and concrete strength. The model described by equation (5.8) is adopted in the present study.

5.2.1.3. Stress-strain model

The stress-strain model for active confined concrete comprises both an ascending and a descending branch. The former is computed according to equation (5.12), proposed by Popovics [33], and the latter is computed according to equation (5.13), proposed by Lim and Ozbakkaloglu [16]:

$$f_c = \frac{f_{cc}^* \left(\varepsilon_c / \varepsilon_{cc}^*\right) r}{r - 1 + \left(\varepsilon_c / \varepsilon_{cc}^*\right)^r}, \text{ if } 0 \le \varepsilon_c \le \varepsilon_{cc}^* \quad (5.12)$$

$$f_c = f_{cc}^* - \frac{f_{cc}^* - f_{c,res}}{1 + \left(\frac{\varepsilon_c - \varepsilon_{cc}^*}{\varepsilon_{c,i} - \varepsilon_{cc}^*}\right)^{-2}}, \text{ if } \varepsilon_c > \varepsilon_{cc}^* \quad (5.13)$$

where f^*_{cc} and ε^*_{cc} are the peak stress and the peak strain of actively confined concrete [15, 34], *r* is the concrete brittleness [35], $f_{c,res}$ is the residual stress [16], and $\varepsilon_{c,i}$ is the axial strain corresponding to the inflection point of the descending branch of stress-strain curve [16]:

$$f_{cc}^* = f_{c0} + 5.2f_{c0}^{0.91}\left(\frac{f_l}{f_{c0}}\right)^a \text{ where } a = {f_{c0}}^{-0.06} \quad (5.14)$$

$$\varepsilon_{cc}^* = \varepsilon_{c0} + 0.045\left(\frac{f_l}{f_{c0}}\right)^{1.15} \quad (5.15)$$

$$r = \frac{E_c}{E_c - f_{cc}^*/\varepsilon_{cc}^*} \quad (5.16)$$

$$f_{c,res} = 1.6f_{cc}^*\left(\frac{{f_l^*}^{0.24}}{{f_{c0}}^{0.32}}\right) \text{ and } f_{c,res} \le f_{cc}^* - 0.15f_{c0} \quad (5.17)$$

$$\varepsilon_{c,i} = 2.8\varepsilon_{cc}^*\left(\frac{f_{c,res}}{f_{cc}^*}\right){f_{c0}}^{-0.12} + 10\varepsilon_{cc}^*\left(1 - \frac{f_{c,res}}{f_{cc}^*}\right){f_{c0}}^{-0.47} \quad (5.18)$$

In equation (5.16), E_c is the elastic modulus of plain concrete [16]:

$$E_c = 4400\sqrt{f_{c0}} \quad (5.19)$$

5.2.2. Design-oriented models

In the present chapter, ultimate condition models were developed to predict the peak axial stress (f_{cc}) and the peak axial strain (ε_{cc}) of hybrid FRP-confined concrete. These are simple linear models based on the general form of the expressions proposed by Richart *et al.* [36], as usual in the vast majority of works dedicated to non-hybrid FRP-confined concrete [6], for the calculation of ultimate conditions of confined concrete:

$$\frac{f_{cc}}{f_{c0}} = c_1 + k_1\left(\frac{f_{lu}}{f_{c0}}\right) \tag{5.20}$$

$$\frac{\varepsilon_{cc}}{\varepsilon_{c0}} = c_2 + k_2\left(\frac{f_{lu}}{f_{c0}}\right) \tag{5.21}$$

where c_1 and c_2 are calibration constants and k_1 and k_2 are strength and strain enhancement coefficients for FRP-confined concrete, respectively.

The tensile strength of all hybrid combinations was predicted according to the model of Jalalvand *et al.* [13], described in Section 5.2.1.1, and to bilinear ROM:

$$\sigma_{hybrid} = \begin{cases} V_L S_L + V_H E_H \varepsilon_L;\ V_H < V_{crit} \\ V_H S_H;\ V_H > V_{crit} \end{cases} \tag{5.22}$$

where σ_{hybrid} is the tensile strength of hybrid composites, ε_L is the failure strain of the LS fibre, V_L and V_H is the volume of low and high strain material.

From equation (22), one realizes that if V_H is lower than the critical value, V_{crit}, the hybrid composite will fail prematurely. On the contrary, if V_H is higher than V_{crit}, the hybrid composite will keep its integrity up to the failure of the HS fibres. V_{crit} was calculated by equating the two branches of equation (5.23), taking into account that $V_L + V_H = 1$, i.e., V_L is equal to $1-V_H$:

$$V_{crit} = \frac{S_L}{S_L + S_H - E_H \varepsilon_L} \tag{5.23}$$

The properties of 1 layer non-hybrid composites were used as input variables for both models (Jalalvand *et al.* [13] and bilinear ROM [14]).

Analytical tensile strength values were used to compute the ultimate confining pressure, f_{lu}, of different combinations, according to equation (5.7). This way, it was possible to compute the confinement ratio (f_{lu}/f_{c0}) and to compare the evolution of this ratio with both the strength enhancement (f_{cc}/f_{c0}) and the strain enhancement ($\varepsilon_{cc}/\varepsilon_{c0}$), resulting in the determination of c_1, c_2, k_1 and k_2.

5.3. Experimental program

5.3.1. Materials

5.3.1.1. Concrete

A ready-mix concrete, prepared by an external concrete company, was used in the present chapter. The maximum aggregate size was 12.5 mm. The experimental campaign of the confined concrete specimens described herein (see details in Section 5.3.2) was conducted in 15 consecutives working days. During this time, the concrete age varied between 294 and 315 days. Until the testing date, all specimens were kept in standard laboratory conditions (temperature around 20 ºC, relative humidity around 50%). In the end of the experimental campaign, 3 plain cylindrical concrete specimens, with a diameter of 150 mm and a height of 300 mm, were tested. The mean values of elastic modulus, according to [37], and compressive strength, according to [38], were 30.29 GPa (CoV = 6.57%) and 33.49 MPa (CoV = 1.33%), respectively.

5.3.1.2. FRP constituents (unidirectional fabrics and epoxy resin)

Four types of dry UD fabrics, with a similar areal mass of 400 g/m^2, were used in the present study: (i) UD high-modulus (HM) carbon (S&P C-Sheet 640), (ii) standard-modulus (ST) carbon (S&P C-Sheet 240), (iii) E-glass (S&P G-sheet E 90/10) and (iv) basalt (Dalla Betta Group U400B-40-50-03), denoted as “CHM”, “C”, “G” and “B”, respectively. In **Table 5.3** the density, areal mass, fibre layer thickness (areal mass density divided by the volumetric mass density), as reported by the manufacture, and the basic tensile properties of the mentioned materials assessed experimentally are presented.

Table 5.3 — Properties of the dry fabrics, fibres and cured composite materials.

Material ID	**Properties of the dry fabric**			**Properties of the fibres (tested according to ASTM D3379)**						**Properties of composites [14]***		
	Density [g/m^3]	**Areal mass** [g/m^2]	**Fibre layer thickness** [mm/layer]	**N. of samples**	**Fibre diameter** [μm] (CoV [%])	**Elastic modulus** [GPa] (CoV [%])	**Tensile strength** [MPa] (CoV [%])	**Strain at the failure** [%] (CoV [%])	**Series ID****	**Elastic modulus** [GPa] (CoV [%])	**Tensile strength** [MPa] (CoV [%])	**Strain at the failure** [%] (CoV [%])
Basalt (B)	2.67	420	0.157	50	18.14 (3.56)	61.41 (31.14)	1886.70 (40.79)	3.10 (27.73)	1B	102.5 (15.46)	2244.2 (20.17)	2.46 (10.61)
									3B	92.6 (13.55)	1974.6 (15.76)	2.40 (8.26)
E-glass (G)	2.60	400	0.154	50	14.98 (16.25)	76.92 (27.97)	2662.06 (33.88)	3.72 (20.45)	1G	81.6 (7.39)	1671.2 (8.59)	2.31 (3.78)
									3G	80.6 (10.10)	1254.8 (15.05)	2.00 (13.95)
ST carbon (C)	1.79	400	0.223	36	7.88 (5.15)	213.95 (43.36)	3920.67 (39.37)	1.38 (17.37)	1C	231.3 (12.50)	2565.9 (10.18)	1.09 (8.81)
									3C	227.6 (5.80)	2363.2 (7.44)	1.02 (6.02)
HM carbon (CHM)	2.10	400	0.190	26	11.03 (6.66)	558.07 (24.67)	2934.24 (19.16)	0.53 (18.99)	1CHM	624.1 (11.13)	1749.4 (24.39)	0.27 (19.61)
									3CHM	588.2 (3.97)	1073.9 (18.27)	0.18 (15.84)

Notes: *The tensile properties were computed considering only the thickness of the dry fabrics, according the recommendation suggested in the guidelines [31];** the number before letters in series ID shows the number of layers.

The tensile properties of the fibres were determined according to ASTM D3379-75 [39]. For each dry fabric, a large number of single fibres (see the details in **Table 5.3**) were randomly taken from the dry fabrics and tested in tension. The initial idea was to test 50 fibres of each fabric. However, during the preparation of tests, it was impossible to prevent the breaking of some fibres. The tests were carried out in a Hounsfield H100KS universal testing machine with a maximum load cell capacity of 2.5 N (with an accuracy of ±0.2% of applied force across load cell force range). Fibres were individually assembled in the tensile jig by means of a work template with a fixed gauge length of 20 mm. Fibre ends were glued to the work template by an ethyl cyanoacrylate-based adhesive. Then the tab ends were gripped in the jaws of the machine. The work template was cut across, so that just the fibre was fixed as a continuous length within the jig, before starting the tensile tests. The measurements were performed at a rate of 1.5 mm/min, until breakage occurred. For each fibre, records of applied load against extension were taken, and using an average mean diameter, determined through the analysis of microscopy images of fibres obtained with Scanning Electronic Microscopy (SEM), the data were converted to stress against strain.

In **Table 5.3** is also presented the tensile proprieties of non-hybrid composites. An epoxy-based resin (S&P Resin Epoxy 55) was used as matrix for laminating the studied composites. According to the supplier, this epoxy resin has the following main properties [40]: (i) tensile strength of 35.8 MPa; (ii) strain failure of 2.3%; and (iii) elastic modulus of 2.6 GPa. In **Table 5.3** it is even possible to observe that elastic modulus of single fibres is lower than the elastic modulus of cured composites. This is due to the fact that in case of composites the tensile properties were evaluated ignoring the contribution of the resin, according to the usual practice of the wet lay-up method and the guidelines [31]. This means that tensile strength was computed considering only the dry fabric thickness which conducted to overestimation of the tensile strength and, consequently, large elastic modulus. Differences of experimental results related to the number layers are due to a size effect, i.e., the higher probability of finding a cluster of weaker fibre in a larger volume of material [21].

5.3.2. Test specimens

In the present chapter, a total of 63 cylindrical specimens, comprising 48 hybrid FRP-confined specimens, 12 non-hybrid FRP-confined specimens and 3 unconfined specimens (referred to in Section 5.3.1.1), were prepared and tested under monotonic uniaxial compression. Each specimen was 150 mm in diameter and 300 mm in height. The experimental variables included (i) the LS fibres relative volume (vol%) and (ii) the type of FRP of jacket.

All possible symmetrical hybrid FRP combinations up to 5 layers were applied as confining material. Whenever possible, LS layers were sandwiched between HS layers. In total, 16 hybrid series were considered: 10 combinations with 3 reinforcing material layers and 6 combinations with 5 reinforcing material layers. Each series was composed of 3 specimens of confined concrete. The combinations of 3 symmetrical layers allowed to analyse the following

approximate levels of LS fibres vol%: 0%, 33%, 66% and 100%. In addition, combinations with 5 layers allowed to analyse the following approximate levels of LS fibres vol%: 20%, 40% and 60%. It should be noted that specimens with 5 layers were only tested on 2 hybrid combinations: HM carbon/glass and ST carbon/glass. In addition to hybrid series, 4 series of non-hybrid composites (1 for each reinforcing material) were produced with 3 layers. All the specimens involved in the experimental campaign are resumed in **Table 5.4**. In the present chapter, in case of composite materials nomenclature, numbers placed before letters are used for indicating number of layers. The sequence according to which these letters appear indicate the stacking sequence of the reinforcing materials. The UD fabrics had slightly different thicknesses and, for this reason, the relative volume of LS fibres (*Vol% LS*) was computed in the next sections, according to Equation (5.24):

$$Vol\%\ LS = \frac{t_L}{t_L + t_H} \times 100 \tag{5.24}$$

where t_L is the half thickness of the LS layers and t_H is the half thickness of the HS layers.

Table 5.4 — Summary of tested compression specimens.

Jacketing type	Designation	Non corrected layer ratio (LS/HS fibres) [%]	Stacking sequence	Jacketing material combinations	N. of tests per type of stacking sequence
Non-hybrid	--	100/0	□□□	G, B, CHM, C	12
Hybrid	1LS/1HS/1LS	66/33	□■□	C/B, CHM/B, CHM/C, C/G, CHM/G	15
	1HS/3LS/1HS	60/40	■□□□■	C/G, CHM/G	6
	1HS/1LS/1HS/1LS/1HS	40/60	■□■□■	C/G, CHM/G	6
	1HS/1LS/1HS	33/66	■□■	C/B, CHM/B, CHM/C, C/G, CHM/G	15
	2HS/1LS/2HS	20/80	■■□■■	C/G, CHM/G	6
None	Unconfined	--	--	--	9

Notes: ■ – HS fibres layer; □ – LS fibres layer.

5.3.3. Specimen manufacturing and test setup

In order to ensure concentric loading and distributed stress throughout the cross-section during the test, both ends of each cylinder were capped. Furthermore, the entire lateral surface of each confined specimen was roughened with an angle grinder and then cleaned with a compressed air blower in order to improve bonding between the jacket and the concrete.

Before the application of the jacket, dry fabrics pieces with 620 mm in fibre direction and 300 mm in perpendicular direction were cut. The total length allowed an overlap length of 150 mm, this value being suggested and adopted by other authors [10, 41, 42] and it has been proved to prevent FRP debonding failure during tests. The FRP jacket was manufactured by wet lay-up method, following the best practices suggested in [31], according to the following protocol: (i) application of a layer of epoxy resin over the dry concrete surface with a brush; (ii) saturation of the fabric layer with epoxy resin; (iii) application of an FRP layer over the epoxy resin wetted concrete surface, adjusting it manually; (iv) pressure application by means of a ribbed rigid roller, in order to expel both the epoxy resin excess and air in the composite, and also stretching the latter; (v) repetition of steps ii to iv for subsequent layers, avoiding coincidence between overlap zones of different layers. All the specimens were then cured at room laboratory for 230 days.

Axial deformations of the specimens were measured with 3 linear variable displacement transducers (LVDTs), which were positioned, equally spaced around the specimen, between the steel plates of the universal testing machine (UTM), with 2000 kN capacity, as shown in **Figure 5.2**. In this case, the measured displacements using full-height LVDTs were amplified because deformations of the testing machine parts and closure of the gaps in the setup were considered. For this reason, the results of three mid-height LVDTs measurements applied directly on plain concrete specimens, using an aluminium ring, were considered to correct the full-height LVDTs measurements of all specimens, as also adopted in [42]. As illustrated in **Figure 5.3**, the lateral strains were measured by 3 or 5 unidirectional 5 mm gauge length strain gauges (one for each layer of fabric). These were bonded to the FRP equally spaced along the circumference.

The specimens were tested under axial compression using a UTM at room temperature. The loading force was applied to the specimen at a displacement rate of 1.20 mm/min. up to failure.

5.4. Results and discussion

5.4.1. Non-hybrid FRP-confined concrete

5.4.1.1. Ultimate conditions

The summary of the test results of each series of non-hybrid FRP-confined concrete are shown in **Table 5.5**, which includes the mean peak axial stress (f_{cc}), the peak axial strain (ε_{cc}), strength enhancement (f_{cc}/f_{c0}), the strain enhancement ($\varepsilon_{cc}/\varepsilon_{c0}$), and the FRP strain reduction factor ($k_{\varepsilon,frp}$). It should be noted that the unconfined concrete strain (ε_{c0}) was computed according to equation (5.10) and $k_{\varepsilon,frp}$ was computed according to equation (5.25):

$$k_{\varepsilon,frp} = \frac{\varepsilon_{l,rup}}{\varepsilon_{frp}} \tag{5.25}$$

where $\varepsilon_{l,rup}$ is the FRP lateral strain at failure, assessed in the test of cylinders, and ε_{frp} is the FRP strain at failure, assessed with tensile tests. The latter were previously presented, in **Table 5.3**, for composites with 3 layers. The $\varepsilon_{l,rup}$ is the mean value of the maximum lateral strain values of each series.

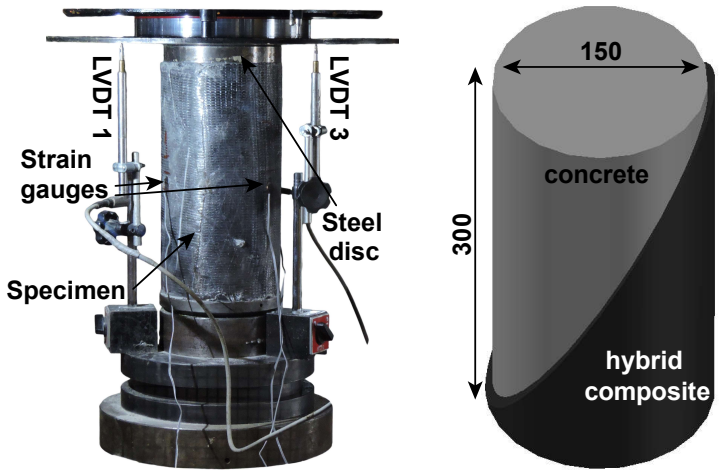

Figure 5.2 — Axial compressive test: (a) illustration of the test and (b) geometry of specimen (dimensions in mm).

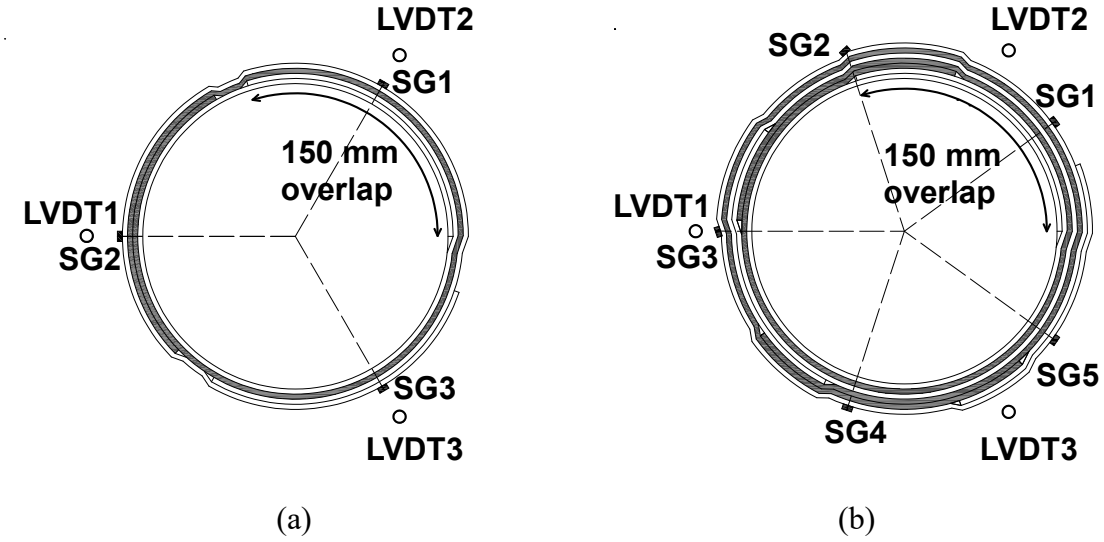

Figure 5.3 — Layers, LVDT and strain gauge arrangement: (a) hybrid jackets with 3 layers and (b) hybrid jackets with 5 layers. Note: different colours in the illustrated hybrid jackets are a schematic representation of a possible stacking sequence of two different reinforcing materials.

Table 5.5 — Ultimate conditions of non-hybrid FRP-confined concrete

Series ID *	f_{cc} [MPa] (CoV [%])	f_{cc}/f_{c0}	ε_{cc} [%] (CoV [%])	$\varepsilon_{cc}/\varepsilon_{c0}$ **	$\varepsilon_{l,rup}$ [%] (CoV [%])	$k_{\varepsilon,frp}$
3B	64.80 (3.48)	1.93	1.09 (15.87)	5.45	1.79 (16.92)	0.75
3G	64.67 (4.21)	1.93	1.48 (30.89)	7.40	1.88 (15.90)	0.94
3C	89.02 (7.03)	2.65	1.40 (27.48)	7.00	0.98 (35.98)	0.96
3CHM	54.89 (12.91)	1.64	0.38 (39.84)	1.90	0.13 (17.17)	0.72

Note: * the number before letters in series ID shows the number of layers; ** it was assumed ε_{c0} = 0.0020 (according equation (5.10)).

Comparing **Table 5.3** and **Table 5.5**, it is possible to observe that, in general, larger tensile strengths of FRP materials imply larger f_{cc} and $\varepsilon_{l,rup}$. However, this tendency is affected by the reduction of efficiency relative to the strain at failure of FRP applied in the jacketing, characterised by the reduction factor. The computed reductions factors varied between 0.72, for the 3CHM series, and 0.96, for the 3C series. Although a reduction of strain at failure of FRP materials has been observed in all cases, apparently the basalt and HM carbon composites were the most affected. Lim and Ozbakkaloglu [8] indicate that reductions factors vary with the elastic modulus of FRP composite, but this tendency was not evidenced in the present chapter. Similar reductions factors were obtained for FRP composites with very different elastic modulus (e.g. glass and ST carbon). The reduction factor is discussed for hybrid jacketing in Section 5.4.2.1. Relatively to $\varepsilon_{cc,}$ no evident tendency was observed.

In **Figure 5.4**, the dispersion of the obtained results and their mean values are plotted. Very similar results were obtained with glass and basalt combinations. The *t* statistical test (t-test) was adopted to assess whether the mean values of these two materials are statistically different from each other. The results are exposed using the *p*-value. This value varies between 0 and 1 and it is the smallest level of significance that would lead to rejection of the null hypothesis (in the present case, the null hypothesis is that the mean value of glass equals the mean value of basalt). In turn, the level of significance is the probability of rejecting the null hypothesis when it is true. The computed *p*-values for f_{cc}, ε_{cc}, and $\varepsilon_{l,rup}$ were 0.952, 0.386, and 0.230, respectively. Given the large computed *p*-values (above 0.05), it can be stated that the null hypothesis cannot be rejected, i.e., glass and basalt lead to identical results.

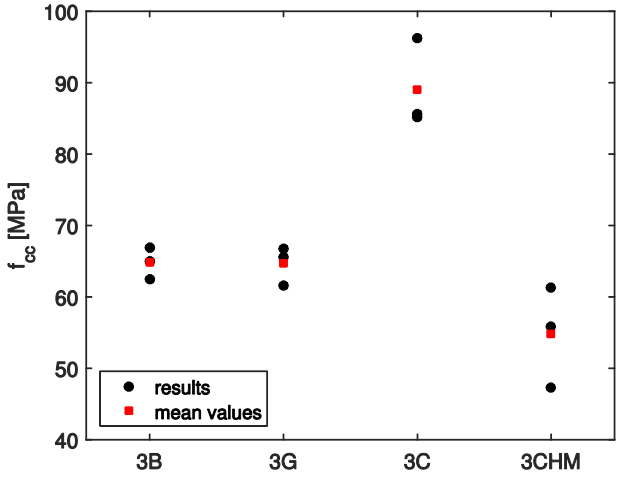

(a)

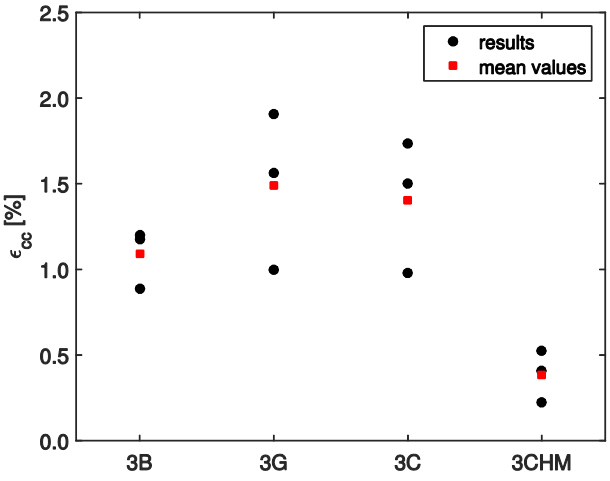

(b)

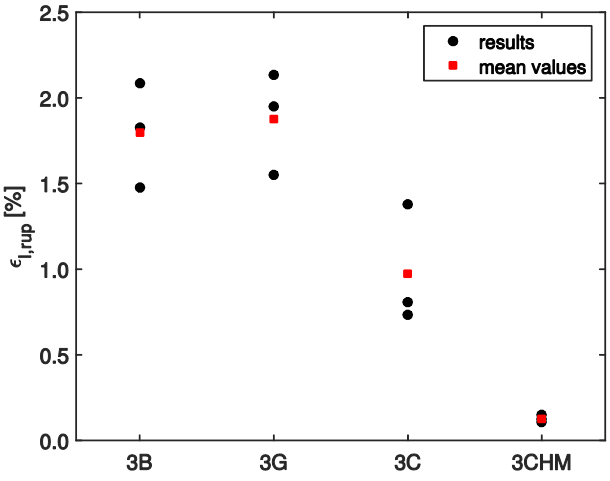

(c)

Figure 5.4 — Scatter diagrams and mean values of the non-hybrid composites confined concrete: (a) ultimate axial compressive stress; (b) ultimate axial strain and (c) hoop rupture strain of FRP

5.4.1.2. Dilation behaviour and axial stress-strain behaviour

The analysis-oriented model of Lim and Ozbakkaloglu [15, 16] was developed to predict the compressive stress-strain curve of non-hybrid FRP-confined concrete. The aim of the work described in this section was to validate (or not) the developed approach for the set of materials and fabrication method used in the present chapter.

Results of non-hybrid FRP with 3 layers, presented in **Table 5.3**, were used as input variables to compute f_l, according to equation (5.1). The lateral strain at failure of the different material combinations was assumed as the mean of the corresponding experimental values. The diameter of all specimens was assumed as D = 150 mm and f_{c0} = 33.49 MPa was used as input variable in equations (5.8) to (5.19).

In **Figure 5.5** and **Figure 5.6** the lateral strain-axial strain curves (dilation behaviour) and the compressive stress-strain curves of non-hybrid FRP-confined concrete are presented, respectively. In the specimen designation, the last number (i.e., 1, 2 or 3) was used to make the distinction between the three identical specimens.

The analysis of the lateral strain-axial strain curves show that these typically present an initial slope, in agreement with initial Poisson's ratio of concrete (equation (5.18)). Moreover, this initial phase is similar for all combinations. After the compressive stress-strain peak of plain concrete (f_{c0}, ε_{c0}), microcracking initiation and propagation occurs and leads to a rapid increase of the lateral strain [15]. The different applied confining materials induce different confining pressures leading to different trends after stress-strain peak of the plain concrete (see **Figure 5.6**). The development of the compressive stress-strain curves follows approximately a bilinear law, where the slope of the first branch depends primarily on the properties of plain concrete, whereas the slope of the second (hardening branch) is controlled by the confining pressures induced by the jacket. It can be observed that the higher the FRP's elastic modulus, the higher the slope of the hardening branch. It is evident that, when HM carbon is used in jacketing, the highest slope of the hardening branch is achieved (**Figure 5.6**(d)). However, the low lateral strain efficiency of this material makes it the worst to use in the non-hybrid jacketing, since the lowest f_{cc} and ε_{cc} are achieved with this combination. On the other hand, the highest f_{cc} and ε_{cc} are achieved with ST carbon jacketing (**Figure 5.6**(c)).

The typical failure modes of non-hybrid FRP-confined specimens tested are illustrated in **Figure 5.7**. It is possible to observe from the figure, that all specimens failed by the FRP jacket rupture. All the failures occurred in an abrupt way, with a rapid release of energy characterized by the projection of small concrete fragments. The failure occurred approximately at mid-height of the specimens, except in the case of HM carbon jackets in which a full height failure occurred.

Analytical curves, obtained with the referred to analysis-oriented model, are also plotted in **Figure 5.5** and **Figure 5.6** to allow the comparison with the corresponding experimental curves. To generate these curves an infinite lateral strain was assumed as input of the model. To plot the latter, experimental mean axial strain was defined as end criterion.

The performance of the analysis-oriented model was quantified comparing the predictions of the f_{cc} and the mean lateral strain ($\varepsilon_{l,rup\ -\ mean}$) at the peak stress (i.e. the mean strain value at the failure measured with the set of strain gauges) with respective experimental results. The comparison is presented in **Table 5.6**. For f_{cc} predictions, the relative error varied between -0.9% and 6.0%. This error's magnitude is acceptable and is actually lower than mean error presented by the authors of the model (|10.5%|±0.8%). For $\varepsilon_{l,rup\ -\ mean}$ predictions, the error varied between -27.0% and 24.9%. This error magnitude is quite high. However, considering that there is a great dispersion of $\varepsilon_{l,rup\ -\ mean}$ results, it can be stated that the model was able to accurately predict the latter.

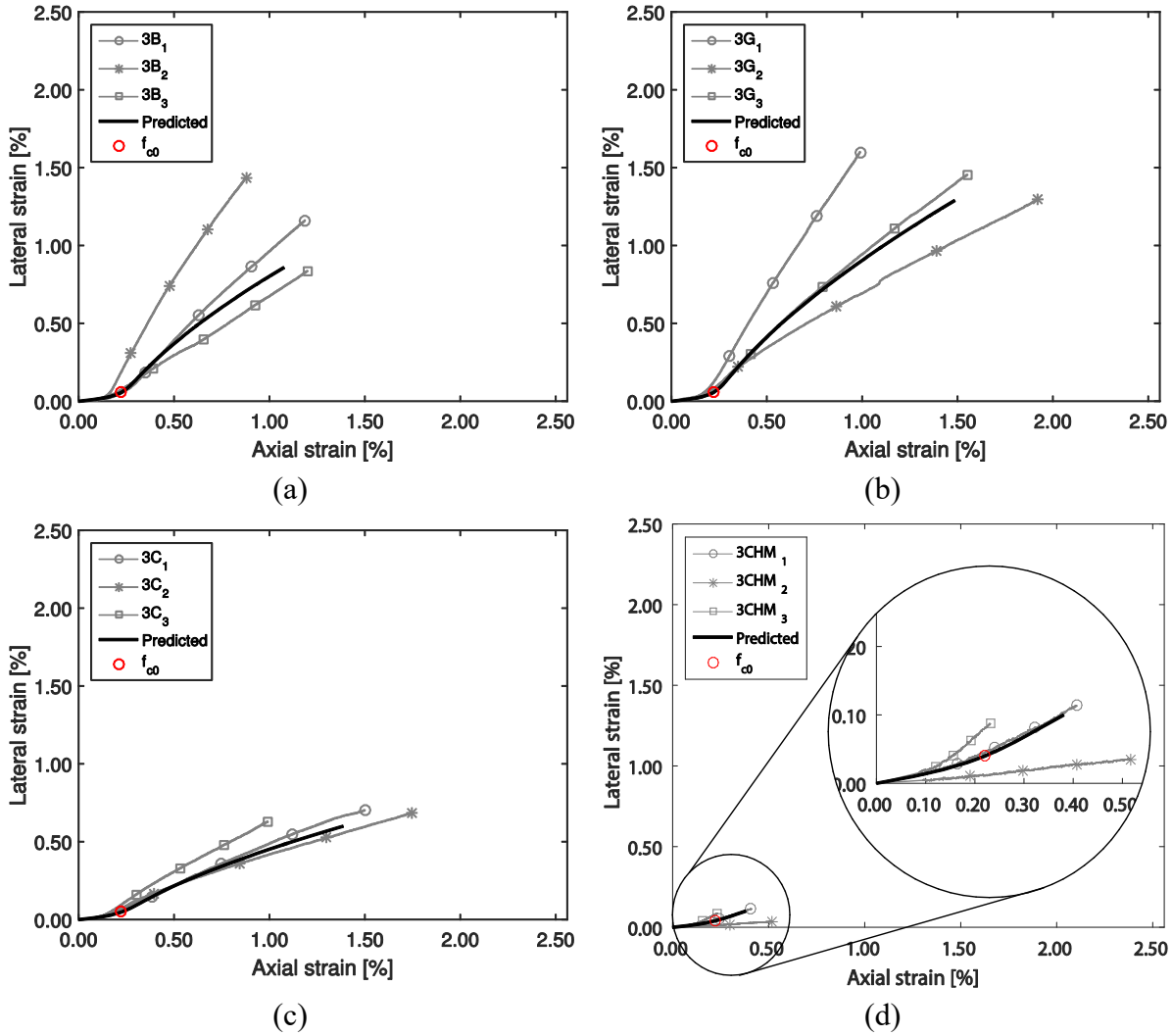

Figure 5.5 — Lateral strain-axial strain curves: (a) basalt; (b) glass; (c) ST carbon; (d) HM carbon composite confined concrete.

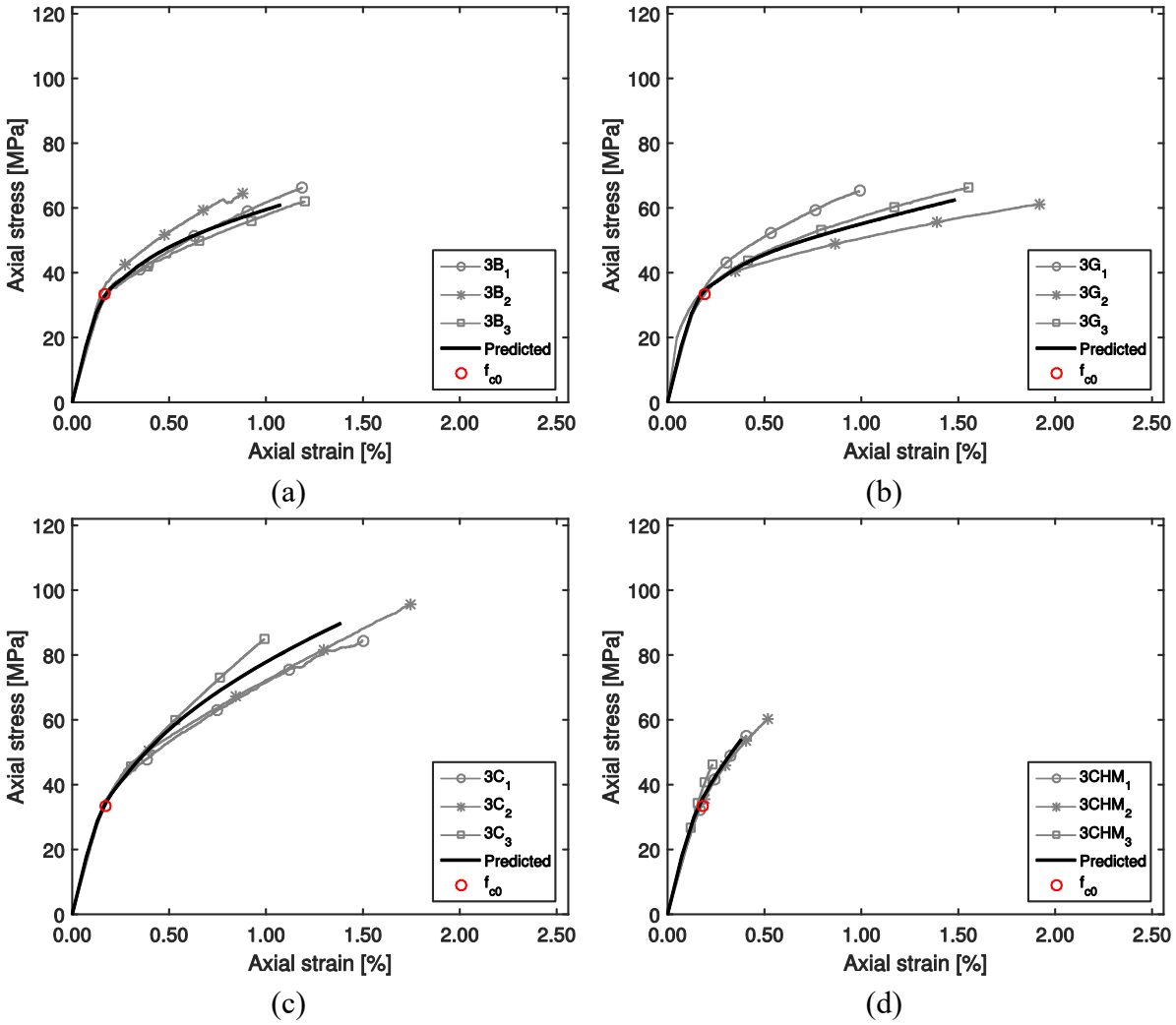

Figure 5.6 — Axial stress-strain curves: (a) basalt; (b) glass; (c) ST carbon; (d) HM carbon composite confined concrete.

Figure 5.7 — Failure modes of non-hybrid FRP-confined concrete: (a) basalt; (b) glass; (c) ST carbon and (d) HM carbon.

Table 5.6 — Comparison of analysis-oriented model predictions with non-hybrid FRP-confined concrete test results

Series ID	f_{cc}			$\varepsilon_{l,rup\ -\ mean}$		
	Exp. [MPa] (CoV [%])	**Prediction** [MPa]	**Rel. error** [%]	**Exp.** [MPa] (CoV [%])	**Prediction** [MPa]	**Rel. error** [%]
3B	64.80 (3.48)	60.93	6.0	1.14 (26.28)	0.86	24.9
3G	64.67 (4.21)	62.52	3.3	1.45 (10.46)	1.29	11.1
3C	89.02 (7.03)	89.79	-0.9	0.67 (5.95)	0.60	10.7
3CHM	54.89 (12.91)	53.95	-1.7	0.08 (50.80)	0.10	-27.0

5.4.2. Hybrid FRP-confined concrete

5.4.2.1. Ultimate conditions

Table 5.7 presents the elastic modulus, tensile strength, and failure strain of LS fibres of cured hybrid composite materials; the peak axial stress (f_{cc}), the strength enhancement (f_{cc}/f_{c0}), the peak axial strain (ε_{cc}), the strain enhancement ($\varepsilon_{cc}/\varepsilon_{c0}$), the lateral failure strain of LS fibres, the lateral strain of HS fibres (for the cases that composites keep their integrity beyond the LS fibres failure and the strain reduction factor of LS fibres of hybrid FRP-confined concrete.

As expected, from **Table 5.7**, it can be observed that, in similar combinations, the replacement of ST carbon by HM carbon resulted in significate reductions of f_{cc} and ε_{cc} because, as it is shown in **Table 5.3**, HM series tensile results are lower than ST series results. Analysing the strength enhancement (f_{cc}/f_{c0}) of combinations of ST carbon with glass and HM carbon with glass, it is possible to note that the results varied between 2.44 and 3.57, for the first case, and 1.63 and 2.40, for the second case. Relatively to strain enhancement ($\varepsilon_{cc}/\varepsilon_{c0}$), it is possible to verify that similar observation can be done, the results varied between 6.15 and 10.65 for the combinations of ST carbon with glass, and between 1.95 and 6.10 for the combination of HM carbon with glass. In this way, the use of HM carbon conducts to the worst f_{cc} and $\varepsilon_{cc.}$ However, the use of HM carbon in some hybrid combinations allows to avoid premature failures of the composite. This happens because HM carbon has a low tensile strength and, for this reason, the stress level at which the first failure in HM carbon material occurs is not sufficient to release significant amounts of energy that lead to catastrophic delamination or high strain material failure [43]. Catastrophic failures of the composite were avoided in five combinations (2G/1CHM/2G, 1G/1CHM/1G, 1G/1CHM/1G/1CHM/1G, 1B/1CHM/1B and 1C/1CHM/1C) exposed in **Table 5.7**. In these cases it was possible to present two values: (i) the lateral failure strain of LS fibres and (ii) the lateral failure strain of HS fibres. This is according to the tensile test results presented in [14], in which catastrophic failures were avoided exactly in the same combinations. A detailed discussion of these results is presented in Section 5.4.2.3.

Table 5.7 — Properties of cured hybrid composite materials and ultimate conditions of hybrid FRP-confined concrete

Material combination	Series ID*	Volume of LS fibres [%]	Cured hybrid composite properties [14]			Ultimate conditions of non-hybrid FRP-confined concrete						
			Elastic modulus [GPa] (CoV [%])	Tensile strength [MPa] (CoV [%])	Failure strain of LS fibres [%] (CoV [%])	f_{cc} [MPa] (CoV [%])	f_{cc}/f_{c0}	ε_{cc} [%] (CoV [%])	$\varepsilon_{cc}/\varepsilon_{c0}$**	Lateral failure strain of LS fibres [%] (CoV [%])	Lateral failure strain of HS fibres [%] (CoV [%])	k_ε at failure of LS fibres
C/B	1C/1B/1C	74.0	218.4 (2.84)	2191.4 (7.28)	0.99 (5.76)	87.4 (--)	2.61	1.41 (--)	7.05	0.81 (--)	--	0.82
	1B/1C/1B	41.5	152.5 (5.93)	1950.2 (7.51)	1.28 (3.46)	73.2 (3.01)	2.19	0.91 (13.74)	4.55	1.03 (7.54)	--	0.80
CHM/B	1CHM/1B/1CHM	70.8	474.1 (2.25)	1150.0 (14.10)	0.24 (11.19)	54.2 (8.59)	1.62	0.51 (17.63)	2.55	0.19 (25.34)		0.79
	1B/1CHM/1B	37.7	297.4 (9.29)	1328.0 (10.74)	0.36 (5.77)	62.9 (5.46)	1.88	0.99 (16.71)	4.95	0.39 (7.05)	1.17 (34.9)	1.00
CHM/C	1CHM/1C/1CHM	63.0	489.6 (7.39)	1352.5 (5.10)	0.27 (5.55)	59.7 (7.76)	1.78	0.48 (7.20)	2.40	0.19 (17.86)	--	0.70
	1C/1CHM/1C	29.5	368.8 (6.43)	1937.5 (6.79)	0.39 (3.59)	79.9 (5.01)	2.39	0.94 (13.95)	4.70	0.46 (28.74)	0.61 (22.66)	1.18
C/G	1C/1G/1C	74.3	201.7 (9.63)	2176.9 (8.55)	1.04 (1.92)	81.7 (1.48)	2.44	1.23 (6.00)	6.15	0.86 (22.99)	--	0.83
	1G/3C/1G	68.5	202.4 (2.64)	2216.0 (8.77)	1.08 (6.26)	119.4 (2.66)	3.57	2.13 (19.54)	10.65	1.19 (1.35)	--	1.09
	1G/1C/1G/1C/1G	49.1	148.9 (11.75)	1776.3 (10.55)	1.19 (3.68)	108.3 (7.53)	3.23	1.60 (8.27)	8.00	1.29 (12.66)	--	1.08
	1G/1C/1G	42.0	146.7 (5.92)	1856.0 (5.67)	1.27 (2.72)	77.5 (5.00)	2.31	1.23 (12.19)	6.15	1.27 (15.16)	--	1.00
	2G/1C/2G	26.6	110.8 (10.21)	1244.4 (1.74)	1.18 (8.27)	98.3 (2.43)	2.94	1.64 (23.68)	8.20	1.44 (15.90)	--	1.22
CHM/G	1CHM/1G/1CHM	71.2	454.5 (11.95)	1168.9 (19.49)	0.25 (11.66)	54.7 (9.00)	1.63	0.39 (29.22)	1.95	0.21 (46.47)	--	0.81
	1G/3CHM/1G	64.9	439.2 (7.35)	1053.5 (10.14)	0.23 (6.43)	74.5 (6.12)	2.22	0.72 (11.63)	3.60	0.24 (8.31)	--	1.00
	1G/1CHM/1G/1CHM/1G	45.1	318.7 (7.33)	1105.8 (9.18)	0.35 (5.02)	76.6 (1.98)	2.29	0.77 (24.58)	3.85	0.37 (32.84)	0.90 (4.71)	1.06
	1G/1CHM/1G	38.2	252.0 (8.55)	1054.7 (9.11)	0.30 (2.39)	63.7 (1.70)	1.90	0.85 (13.86)	4.25	0.38 (7.71)	1.27 (14.54)	1.27
	2G/1CHM/2G	23.6	214.3 (8.45)	1164.7 (14.47)	0.33 (14.65)	80.5 (3.93)	2.40	1.22 (20.72)	6.10	0.39 (5.96)	1.49 (9.11)	1.18

Note: * the number before letters in series ID shows the number of layers of each material; ** it was assumed $\varepsilon_{c0} = 0.20$ (according equation (5.10)).

From **Table 5.7**, it can also be observed that, for each combination, failure strain of LS fibres increases with the decrease of LS fibres vol%. This tendency is reflected in the strain reduction factor that as well increases as the volume of LS fibres decreases. In some cases, the strain reduction factor is higher than 1, which proves that hybridisation, discussed in Section 5.4.2.2, allows to fully eliminate the reduction of LS fibres strain efficiency.

The same table reveals that the failure strain of HS fibres is significantly lower in hybrid than in non-hybrid jacketing. Sometimes, this observation has been done even in tensile tests of hybrid composites [43]. Since no substantiated explanation exists today in literature, this subject should be further investigated. Moreover, the failure strain of HS fibres appears to increase as the volume of LS fibres decreases.

The relationship between the confinement ratio (f_{lu}/f_{c0}) and the strength enhancement (f_{cc}/f_{c0}), as well as the relationship between the confinement ratio and the strain enhancement ($\varepsilon_{cc}/\varepsilon_{c0}$), are presented in **Figure 5.8** and **Figure 5.9**, respectively. The f_{lu} was established based on the σ_{hybrid} input computed according the model of Jalalvand *et al.* [13] and the bilinear ROM model [14]. In the present chapter, the σ_{hybrid} is designated J-σ_{hybrid}, in the cases that the value was computed according to the model of Jalalvand *et al.* [13], and B-σ_{hybrid}, in the cases that the value was computed according to the bilinear ROM model [14]. In **Figure 5.8** and **Figure 5.9** the corresponding linear regression models (design-oriented models) and their coefficient of determination (R^2) are also presented. Relatively large values of R^2 (0.84 and 0.80) were found between predictions of f_{cc}/f_{c0} and the corresponding experimental values. The resulting regression models are in fact very similar to the Lam and Teng [11] model, referred to in [6] as the most accurate model to predict the strength of non-hybrid confined concrete. Relatively to $\varepsilon_{cc}/\varepsilon_{c0}$ predictions, lower values of R^2 (0.62) in both cases were achieved.

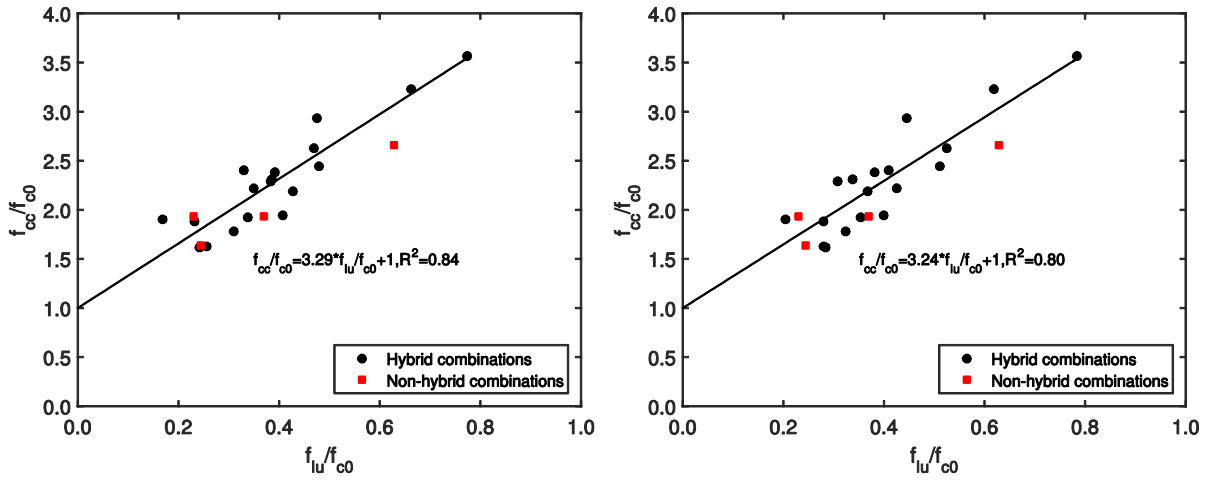

Figure 5.8 — Variation of strength enhancement ratio with confinement ratio: (a) f_{lu} based on J-σ_{hybrid}; (b) f_{lu} based on B-σ_{hybrid}.

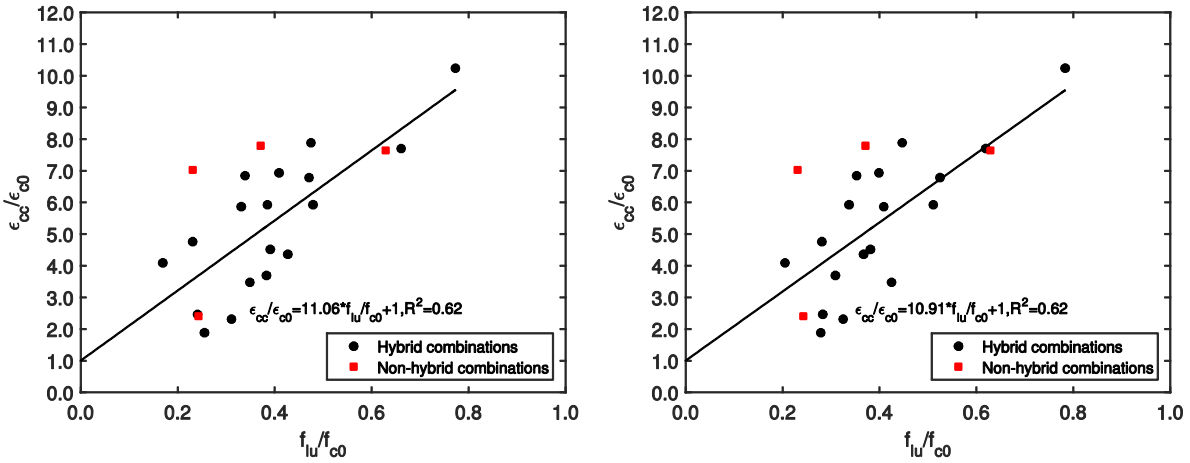

(a) (b)

Figure 5.9 — Variation of strain enhancement ratio with confinement ratio: (a) f_{lu} based on J-σ_{hybrid}; (b) f_{lu} based on B-σ_{hybrid}.

The tensile strength of the composite of all hybrid combinations, ultimate confining pressure, peak axial stress and peak axial strain predictions are presented in **Table 5.8**. For f_{cc} predictions, the relative error varied between -13.3% and 18.1%, when f_{lu} values were computed based on J-σ_{hybrid}, and varied between -18.6% and 16.7%, when f_{lu} values were computed based on B-σ_{hybrid}. This error magnitude (maximum absolute value of 20%) is acceptable and is in agreement with other published studies [6]. Thus, it can be stated that both models (Jalalvand *et al.* [13] and bilinear ROM [14]) can be used to accurately predict f_{lu} and, consequently, the f_{cc}.

For ε_{cc} predictions the obtained relative errors varied between -104.0% and 29.8%, when f_{lu} values were computed based on J-σ_{hybrid}, and varied between -115.7% and 25.6%, when f_{lu} values were computed based on the B-σ_{hybrid}. With this error magnitude, it can be stated that the suggested models cannot be used to predict ε_{cc}. This statement is in agreement with the bibliography [6]. In fact, usually, the relative errors associated to $\varepsilon_{cc}/\varepsilon_{c0}$ predictions are much higher than those associated to f_{cc}/f_{c0} predictions [6] and, for this reason, some authors propose a model for the peak stress only [6].

5.4.2.2. Hybrid effect

In the present chapter, different ways of computing the hybrid effect were considered, varying the numerator and denominator of equation (5.26):

$$Hybrid\ effect = \frac{\Delta\varepsilon_L}{\varepsilon_L} \times 100 \tag{5.26}$$

where $\Delta\varepsilon_L$ is the absolute variation between the strain of LS material at failure in hybrid and non-hybrid composites and ε_L is the reference strain of the non-hybrid LS composite at failure.

Table 5.8 — Ultimate conditions of hybrid FRP-confined concrete predictions.

Material combination	Series ID	Composite tensile strength				f_{lu}		f_{cc}					ε_{cc}				
		Experimental [MPa] (CoV [%])	Jalalvand model [MPa]	Bi. ROM [MPa]	t_{frp} [mm]	Based on J-σ_{hybrid} [MPa]	Based on B-σ_{hybrid} [MPa]	Experim. [MPa] (CoV [%])	Based on J-σ_{hybrid} [MPa]	Based on B-σ_{hybrid} [MPa]	Based on J-σ_{hybrid} rel. error [%]	Based on B-σ_{hybrid} rel. error [%]	Experimental [%] (CoV [%])	Based on J-σ_{hybrid} [%]	Based on B-σ_{hybrid} [%]	Based on J-σ_{hybrid} rel. error [%]	Based on B-σ_{hybrid} rel. error [%]
C/B	1C/1B/1C	2191.4 (7.28)	1957.9	2189.3	0.60	15.7	17.6	87.4 (--)	85.3	90.5	2.4	-3.5	1.41 (--)	1.29	1.40	8.6	0.7
	1B/1C/1B	1950.2 (7.51)	1996.6	1718.4	0.54	14.3	12.3	73.2 (3.01)	80.5	73.3	-10.0	-0.2	0.91 (13.74)	1.19	1.04	-30.7	-14.4
CHM/B	1CHM/1B/1CHM	1150.0 (14.10)	1131.8	1325.4	0.54	8.1	9.5	54.2 (8.59)	60.1	64.2	-11.0	-18.6	0.51 (17.63)	0.76	0.85	-49.9	-66.8
	1B/1CHM/1B	1328.0 (10.74)	1152.3	1398.1	0.50	7.7	9.4	62.9 (5.46)	59.0	63.9	6.3	-1.6	0.99 (16.71)	0.74	0.84	25.3	14.7
CHM/C	1CHM/1C/1CHM	1352.5 (5.10)	1292.7	1350.3	0.60	10.4	10.9	59.7 (7.76)	67.7	68.6	-13.3	-14.9	0.48 (7.20)	0.92	0.94	-92.0	-96.5
	1C/1CHM/1C	1937.5 (6.79)	1544.9	1809.0	0.64	13.1	15.3	79.9 (5.01)	76.6	83.2	4.1	-4.1	0.94 (13.95)	1.11	1.25	-17.8	-32.6
C/G	1C/1G/1C	2176.9 (8.55)	2005.5	2135.1	0.60	16.0	17.1	81.7 (1.48)	86.3	88.8	-5.6	-8.7	1.23 (6.00)	1.31	1.36	-6.5	-10.9
	1G/3C/1G	2216.0 (8.77)	1988.4	2037.8	0.98	25.9	26.5	119.4 (2.66)	118.7	114.5	0.6	-0.1	2.13 (19.54)	1.99	2.01	6.7	5.9
	1G/1C/1G/1C/1G	1776.3 (10.55)	1830.5	1712.6	0.91	22.2	20.7	108.3 (7.53)	106.4	100.6	1.8	7.1	1.60 (8.27)	1.73	1.61	-8.1	-0.7
	1G/1C/1G	1856.0 (5.67)	1820.3	1593.6	0.53	12.9	11.3	77.5 (5.00)	75.9	70.0	2.1	9.7	1.23 (12.19)	1.09	0.97	11.2	21.0
	2G/1C/2G	1244.4 (1.74)	1420.3	1335.4	0.84	15.9	14.9	98.3 (2.43)	85.8	81.9	12.7	16.7	1.64 (23.68)	1.30	1.22	20.8	25.6
CHM/G	1CHM/1G/1CHM	1168.9 (19.49)	1201.9	1313.7	0.53	8.6	9.4	54.7 (9.00)	61.6	63.8	-12.8	-16.7	0.39 (29.22)	0.80	0.84	-104.0	-115.7
	1G/3CHM/1G	1053.5 (10.14)	997.7	1218.4	0.88	11.7	14.3	74.5 (6.12)	71.9	79.7	3.4	-7.0	0.72 (11.63)	1.01	1.17	-40.3	-63.0
	1G/1CHM/1G/1CHM/1G	1105.8 (9.18)	1142.5	918.9	0.84	12.8	10.3	76.6 (1.98)	75.7	66.9	1.1	12.6	0.77 (24.58)	1.09	0.91	-41.4	-17.7
	1G/1CHM/1G	1054.7 (9.11)	852.4	1032.8	0.50	5.7	6.9	63.7 (1.70)	52.1	55.7	18.1	12.5	0.85 (13.86)	0.60	0.67	29.8	20.9
	2G/1CHM/2G	1164.7 (14.47)	1028.7	1276.8	0.81	11.1	13.7	80.5 (3.93)	69.9	77.9	13.2	3.2	1.22 (20.72)	0.97	1.14	20.7	6.8

Firstly, the hybrid effect was computed only considering tensile tests results. In this case, the failure strain values of both 1 and 3 layers non-hybrid composites, presented in **Table 5.3**, were assumed as reference to compute the hybrid effect. Secondly, the hybrid effect of lateral strains, registered in compression tests, was computed considering 3 reference failure strain values: the failure strain results of both 1 and 3 layers non-hybrid composites and the lateral failure strain of the 3 layers jacket, presented in **Table 5.5**. The different values obtained are presented in **Table 5.9**.

Table 5.9 — Hybrid effect computed considering different failure strains of non-hybrid composite as reference.

Material combination	Series ID	Volume of LS fibres [%]	Hybrid effect				
			Tensile tests		Compression tests (lateral strain)		
			1 layer composite tensile results	3 layers composite tensile results	1 layer composite tensile results	3 layers composite tensile results	3 layers composite lateral results
C/B	1C/1B/1C	74.0	-8.99	-1.47	-26.12	-21.05	-17.42
	1B/1C/1B	41.5	17.37	27.07	-5.17	1.33	5.98
CHM/B	1CHM/1B/1CHM	70.8	-12.95	31.43	-31.28	3.07	45.86
	1B/1CHM/1B	37.7	30.19	96.57	45.17	117.8	208.14
CHM/C	1CHM/1C/1CHM	63.0	-1.50	48.71	-31.29	3.06	45.83
	1C/1CHM/1C	29.5	44.52	118.19	69.43	154.15	259.64
C/G	1C/1G/1C	74.3	-4.44	3.45	7.92	-15.92	-12.07
	1G/3C/1G	68.5	-0.20	8.04	8.96	16.44	21.78
	1G/1C/1G/1C/1G	49.1	9.15	18.17	9.76	12.29	17.44
	1G/1C/1G	42.0	16.33	25.94	16.34	24.32	30.03
	2G/1C/2G	26.6	7.33	16.20	15.36	23.28	28.94
CHM/G	1CHM/1G/1CHM	71.2	-7.07	40.3	-20.69	18.96	68.35
	1G/3CHM/1G	64.9	-14.09	29.71	-6.02	40.97	99.49
	1G/1CHM/1G/1CHM/1G	45.1	27.66	92.74	37.09	105.63	190.99
	1G/1CHM/1G	38.2	9.97	66.03	42.56	113.83	202.59
	2G/1CHM/2G	23.6	21.94	84.10	45.72	118.59	209.33

Associations between hybrid effects computed according cited different ways were analysed by a Spearman's rank test, using SPSS version 23 [44]. Spearman's correlation coefficient, *r*, is a statistical measure of the "strength" of a monotonic relationship between paired data [45].

Additionally, associations between the hybrid effects and the FRP strain reduction factor were also analysed. Results are presented in **Table 5.10**. The *p*-values are also presented in **Table 5.10**. In this case, the null hypothesis is defined as: there is no monotonic correlation between the variables. When very low *p*-values (below 0.05) are presented the null hypothesis should be reject, i.e., there is evidences to believe that variables are monotonically correlated. In the same table, N is the number of considered different hybrid composite combinations.

Spearman's rank of data revealed both moderately strong (above 0.5) and strong (above 0.7) correlations between all ways of calculating the hybrid effect. As expected, this indicate that the magnitude of hybrid effect depends on the considered reference strain to failure of LS fibres.

Excluding the correlation between the hybrid effect (computed using the failure strain obtained with 3 layers non-hybrid composite as reference) and FRP strain reduction factor, moderately strong (above 0.5) and strong (above 0.7) correlations exist as well between hybrid effects and FRP strain reduction factors. This proves that the hybrid effect actually contributes to eliminate the reduction of the FRP strain efficiency. This is clear from **Figure 5.10**, in which it is possible to observe that the uniaxial failure strains of LS fibres are almost coincident with the lateral failure strain of LS fibres, for all of the analysed hybrid FRP combinations.

5.4.2.3. Dilation behaviour and axial stress-strain behaviour

Lateral strain-axial strain curves (dilation behaviour) of hybrid FRP-confined concrete can be significantly different of the ones obtained in non-hybrid cases. **Figure 5.11** illustrates the different stages observed on a lateral strain-axial strain curves of the specimens exhibiting pseudo-ductile behaviour. The different stages are marked on this curve. It is possible to observe that the first two branches of the curve are very similar to the curve obtained for the non-hybrid cases, i.e., there is an initial phase, herein named first ascending branch, that depends on Poisson's ratio of concrete (equation (5.18)) and next, from approximately stress-strain peak of plain concrete (f_{c0}, ε_{c0}), a second ascending branch in which microcrack initiation and propagation occurs resulting in a rapid increase in the lateral strain. After, in specimens with pseudo-ductile behaviour, a last branch, which corresponds to the flat-topped stress-strain curve observed in monotonic tensile tests of hybrid FRP, can be achieved, after the failure of LS fibres.

Experimental lateral strain-axial strain curves of hybrid FRP-confined concrete as well as the corresponding analytical curves are plotted in **Figure 5.12** to **Figure 5.16**. In general, there is a good agreement between predicted and measured values. In combination 1C/1B/1C, there are two outlier experimental results which were ignored because they are abnormally low.

Table 5.10 — Correlation matrix between different ways of compute hybrid effect (considering different failure strains of non-hybrid composite as reference) and strain reduction factor.

			Tensile tests		Compression tests (lateral strain)			
			1 layer composite tensile results	3 layers composite tensile results	1 layer composite tensile results	3 layers composite tensile results	3 layers composite lateral results	k_ε at failure of LS fibres
Tensile tests	**1 layer composite tensile results**	***r***	1.000	0.602**	0.858**	0.651**	0.521*	0.533*
		***p*-value**	--	0.008	0.000	0.003	0.027	0.023
		N	18	18	18	18	18	18
	3 layers composite tensile results	***r***	0.602**	1.000	0.573*	0.820**	0.936**	0.330
		***p*-value**	0.008	--	0.013	0.000	0.000	0.181
		N	18	18	18	18	18	18
Compression tests (lateral strain)	**1 layer composite tensile results**	**r**	0.858**	0.573*	1.000	0.837**	0.657**	0.831**
		***p*-value**	0.000	0.013	--	0.000	0.003	0.000
		N	18	18	18	18	18	18
	3 layers composite tensile results	***r***	0.651**	0.820**	0.837**	1.000	0.936**	0.737**
		***p*-value**	0.003	0.000	0.000	--	0.000	0.000
		N	18	18	18	18	18	18
	3 layers composite lateral results	**r**	0.521*	0.936**	0.657**	0.936**	1.000	0.531*
		***p*-value**	0.027	0.000	0.003	0.000	--	0.023
		N	18	18	18	18	18	18
	k_ε at failure of LS fibres	***r***	0.533*	0.330	0.831**	0.737**	0.531*	1.000
		***p*-value**	0.023	0.181	0.000	0.000	0.023	--
		N	18	18	18	18	18	18

Notes: N is the number of considered different hybrid composite combinations; ** correlation is significant at the 0.01 level; * correlation is significant at the 0.05 level.

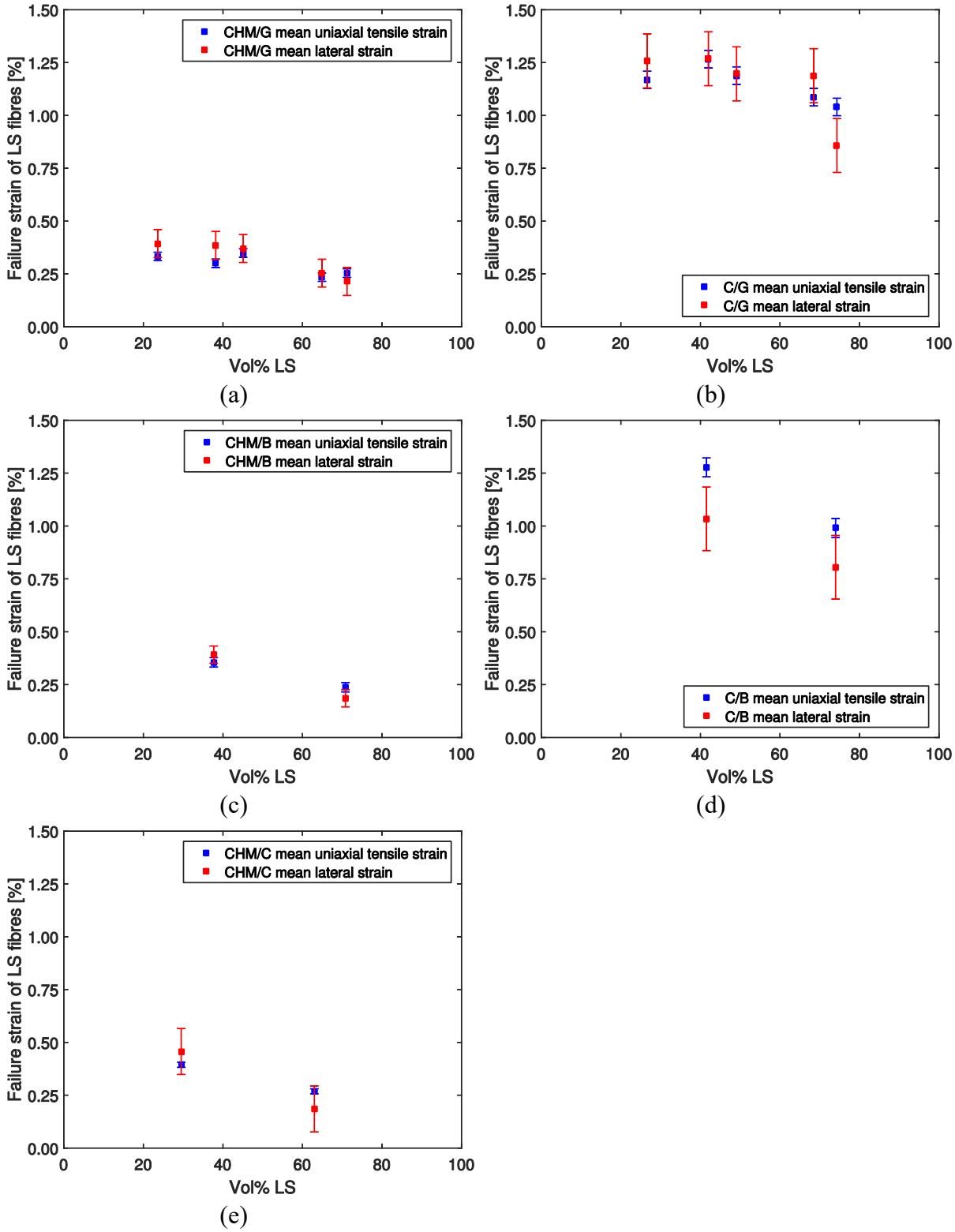

Figure 5.10 — Comparison between uniaxial tensile and lateral failure strains of LS fibres of the: (a) HM carbon/glass; (b) ST carbon/glass; (c) HM carbon/basalt; (d) ST carbon/basalt and (e) HM carbon/ST carbon composites

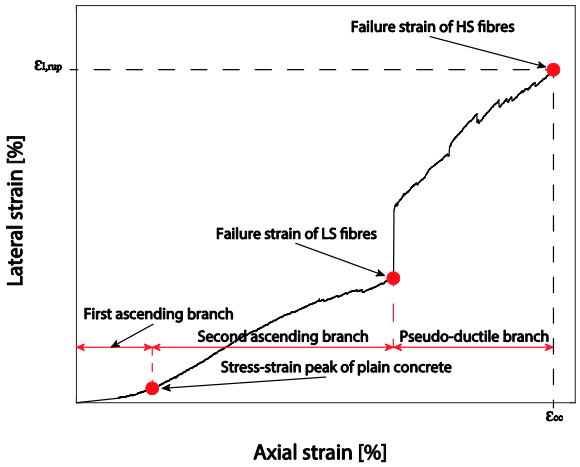

Figure 5.11 — Illustration of different stages of lateral strain–axial strain curves of specimens with pseudo-ductile behaviour.

It is possible to notice that, in most cases, hybrid FRP-confined concrete has a similar behaviour to that of non-hybrid FRP-confined concrete. As explained before, the different applied confining materials induce different confining pressures leading to curves exhibiting different trends after stress-strain peak of plain concrete (f_{c0}, ε_{c0}). This similarity between hybrid and non-hybrid behaviours exists because almost all the analysed hybrid combinations have premature tensile failure modes of the HS fibres [14], i.e., the tensile behaviour of these hybrid combinations is linear elastic up to failure. However, in 3 hybrid combinations, pseudo-ductile behaviour with simultaneous multiple fractures of LS fibres and dispersed delamination occurred in tensile tests, namely in 2G/1CHM/G, 1G/1CHM/1G, and 1B/1CHM/1B combinations [14]. The corresponding lateral strain-axial strain curves of the combinations referred to (**Figure 5.12**(a), **Figure 5.12**(b), **Figure 5.14**(a)) show a last branch that corresponds to the flat-topped stress-strain curve observed in monotonic tensile tests. According to [14], it was expected that the same behaviour occurred in 1C/1CHM/1C combination (**Figure 5.16**(a)). However, in this combination apparently very short pseudo-ductile branches took place that, in practice, lead to the consideration that premature failure of HS fibres occurred. This is according to the fact that in this combination a low lateral failure strain of HS fibres (0.61%) was registered (see **Table 5.7**). For this reason, the hybrid FRP failure of composite occurs too soon.

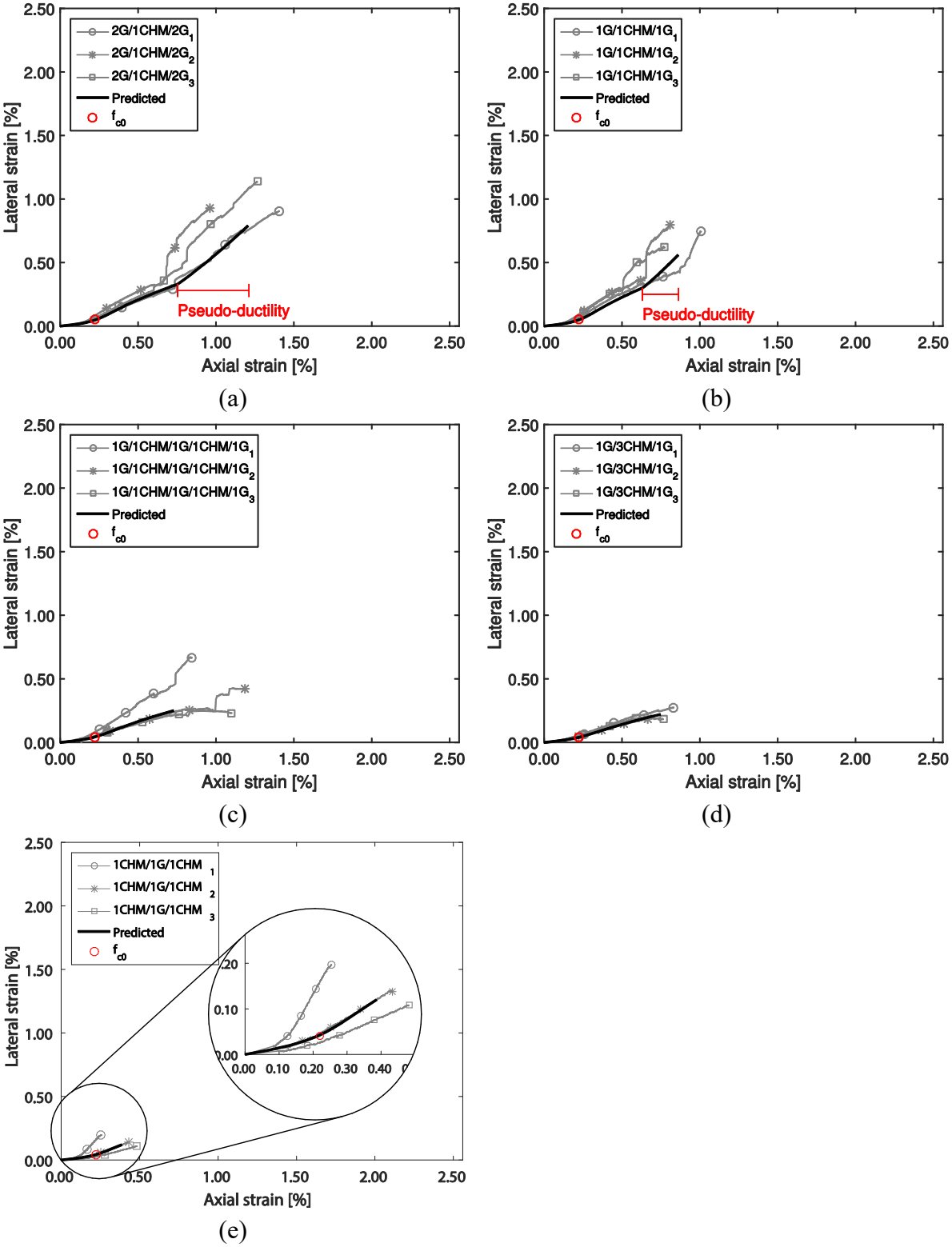

Figure 5.12 — Lateral strain-axial strain curves of CHM/G combinations: experimental *versus* predicted values.

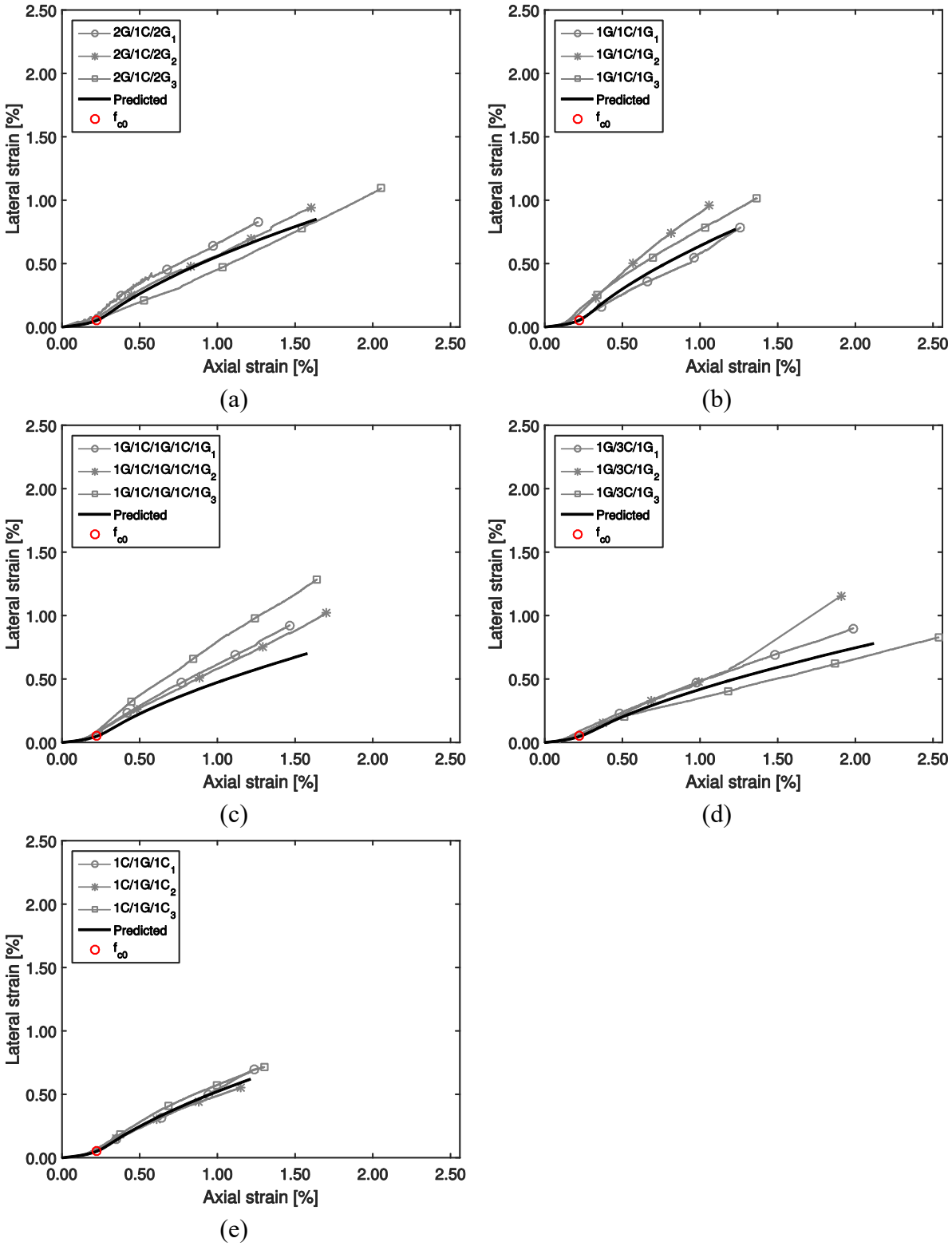

Figure 5.13 — Lateral strain-axial strain curves of C/G combinations: experimental *versus* predicted values.

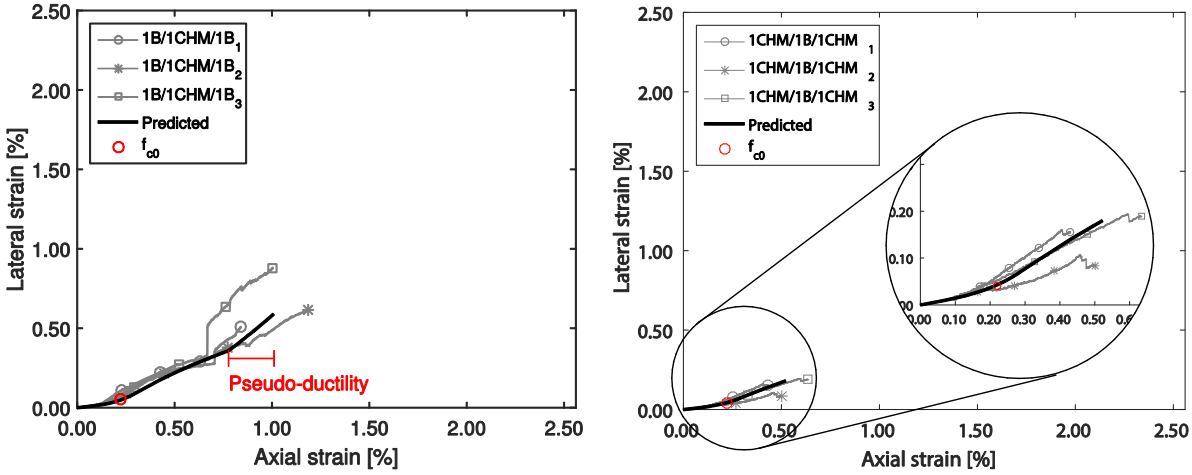

(a) (b)

Figure 5.14 — Lateral strain-axial strain curves of CHM/B combinations: experimental *versus* predicted values.

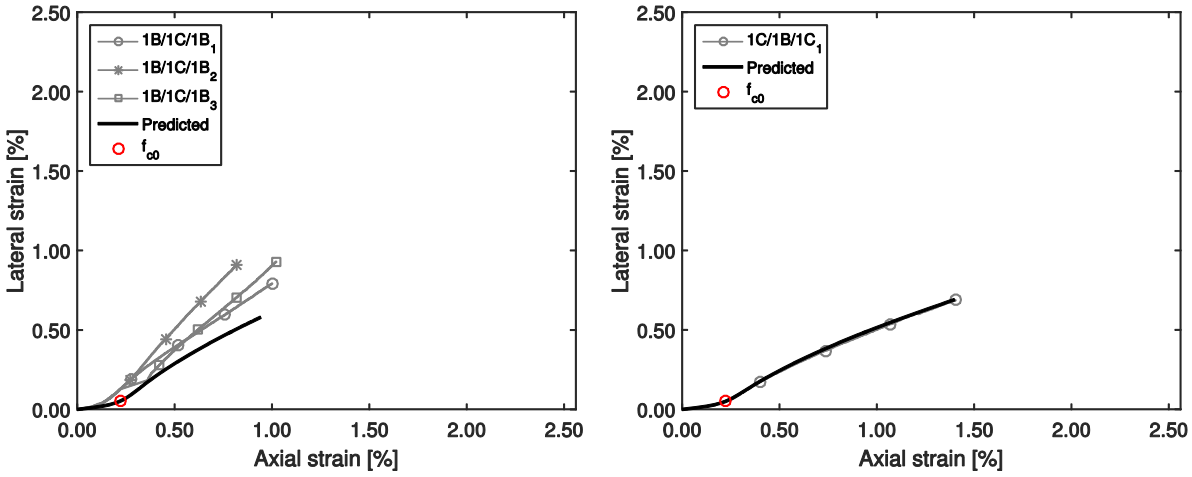

(a) (b)

Figure 5.15 — Lateral strain-axial strain curves of C/B combinations: experimental *versus* predicted values.

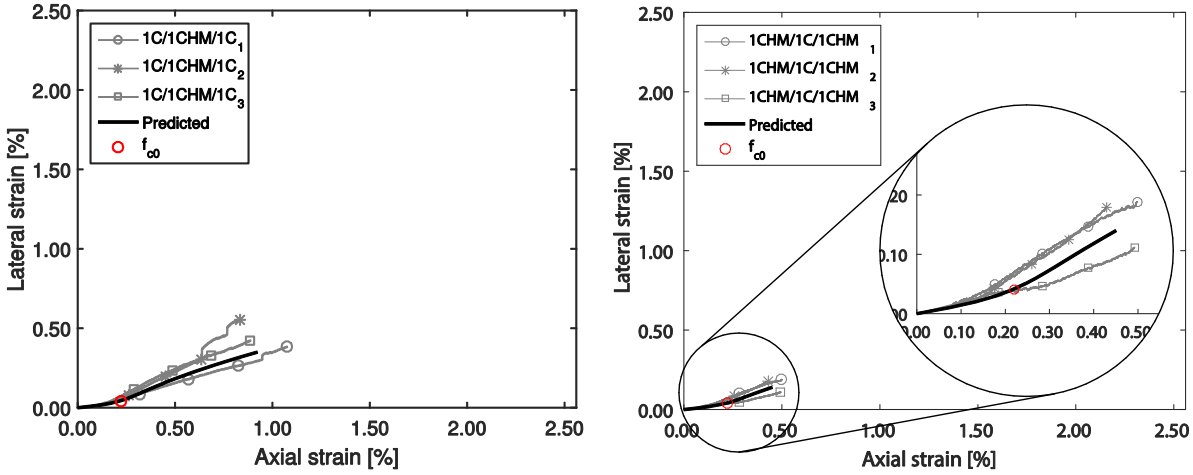

(a) (b)

Figure 5.16 — Lateral strain-axial strain curves of CHM/C combinations: experimental *versus* predicted values

As discussed in [14], tensile tests of 1G/1CHM/1G/1CHM/1G combination reveals that failure mode is in a transition zone, for this reason, it is expected that there is some random alternation between catastrophic delamination and premature HS fibres failure modes (see **Figure 5.12**(c)).

The compressive stress-strain curves are presented in **Figure 5.17** to **Figure 5.21**. It can be seen in these that there is as well a good agreement between predicted and measured values. Similarly to non-hybrid cases, most curves development follows approximately a bilinear law. However, an approximately flat-topped curve is evident in **Figure 5.17**(a), **Figure 5.17**(b) and **Figure 5.19**(a). This was expected because in 3 used hybrid combination (2G/1CHM/G, 1G/1CHM/1G, and 1B/1CHM/1B) a pseudo-ductile behaviour occurred in tensile tests [14]. However, this plateau exhibits a slight hardening component, which is not captured by the model. In tensile test results, it has been already observed some hardening at the 'yielding' plateau [14], which again confirms the relationship between f_l and f_c. In compressive stress-strain curve obtained with 1B/1CHM/1B combination, the extension of the predicted plateau is significantly lower than the experimental one. This is due to a slight overestimation of lateral failure strain of LS fibres, which defines the 'yield' point, as it can be seen in **Figure 5.14**(a).

Comparing HM carbon/glass and HM carbon/basalt (**Figure 5.17** and **Figure 5.19**) with ST carbon/glass and ST carbon/basalt confined concrete results (**Figure 5.18** and **Figure 5.20**), it is possible to notice that the formers lead to the worst f_{cc} and ε_{cc} values. The previous observation makes sense because ST carbon has higher tensile strength than HM carbon composite, which leads to major f_{lu} and, consecutively, to larger f_{cc} and ε_{cc}.

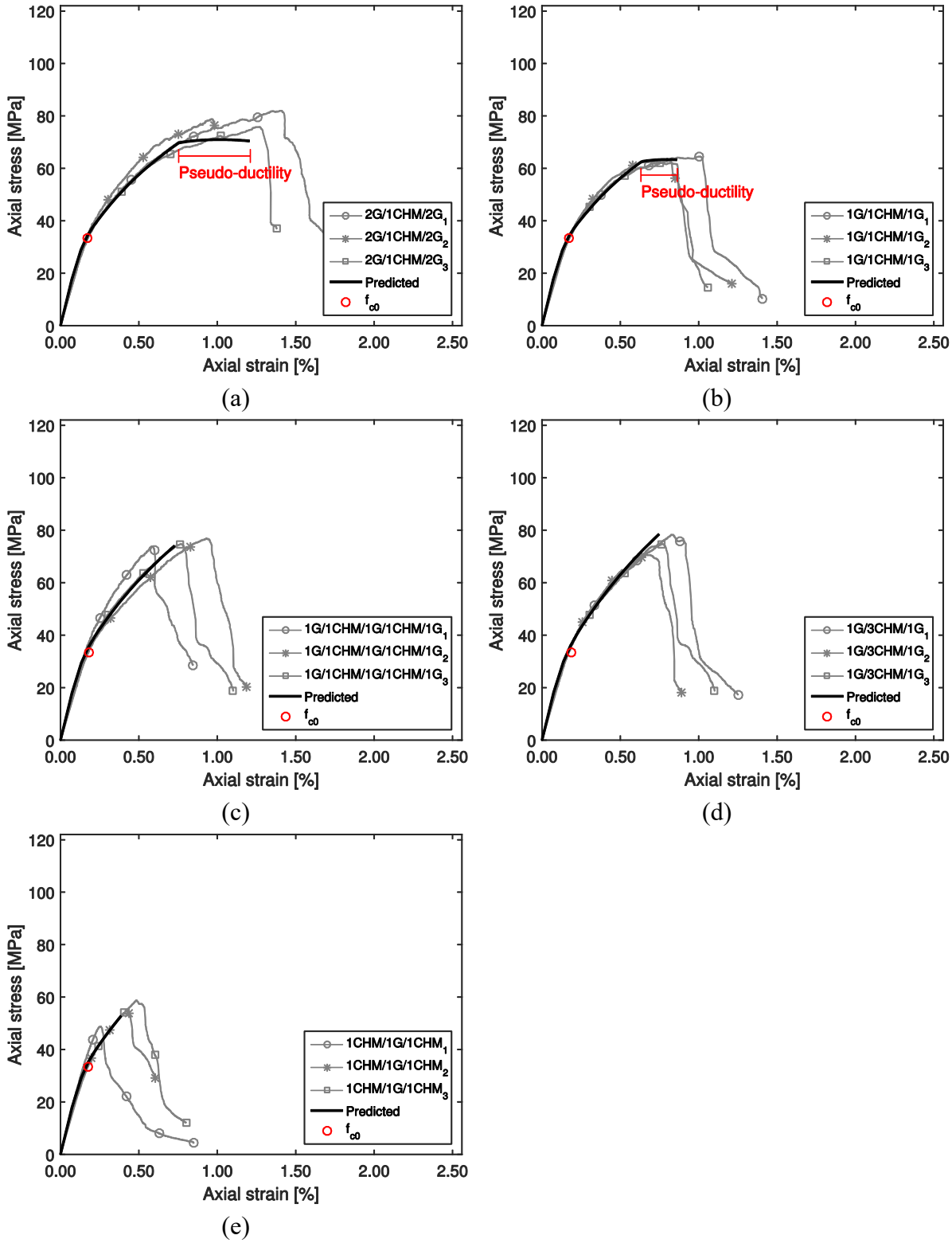

Figure 5.17 — Stress–strain curves of CHM/G combinations: experimental *versus* predicted values.

The HM carbon/glass and ST carbon/glass confined concrete failure modes are illustrated in **Figure 5.22** and **Figure 5.23**. It was decided to show these combinations because the translucence of the glass allows to visualize the possible fragmentation and delamination that may occur in LS material. As expected, fragmentation is evident in 2G/1CHM/2G (**Figure 5.22**(a) and **Figure 5.22**(b)) and 1G/1CHM/1G (**Figure 5.22**(c)) jackets because they promoted pseudo-ductile behaviours. In these combinations, the specimens were initially black due to the carbon natural colour but, after fragmentation and delamination, light was reflected from the interface, and these zones of specimens looked white, as it is marked in the figures. In the remaining cases, there are no evidences of fragmentation of LS material.

With exception of two cited cases (2G/1CHM/2G and 1G/1CHM/1G) in which fragmentation took place, all specimens failed explosively with the projection of small concrete fragments. Again, the jacket with highest elastic modulus (1CHM/1G/1CHM) promoted an almost full height failure.

As exposed in **Table 5.11**, the analysis of performance of the analysis-oriented model reveal that for f_{cc} predictions, the relative error varied between -14.0% and 14.2%, and for $\varepsilon_{l,rup-mean}$ predictions, the error varied between -26.3% and 35.1%. In the case of f_{cc}, it can be stated that the model was able to accurately predict the experimental results. However, in the case of $\varepsilon_{l,rup-mean}$ the error magnitude is quite high. In this case, the model should be used with care. Anyway, the biggest advantage of the analysis-oriented model, if compared to the design-oriented model, is that it allows to predict complete lateral strain-axial strain and axial stress-strain curves, not only strength and failure strain.

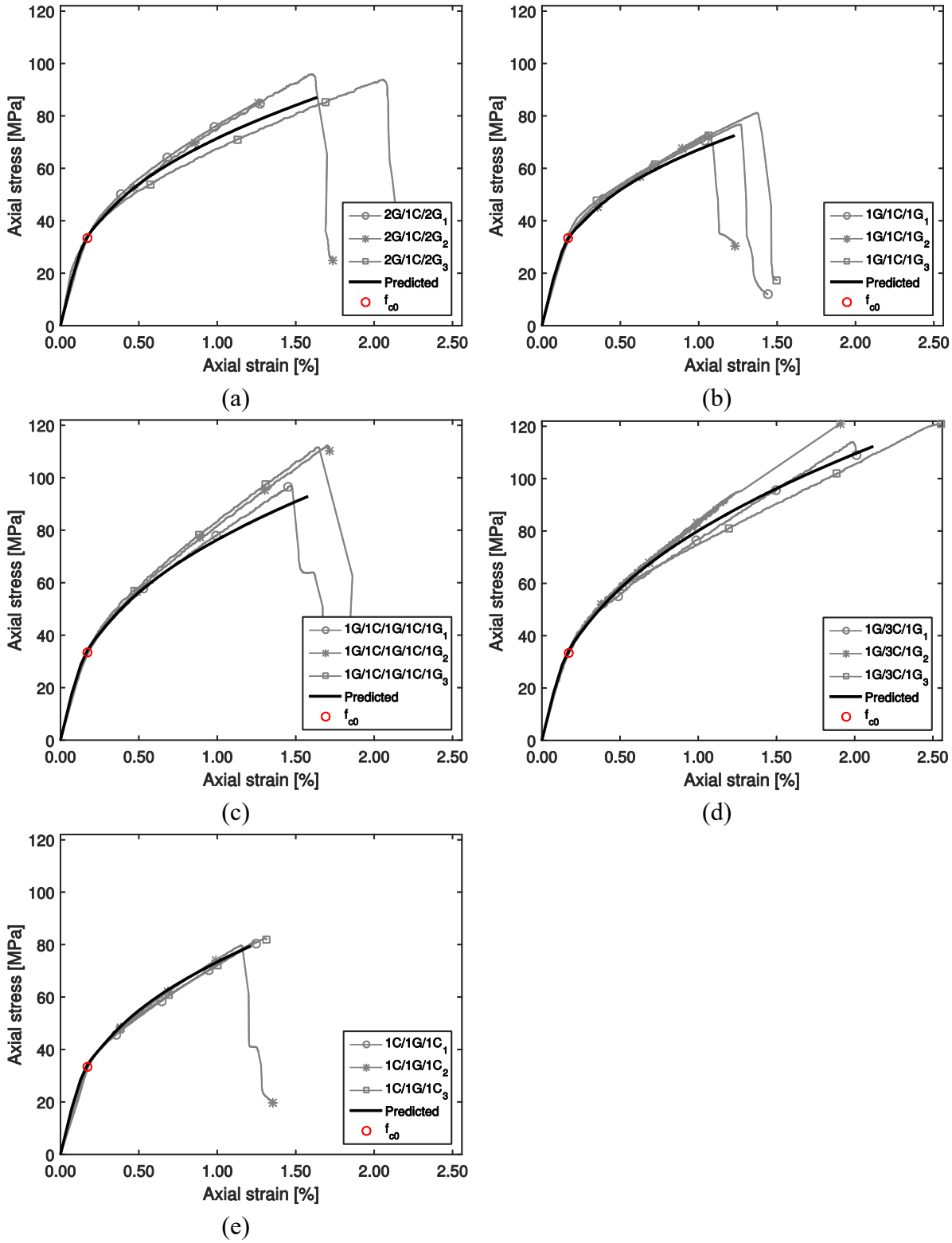

Figure 5.18 — Stress–strain curves of C/G combinations: experimental *versus* predicted values.

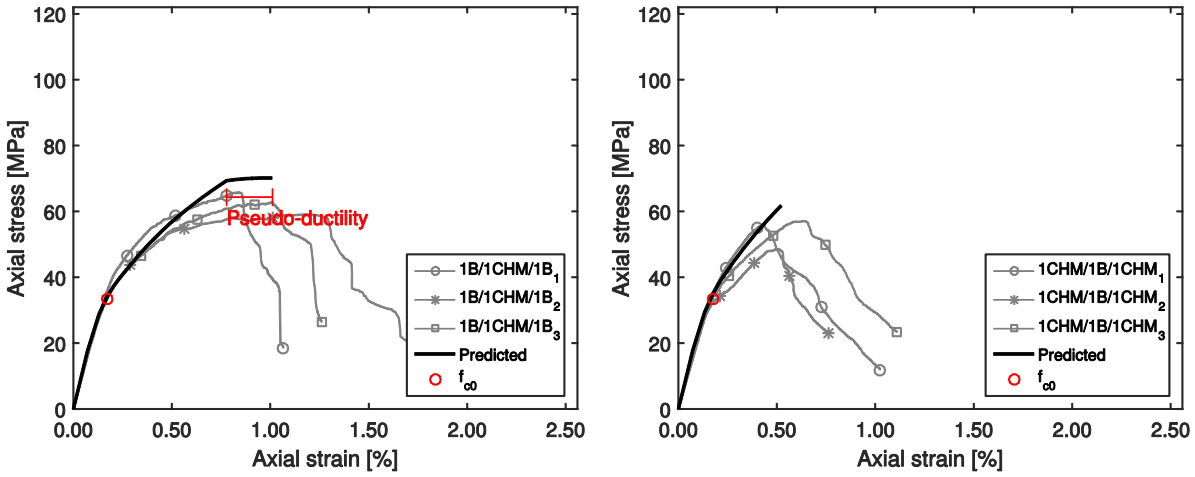

(a) (b)

Figure 5.19 — Stress–strain curves of CHM/B combinations: experimental *versus* predicted values.

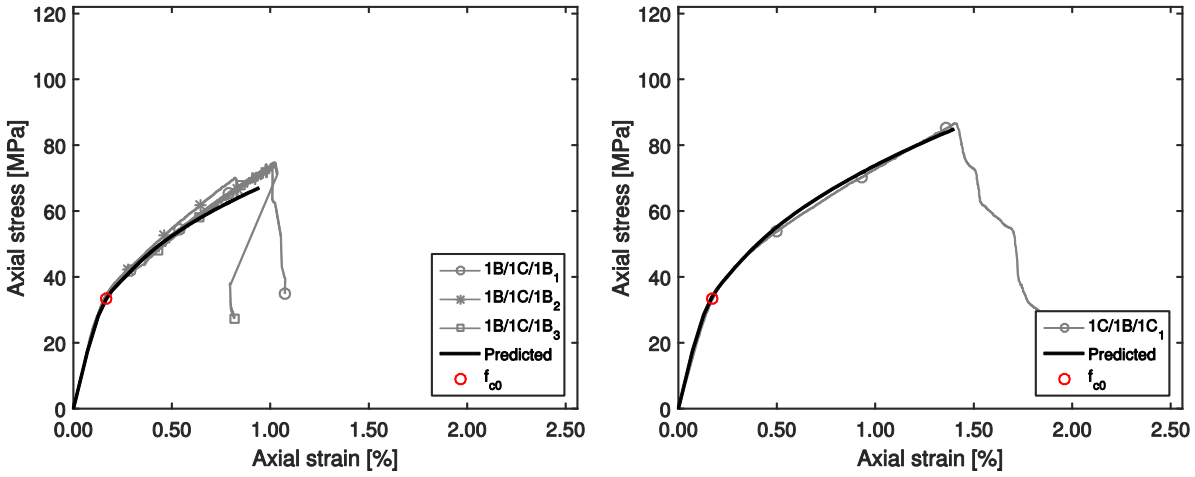

(a) (b)

Figure 5.20 — Stress–strain curves of C/B combinations: experimental *versus* predicted values.

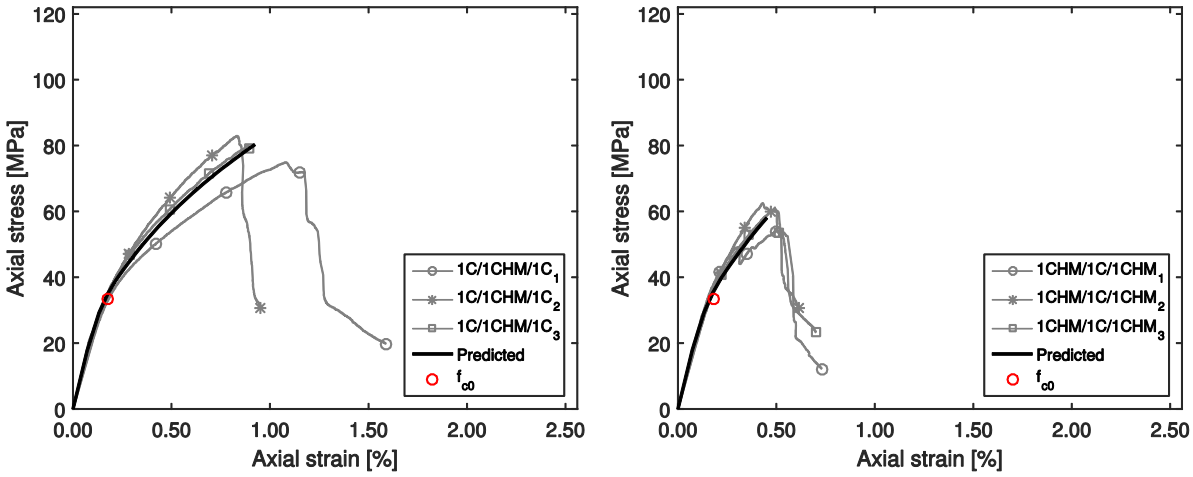

(a) (b)

Figure 5.21 — Stress–strain curves of CHM/C combinations: experimental *versus* predicted values.

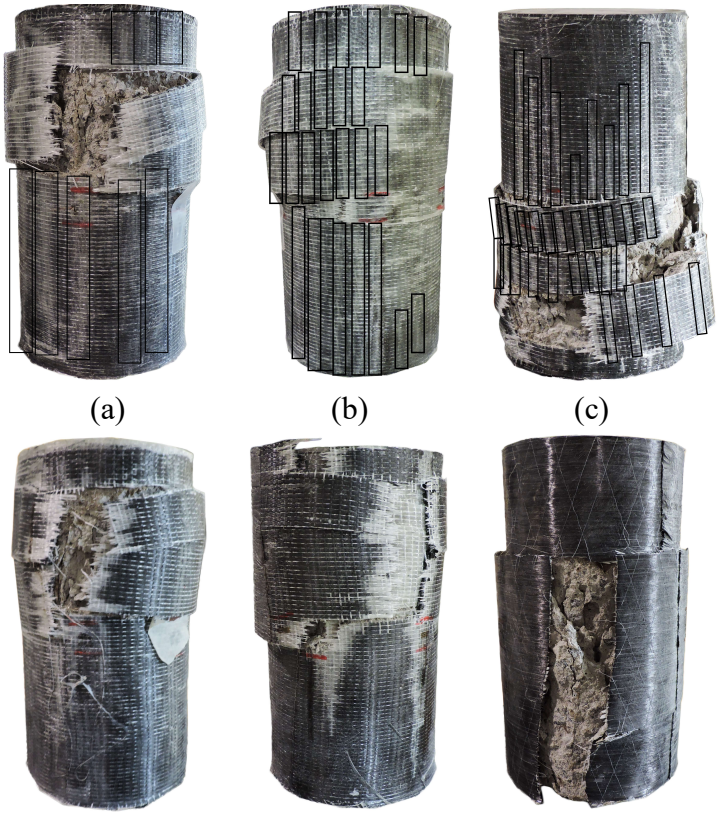

(a) (b) (c)

(d) (e) (f)

Figure 5.22 — Failure modes of HM carbon/glass FRP-confined concrete: (a) 2G/1CHM/2G – view 1; (b) 2G/1CHM/2G – view 2; (c) 1G/1CHM/1G; (d) 1G/1CHM/1G/1CHM/1G; (e) 1G/3CHM/1G and (f) 1CHM/1G/1CHM.

(a) (b) (c) (d) (e)

Figure 5.23 — Failure modes of ST carbon/glass FRP-confined concrete: (a) 2G/1C/2G; (b) 1G/1C/1G; (c) 1G/1C/1G/1C/1G; (d) 1G/3C/1G and (e) 1C/1G/1C.

Table 5.11 — Comparison of analysis-oriented model predictions with hybrid FRP-confined concrete test results

Series ID *	f_{cc}			$\varepsilon_{l,rup\ -\ mean}$		
	Exp. [MPa] (CoV [%])	**Prediction** [MPa]	**Rel. error** [%]	**Exp.** [MPa] (CoV [%])	**Prediction** [MPa]	**Rel. error** [%]
1C/1B/1C	87.4 (--)	84.88	2.9	0.66 (--)	0.69	-4.9
1B/1C/1B	73.2 (3.01)	67.01	8.5	0.88 (8.56)	0.58	33.9
1CHM/1B/1CHM	54.2 (8.59)	61.79	-14.0	0.14 (38.13)	0.18	-26.3
1B/1CHM/1B	62.9 (5.46)	70.19	-11.6	0.67 (28.56)	0.59	11.8
1CHM/1C/1CHM	59.7 (7.76)	58.03	2.8	0.16 (26.25)	0.14	12.4
1C/1CHM/1C	79.9 (5.01)	80.28	-0.5	0.45 (19.92)	0.35	22.9
1C/1G/1C	81.7 (1.48)	79.45	2.8	0.66 (13.60)	0.62	5.4
1G/3C/1G	119.4 (2.66)	112.32	5.9	0.96 (17.86)	0.78	18.8
1G/1C/1G/1C/1G	108.3 (7.53)	92.87	14.2	1.08 (17.29)	0.70	35.1
1G/1C/1G	77.5 (5.00)	72.50	6.5	0.92 (13.03)	0.77	16.2
2G/1C/2G	98.3 (2.43)	87.03	11.5	0.95 (14.03)	0.85	10.9
1CHM/1G/1CHM	54.7 (9.00)	52.80	3.5	0.15 (30.30)	0.12	18.8
1G/3CHM/1G	74.5 (6.12)	78.52	-5.4	0.21 (24.17)	0.22	-2.5
1G/1CHM/1G/1CHM/1G	76.6 (1.98)	67.45	11.9	0.29 (27.88)	0.36	-26.0
1G/1CHM/1G	63.7 (1.70)	63.28	0.7	0.72 (12.50)	0.56	22.3
2G/1CHM/2G	80.5 (3.93)	70.47	12.5	0.99 (12.93)	0.79	20.3

5.5. Conclusions

The compression behaviour of several hybrid FRP-confined small-scale plain concrete columns has been investigated using experimental testing and analytical modelling. All the jackets were

made through the hand lamination of four different commercially available dry UD fabrics: high-modulus carbon (CHM), standard-modulus carbon (C), E-glass (G), and basalt (B). Additionally to hybrid FRP series, few non-hybrid confined concrete columns were also analysed in order to obtain reference values. Main observations and conclusions drawn are presented next.

Analysing non-hybrid FRP-confined concrete results, a minimum FRP strain reduction factor of 0.72 and a maximum of 0.96 were achieved respectively in the CHM and C series. This way, it was concluded that FRP tensile strain at failure is not reachable *in situ* with FRP jackets. However, it was demonstrated that this reduction of efficiency can be minimized, or even eliminated, with hybridisation. In fact, it was observed that for a large number of hybrid combinations the strain reduction factor was even higher than 1. It was verified that moderately strong (above 0.5) and strong (above 0.7) correlations exist between the hybrid effect and the FRP strain reduction factor. This means that there is an increase of the strain reduction factor as the volume of LS fibres decreases, i.e, hybrid effect increases.

Two models to predict the tensile strength of hybrid FRP were adopted, namely the model of Jalalvand *et al*. [13] and bilinear ROM [14] and it was proven that these can be used to accurately predict the ultimate confining pressure provided by the hybrid composites. Consequently, two new design-oriented models, in which the confining pressure is used as input variable, were proposed to predict the peak stress of hybrid FRP-confined concrete. Relatively large R^2 of 0.84 and 0.80 were found in predictions of peak axial stress with the proposed models, respectively, for first and second models.

In the three tested hybrid combinations, which included HM carbon as LS material (2G/1CHM/G, 1G/1CHM/1G and 1B/1CHM/1B), pseudo-ductile tensile responses with fragmentation and dispersed delamination of the jacket were observed, leading that, in the compressive stress-strain curves of these combinations, a flat-topped curve is evident. In these combinations abrupt and explosive failure modes were avoided.

Finally, the presented analysis-oriented confinement model, based on the modification of the approach of Lim and Ozbakkaloglu [15, 16], allowed to accurately simulate both the dilation behaviour and the compressive stress-strain behaviour of all hybrid confined concrete series analysed.

5.6. References

[1] Pellegrino C, Sena-Cruz J. Design Procedures for the Use of Composites in Strengthening of Reinforced Concrete Structures. State-of-the-Art Report of the RILEM Technical Committee 234-DUC, Springer, ISBN 978-94-017-7335-5. 2016.
[2] Bank L. Composites for Construction - Structural Design with FRP Materials. John Wiley & Sons, Inc. 2006.

[3] Zheng J, Ozbakkaloglu T. Sustainable FRP–recycled aggregate concrete–steel composite columns: Behavior of circular and square columns under axial compression. Thin-Walled Structures. 2017;120(Supplement C):60-9.
[4] Vincent T, Ozbakkaloglu T. Influence of fiber orientation and specimen end condition on axial compressive behavior of FRP-confined concrete. Construction and Building Materials. 2013;47(Supplement C):814-26.
[5] Ozbakkaloglu T. Compressive behavior of concrete-filled FRP tube columns: Assessment of critical column parameters. Engineering Structures. 2013;51(Supplement C):188-99.
[6] Ozbakkaloglu T, Lim JC, Vincent T. FRP-confined concrete in circular sections: Review and assessment of stress–strain models. Engineering Structures 2013;49 1068–88.
[7] Ozbakkaloglu T, Lim JC. Axial compressive behavior of FRP-confined concrete: Experimental test database and a new design-oriented model. Composites: Part B. 2013;55:607–34.
[8] Lim JC, Ozbakkaloglu T. Confinement Model For FRP-Confined High-Strength Concrete. Journal of Composites for Construction doi:101061/(ASCE)CC1943-56140000376. 2013.
[9] Lim JC, Ozbakkaloglu T. Design model for FRP-confined normal- and high-strength concrete square and rectangular columns. Magazine of Concrete Research. 2014;66(20):1020–35.
[10] Lim J, Ozbakkaloglu T. Hoop strains in FRP-confined concrete columns: experimental observations. Materials and Structures DOI 101617/s11527-014-0358-8. 2014.
[11] Lam L, Teng JG. Design-oriented stress–strain model for FRP-confined concrete. Constr Build Mater. 2003;17(6–7):471–89.
[12] Wu Y-F, Jiang J-F. Effective strain of FRP for confined circular concrete columns. Composite Structures. 2012;95:479–91.
[13] Jalalvand M, Czél G, Wisnom MR. Damage analysis of pseudo-ductile thin-ply UD hybrid composites – A new analytical method. Composites: Part A. 2015;69:83–93.
[14] Ribeiro F, Sena-Cruz J, Branco FG, Júlio E. Hybrid effect and pseudo-ductile behaviour of unidirectional interlayer hybrid FRP composites for civil engineering applications. Construction and Building Materials. 2018;171:871-90.
[15] Lim JC, Ozbakkaloglu T. Lateral Strain-to-Axial Strain Relationship of Confined Concrete. Journal of Structural Engineering. 2014;141(5).
[16] Lim JC, Ozbakkaloglu T. Unified Stress-Strain Model for FRP and Actively Confined Normal-Strength and High-Strength Concrete. Journal of Composites for Construction, ASCE, ISSN 1090-0268/04014072 (14). 2014.
[17] Czél G, Wisnom MR. Demonstration of pseudo-ductility in high performance glass/epoxy composites by hybridisation with thin-ply carbon prepreg. Composites: Part A: Applied Science and Manufacturing. 2013;52:23–30.
[18] Jalalvand M, Czél G, Wisnom MR. Numerical modelling of the damage modes in UD thin carbon/glass hybrid laminates. Composites Science and Technology. 2014;94:39–47.
[19] Jalalvand M, Czél G, Wisnom MR. Parametric study of failure mechanisms and optimal configurations of pseudo-ductile thin-ply UD hybrid composites. Composites: Part A. 2015; 74:123–31.
[20] Czél G, Jalalvand M, Wisnom MR. Design and characterisation of advanced pseudo-ductile unidirectional thin-ply carbon/epoxy–glass/epoxy hybrid composites. Composite Structures. 2016;143:362–70.
[21] Wisnom MR, Czél G, Swolfs Y, Jalalvand M, Gorbatikh L, Verpoest I. Hybrid effects in thin ply carbon/glass unidirectional laminates: Accurate experimental determination and prediction. Composites: Part A. 2016;88:131–9.

[22] Yu H, Longana ML, Jalalvand M, Wisnom MR, Potter KD. Pseudo-ductility in intermingled carbon/glass hybrid composites with highly aligned discontinuous fibres. Composites: Part A 2015;73:35–44.
[23] Swolfs Y, Gorbatikh L, Verpoest I. Fibre hybridisation in polymer composites: a review. Composites Part A: Applied Science and Manufacturing. 2014;67:181-200.
[24] Hayashi T. On the improvement of mechanical properties of composites by hybrid composition. Proc 8th Intl Reinforced Plastics Conference. 1972:149-52.
[25] Wu G, Wu ZS, Lu ZT, Ando YB. Structural Performance of Concrete Confined with Hybrid FRP Composites. Journal of reinforced plastics and composites. 2008;27(12).
[26] Luca AD, Nardone F, Matta F, Nanni A, Lignola GP, Prota A. Structural Evaluation of Full-Scale FRP-Confined Reinforced Concrete Columns. J Compos Constr. 2011;15:112-23.
[27] Li L-J, Xu S-D, Zeng L, Guo Y-C. Study on mechanical behavior of circular concrete columns confined by HFRP under axial compressive load. Research and Applications in Structural Engineering, Mechanics and Computation – Zingoni (Ed) Taylor & Francis Group, London, ISBN 978-1-138-00061-2. 2013.
[28] Long Y-L, Zhu J. Experimental Study on Concrete Columns with Various Sizes Confined by BFRP and hybrid FRP under Axial Compression. Advanced Materials Research. 2013;838-841:407-11.
[29] Deng Z-c, Qu J-l. The Experimental Studies on Behavior of Ultrahigh-Performance Concrete Confined by Hybrid Fiber-Reinforced Polymer Tubes. Advances in Materials Science and Engineering, Article ID 201289, 18 pages. 2015.
[30] Tamuzs V, Tepfers R, Zile E, Ladnova O. Behavior of concrete cylinders confined by a carbon composite III: deformability and the ultimate axial strain. Mech Compos Mater. 2006;42(4):303–14.
[31] CNR-DT200. Guide for the Design and Construction of Externally Bonded FRP Systems for Strengthening Existing Structures. Advisory Committee on Techincal Recommendations for Construction, National Research Council, Rome, Italy. 2013.
[32] Candappa DC, Sanjayan JG, Setunge S. Complete Triaxial Stress-Strain Curves of High-Strength Concrete. Journal of Materials in Civil Engineering. 2001;13(3):209-32.
[33] Popovics S. A Numerical Approach to the Complete Stress-Strain Curves for Concrete. Cement and Concrete Research. 1973;3(5):583-99.
[34] Lim JC, Ozbakkaloglu T. Stress–strain model for normal- and light-weight concretes under uniaxial and triaxial compression. Construction and Building Materials. 2014;71(Supplement C):492-509.
[35] Domingo JC, Kuang-Han C. Stress-Strain Relationship for Plain Concrete in Compression. Journal Proceedings.82(6).
[36] Richart F, Brandtzaeg A, Brown R. A study of the failure of concrete under combined compressive stresses. Bulletin no 185, Engineering Experimental Station, University of Illinois. 1928.
[37] CEN. EN 12390-13:2013 - Testing hardened concrete - Part 13: Determination of secant modulus of elasticity in compression. 2013.
[38] CEN. EN 12390-3:2009 - Testing hardened concrete - Part 3: Compressive strength of test specimens. 2009.
[39] ASTM. D 3379 – 75 - Standard Test Method for Tensile Strength and Young's Modulus for High-Modulus Single-Filament Materials. 1989.
[40] S&P. Technical Data Sheet S&P Resin 55. 2015.
[41] Lim JC, Ozbakkaloglu T. Influence of silica fume on stress–strain behavior of FRP-confined HSC. Construction and Building Materials. 2014;63(Supplement C):11-24.

[42] Lim JC, Ozbakkaloglu T. Influence of concrete age on stress–strain behavior of FRP-confined normal- and high-strength concrete. Construction and Building Materials. 2015;82(Supplement C):61-70.
[43] Czél G, Jalalvand M, Wisnom MR, Czigány T. Design and characterisation of high performance, pseudo-ductile all-carbon/epoxy unidirectional hybrid composites. Composites Part B. 2017;111 348-56.
[44] IBM-Corp. IBM SPSS Statistics for Windows, Version 23.0. Armonk, NY: IBM Corp. 2015.
[45] Hinton PR, McMurray I, Brownlow C. SPSS explained. 2 ed: Routledge 27 Church Road, Hove, East Sussex BN3 2FA; 2014.

6. FINITE ELEMENT MODEL FOR HYBRID FRP-CONFINED CONCRETE

6.1. Introduction

In the last three decades, FRP composites have been used as jackets in the confinement of concrete columns. Today, it is known that FRP jackets allow concrete to reach higher compressive strength and higher ultimate axial and lateral strains, contributing to delay concrete cracking and preventing the relative displacement of disaggregated concrete pieces [1]. These confining systems are typically produced through the hand lay-up method [1]. Columns are retrofitted through FRP wrapping, positioning the fibres transversely oriented, relatively to the longitudinal axis of the column.

Although FRP systems have important advantages over traditional structural materials (such as lightweight, durability, high strength and stiffness), they also present a significant drawback: brittleness. In fact, a linear elastic behaviour up to failure is observed. For this reason, FRP-confined concrete submitted to pure compression fails abruptly, being this behaviour dominated by FRP failure. However, it was proved by Ribeiro *et al.* [2] that the drawback referred to can be mitigated through the hybridisation of reinforcing materials, i.e., by combining two different types of unidirectional (UD) dry fabrics in the same matrix (thus obtaining a hybrid FRP composite). If this combination of fibres is properly materialized, it is possible to promote synergies between the reinforcing materials, conducting, for instance, to pseudo-ductile tensile response (characterized by fragmentation in the low strain material and dispersed delamination, please see details in [3]), and an increase of the apparent failure strain of low strain fibres, known as 'hybrid effect'. Achieving pseudo-ductility may help composite structures to maintain functionality (even when they are overloaded) and to improve safety, thus enabling the reduction of the safety design factors.

Although there are already several examples of hybrid composites developed for civil engineering [4-20], the study of the same was initially motivated in the scope of aerospace and automotive industries [6, 21, 22]. Today, the last referred to industries continue to show the greatest interest in the subject. In this context, an exhaustive work to achieve pseudo-ductile tensile response with UD hybrid composites has been carried out [3, 23-28]. Research demonstrated that, to achieve pseudo-ductility in hybrid composites, two damage mechanisms should take place simultaneously, namely: (i) the fragmentation of the low strain (LS) material and (ii) the stable delamination of the LS material from the high strain (HS) material layers close to the LS material fractures. The described properties of hybrid composites were explored, for the first time, in the confinement of small-scale circular concrete columns in the work of Ribeiro *et al*. [2]. In this work, it has been demonstrated that an analysis-oriented confinement model, based on a modified approach of Lim and Ozbakkaloglu [29, 30] (incorporating the model of Jalalvand *et al*. [3] to simulate the tensile stress-strain curve of hybrid composite)

allows to accurately simulate both the dilation behaviour and the compressive stress-strain behaviour of all hybrid confined concrete series analysed.

According to the author's knowledge, up to the current date, an accurate finite element (FE) model to predict the hybrid FRP-confined concrete compressive behaviour has not been developed yet. As it is known, such models allow modelling the three-dimensional behaviour of confined concrete subjected to complex stress states. This is important, for instance, to simulate non-circular FRP-confined columns, since in this case the confining pressure provided by the jacket is non-uniform and analytical analysis-oriented models developed for circular confined concrete columns cannot be readily used [31]. In case of FRP-confined concrete columns under eccentric loading, three-dimensional FE models allow as well to overcome the difficulties associated with laboratory studies, namely the lack of information about the interaction mechanism between FRP and concrete and the distribution of axial stress and confining pressure over the section [32].

Recently, modified plasticity-damage models [31-34], based on the proposed models of Lubliner *et al*. [35] and Lee and Fenves [36], have been suggested as the best models to predict axial compression responses of FRP-confined concrete columns. To achieve this goal, the confinement-dependent characteristics of FRP-confined concrete have to be incorporated into the yield function, flow rule, and damage variable [31]. These modifications have been implemented within the theoretical framework of the concrete damaged plasticity model (CDPM) available in ABAQUS software [37]. More specifically, it is common the use of lateral strain-to-axial strain analytical models to compute the dilation angle and, consequently, to modify the flow rule in function of confining pressure and axial strain. Besides, compressive stress-strain analytical models have been used to compute the effective compressive cohesion stress (also known as strain-hardening/softening rule) for different levels of confinement [31]. Finally, the damage variable, which allows simulating the reduction of elastic stiffness of concrete, has been computed as well in function of the confining pressure. However, it has been proved that, in case of monotonic compression tests simulation, this parameter has little effect on the predicted stress-strain curve of FRP-confined concrete [33].

The aim of the present work is to develop and apply a modified CDPM for hybrid FRP-confined columns. The analysis-oriented model for hybrid FRP-confined concrete presented in the work of Ribeiro *et al*. [2], based on models of Lim and Ozbakkaloglu [29, 30], is adopted to compute all the necessary input parameters of the CDPM. ABAQUS software [37] was used to perform all the simulations. The modifications in the yield surface and flow rule were made through a user subroutine in order to redefine the field variables at material points (USDFLD). This type of subroutine allows users to define the values of field variables (in the present case, the confining pressure and the axial strain) directly at the integration points of FE. This was accomplished using tabular input and a FORTRAN code to define the field variables. The proposed modifications to improve the CDPM are discussed in detail in the following sections. Comparisons with experimental and analytical results show that the predictions of the proposed model are in close agreement with measured parameters.

6.2. Concrete damaged plasticity model

6.2.1. Theoretical background

The CDPM is a continuum plasticity-based damage model in which the concept of isotropic damaged elasticity in combination with isotropic plasticity is adopted [38]. In this way, the CDPM can be used for modelling the nonlinear deformation and irreversible damage, generally associated to cracking, of plain concrete with high accuracy [38]. As any other plasticity model, the CDPM depends on yield criterion, which is a mathematical description of the stresses under which yielding occurs (known as yield function), and the flow rule that establishes the general relations between plastic strains and the stress states.

The yield function is defined as follows:

$$F = \frac{1}{1-A}\left(\sqrt{3\bar{J}_2} - A\bar{I}_1 + B\langle -\bar{\sigma}_{min}\rangle - C\langle \bar{\sigma}_{min}\rangle\right) - \bar{\sigma}_{cn}\left(\tilde{\varepsilon}_{p,c}\right) = 0 \tag{6.1}$$

with

$$A = \frac{\frac{f_b}{f_{c0}} - 1}{2\frac{f_b}{f_{c0}} - 1}; 0 \leq A < 0.5 \tag{6.2}$$

$$B = \frac{\bar{\sigma}_{cn}\left(\tilde{\varepsilon}_{p,c}\right)}{\bar{\sigma}_{tn}\left(\tilde{\varepsilon}_{p,t}\right)}(1-A) - (1+A) \tag{6.3}$$

$$C = \frac{3(1-K)}{2K-1} \tag{6.4}$$

where $\bar{I}_1$ is the first effective stress invariant (see equation (6.5)) and $\bar{J}_2$ is the second effective deviatoric stress invariant (see equation (6.6)), the $\bar{\sigma}_{min}$ is the minimum principal effective stress, $\langle\cdot\rangle$ denotes the Macauley bracket defined as $\langle x\rangle = (|x| + x)/2$, f_b is the concrete strength under equal biaxial compression, f_{c0} is the peak stress of the unconfined concrete, $\bar{\sigma}_{cn}$ and $\bar{\sigma}_{tn}$ are the effective compressive and tensile cohesion stresses respectively, $\tilde{\varepsilon}_{p,c}$ and $\tilde{\varepsilon}_{p,t}$ are the equivalent compressive and tensile plastic strains respectively, and K is the strength ratio of concrete under equal biaxial compression to triaxial compression. It should be highlighted that throughout this work the soil mechanics sign convention is adopted, whereby compressive stresses/strains are considered positive while tensile stresses/strains are considered negative.

$$\bar{I}_1 = \bar{f}_c + \bar{f}_{l,1} + \bar{f}_{l,2} \tag{6.5}$$

$$\bar{J}_2 = \frac{(\bar{f}_c - \bar{f}_{l,1})^2 + (\bar{f}_{l,1} - \bar{f}_{l,2})^2 + (\bar{f}_{l,2} - \bar{f}_c)^2}{6} \tag{6.6}$$

where $\overline{f}_c$ is the effective principal compressive stress, $\overline{f}_{l,1}$ and $\overline{f}_{l,2}$ are the effective principal lateral stresses. Please note that, in the present chapter, only the case of triaxial compression is being considered.

The term effective stress is used because all the stress quantities are understood as:

$$\overline{f}_{ij} = \frac{f_{ij}}{1-d_{ij}} \tag{6.7}$$

where $\overline{f}_{ij}$ is the effective stress tensor, f_{ij} is the stress tensor (see equation (6.8)), and d_{ij} is the damage tensor which characterizes the degradation of the elastic stiffness.

$$f_{ij} = (1 - d_{ij}) D^e_{ijkl} (\varepsilon_{ij} - \varepsilon^p_{ij}) \tag{6.8}$$

where ε_{ij} and ε^p_{ij} are the strain and the plastic strain tensors and D^e_{ijkl} is the initial (undamaged) elasticity matrix.

For concrete with a constant confining pressure, the damage tensor is reduced to the compressive damage parameter [31]:

$$d_c = 1 - \frac{f_c - \frac{1+C+2A}{1-A} f_l}{f^*_{cc} - \frac{1+C+2A}{1-A} f_l} \tag{6.9}$$

where f_c is the compressive stress of concrete, f_l is the confining pressure, and f^*_{cc} is the peak stress of actively confined concrete and can be estimated using equation (6.10) [29, 39]:

$$f^*_{cc} = f_{c0} + 5.2 f_{c0}^{0.91} \left(\frac{f_l}{f_{c0}}\right)^a \text{ where } a = {f_{c0}}^{-0.06} \tag{6.10}$$

In the work of Hany *et al*. [33], it was stated that damage parameter has significant effect on the stress-strain curve when FRP-confined concrete is subjected to cyclic loading, but it is negligible for monotonic loading situations. In the present chapter, two scenarios were tested: (i) to adopt the damage parameter, according to equation (6.9), and (ii) to neglect the damage parameter. It was confirmed that, in both situations, no significant differences occurred. However, the damage parameter, computed according equation (6.9), was implemented in the final model.

The flow rule, $d\varepsilon^p_{ij}$, that defines the direction of plastic deformation and dictates the evolution of dilation behaviour of concrete is non-associated:

$$d\varepsilon^p_{ij} = \frac{\delta G}{\delta \sigma_{ij}} \tag{6.11}$$

where G is the Drucker-Prager hyperbolic function, defined by equation (6.12):

$$G = \sqrt{(\ni \sigma_{t0} tan\Psi)^2 + 3\overline{J}_2^{\,2}} - \frac{\overline{I}_1}{3} \tan \Psi \tag{6.12}$$

where σ_{to} is the uniaxial tensile stress at failure; ∋ is the eccentricity parameter, and Ψ is the plastic dilation angle, according to equation (6.13):

$$\tan\Psi = -\frac{3(\varepsilon_{c,p}+2\varepsilon_{l,p})}{2(\varepsilon_{c,p}-\varepsilon_{l,p})} \tag{6.13}$$

where $\varepsilon_{c,p}$ is the axial plastic strain and $\varepsilon_{l,p}$the lateral plastic strain.

For actively confined concrete, the referred to plastic strains can be computed according to equations (6.14) and (6.15) [34]:

$$\varepsilon_{c,p} = \varepsilon_c - \frac{1}{E_c}(f_c - 2\nu_i f_l) \tag{6.14}$$

$$\varepsilon_{l,p} = \varepsilon_l - \frac{1}{E_c}\left((1-\nu_i)f_l - \nu_i f_c\right) \tag{6.15}$$

where E_c is the elastic modulus of plain concrete and ν_i is the initial Poisson's ratio of concrete ($\varepsilon_l/\varepsilon_c$) [40]:

$$\nu_i = 8\times10^{-6}{f_{c0}}^2 + 0.0002f_{c0} + 0.138 \tag{6.16}$$

For concrete under non-uniform confinement, the confining pressure should be computed using the equation (6.17) [31]:

$$f_l = \frac{2(f_{l,1}+0.039f_{c0})(f_{l,2}+0.039f_{c0})}{f_{l,1}+f_{l,2}+2\times0.039f_{c0}} - 0.039f_{c0} \tag{6.17}$$

In the present chapter, since the compressive behaviour of confined small-scale plain circular concrete columns is analysed, it is expected that $f_l = f_{l,1} = f_{l,2}$. However, equation (6.17) was implemented in the final model in order to turn the same capable of simulating the compressive behaviour of concrete under non-uniform confinement.

6.2.2. Proposed modifications

It has been stated that original CDPM is not successful in predicting the compressive behaviour of actively confined concrete and, consequently, the passively confined concrete [31, 33, 34]. This is due to the fact that a unique stress-strain curve of plain concrete cannot be used to define the compressive cohesion stress, $\overline{\sigma}_{cn}$, or, in other words, the hardening rule of concrete. As discussed in Section 6.2.2.1, the hardening rule has to be dependent on the confining pressure, which leads to the modification of the original yield function. Furthermore, the plastic dilation angle should vary in function of lateral strain-axial strain curve, as discussed in Section 6.2.2.2.

6.2.2.1. Hardening/softening rule

In the present subsection, the modification of the hardening rule is proposed. Numerical predictions are compared with analytical results obtained through the stress-strain model for actively and passively confined concrete of Lim and Ozbakkaloglu [30]. These were computed

according to both equation (6.18), proposed by Popovics [41], and equation (6.19), proposed by Lim and Ozbakkaloglu [30]:

$$f_c = \frac{f_{cc}^* \left(\varepsilon_c / \varepsilon_{cc}^*\right) r}{r - 1 + \left(\varepsilon_c / \varepsilon_{cc}^*\right)^r}, \text{ if } 0 \le \varepsilon_c \le \varepsilon_{cc}^* \tag{6.18}$$

$$f_c = f_{cc}^* - \frac{f_{cc}^* - f_{c,res}}{1 + \left(\frac{\varepsilon_c - \varepsilon_{cc}^*}{\varepsilon_{c,i} - \varepsilon_{cc}^*}\right)^{-2}}, \text{ if } \varepsilon_c > \varepsilon_{cc}^* \tag{6.19}$$

where f_c and ε_c are the compressive stress and the axial strain of confined concrete, ε_{cc}^* is the peak strain of actively confined concrete [29, 39], r is the concrete brittleness [42], $f_{c,res}$ is the residual stress, and $\varepsilon_{c,i}$ is the axial strain corresponding to the inflection point of the descending branch of stress-strain curve [30]. These last parameters are defined in the next equations:

$$\varepsilon_{cc}^* = \varepsilon_{c0} + 0.045 \left(\frac{f_l}{f_{c0}}\right)^{1.15} \tag{6.20}$$

$$r = \frac{E_c}{E_c - f_{cc}^* / \varepsilon_{cc}^*} \tag{6.21}$$

$$f_{c,res} = 1.6 f_{cc}^* \left(\frac{{f_l}^{0.24}}{{f_{c0}}^{0.32}}\right) \text{ and } f_{c,res} \le f_{cc}^* - 0.15 f_{c0} \tag{6.22}$$

$$\varepsilon_{c,i} = 2.8 \varepsilon_{cc}^* \left(\frac{f_{c,res}}{f_{cc}^*}\right) {f_{c0}}^{-0.12} + 10 \varepsilon_{cc}^* \left(1 - \frac{f_{c,res}}{f_{cc}^*}\right) {f_{c0}}^{-0.47} \tag{6.23}$$

In equation (6.20), ε_{c0} is the axial strain at the peak stress of the unconfined concrete (f_{c0}) given by [29]:

$$\varepsilon_{c0} = \left(-0.067 {f_{c0}}^2 + 29.9 f_{c0} + 1053\right) \times 10^{-6} \tag{6.24}$$

In equation (6.21), E_c is defined according to the next equation [30]:

$$E_c = 4400 \sqrt{f_{c0}} \tag{6.25}$$

The model of Lim and Ozbakkaloglu [30] was used to define the compressive stress-strain curve of plain concrete, i.e., the material input data of the numerical model that gave rise to the results of **Figure 6.1** (a), assuming f_{c0} = 33.49 MPa and f_l = 0 MPa. Four levels of constant confining pressure were considered in both models (numerical and analytical): 5, 10, 20, and 30 MPa. This range was selected because it is intended to validate the proposed FE model against experimental results published in a previous work by the authors [2]. In the mentioned work, it is possible to observe that the ultimate confining pressure in tested specimens varied between 6 and 26 MPa, approximately. These values are within the considered range. The detailed description of the several parameters and assumptions used in FE modelling is present in Section 6.3.

In **Figure 6.1** (a) it is possible to observe that the shape of the numerical curves is the same for the different levels of confining pressure. According to the original CDPM, the increase of the

confining pressure imposes a vertical and horizontal translation of the compressive stress-strain curve. The former is dependent on the yield function, and the latter is defined by the elastic modulus of plain concrete, i.e., since the axial stress increases with the increase of the confining pressure, the initial elastic branch is prolonged, leading to the observable lateral translation of the initial stress-strain curve.

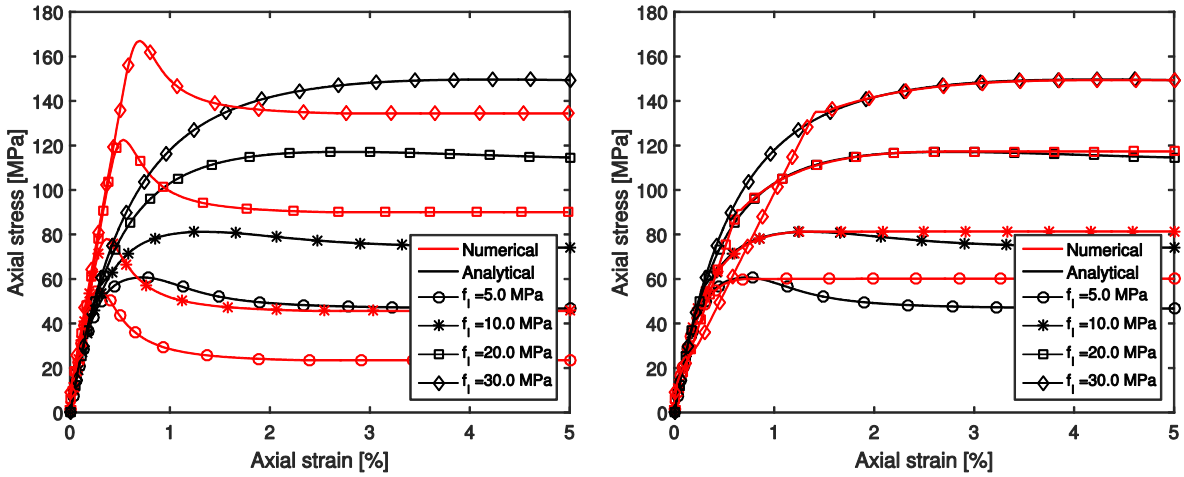

Figure 6.1 — Numerical versus analytical stress-strain curves of actively-confined concrete: (a) original and (b) modified CDPM.

In **Figure 6.1** (a) it is also demonstrated that original CDPM leads to inaccurate predictions of actively confined concrete compressive behaviour, for the presented levels of confining pressure. It should be noted that a large number of actively confined and FRP-confined specimen results were used in the development of the presented stress-strain analytical model. It was proved that the analytical model provides improved predictions when compared to the previous models presented in the literature, see the details in [29, 30]. For this reason, it was expected that the numerical curve matched the analytical one.

Due to the lack of the observed accuracy between the numerical and analytical curves, it is mandatory to turn the hardening rule dependent of the confining pressure in order to correct the results. In ABAQUS software [37] the introduction of the hardening rule is made in tabular format. To turn the hardening rule dependent on the confining pressure, several compressive stress-strain curves have to be defined in function of specific values of confining pressure. The last is considered a field variable that should be specified through USDFLD subroutine, programmed in FORTRAN language. Furthermore, the elastic modulus has to be modified, as well, in function of the confining pressure. The following procedure was used to correct the hardening rule:

i. The stress-strain analytical model, presented in equations (6.18) and (6.19), is used to define the expected compressive stress-strain curves of plain concrete subjected to different levels of constant confining pressure;
ii. The yield function, presented in equation (6.1), is used to define the value of f_c when the effective compressive cohesion stress is equal to zero;
iii. An actual elastic modulus is computed dividing the f_c value (obtained in step ii) by the corresponding strain;
iv. The strain that corresponds to the f_c value (obtained in step ii) is subtracted to all strain values of the compressive stress-strain curve computed in step i;
v. The f_c value (obtained in step ii) is subtracted to all stress values of the compressive stress-strain curve defined in step i;
vi. Since the strain that corresponds to the f_c value (defined in step ii) is a positive value and the same is subtracted to all strain values of stress-strain curve, negative strain values results from step iv. In this step, negative values are deleted.

It should be noted that the presented procedure is different from all others found in published studies. In the present chapter, the perfectly-plastic behaviour assumption used by Yu *et al.* [31] is assumed as well, i.e., after the peak stress, the stress-strain curve is truncated and the yield function remains unchanged. This option has implications in the dilation concrete behaviour predictions. If a complete stress-curve curve was considered, it would not be possible to control the concrete dilation behaviour.

In **Figure 6.1** (b) the numerical results obtained after the correction are presented and compared against analytical ones. It is possible to observe that after an initial branch, that was intentionally assumed as elastic, there is a perfect match between numerical and analytical curves until the peak stress is reached.

6.2.2.2. Flow rule

Many authors have used the CDPM assuming a constant Ψ [43-49]. However, this assumption does not lead to accurate prediction of the dilation behaviour (lateral strain-axial strain curves) of actively confined concrete, as demonstrated in **Figure 6.2** (a). In this case, a constant Ψ = 35º was assumed to obtain the lateral strain-axial strain numerical curves. As it is possible to observe, the last assumption leads to confining pressure having only a residual influence on the numerical curve developing. Therefore, all numerical curves are almost coincident and differ substantially from the analytical ones (presented as well in **Figure 6.2** (a)). The last was obtained with the model proposed by Lim and Ozbakkaloglu [29], see equation (6.26):

$$\varepsilon_c = \frac{\varepsilon_l}{\nu_i\left[1+\left(\frac{\varepsilon_l}{\nu_i\varepsilon_{c0}}\right)^n\right]^{1/n}} + 0.04{\varepsilon_l}^{0.7}\left[1+21\left(\frac{f_l}{f_{c0}}\right)^{0.8}\right] \tag{6.26}$$

where n is the curve shape parameter:

$$n = 1 + 0.03 f_{c0} \tag{6.27}$$

The analytical model was developed based on large database of unconfined and actively confined concrete results, please see the details in [29]. It was also proved that the model is able to predict the dilation behaviour of hybrid FRP confined concrete, please see details in [2].

Figure 6.2 (a) also shows that the numerical predictions of dilation behaviour of actively confined concrete are not in agreement with analytical ones. For this reason, they need to be corrected. This can be done considering the evolution of Ψ, according to equation (6.13). In **Figure 6.3** the referred evolution of Ψ is presented as a function of axial plastic strain (see equation (6.14)) for the considered levels of confining pressure. It is important to note that, according to the sign convention, lateral strain was considered negative and axial strains positive in the computation of Ψ.

Similarly to what was stated for the hardening rule, in ABAQUS software [24] the introduction of Ψ is also carried out in tabular format. However, the software only admits values of Ψ between 0.1º and 56º. This limitation implies that, even with the modification of Ψ, a precise dilation behaviour of confined concrete cannot be simulated. Since Ψ is negative in some cases and higher than 56º in others, it is possible to observe in **Figure 6.2** (b) that there are still some mismatches between numerical and analytical curves. However, the suggested modifications proved to be sufficient to reach good predictions of hybrid FRP confined concrete behaviour, as it is demonstrated in Section 6.4.

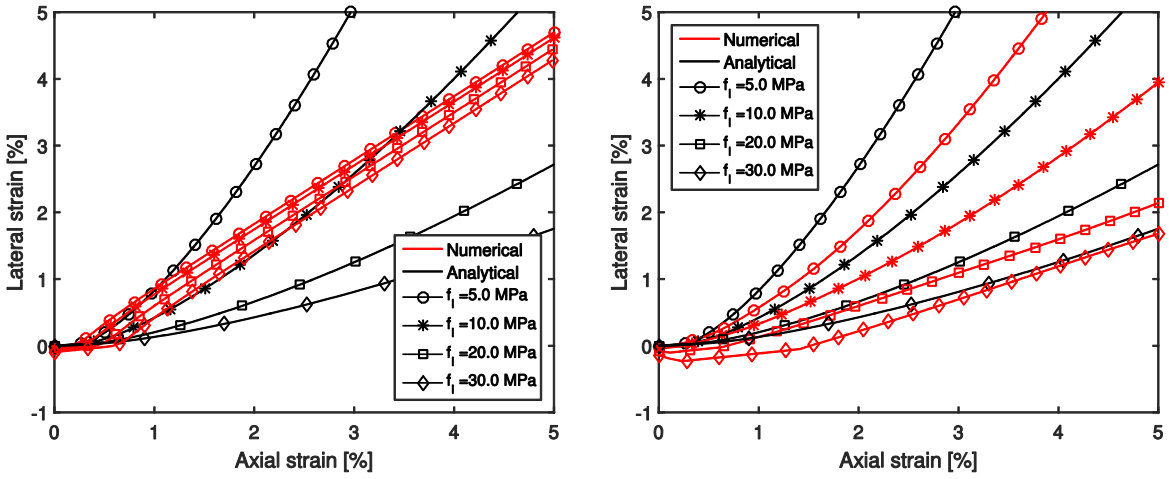

Figure 6.2 — Numerical *versus* analytical lateral strain-axial strain curves: (a) considering a constant dilation angle, and (b) considering variation of the dilation angle in function of level of confining pressure.

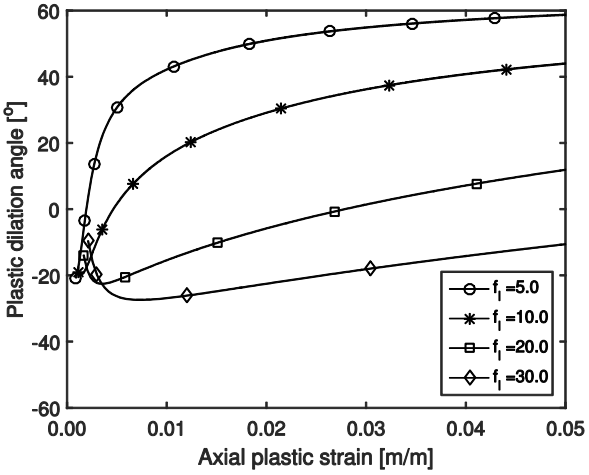

Figure 6.3 — Plastic dilation angle of actively-confined concrete in function of axial plastic strain for several levels of confining pressure.

6.3. Finite element modelling

6.3.1. Experimental database

In the present chapter, experimental results obtained in monotonic uniaxial compression tests of 60 cylindrical specimens, comprising 48 hybrid FRP-confined and 12 non-hybrid FRP-confined specimens, are compared with numerical predictions obtained with the suggested modified CDPM. Each tested specimen was 150 mm in diameter and 300 mm in height. The experimental variables included (i) the LS fibres relative volume (vol%) and (ii) the type of FRP of jacket, i.e., jackets made with different combinations of reinforcing materials. The details of the experimental results can be found in [2].

Four types of dry UD fabrics were used to produce the FRP jackets: UD HM carbon (S&P C-Sheet 640), ST carbon (S&P C-Sheet 240), E-glass (S&P G-sheet E 90/10), and basalt (Dalla Betta Group U400B-40-50-03) fabrics. In **Table 6.1** the density, areal mass, fibre layer thickness (areal mass density divided by the volumetric mass density) and the basic tensile properties of the mentioned materials are presented. For each dry fabric, a large number of single fibres (see the details in **Table 6.1**) were randomly taken from the dry fabrics and tested in uniaxial tension, according to ASTM D3379-75 [50].

The tensile properties of 1 layer non-hybrid composites, determined according to ISO 527-5:2009 [51], are also presented in **Table 6.1**. All the composites referred to in the present chapter were laminated using an epoxy-based resin (S&P Resin Epoxy 55). According to the supplier, this epoxy resin has the following main properties [52]: (i) 35.8 MPa tensile strength; (ii) 2.3% strain failure; and (iii) of 2.6 GPa elastic modulus.

In **Table 6.1**, it is possible to observe that tensile strength and, consequently, the elastic modulus of non-hybrid composites are higher than the values obtained for single fibres. This is due to

the fact that, in the case of composites, the tensile properties were evaluated ignoring the contribution of the resin, according to the usual practice of the wet lay-up method and guidelines [53]. This means that tensile strength was computed considering only the dry fabric thickness, thus leading to overestimation of the tensile strength.

Relatively to hybrid combinations, 16 series were considered in the confinement application: 10 combinations with 3 reinforcing material layers and 6 combinations with 5 reinforcing material layers. Each series was composed of 3 specimens of confined concrete. Specimens with 5 layers were tested only on 2 hybrid combinations: HM carbon/glass and ST carbon/glass.

In addition to hybrid series, 4 series of 3 layer non-hybrid composites (1 for each reinforcing material) were produced. All specimens involved in the experimental campaign are listed in **Table 6.2**. In the present chapter, regarding composite materials nomenclature, numbers placed before letters are used for indicating the number of layers. The sequence according to which these letters appear indicate the stacking sequence of the reinforcing materials. The relative volume of LS fibres (*Vol% LS*) was computed and presented in the next section, according to equation (6.28):

$$Vol\%\ LS = \frac{t_L}{t_L + t_H} \times 100 \tag{6.28}$$

where t_L is the half thickness of the LS layers and t_H is the half thickness of the HS layers.

Table 6.1 — Properties of the dry fabrics, fibres and cured composite materials determined experimentally.

Material ID	**Properties of the dry fabric, as reporter by the manufacturer**			**Properties of the fibres (tested according to ASTM D3379)**					**Properties of 1 ply composites [54]***		
	Density [g/m^3]	**Areal mass** [g/m^2]	**Fibre layer thickness** [mm/layer]	**N. of samples**	**Fibre diameter** [μm] (CoV [%])	**Elastic modulus** [GPa] (CoV [%])	**Tensile strength** [MPa] (CoV [%])	**Strain at the failure** [%] (CoV [%])	**Elastic modulus** [GPa] (CoV [%])	**Tensile strength** [MPa] (CoV [%])	**Strain at the strain** [%] (CoV [%])
Basalt (B)	2.67	420	0.157	50	18.14	61.41	1886.70	3.10	102.5	2244.2	2.46
					(3.56)	(31.14)	(40.79)	(27.73)	(15.46)	(20.17)	(10.61)
E-glass (G)	2.60	400	0.154	50	14.98	76.92	2662.06	3.72	81.6	1671.2	2.31
					(16.25)	(27.97)	(33.88)	(20.45)	(7.39)	(8.59)	(3.78)
ST carbon (C)	1.79	400	0.223	36	7.88	213.95	3920.67	1.38	231.3	2565.9	1.09
					(5.15)	(43.36)	(39.37)	(17.37)	(12.50)	(10.18)	(8.81)
HM carbon (CHM)	2.10	400	0.190	26	11.03	558.07	2934.24	0.53	624.1	1749.4	0.27
					(6.66)	(24.67)	(19.16)	(18.99)	(11.13)	(24.39)	(19.61)

Note: *The tensile properties were computed considering only the thickness of the dry fabrics, according the recommendation suggested in the guidelines [31].

Table 6.2 — Summary of tested compression specimens.

Jacketing type	Designation	Stacking sequence	Jacketing material combinations	Number of tests per type of stacking sequence
Non-hybrid	--	□□□	G, B, CHM, C	12
Hybrid	1LS/1HS/1LS	□■□	C/B, CHM/B, CHM/C, C/G, CHM/G	15
	1HS/3LS/1HS	■□□□■	C/G, CHM/G	6
	1HS/1LS/1HS/1LS/1HS	■□■□■	C/G, CHM/G	6
	1HS/1LS/1HS	■□■	C/B, CHM/B, CHM/C, C/G, CHM/G	15
	2HS/1LS/2HS	■■□■■	C/G, CHM/G	6

Notes: ■ – HS fibres layer; □ – LS fibres layer.

6.3.2. Geometry, element types and meshing

Taking into account the double symmetry of both the loading and the specimen, only a quarter of cylinders was modelled, as illustrated in **Figure 6.4**.

Two different FE types (three dimensional 8-node linear bricks with reduced integration (C3D8R) and 4-node shell elements with reduced integration (S4R)) were used to discretize the concrete cylinders and the FRP jacket, respectively.

Care was taken to ensure that the mesh had, as much as possible, a regular geometry. Several decreasing mesh sizes were studied to evaluate the convergence of the model. It was concluded that elements with edges of about 8 mm provide accurate solutions.

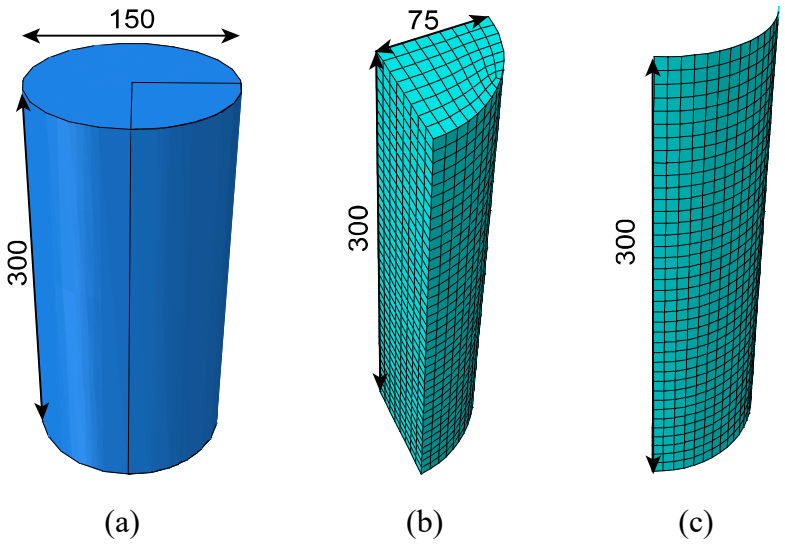

Figure 6.4 — Geometric representation of FE model: (a) full specimen, (b) mesh of 1/4 concrete specimen, and (c) mesh of 1/4 FRP jacket (dimensions in mm).

6.3.3. Boundary conditions and interactions

Traditionally, in uniaxial compression tests of concrete specimens, the load is applied through rigid steel plates. In this way, it is inevitable frictional forces to occur at the concrete–steel interface. These forces lead to the development of a stress field which restrains the transverse expansion of concrete within the end regions of specimens [55].

In this section, it is discussed if the detail of surface-to-surface contact (steel–concrete) should or should not be considered in the numerical model. Thus, two scenarios were considered in the simulation of compressive behaviour of plain concrete:

- In the first scenario, three dimensional steel plates with the same cross section as concrete and 50 mm of thickness were assembled to the ends of the concrete core. C3D8R elements were used to discretize the steel plates. It was assumed that these elements are rigid. A friction model to define the force resisting relative to tangential motion between concrete and steel plates was specified. A friction coefficient of 0.1 was assumed, according to the recommendation suggested in the guideline [56]. In normal direction (i.e., in the loading direction) a hard contact was defined. It was concluded that the consideration of end restrains leads to highly non-uniform distribution of lateral displacements, as shown in **Figure 6.5** (a). It is possible to observe that at middle height of the cylinder, the lateral deformation is maximum. The presented values of lateral displacement are relative to the peak axial stress of plain concrete;
- In the second scenario, the end restrains were not detailed. This leads to uniform distribution of lateral displacement, as shown in **Figure 6.5** (b). It is possible to observe that the values of lateral displacement are approximately 14% lower than the ones observed in the first scenario, comparing the middle sections, for the same axial displacement.

It should be noted that, in both scenarios, compatible boundary conditions with the simplifications of the geometry assumed in the model were defined, i.e., lateral displacement restraints were applied orthogonally to the sliced faces. Axial displacements were restrained in the base of the model and uniformly imposed on the top the latter. Again, the model of Lim and Ozbakkaloglu [30] was used to define the compressive stress-strain curve of plain concrete, assuming f_{c0} = 33.49 MPa and f_l = 0.00 MPa.

Analytical axial stress-strain curves are compared with numerical ones in **Figure 6.6**. Since the analytical model of Lim and Ozbakkaloglu [30] was used to define compressive stress-strain curve of plain concrete and there is no other action on the concrete than axial compression (in the case frictional forces were not contemplated), it was expected that both numerical and analytical curves were coincident.

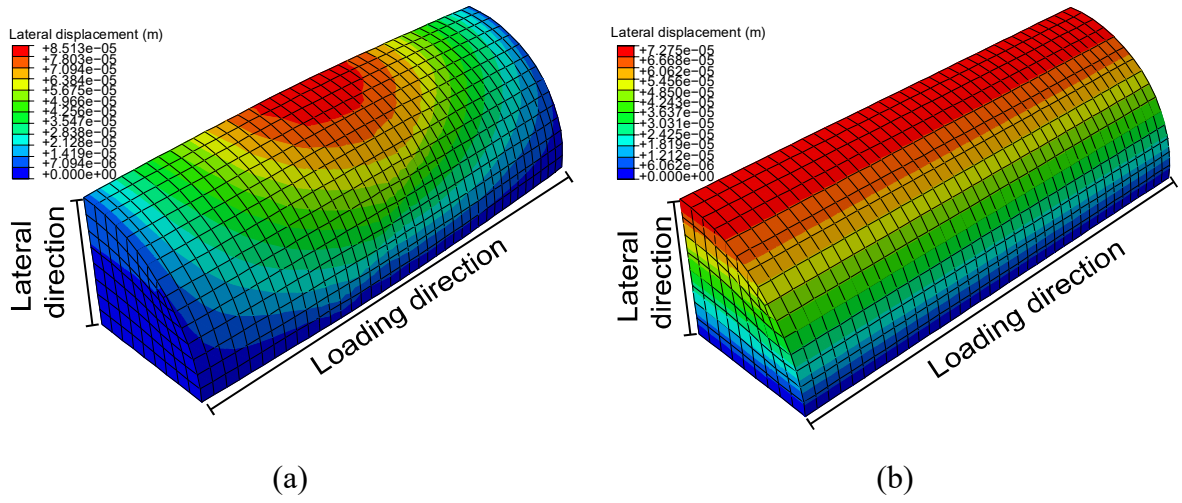

(a) (b)

Figure 6.5 — Distribution of lateral displacement of plain concrete at the peak stress in one of the two lateral principal stress directions: (a) considering frictional forces and (b) without considering frictional forces.

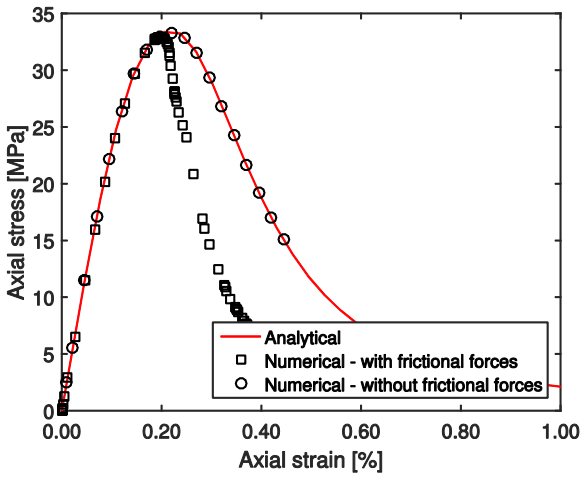

Figure 6.6 — Evaluation of the effect of end restrains contemplation in the compressive stress-strain curve of plain concrete.

It is possible to conclude that end restraints have no influence in the pre-ultimate compressive response of concrete and strength predictions but the post peak behaviour of concrete is dependent of friction between concrete and steel plates.

It should be highlighted that the analytical model of Lim and Ozbakkaloglu [30] was calibrated from experimental results in which the influence of end restraints were not suppressed. In this way, the obtained stress-strain curve implicitly considers the effect of end restraints. For this reason, it is not correct to consider the detail of end restraints in the numerical model, if the

referred to analytical model is used to obtain the material input parameters of concrete. Otherwise, the end restraints effect would be contemplated twice.

Due to the above reasons, the influence of end restraints were not explicitly considered in the present chapter.

6.3.4. Plasticity parameters

Beyond hardening and flow rules, there are several parameters that have to be specified in order to use the CDPM, namely ∋, f_b/f_{c0}, viscosity, and K.

According to published studies [31, 32, 57], ∋ and f_b/f_{c0} should be defined as 0.00 and 1.16, respectively. The definition of ∋ as null implies that the potential function tends to a straight line. In this way, the strategy exposed in section 6.2.2.2 to compute Ψ and to predict the dilation behaviour of concrete is valid. According to the work of Kupfer *et al*. [58], f_b/f_{c0} assumes a constant value of 1.16. However, in the work of Papanikolaou and Kappos [59] it was suggested that f_b/f_{c0} should vary according to equation (6.29):

$$\frac{f_b}{f_{c0}} = 1.5 \times {f_{c0}}^{-0.075} \tag{6.29}$$

According to this equation, if f_{c0} varies between 19 and 30 MPa, f_b/f_{c0} will vary approximately between 1.16 and 1.20. Teng *et al*. [57] found that, within this range, the variation of f_b/f_{c0} has no significant effect on the numerical predictions. Due to the lack of information about the subject, and taking into account that 1.16 is the most used value in published studies, it was decided to maintain this value in the present chapter.

Few studies [33, 60] on the viscosity parameter state that it has residual influence on the prediction's accuracy. For this reason, this parameter was ignored in the present chapter.

Although the influence of K on the compressive behaviour predictions of confined concrete was studied in the present chapter, since only triaxial compression situations are analysed, a simplification of equation (6.1) was adopted [31]:

$$\left(\frac{1}{3}C + 1\right)\sqrt{3\bar{J}_2} - \frac{(C+3A)}{3}\bar{I}_1 = (1-A)\bar{\sigma}_{cn} \tag{6.30}$$

This equation is known as Drucker-Prager yield function and it defines a conic yield surface in the principal stress space, as presented in **Figure 6.7** (a). It is possible to observe that changing the value of K leads to substantial changes in the diameter of the yield surface, as seen for instance in the deviatoric plane defined as $\bar{I}_1/3 = 100$ (see **Figure 6.7** (b)).

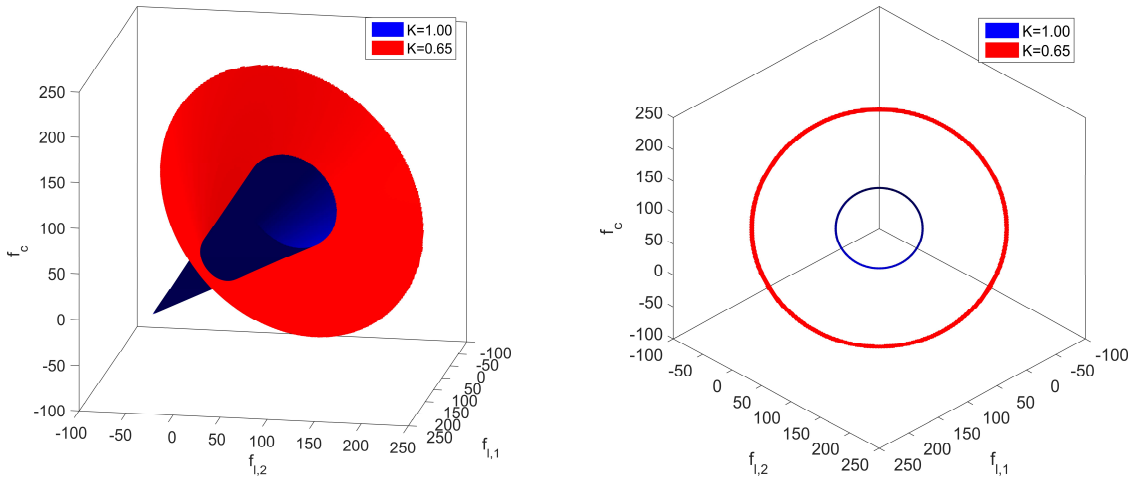

Figure 6.7 — Influence of K the yield surface of CDPM: (a) principal stress space and (b) deviatoric plane ($(f_c+f_{l,1}+f_{l,2})/3=100$).

In **Figure 6.8**, it is possible to observe that, for a constant level of confining pressure ($f_l = f_{l,1} = f_{l,2}$), the peak stress of confined concrete (f_{cc}^*) decreases with the increase of K. A sensitivity analysis was carried out to find out the value of K leading to lowest initial prediction errors of the peak stress of actively confined concrete. From this analysis, it was concluded that $K = 0.68$ leads to the lowest differences between unmodified CDPM and analytical peak stress predictions. For this reason, this value (0.68) was assumed in the present chapter.

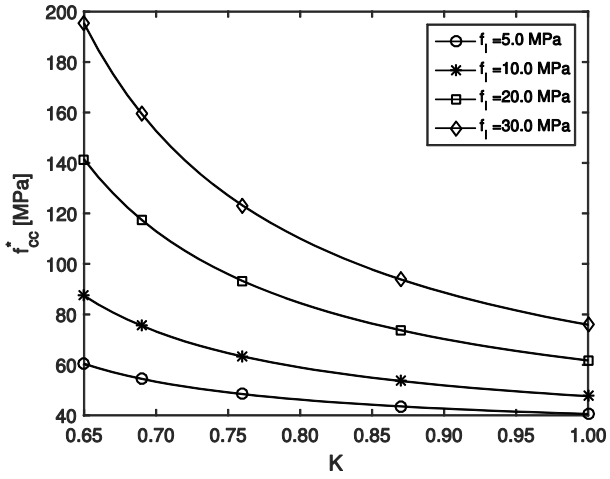

Figure 6.8 — Peak stress of actively confined concrete in function of f_l and K.

6.3.5. Material properties

6.3.5.1. FRP

In a unidirectional (UD) hybrid FRP submitted to uniaxial tension, the first damage mode is always the failure of the LS fibres. However, other damage modes depend on the properties and configuration of the composite reinforcing materials [25]. The analytical approach proposed by Jalalvand *et al*. [3], validated in the scope of the present work in [54], considers that four different damage modes may occur after LS fibres failure: (i) premature HS failure, (ii) unstable delamination, (iii) LS layer fragmentation, and (iv) combination of LS fragmentation with stable delamination. For each hybrid configuration, three stress levels can be computed [3]: (i) the stress at which the first crack in the LS material occurs, *σ@LF*, (ii) the stress at which delamination starts, *σ@del*, and (iii) the stress at which the HS material fails, *σ@HF*, in accordance with equations (6.31) to (6.33), respectively.

$$\sigma@LF = S_L \frac{\alpha\beta+1}{\alpha(\beta+1)} \tag{6.31}$$

$$\sigma@del = \frac{1}{1+\beta}\sqrt{\left(\frac{1+\alpha\beta}{\alpha\beta}\right)\left(\frac{2G_{IIC}E_H}{t_H}\right)} \tag{6.32}$$

$$\sigma@HF = \frac{1}{(1+\beta)}\frac{S_H}{K_t \sqrt[m_H]{V}} \tag{6.33}$$

where S_L is the reference strength of the LS material, α and β are respectively the elastic modulus and thickness ratios of the LS to HS fibre, G_{IIC} is the mode II interlaminar fracture toughness of the interface between LS layers and HS layers of the hybrid composite, E_H is the elastic modulus of the HS fibres, t_H is the half thickness of the HS fibre, m_H is the Weibull strength distribution modulus of the HS fibre, S_H is the reference strength of the HS material, K_t is the stress concentration factor in the high strain material, and V is the volume of the specimen (free length × width × total fibre layer thickness). The details of the adopted parameters are fully discussed in [54].

Knowing the magnitude of all three possible stresses allows assessing their order of occurrence and, consecutively, the identification of the damage modes, according to **Table 6.3**. In the present case, the studied combinations of materials (presented in **Table 6.4**) lead to the appearance of 3 damage modes, namely premature failure, catastrophic delamination and combination of fragmentation of LS material and dispersed delamination. When the last damage mode occurs, the behaviour of hybrid composite is pseudo-ductile because a flat-topped stress-strain curve is achieved.

As it has been exposed in [54], the damage mode of 2G/1CHM/2G, 1G/1CHM/1G, 1B/1CHM/1B and 1C/1CHM/1C series was combination of fragmentation and dispersed delamination and, in the case of 1G/1CHM/1G/1CHM/1G and 1G/3CHM/1G series, catastrophic delamination occurred. In the remaining cases, the damage mode was premature failure.

Table 6.3 — Summary of different damage modes as a function of stress level (adapted from [25]).

Damage mode	Stress level
Premature failure	$\sigma@HF \leq \sigma@LF \leq \sigma@del$
Catastrophic delamination	$\sigma@HF \leq \sigma@del \leq \sigma@LF$
	$\sigma@del \leq \sigma@HF \leq \sigma@LF$
	$\sigma@del \leq \sigma@LF \leq \sigma@HF$
Fragmentation	$\sigma@LF \leq \sigma@HF \leq \sigma@del$
Fragmentation & dispersed delamination	$\sigma@LF \leq \sigma@del \leq \sigma@HF$

After the determination of the damage modes, it is possible to plot the tensile stress–strain curve of hybrid FRP. Five stress-strain coordinates are sufficient to define all possible tensile stress-strain curves of hybrid FRP, see **Figure 6.9**. The sets of coordinates that define the stress-strain curves for all the studied combinations are presented in **Table 6.4**. Please note that, when premature failure occurs, only the linear elastic branch is defined with two sets of stress-strains coordinates.

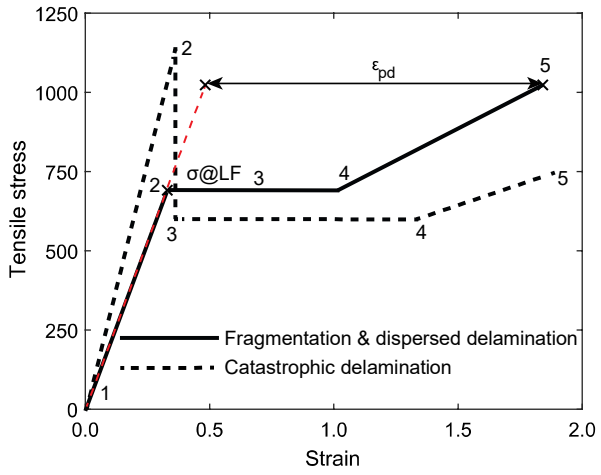

Figure 6.9 — Tensile nonlinear behaviour of hybrid FRP.

The FRP properties were specified using "Lamina" material type [37] in which the elastic modulus in the fibre direction is defined in accordance with the value provided in **Table 6.1**, in case of non-hybrid confinement, and **Table 6.4**, in case of hybrid confinement. In the orthogonal direction, an almost null elastic modulus (0.001 GPa) was assigned, and the Poisson's ratio was set equal to zero. Tie constraint was used to model the interaction between FRP jackets and concrete.

Table 6.4 — Tensile properties of hybrid FRP composites [54].

Combination	Series ID	Volume of LS fibres [%]	Elastic modulus [GPa]	t_{FRP} [mm]	Tensile stress-strain analytical curve									
					Point 1		Point 2		Point 3		Point 3		Point 5	
					Strain [%]	Stress [MPa]	Strain [%]	Stress [MPa]	Strain [%]	Stress [MPa]	Strain [%]	Stress [MPa]	Strain [%]	Stress [MPa]
C/B	1C/1B/1C	74.0	218.4	0.60	0.00	0.0	0.99	1957.9	--	--	--	--	--	--
	1B/1C/1B	41.5	152.5	0.54	0.00	0.0	1.28	1996.6	--	--	--	--	--	--
CHM/B	1CHM/1B/1CHM	70.8	474.1	0.54	0.00	0.0	0.24	1131.8	--	--	--	--	--	--
	1B/1CHM/1B	37.7	297.4	0.50	0.00	0.0	0.36	1077.0	1.17	1077.0	1.73	1106.0	2.03	1152.3
CHM/C	1CHM/1C/1CHM	63.0	489.6	0.60	0.00	0.0	0.27	1292.7	--	--	--	--	--	--
	1C/1CHM/1C	29.5	368.8	0.64	0.00	0.0	0.39	1359.8	0.66	1359.8	0.95	1544.3	0.94	1544.9
C/G	1C/1G/1C	74.3	201.7	0.60	0.00	0.0	1.04	2005.5	--	--	--	--	--	--
	1G/3C/1G	68.5	202.4	0.98	0.00	0.0	1.08	1988.4	--	--	--	--	--	--
	1G/1C/1G/1C/1G	49.1	148.9	0.91	0.00	0.0	1.19	1830.5	--	--	--	--	--	--
	1G/1C/1G	42.0	146.7	0.53	0.00	0.0	1.27	1820.3	--	--	--	--	--	--
	2G/1C/2G	26.6	110.8	0.84	0.00	0.0	1.18	1420.3	--	--	--	--	--	--
CHM/G	1CHM/1G/1CHM	71.2	454.5	0.53	0.00	0.0	0.25	1201.9	--	--	--	--	--	--
	1G/3CHM/1G	64.9	439.2	0.88	0.00	0.0	0.23	997.7	0.23	451.5	1.58	451.5	1.91	483.5
	1G/1CHM/1G/1CHM/1G	45.1	318.7	0.84	0.00	0.0	0.35	1142.5	0.35	599.9	1.34	599.9	1.88	745.8
	1G/1CHM/1G	38.2	252.0	0.50	0.00	0.0	0.30	846.2	1.14	846.2	1.68	846.9	1.91	852.4
	2G/1CHM/2G	23.6	214.3	0.81	0.00	0.0	0.33	691.3	0.81	691.3	1.29	802.1	1.86	1028.7

For all non-hybrid as well as for hybrid composites in which premature failure occurred, only elastic properties were defined. For the remaining cases, a plastic behaviour was defined using as input the coordinates exposed in **Table 6.4**. In these cases, strains have to be converted first in plastic strains, according to equation (6.34):

$$\varepsilon_{t,hybrid}^{pl} = \varepsilon_{t,hybrid} - {}^{\sigma_{hybrid}}/_{E_{hybrid}} \tag{6.34}$$

where $\varepsilon_{t,hybrid}^{pl}$ is the tensile plastic strain, $\varepsilon_{t,hybrid}$ is the total tensile stain, σ_{hyb} is the tensile stress, and E_{hybrid} is the elastic modulus of hybrid composite.

All simulations carried out showed that the tensile behaviour of both 1G/1CHM/1G/1CHM/1G and 1G/3CHM/1G series has to be defined as linear elastic, otherwise the numerical analysis will abort. This is due to the fact that the stress drop that occurs in the stress-strain curve of these series leads to convergence errors.

6.3.5.2. Concrete

A ready-mix concrete was used in the experimental campaign [2]. The experimental campaign of the confined concrete specimens herein described was conducted in 15 consecutives working days. During this time, the concrete age varied between 294 and 315 days. Until the testing date, all specimens were kept in standard laboratory conditions (temperature of circa 20 ºC, and relative humidity of approximately 50%). In the end, three identical plain cylindrical concrete specimens were submitted to compressive tests. The mean values of the elastic modulus, according to [61], and compressive strength, according to [62], were 30.29 GPa (CoV = 6.57%) and 33.49 MPa (CoV = 1.33%), respectively.

In ABAQUS software [37], two parameters are needed to describe the elastic behaviour of concrete: (i) the elastic modulus, and (ii) the Poisson's ratio. Equations (6.25) and (6.16) were used to define these parameters, in order to maintain coherence with the analytical model that was used to calibrate the numerical parameters.

Although the tensile behaviour of concrete is not important for the simulations conducted in the present study, it was defined aiming at widening the field of application of the model. The parameters required to define the tensile behaviour (the tensile strength, f_t, and the fracture energy, G_F) were obtained according to equations (6.35) and (6.36) [32]:

$$f_t = 1.4\left(\frac{f_{c0}-8}{10}\right)^{2/3} \tag{6.35}$$

$$G_F = (0.0469d_a^2 - 0.5d_a + 26)\left(\frac{f_{c0}}{10}\right)^{0.7} \tag{6.36}$$

where d_a is the maximum aggregate size (assumed to be 12.5 mm in the present chapter). In the last equation, f_{c0} is in MPa and d_a is in millimetres. In this way, f_t, obtained from equation (6.35), is in MPa and G_F, obtained from equation (6.36), is in N/m.

The parameters used to define the non-linear compressive behaviour are already detailed in sections 6.2.2 and 6.3.4.

6.4. Comparison of FE model predictions with experimental results

The performance of the proposed CDPM is validated with the experimental results described in Section 6.3.1. In the work of Ribeiro *et al*. [2], it has already been proven that the analytical model here presented allows to accurately simulate both the dilation behaviour and the compressive stress-strain behaviour of all confined concrete specimens analysed. Since the material parameters for the modified CDPM were obtained from the referred to analytical model, predictions obtained with both models (analytical and numerical) are expected to have similar accuracy.

6.4.1. Non-hybrid FRP-confined concrete

In **Figure 6.10** the evolution of Ψ for the studied non-hybrid FRP-confined concrete combinations is presented. This parameter was computed according to equations (6.13) and (6.26) and it was introduced in CDPM in order to define the flow rule, taking into account the software limitations exposed in Section 6.2.2.2, i.e., negative values and values higher than 56º were not considered. Although, in the computation of Ψ, an infinite axial tensile strain was assumed to generate the input parameters, then the peak axial strain (ε_{cc}) of different combinations was assumed as the of the corresponding main experimental value.

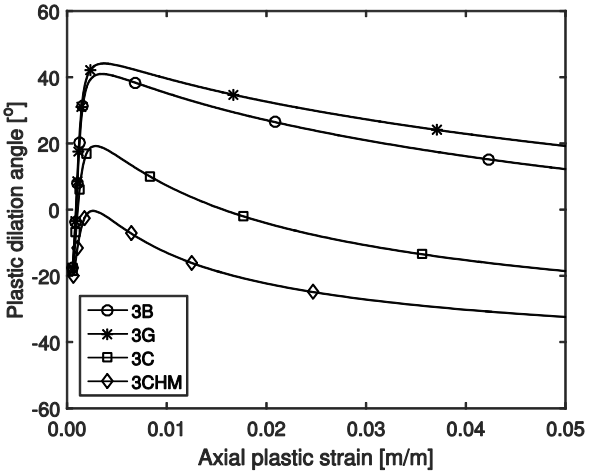

Figure 6.10 — Plastic dilation angle of non-hybrid FRP-confined concrete in function of axial plastic strain.

In **Figure 6.11** and **Figure 6.12** the lateral strain-axial strain and the compressive stress-strain curves of non-hybrid FRP-confined concrete are presented. In the specimen designation, the last number (i.e., 1, 2 or 3) was used to make the distinction between the three identical specimens. Analytical and numerical curves are also plotted to allow the comparison with the corresponding experimental curves. A good agreement between theoretical and experimental results is observed.

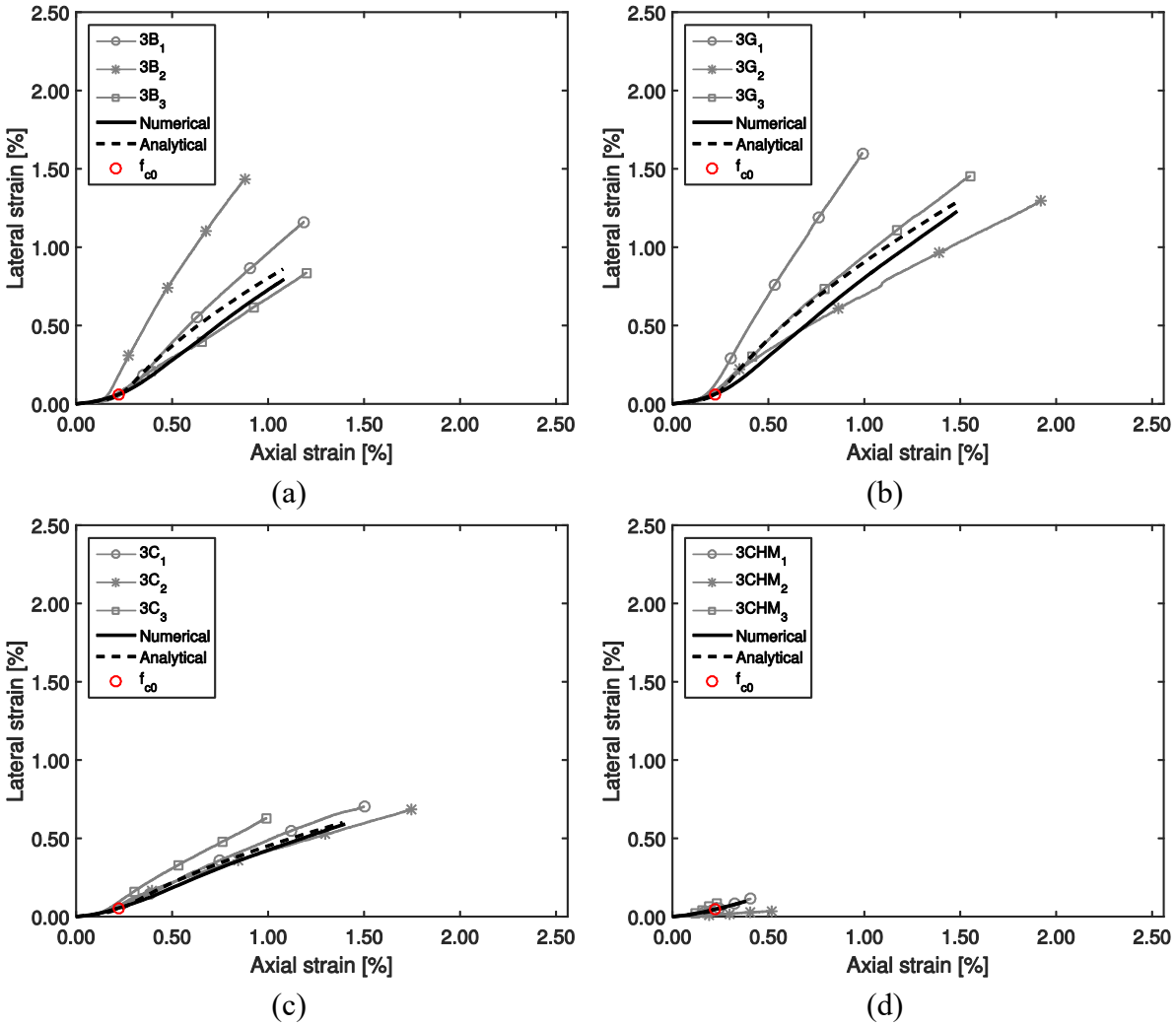

Figure 6.11 — Lateral strain-axial strain curves: (a) basalt; (b) glass; (c) ST carbon and (d) HM carbon composite confined concrete.

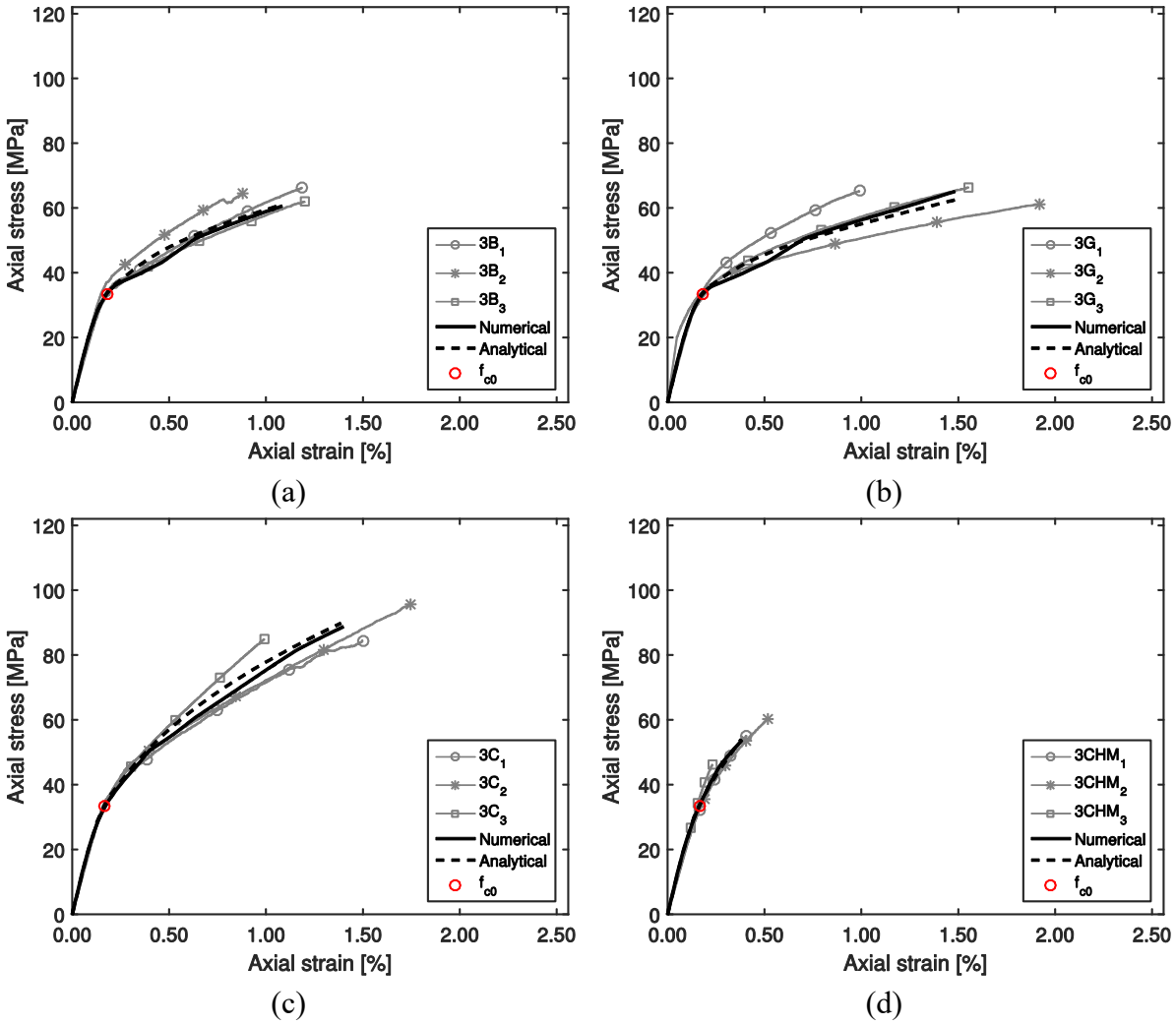

Figure 6.12 — Axial stress-strain curves: (a) basalt; (b) glass; (c) ST carbon and (d) HM carbon composite confined concrete.

As expected, all the numerical predictions obtained using the proposed modified CDPM are in close agreement with test results. Nevertheless, some differences are observed between analytical and numerical values. This is essentially due to two factors: (i) the allowed range of Ψ have influence in the prediction of lateral strain-axial strain curves and (ii) the fact that stress-strain curves of FRP-confined concrete are interpolated from a reduced and fixed number of stress-strain curves for actively confined concrete (see **Figure 6.1** (b)) leads to slope variations after the compressive stress-strain peak of plain concrete (f_{c0}, ε_{c0}), represented in simulations with a red circle.

As expected, the development of the compressive stress-strain curves follows approximately a bilinear law, where the slope of the first branch depends primarily on the properties of plain concrete. For this reason, the initial phase of the curves is similar for all combinations. The

second branch depends on the confining pressure applied by the confining materials. The higher the elastic modulus of the jacket, the higher the slope of the second branch.

6.4.2. Hybrid FRP-confined concrete

All the Ψ-axial plastic strain curves used as input in the simulation of compressive behaviour of hybrid FRP-confined concrete are presented in **Figure 6.13**. It is possible to observe that, in hybrid jackets with non-linear tensile behaviour (see **Table 6.4**) there is an increase of Ψ comparatively to cases in which premature failure of hybrid composites take place. This is due to the fact that tensile non-linear behaviour of jackets allows the rapid increase of the lateral strain of concrete, and, consequently the increase of Ψ. Again, it should be noted that in the computation of Ψ, an infinite tensile strain of hybrid FRP was assumed. However, the numerical simulations were interrupted when ε_{cc} was reached.

Experimental lateral strain-axial strain and compressive stress-strain curves of hybrid FRP-confined are compared with corresponding analytical and numerical curves in **Figure 6.14** to **Figure 6.23**. It is possible to observe that predictions are generally in reasonable agreement with test results.

It is also possible to observe that pseudo-ductile branches were predicted in 3 combinations, namely in 2G/1CHM/G, 1G/1CHM/1G, and 1B/1CHM/1B. This was expected since pseudo-ductile tensile responses (i.e., simultaneous multiple fractures of LS fibres and dispersed delamination) occurred in tensile tests of these combinations [54]. Although pseudo-ductile tensile response has occurred as well in 1C/1CHM/1C combination [54], this behaviour did not have a significant influence in the compressive results. This is due to the fact that (i) pseudo-ductile strain (defined as the extra strain between the final failure strain and the strain on the extrapolated initial slope line at the failure stress of the stress-strain diagram, as it is shown in **Figure 6.9**) of this combination is very low, and (ii) the hybrid FRP failure of the jacket occurred sooner that it was expected [2]. In this way, the application in practice of this combination in confinement would lead to fragile failures.

The predicted tensile behaviour of 1G/1CHM/1G/1CHM/1G and 1G/3CHM/1G combinations indicates catastrophic delamination modes, meaning that there is an abrupt drop of stress after the failure of LS fibres. This leads to compressive behaviour of confined concrete very similar to the one that is obtained in non-hybrid FRP-confined concrete series, when these combinations are used as confining materials, as it is evident from experimental results.

In the remaining cases, stress-strain curves development follows approximately a bilinear law, similarly to what was observed in non-hybrid FRP-confined concrete series. Please note that, in combination 1C/1B/1C, there are two outlier experimental results which were therefore ignored.

In all cases, analytical and numerical curves are almost coincident. This validates the strategy of CDPM modification that is proposed in the present chapter.

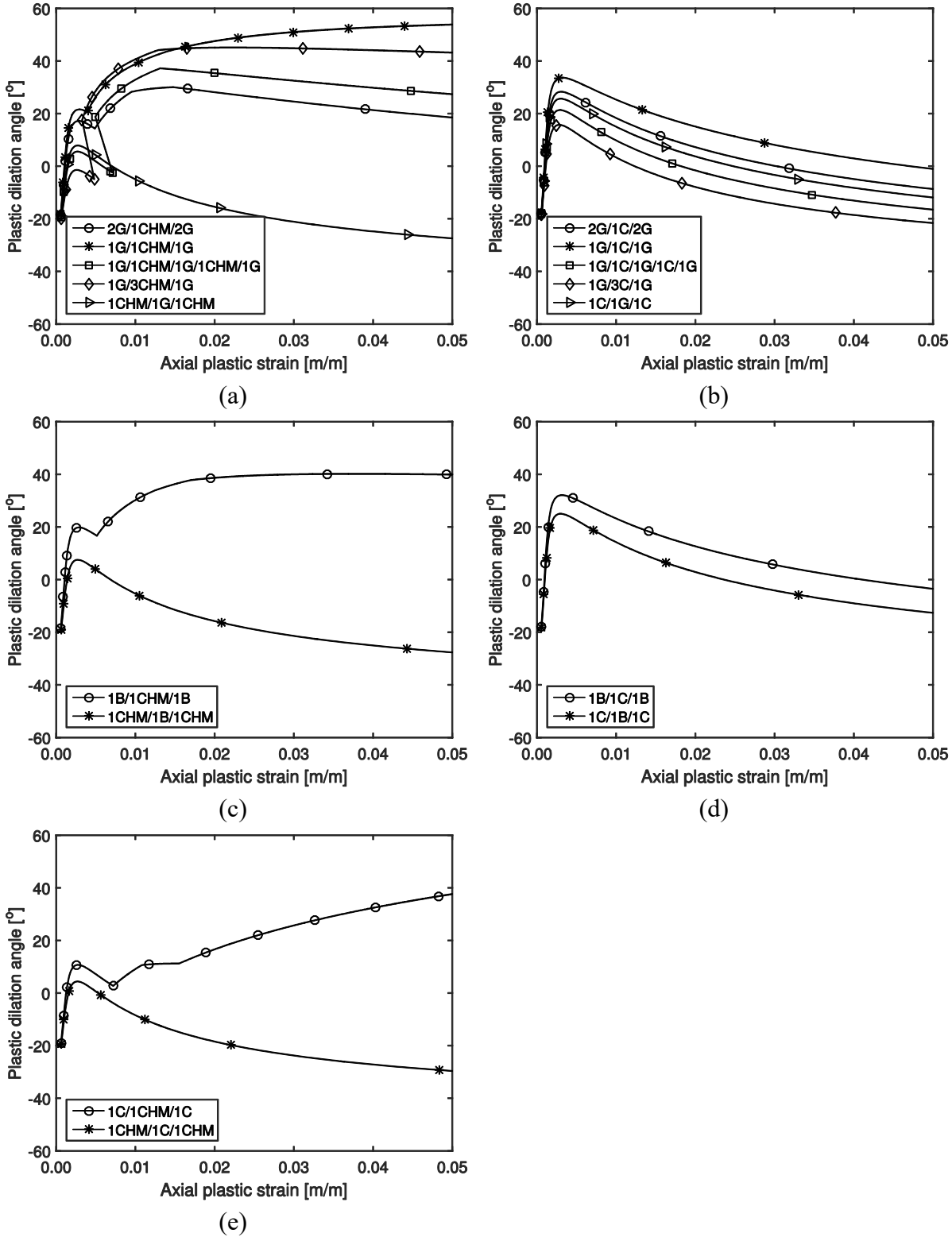

Figure 6.13 — Plastic dilation angle of hybrid FRP-confined concrete in function of axial plastic strain: (a) HM carbon/glass; (b) ST carbon/glass; (c) HM carbon/basalt; (d) ST carbon/basalt and (e) HM carbon/ST carbon composites.

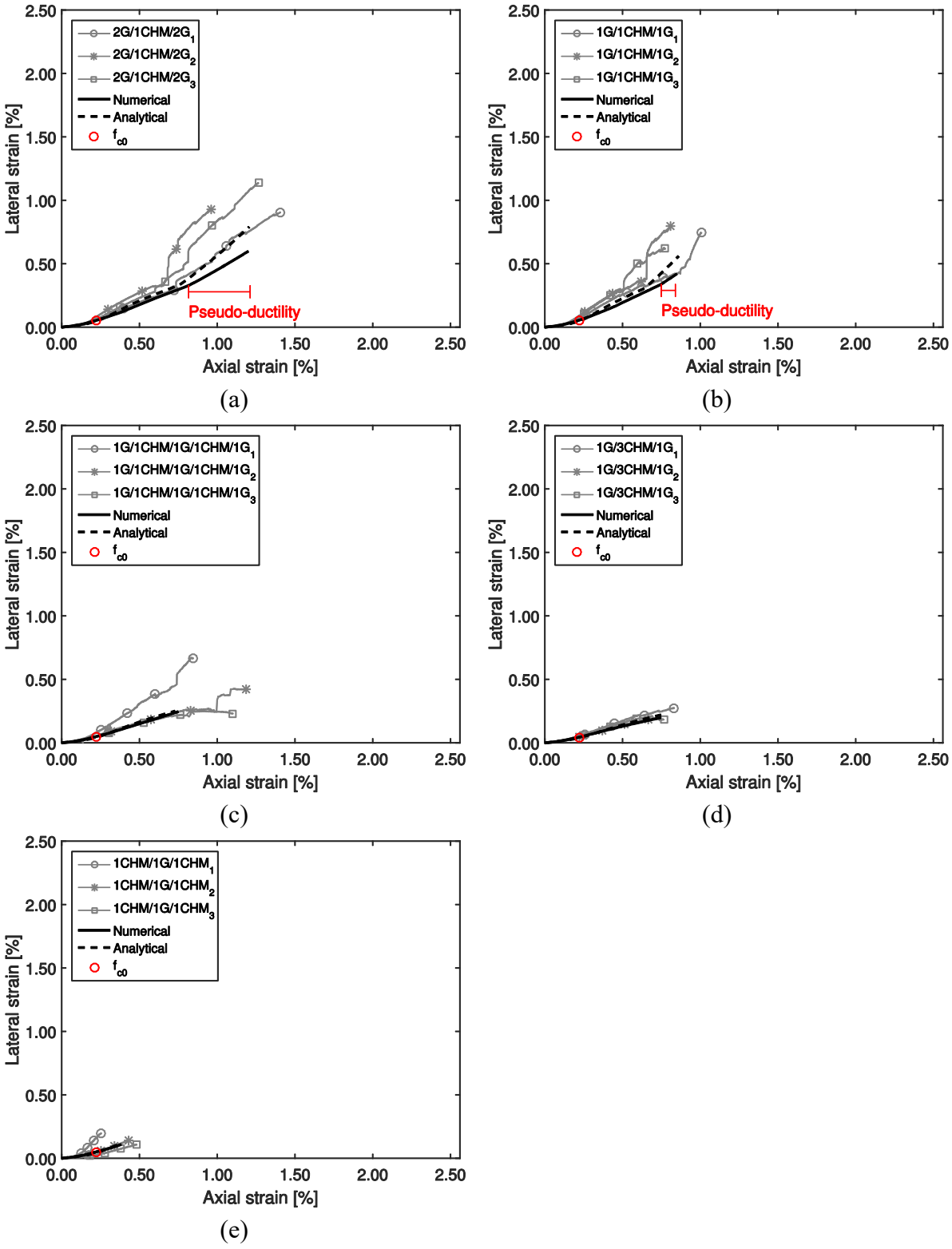

Figure 6.14 — Lateral strain-axial strain curves of CHM/G combinations: experimental *versus* predicted values.

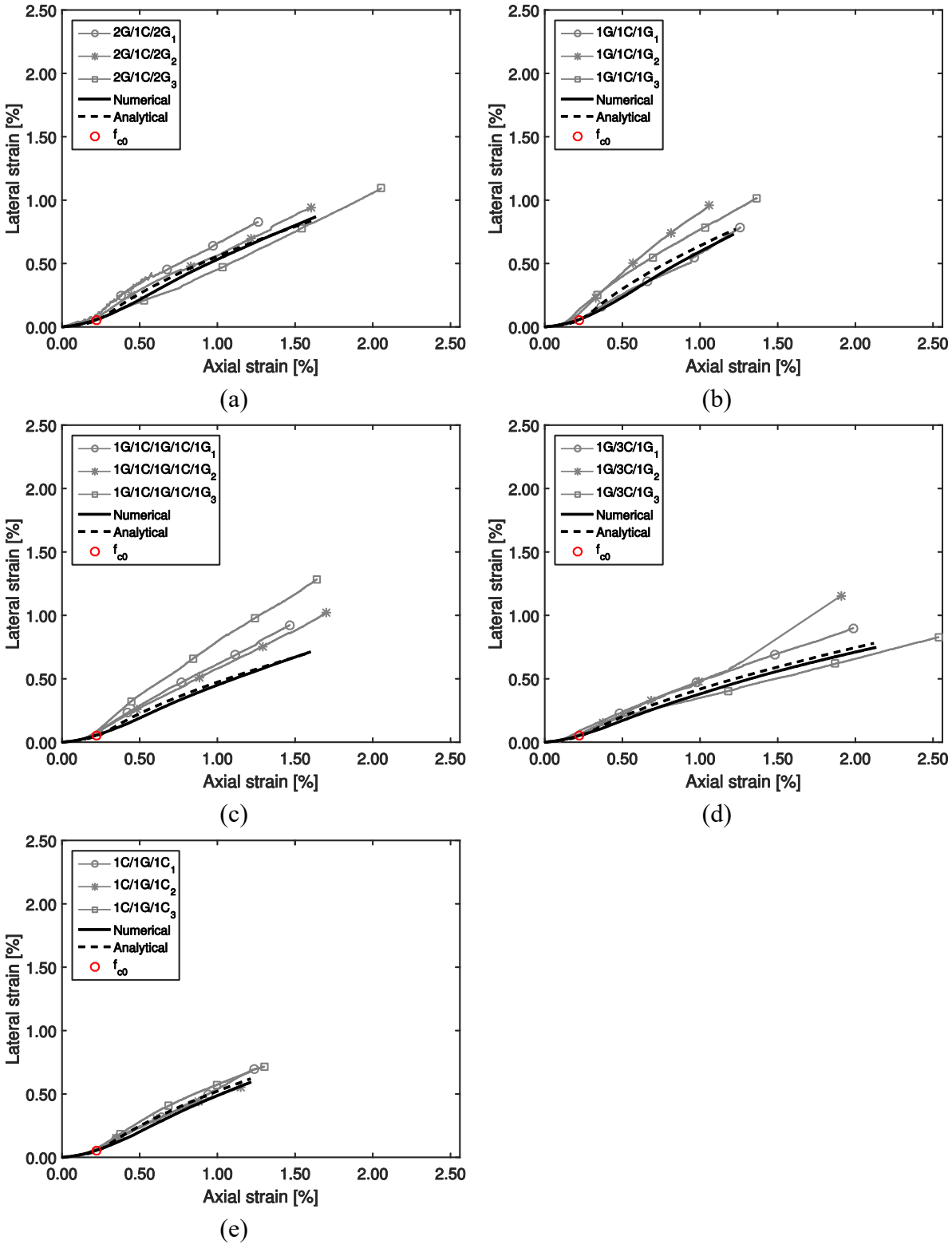

Figure 6.15 — Lateral strain-axial strain curves of C/G combinations: experimental *versus* predicted values.

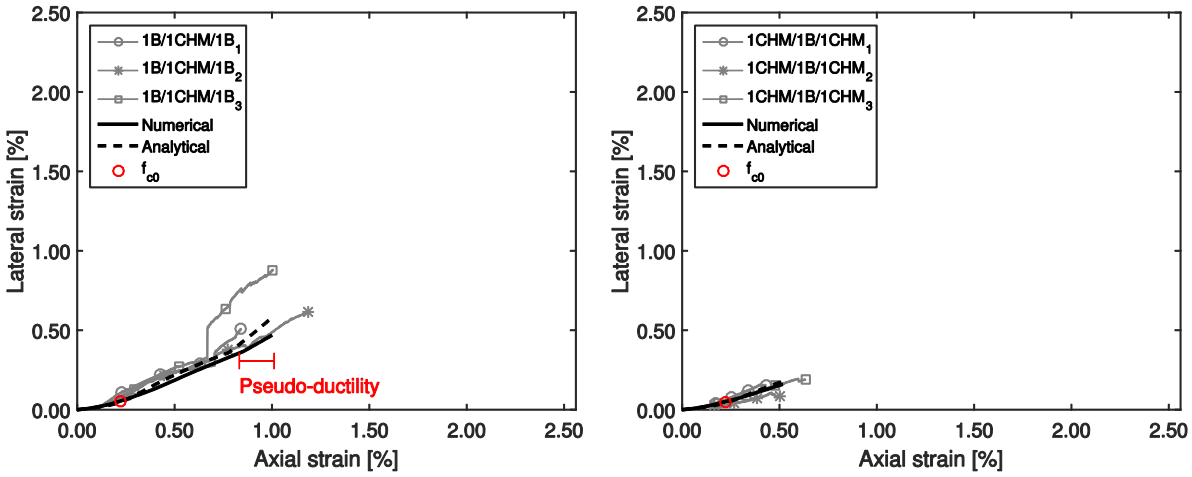

(a) (b)

Figure 6.16 — Lateral strain-axial strain curves of CHM/B combinations: experimental *versus* predicted values.

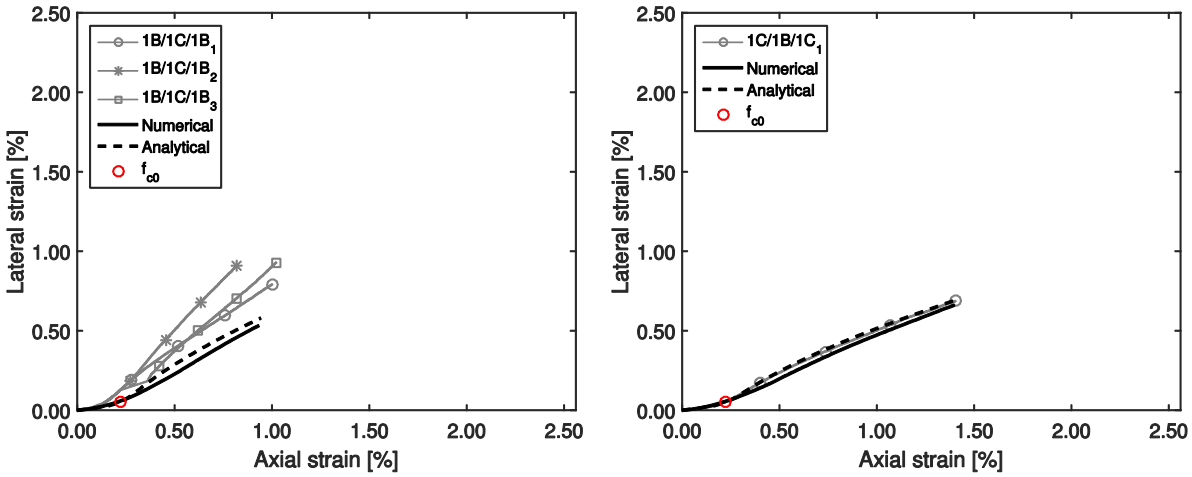

(a) (b)

Figure 6.17 — Lateral strain-axial strain curves of C/B combinations: experimental *versus* predicted values.

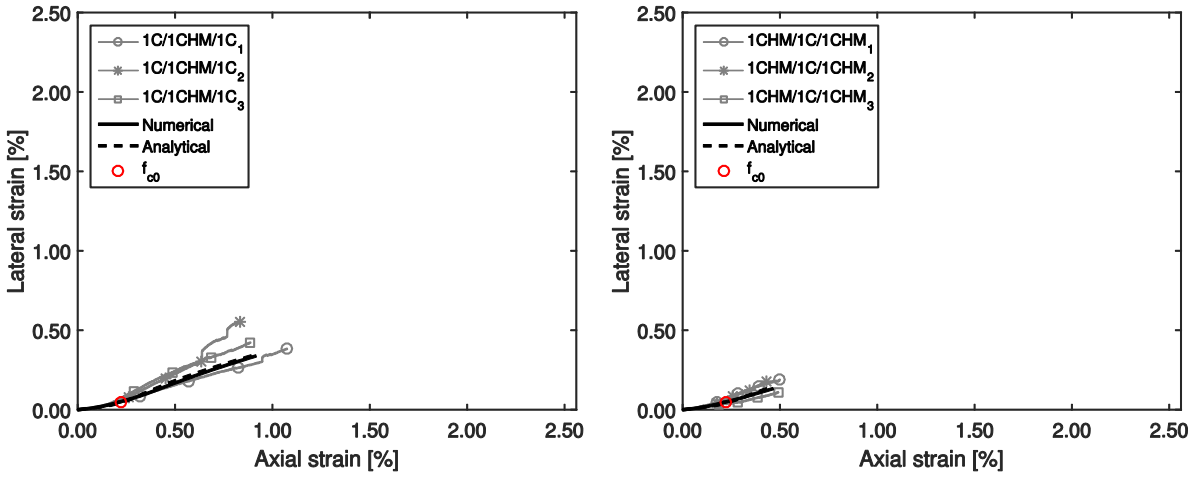

(a) (b)

Figure 6.18 — Lateral strain-axial strain curves of CHM/C combinations: experimental *versus* predicted values.

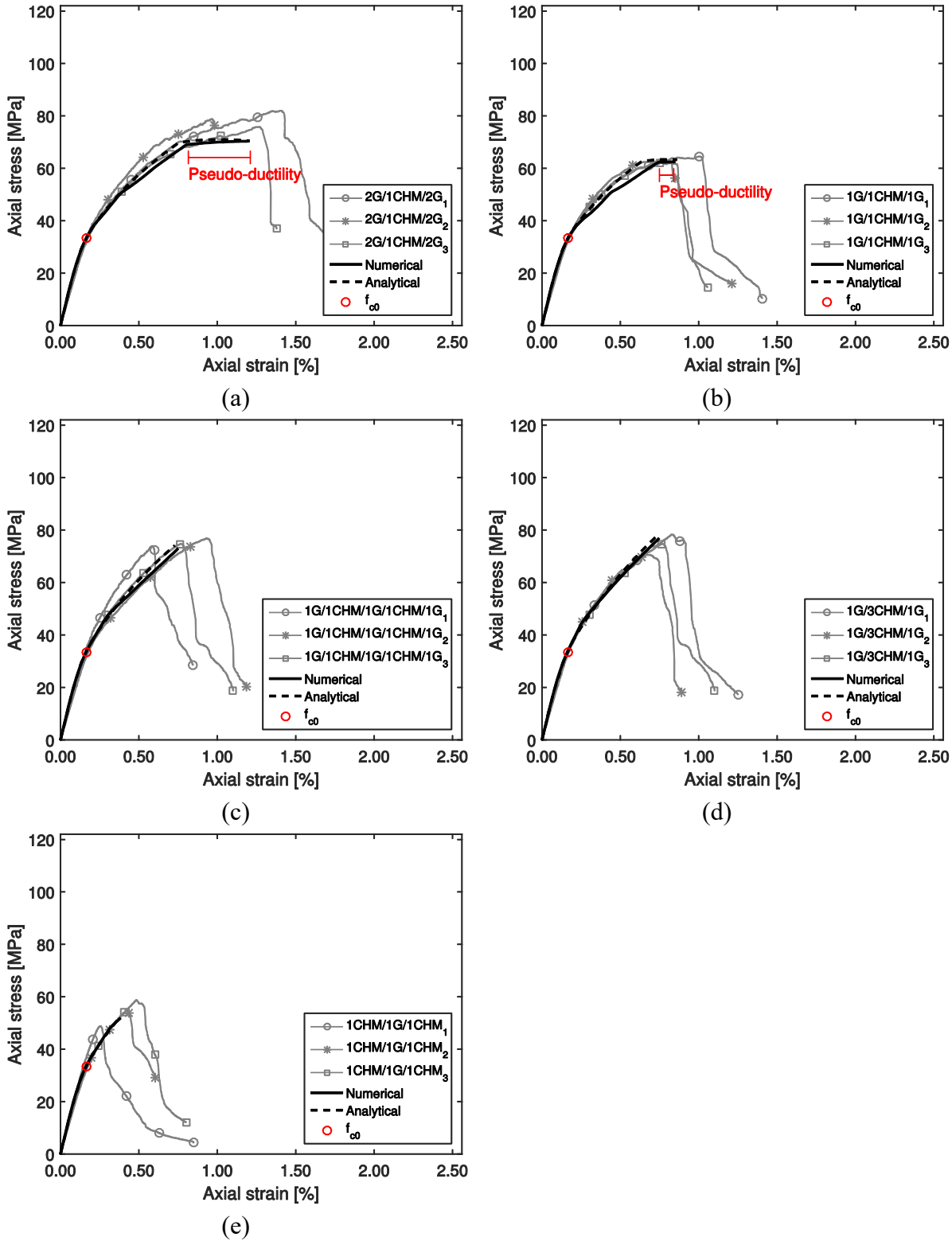

Figure 6.19 — Stress-strain curves of CHM/G combinations: experimental *versus* predicted values.

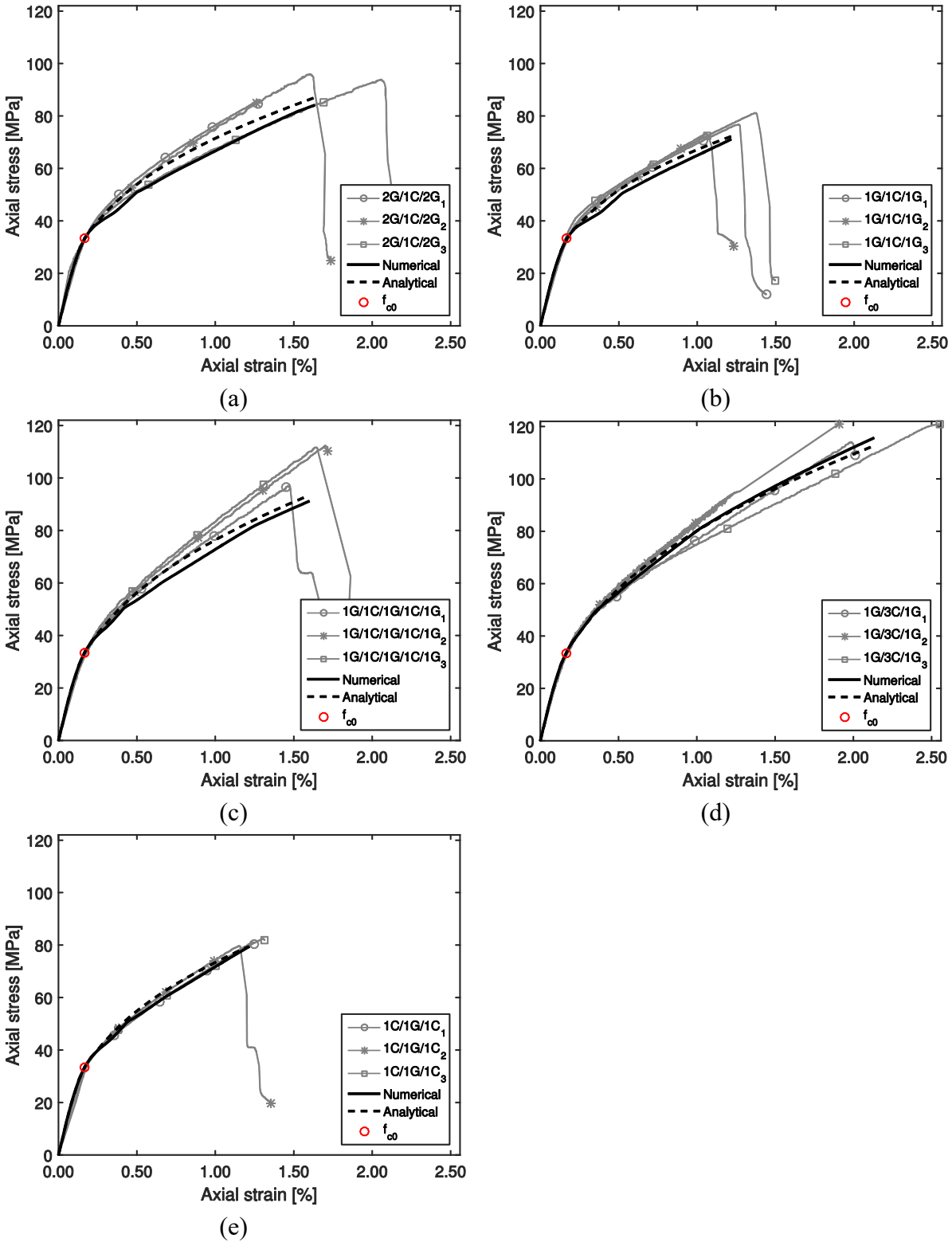

Figure 6.20 — Stress-strain curves of C/G combinations: experimental *versus* predicted values.

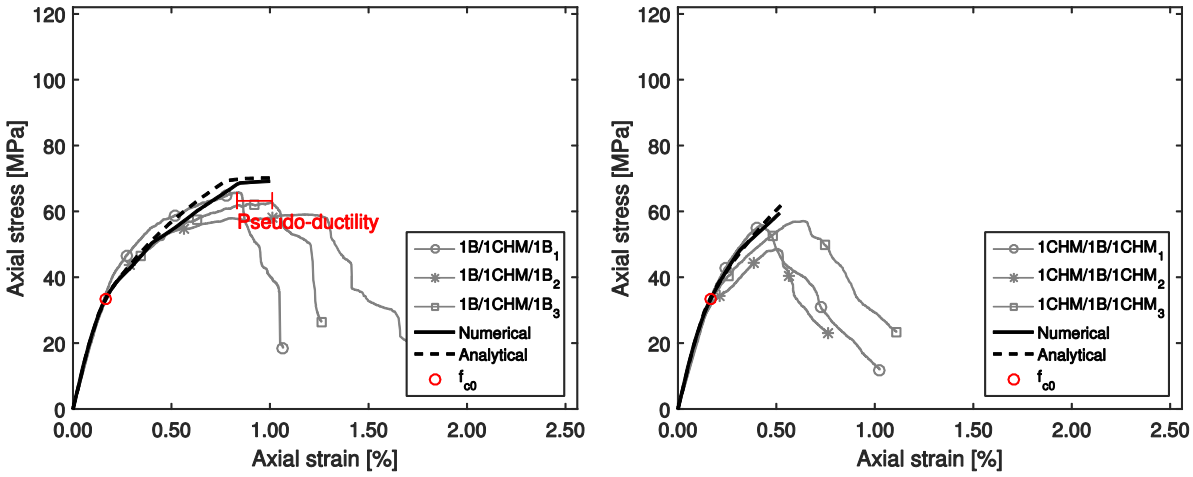

(a) (b)

Figure 6.21 — Stress-strain curves of CHM/B combinations: experimental *versus* predicted values.

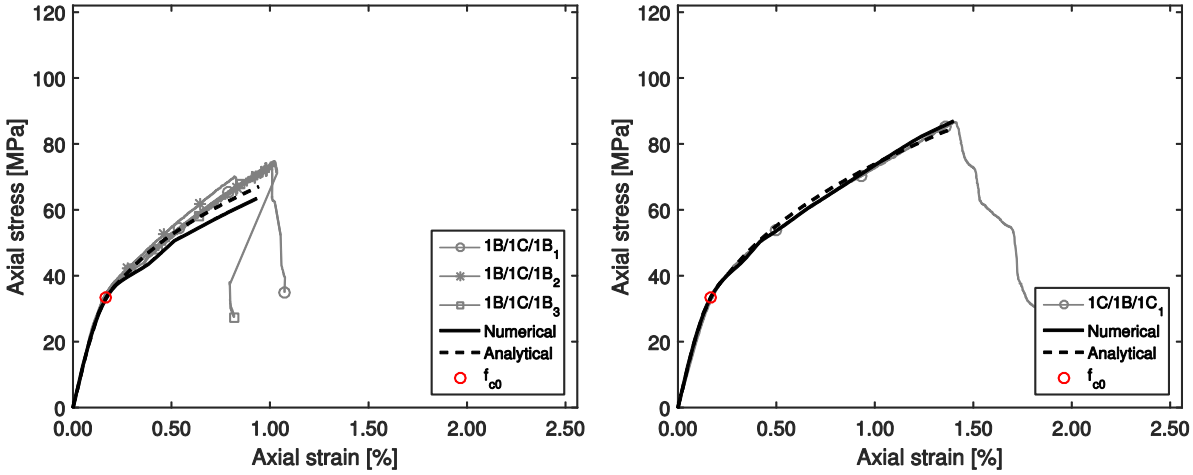

(a) (b)

Figure 6.22 — Stress-strain curves of C/B combinations: experimental *versus* predicted values.

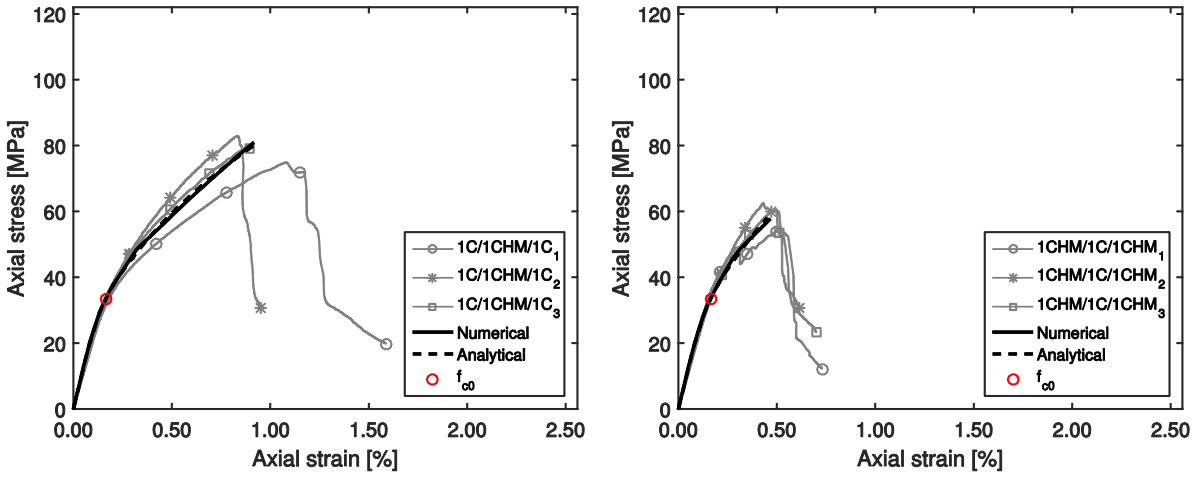

(a) (b)

Figure 6.23 — Stress-strain curves of CHM/C combinations: experimental *versus* predicted values.

The performance of the models was quantified comparing the predictions of the peak axial stress (f_{cc}) and the mean lateral strain ($\varepsilon_{l,rup\ -\ mean}$) at the peak stress (i.e. the mean strain value at the failure measured with the set of strain gauges) with respective experimental results. The comparison is presented in **Table 6.5**. As it was expected, there are no significant differences between analytical and numerical predictions. For f_{cc} predictions, the relative error varied between -14.0% and 14.2%, when analytical model is considered, and between -10.1% and 15.8%, when numerical model is considered. This error's magnitude is acceptable (maximum absolute value of 20%). For $\varepsilon_{l,rup\ -\ mean}$ predictions, the error varied between -27.0% and 35.1%, when analytical model is considered, and between -24.1% and 41.7%, when numerical model is considered. This error magnitude is quite high. However, it should be noted that comparing very low values generates situations where small variations of absolute values lead to very high relative errors. Furthermore, considering that there is a great dispersion of $\varepsilon_{l,rup\ -\ mean}$ results, it can be stated that experimental research should be further explored in order to understand which factors contribute to variation of lateral strain.

Table 6.5 — Comparison of models predictions with test results

Series ID *	f_{cc}					$\varepsilon_{l,rup\ -\ mean}$				
	Experimental [MPa] (CoV [%])	Analytical		Numerical		Experimental [MPa] (CoV [%])	Analytical		Numerical	
		Prediction [MPa]	Rel. error [%]	Prediction [MPa]	Rel. error [%]		Prediction [MPa]	Rel. error [%]	Prediction [MPa]	Rel. error [%]
3B	64.80 (3.48)	60.93	6.0	60.57	6.5	1.14 (26.28)	0.86	24.9	0.79	30.6
3G	64.67 (4.21)	62.52	3.3	65.10	-0.7	1.45 (10.46)	1.29	11.1	1.23	15.4
3C	89.02 (7.03)	89.79	-0.9	88.74	0.3	0.67 (5.95)	0.60	10.7	0.59	12.1
3CHM	54.89 (12.91)	53.95	1.7	53.67	2.2	0.08 (50.80)	0.10	-27.0	0.10	-24.1
1C/1B/1C	87.4 (--)	84.88	2.9	86.89	0.6	0.66 (--)	0.69	-4.9	0.66	-0.6
1B/1C/1B	73.2 (3.01)	67.01	8.5	63.44	13.3	0.88 (8.56)	0.58	33.9	0.53	39.2
1CHM/1B/1CHM	54.2 (8.59)	61.79	-14.0	59.45	-9.7	0.14 (38.13)	0.18	-26.3	0.16	-11.9
1B/1CHM/1B	62.9 (5.46)	70.19	-11.6	69.23	-10.1	0.67 (28.56)	0.59	11.8	0.47	29.8
1CHM/1C/1CHM	59.7 (7.76)	58.03	2.8	57.76	3.2	0.16 (26.25)	0.14	12.4	0.13	16.7
1C/1CHM/1C	79.9 (5.01)	80.28	-0.5	80.90	-1.3	0.45 (19.92)	0.35	22.9	0.34	25.3
1C/1G/1C	81.7 (1.48)	79.45	2.8	79.45	2.8	0.66 (13.60)	0.62	5.4	0.59	9.4
1G/3C/1G	119.4 (2.66)	112.32	5.9	115.68	3.1	0.96 (17.86)	0.78	18.8	0.75	22.2
1G/1C/1G/1C/1G	108.3 (7.53)	92.87	14.2	91.19	15.8	1.08 (17.29)	0.70	35.1	0.71	33.9
1G/1C/1G	77.5 (5.00)	72.50	6.5	71.11	8.2	0.92 (13.03)	0.77	16.2	0.73	20.4
2G/1C/2G	98.3 (2.43)	87.03	11.5	84.13	14.4	0.95 (14.03)	0.85	10.9	0.87	9.0
1CHM/1G/1CHM	54.7 (9.00)	52.80	3.5	51.86	5.2	0.15 (30.30)	0.12	18.8	0.11	26.7
1G/3CHM/1G	74.5 (6.12)	78.52	-5.4	76.87	-3.2	0.21 (24.17)	0.22	-2.5	0.20	7.3
1G/1CHM/1G/1CHM/1G	76.6 (1.98)	67.45	11.9	72.94	4.8	0.29 (27.88)	0.36	-26.0	0.25	14.1
1G/1CHM/1G	63.7 (1.70)	63.28	0.7	62.47	1.9	0.72 (12.50)	0.56	22.3	0.42	41.7
2G/1CHM/2G	80.5 (3.93)	70.47	12.5	70.37	12.6	0.99 (12.93)	0.79	20.3	0.60	39.5

6.5. Conclusions

In the present chapter, the performance of a modified concrete damage plasticity model (CDPM) is validated against both experimental and analytical results. The modifications were implemented in both hardening and flow rules, turning them confining dependent. An analysis-oriented confinement model, based on the approach of Lim and Ozbakkaloglu [29, 30], was adopted to define the input parameters of the CDPM. Major conclusions drawn from this study are presented in the following paragraphs.

The need to contemplate friction forces in surface-to-surface contact between rigid steel plates and concrete was analysed. It was concluded that, if an analytical model that implicitly considers the frictions forces (such as the one considered in the present chapter) is used, to compute the input parameters of the numerical model, the end restrain does not need to be detailed.

It was observed that K parameter (strength ratio of concrete under equal biaxial compression to triaxial compression) has a significant influence in the prediction of the peak stress of confined concrete. Then, a sensitivity analysis was carried out and it was concluded that assuming K = 0.68 leads to residual errors in initial numerical predictions. For this reason, this value was assumed in the remaining part of the work.

The analytical model of Jalalvand *et al*. [3] was used to predict the input tensile parameters of hybrid FRP. In the 2G/1CHM/G, 1G/1CHM/1G, 1B/1CHM/1B, and 1C/1CHM/1C combinations, plasticity was defined in order to take into account the pseudo-ductile tensile responses of the latter. In the remaining cases, a linear elastic behaviour was assumed. This approach has shown to provide accurate predictions for all FRP-confined circular concrete columns. As expected, pseudo-ductility was predicted in cases in which it was experimentally observed. Moreover, it should be highlighted that analytical and numerical curves are almost coincident.

As a final conclusion, taking into account what has been stated previously, it can be concluded that the developed 3D finite element model, using modified CDPM, can be adopted to accurately predict the compressive behaviour of hybrid FRP-confined concrete.

6.6. References

[1] Bank L. Composites for Construction - Structural Design with FRP Materials. John Wiley & Sons, Inc. 2006.
[2] Ribeiro F, Sena-Cruz J, Branco FG, Júlio E. Hybrid FRP jacketing for enhanced confinement of circular concrete columns in compression. Construction and Building Materials. 2018;184:681-704.
[3] Jalalvand M, Czél G, Wisnom MR. Damage analysis of pseudo-ductile thin-ply UD hybrid composites – A new analytical method. Composites: Part A. 2015;69:83–93.

[4] Grace NF, Abdel-Sayed G, Ragheb WF. Strengthening of Concrete Beams Using Innovative Ductile Fiber-Reinforced Polymer Fabric. ACI Structural Journal. 2002;103(5)(99(5)):672–700.
[5] Grace NF, Ragheb WF, Abdel-Sayed G. Development and application of innovative triaxially braided ductile FRP fabric for strengthening concrete beams. Composite Structures 2004;64 521–30.
[6] Wu Z, Shao Y, Iwashita K, Sakamoto K. Strengthening of Preloaded RC Beams Using Hybrid Carbon Sheets. J Compos Constr. 2007;11:299-307.
[7] Attari N, Amziane S, Chemrouk M. Flexural strengthening of concrete beams using CFRP, GFRP and hybrid FRP sheets. Construction and Building Materials 2012;37 746–57.
[8] Hosny A, Shaheen H, Abdelrahman A, Elafandy T. Performance of reinforced concrete beams strengthened by hybrid FRP laminates. Cement & Concrete Composites. 2006;28:906–13.
[9] Hawileh RA, Rasheed HA, Abdalla JA, Al-Tamimi AK. Behavior of reinforced concrete beams strengthened with externally bonded hybrid fiber reinforced polymer systems. Materials and Design. 2014;53:972–82.
[10] Kang TH-K, Kim W, Ha S-S, Choi D-U. Hybrid Effects of Carbon-Glass FRP Sheets in Combination with or without Concrete Beams. International Journal of Concrete Structures and Materials Vol8, No1, pp27–41, March 2014 DOI 101007/s40069-013-0061-0. 2014.
[11] Zhang P, Zhu H, Wu G, Meng S, Wu Z. Flexural Performance of HFRP-RC Composite T-Beams with Different Interfaces. J Compos Constr, 04016101. 2016.
[12] Nikopour H, Nehdi M. Shear repair of RC beams using epoxy injection and hybrid external FRP. Materials and Structures. 2011;44:1865–187.
[13] Wu G, Wu ZS, Lu ZT, Ando YB. Structural Performance of Concrete Confined with Hybrid FRP Composites. Journal of reinforced plastics and composites. 2008;27(12).
[14] Luca AD, Nardone F, Matta F, Nanni A, Lignola GP, Prota A. Structural Evaluation of Full-Scale FRP-Confined Reinforced Concrete Columns. J Compos Constr. 2011;15:112-23.
[15] Xu S, Li L, Guo Y. Study on experimental behavior of concrete circular column confined by HFRP under axial compression. Advanced Materials Research. 2012;450-451:491-4.
[16] Li L-J, Xu S-D, Zeng L, Guo Y-C. Study on mechanical behavior of circular concrete columns confined by HFRP under axial compressive load. Research and Applications in Structural Engineering, Mechanics and Computation – Zingoni (Ed) Taylor & Francis Group, London, ISBN 978-1-138-00061-2. 2013.
[17] Li J, Samali B, Ye L, Bakoss S. Behaviour of concrete beam–column connections reinforced with hybrid FRP sheet. Composite Structures 2002;57:357–65.
[18] Li J, Bakoss SL, Samali B, Ye L. Reinforcement of concrete beam-column connections with hybrid FRP sheet. Composite Structures 1999;47:805-12.
[19] Attari N, Amziane S, Chemrouk M. Efficiency of Beam–Column Joint Strengthened by FRP Laminates. Advanced Composite Materials. 2010;19:171–83.
[20] Ispir M, Dalgic KD, Ilki A. Hybrid confinement of concrete through use of low and high rupture strain FRP. Composites Part B: Engineering. 2018;153:243-55.
[21] Swolfs Y, Gorbatikh L, Verpoest I. Fibre hybridisation in polymer composites: a review. Composites Part A: Applied Science and Manufacturing. 2014;67:181-200.
[22] Summerscales J, Short D. Carbon fibre and glass fibre hybrid reinforced plastics. Composites. 1978;9(3):157–66.
[23] Czél G, Wisnom MR. Demonstration of pseudo-ductility in high performance glass/epoxy composites by hybridisation with thin-ply carbon prepreg. Composites: Part A: Applied Science and Manufacturing. 2013;52:23–30.

[24] Jalalvand M, Czél G, Wisnom MR. Numerical modelling of the damage modes in UD thin carbon/glass hybrid laminates. Composites Science and Technology. 2014;94:39–47.
[25] Jalalvand M, Czél G, Wisnom MR. Parametric study of failure mechanisms and optimal configurations of pseudo-ductile thin-ply UD hybrid composites. Composites: Part A. 2015; 74:123–31.
[26] Czél G, Jalalvand M, Wisnom MR. Design and characterisation of advanced pseudo-ductile unidirectional thin-ply carbon/epoxy–glass/epoxy hybrid composites. Composite Structures. 2016;143:362–70.
[27] Wisnom MR, Czél G, Swolfs Y, Jalalvand M, Gorbatikh L, Verpoest I. Hybrid effects in thin ply carbon/glass unidirectional laminates: Accurate experimental determination and prediction. Composites: Part A. 2016;88:131–9.
[28] Yu H, Longana ML, Jalalvand M, Wisnom MR, Potter KD. Pseudo-ductility in intermingled carbon/glass hybrid composites with highly aligned discontinuous fibres. Composites: Part A 2015;73:35–44.
[29] Lim JC, Ozbakkaloglu T. Lateral Strain-to-Axial Strain Relationship of Confined Concrete. Journal of Structural Engineering. 2014;141(5).
[30] Lim JC, Ozbakkaloglu T. Unified Stress-Strain Model for FRP and Actively Confined Normal-Strength and High-Strength Concrete. Journal of Composites for Construction, ASCE, ISSN 1090-0268/04014072 (14). 2014.
[31] Yu T, Teng JG, Wong YL, Dong SL. Finite element modeling of confined concrete-II: Plastic-damage model. Engineering Structures. 2010;32(3):680-91.
[32] Lin G, Teng JG. Three-Dimensional Finite-Element Analysis of FRP-Confined Circular Concrete Columns under Eccentric Loading. Journal of Composites for Construction. 2017;21(4):04017003.
[33] Hany NF, Hantouche EG, Harajli MH. Finite element modeling of FRP-confined concrete using modified concrete damaged plasticity. Engineering Structures. 2016;125:1-14.
[34] Ozbakkaloglu T, Gholampour A, Lim JC. Damage-Plasticity Model for FRP-Confined Normal-Strength and High-Strength Concrete. Journal of Composites for Construction. 2016;20(6):04016053.
[35] Lubliner J, Oliver J, Oller S, Oñate E. A plastic-damage model for concrete. International Journal of Solids and Structures. 1989;25(3):299-326.
[36] Lee J, Fenves GL. Plastic-Damage Model for Cyclic Loading of Concrete Structures. Journal of Engineering Mechanics. 1998;124(8):892-900.
[37] ABAQUS version 6.14 [Computer software]. Dassault Systèmes, Waltham, MA.
[38] Chi Y, Yu M, Huang L, Xu L. Finite element modeling of steel-polypropylene hybrid fiber reinforced concrete using modified concrete damaged plasticity. Engineering Structures. 2017;148:23-35.
[39] Lim JC, Ozbakkaloglu T. Stress–strain model for normal- and light-weight concretes under uniaxial and triaxial compression. Construction and Building Materials. 2014;71(Supplement C):492-509.
[40] Candappa DC, Sanjayan JG, Setunge S. Complete Triaxial Stress-Strain Curves of High-Strength Concrete. Journal of Materials in Civil Engineering. 2001;13(3):209-32.
[41] Popovics S. A Numerical Approach to the Complete Stress-Strain Curves for Concrete. Cement and Concrete Research. 1973;3(5):583-99.
[42] Domingo JC, Kuang-Han C. Stress-Strain Relationship for Plain Concrete in Compression. Journal Proceedings.82(6).

[43] Duarte APC, Silva BA, Silvestre N, de Brito J, Júlio E, Castro JM. Finite element modelling of short steel tubes filled with rubberized concrete. Composite Structures. 2016;150:28-40.
[44] Tysmans T, Wozniak M, Remy O, Vantomme J. Finite element modelling of the biaxial behaviour of high-performance fibre-reinforced cement composites (HPFRCC) using Concrete Damaged Plasticity. Finite Elements in Analysis and Design. 2015;100:47-53.
[45] Kmiecik P, KamiŃSki M. Modelling of reinforced concrete structures and composite structures with concrete strength degradation taken into consideration. Archives of Civil and Mechanical Engineering. 2011;11(3):623-36.
[46] Jankowiak T, Łodygowski T. Identification of parameters of concrete damage plasticity constitutive model. Foundations of Civil and Environmental Engineering. 2005;6:53-69.
[47] Behnam H, Kuang JS, Samali B. Parametric finite element analysis of RC wide beam-column connections. Computers & Structures. 2018;205:28-44.
[48] Nzabonimpa JD, Hong W-K. Structural performance of detachable precast composite column joints with mechanical metal plates. Engineering Structures. 2018;160:366-82.
[49] Singh M, Sheikh AH, Mohamed Ali MS, Visintin P, Griffith MC. Experimental and numerical study of the flexural behaviour of ultra-high performance fibre reinforced concrete beams. Construction and Building Materials. 2017;138:12-25.
[50] ASTM. D 3379 – 75 - Standard Test Method for Tensile Strength and Young's Modulus for High-Modulus Single-Filament Materials. 1989.
[51] ISO. 527-5 Plastics — Determination of tensile properties; Part 5: Test conditions for unidirectional fibre-reinforced plastic composites. EUROPEAN COMMITTEE FOR STANDARDIZATION. 2009.
[52] S&P. Technical Data Sheet S&P Resin 55. 2015.
[53] CNR-DT200. Guide for the Design and Construction of Externally Bonded FRP Systems for Strengthening Existing Structures. Advisory Committee on Techincal Recommendations for Construction, National Research Council, Rome, Italy. 2013.
[54] Ribeiro F, Sena-Cruz J, Branco FG, Júlio E. Hybrid effect and pseudo-ductile behaviour of unidirectional interlayer hybrid FRP composites for civil engineering applications. Construction and Building Materials. 2018;171:871-90.
[55] Kotsovos MD. Finite-Element Modelling of Structural Concrete: Short-Term Static and Dynamic Loading Conditions. 1st ed: CRC Press; 2017.
[56] BSI. BS 5975:2008+A1:2011 - Code of practice for temporary works procedures and the permissible stress design of falsework.2008.
[57] Teng JG, Xiao QG, Yu T, Lam L. Three-dimensional finite element analysis of reinforced concrete columns with FRP and/or steel confinement. Engineering Structures. 2015;97:15-28.
[58] Kupfer H, Hilsdorf HK, Rusch H. Behavior of concrete under biaxial stresses. ACI Journal. 1969(66-52).
[59] Papanikolaou VK, Kappos AJ. Confinement-sensitive plasticity constitutive model for concrete in triaxial compression. International Journal of Solids and Structures. 2007;44(21):7021-48.
[60] Tao Z, Wang Z-B, Yu Q. Finite element modelling of concrete-filled steel stub columns under axial compression. Journal of Constructional Steel Research. 2013;89:121-31.
[61] CEN. EN 12390-13:2013 - Testing hardened concrete - Part 13: Determination of secant modulus of elasticity in compression. 2013.
[62] CEN. EN 12390-3:2009 - Testing hardened concrete - Part 3: Compressive strength of test specimens. 2009.

7. CONCLUSIONS AND FUTURE PERSPECTIVES

7.1. Conclusions

This PhD thesis has been oriented aiming at the development of a hybrid FRP confining system for concrete columns with improved properties, compared to the conventional methods. As it is known, FRP jacketing has become an attractive technique for strengthening reinforced concrete columns. However, two main drawbacks can still be pointed out:

i) The ultimate strain of FRP jackets is often lower than the ultimate tensile strain of laminates of the same material;
ii) Being fragile materials, the failure of conventional FRP is abrupt, i.e., without warning.

In the course of this work, it has been demonstrated that the above mentioned drawbacks can be mitigated through the use of hybrid FRP composites. If a proper combination of constituent materials is chosen, it is possible to promote synergies between fibres, conducting to both (i) an increase of the apparent failure strain of the low strain (LS) reinforcing material and (ii) a pseudo-ductile tensile response.

First, specific attention has been paid to developing the hybrid FRP composite at the material level. An experimental and analytical investigation was carried out in an attempt to understand the tensile behaviour of these innovative composites. All the hybrid FRP samples were made through hand lamination of four different dry unidirectional fabrics, namely high-modulus carbon (CHM), standard-modulus carbon (C), E-glass (G) and basalt (B).

Then, the performance of the different hybrid FRP combinations was assessed in the confinement of small-scale plain concrete columns. Besides the experimental study, this work also included the development of both analytical and numerical models.

In the presented work, for the first time, the pseudo-ductile of composite materials, which is dependent of fragmentation of LS material, was explored in the confinement of concrete. The latter concept is relative new in composite field (in general), and completely unexplored in civil engineering applications. Thus, this is main innovation of the present thesis, which aimed to bring a first contribution in this research area. It has been shown that abrupt failure can be avoided, if the hybrid FRP is materialized for this purpose. Furthermore, is was demonstrated that efficiency of LS material can be improved with hybrid FRP combinations.

The six specific goals of this work were enunciated in Section 1.2, whereas in the present chapter the main findings derived from those goals are synthesized.

7.1.1. Identification of properties of the constituent materials that influence most the tensile response of hybrid FRP composites

Initiation and propagation of damage in hybrid FRP composites depend primarily on the strength, stiffness, volume fractions of the reinforcing materials, ply thickness, stacking sequence, and toughness of mode II fracture of the interface between the reinforcing materials.

The elastic modulus of hybrid FRP composites increases linearly with the increase of the relative volume (vol%) of low strain (LS) fibres. As expected, combinations that include CHM (the material with the highest elastic modulus) are the ones that lead to higher elastic modulus. The combination of CHM with C results in the highest elastic modulus, whereas the combination of C with G leads to the lowest values.

The strength varies with the vol% of LS material and the total volume of composite. The highest strength was achieved with the combination of C with B. Since CHM is one of the materials with lower tensile strength, increasing the volume of CHM in combinations with this material would not lead to improvements in the resulting tensile strength.

It was verified that hybrid effect depends not only on the vol% of LS fibres but also on the non-dimensional stiffness parameter (E_{ND}). Moderately strong negative correlations between hybrid effect and Vol% LS fibres (r = - 0.526) and E_{ND} (r = - 0.515) were found with Spearman's rank tests carried out. The hybrid effect varied between -14.1% and 44.5%. The maximum hybrid effect was obtained by combining CHM with C, and the minimum hybrid effect was obtained by combining CHM with G. In all studied combinations, it was possible to observe that above 60% of LS fibres vol% the hybrid effect was nearly zero or even negative.

7.1.2. Characterization of hybrid pseudo-ductile tensile behaviour

In four tested hybrid combinations, that included CHM as LS material (2G/1CHM/2G, 1G/1CHM/1G, 1B/1CHM/1B, and 1C/1CHM/1C), pseudo-ductile tensile responses with fragmentation and dispersed delamination were achieved. In these combinations, the mean 'yield' stress varied between 732.6 and 1504.5 MPa and the pseudo-ductile strain between 0.4% and 2.0%.

The effect of geometric and material parameters on the tensile response of hybrid composites was interpreted using damage mode maps (DMMs). It was possible to observe that the highest value of pseudo-ductile strain can be achieved close to the intersection of the boundaries within fragmentation & delamination zone. The highest values of pseudo-ductile behaviour were achieved in the combination of CHM with B.

DMMs also allowed to observe that the highest value of 'yield' stress can be achieved if the coordinates (ratio between the thickness of the two fibre type layers vs. absolute thickness of the LS layer) of a given hybrid configuration are close to LS fragmentation/HS failure boundary. In configurations in which C was considered as the LS material, it was possible to

observe that the fragmentation and fragmentation & delamination zones were very reduced, indicating that it is almost impossible to get these types of damage modes in practice. In this way, the combination of CHM with C is the most plausible choice to reach the highest 'yield' stress.

7.1.3. Validation of accuracy of different analytical models to predict several tensile properties of hybrid FRP composites, namely elastic modulus, strength, hybrid effect, 'yield' stress and pseudo-ductile strain

The elastic modulus was well-predicted using the rule of mixtures (ROM). Predictions showed a good agreement with the experimental results. The obtained relative errors ranged between -14.5% and 9.6%. It was concluded that ROM can be used for quality control of hand lay-up hybrid composites, since it allows checking both the volume and the alignment of the reinforcing materials used in this type of composites.

In the case of tensile strength, predictions were carried out using two models: (i) bilinear ROM and (ii) a modification of model of Jalalvand *et al*. [1], taking into account the hybrid effect and assuming the maximum value between the stress level at which the first crack in the LS material occurs and the stress level at which the HS material fails. In the first case, the relative errors between the bilinear ROM prediction and the experimental results varied between -15.7% and 16.9%. In the second case, the relative errors varied between -36.1% and 26.1%. In this way, it can be stated that, from both models considered, bilinear ROM is the one that best predicts strength.

The analytical approach developed by Jalalvand *et al*. [1] allowed to predict all the failure modes and the pseudo-ductile strain successfully. In this way, this model was validated for the set of materials and fabrication method used.

Finally, it was concluded that progressive damage model, if carefully used, can predict reasonably the hybrid effect. Relative errors between analytical and experimental positive hybrid effects varied between -20.4% and 31.1%. It should be highlighted that this model has some limitations, because the latter does not take into account neither scale effects nor dispersion of fibres. Furthermore, Weibull parameters, which are used as inputs, are prone to several error sources, being dependent on both the number of tests and the gauge length of specimens.

7.1.4. Understanding how the hybrid effect and the pseudo-ductility can contribute to improve the performance of FRP-confined circular concrete columns

It was demonstrated that the reduction of efficiency of LS material in FRP jackets can be minimized, or even eliminated, with hybridisation. It was observed that for a large number of hybrid combinations, the strain reduction factor is higher than 1. It was verified that moderately

strong (above 0.5) and strong (above 0.7) correlations exist between the hybrid effect and the FRP strain reduction factor. This means that there is an increase of the strain reduction factor as the volume of LS fibres decreases, i.e., the hybrid effect increases.

In all three tested hybrid combinations, which included CHM as LS material (2G/1CHM/2G, 1G/1CHM/1G and 1B/1CHM/1B), pseudo-ductile tensile responses with fragmentation and dispersed delamination of the jacket were observed, leading to flat-topped compressive stress-strain curves. Moreover, abrupt failure modes were avoided in these combinations. According to tensile tests results, the same behaviour was expected to occur in 1C/1CHM/1C combination. However, in this combination, allegedly a very short pseudo-ductile branches took place and, in practice, this led to the consideration that premature failure of HS fibres occurred. This is in agreement with the fact that in this combination a low lateral failure strain of HS fibres (0.61%) was registered. In tensile tests, the failure strain of this combination was 0.94%. For this reason, the hybrid FRP failure of composite occurs too soon.

7.1.5. Development of analytical models to predict different properties of hybrid FRP-confined concrete, namely compressive strength, stress-strain curve, and dilation behaviour

Two new design-oriented models were proposed to predict the peak stress of hybrid FRP-confined concrete. Relatively large R^2 of 0.84 and 0.80 were found in predictions of peak stress using the first and the second model, respectively. The relative errors for peak stress predictions, varied between -13.3% and 18.1%, with the first model, and between -18.6% and 16.7%, with the second model.

Next, an analysis-oriented confinement model, based on the modification of the approach of Lim and Ozbakkaloglu [2, 3], was proposed. It was verified that this model allows to accurately simulate both the dilation behaviour and the compressive stress-strain curves of all hybrid confined concrete series analysed. Using this model, error's prediction of the peak stress varied between -14.0% and 14.2%.

7.1.6. Proposal of an accurate three-dimensional finite element model to predict the compressive behaviour of hybrid FRP-confined concrete

It was verified that the concrete damage plasticity model (CDPM), available in ABAQUS, can be adopted, if adequately modified, to accurately predict the compressive behaviour of hybrid FRP-confined concrete. This was validated using both experimental and analytical results.

The modifications were implemented in both hardening and flow rules, turning these confining dependent. An analysis-oriented confinement model, based on the approach of Lim and Ozbakkaloglu [2, 3], was adopted to define the input parameters of the CDPM.

The analytical model of Jalalvand *et al*. [3] was used to predict the input tensile parameters of hybrid FRP. In the 2G/1CHM/2G, 1G/1CHM/1G, 1B/1CHM/1B, and 1C/1CHM/1C combinations, plasticity was defined in order to take into account the pseudo-ductile tensile responses. In the remaining cases, a linear elastic behaviour was assumed. In this way, pseudo-ductility was predicted in cases in which it was experimentally observed.

Since the material parameters for the modified CDPM were obtained from the referred to analysis-oriented model, it was expected that predictions obtained with both models (analytical and numerical) have similar accuracy. In fact, it was verified that the analytical and numerical curves are almost coincident. The relative error for peak stress predictions varied between -10.1% and 15.8% with the developed numerical model.

7.2. Future research

In this subsection, based on remaining open questions as well as on newly-formed questions, future research studies are proposed.

Despite all the research work carried out, the hybrid effect remains not thoroughly understood. There are still doubts on the best way to measure the strain at the failure of non-hybrid composites. This has implications in the definition of the baseline tensile failure strain of non-hybrid composite against which the strain at failure of the hybrid FRP composites is compared to determine the hybrid effect. The influence of scale effect, thermal residual stresses and dynamic stress concentrations on hybrid effect has not yet been thoroughly evaluated. Lastly, a robust model (analytical or numerical) to predict the hybrid effect remains to be proposed.

Relatively to the hybrid FRP-confined concrete results, it should be noted that these cannot be taken as representative of large scale concrete columns. Although the obtained results regarding concrete behaviour are an important part of the overall input required for the structural analysis of concrete structures, further work needs to be conducted in large scale specimens before hybrid composites can be implemented in real cases. The relationship between the confinement ratio and the strength enhancement of concrete is dependent on the diameter of the cross section of the concrete specimens. On the other hand, the tensile behaviour of hybrid FRP composites is dependent of absolute LS layer thickness. In this way, two problems can be anticipated for larger specimens: (i) the obtained concrete strength will not be reached if the studied hybrid FRP configurations are adopted and (ii) the tensile behaviour of the hybrid FRP composites will be different if the proportion of the constituents of hybrid FRP composites is maintained but the thickness is increased, aiming to obtain the same confinement levels. This implies that it may not be possible to obtain pseudo-ductility in these cases.

While the presented study has demonstrated that hybrid FRP confinement can substantially enhance both the compressive strength and ductility of confined concrete in circular specimens, the same solution has to be validated in specimens of different cross sections. This is

particularly relevant for rectangular cross sections. As it is known, the confinement in this type of columns has been found to be much less effective than for circular ones. The lower FRP confinement effectiveness in a rectangular column is mainly attributed to the non-uniform FRP confinement, due to the fact that concrete near the flat sides is subjected to lower confinement stresses than in the corner regions. The 3D numerical model developed in the present PhD thesis can be adopted in this scope, since the latter is capable of simulating the compressive behaviour of concrete under non-uniform confinement. The numerical study can be refined by considering the steel (longitudinal and transverse) reinforcement and other actions and types of loading (monotonic or cyclic).

Hybrid FRP composite can also be explored in other application's context, namely: (i) flexural strengthening of concrete beams and (ii) production of pultruded profiles. Pseudo-ductility can greatly contribute to the increase of structural safety of these elements. It should be noted that this is a very interesting and completely unexplored topic.

Lastly, the durability of hybrid FRP composites is a critical issue for safe and economical implementation of these materials. Future research should be as well focused on this topic.

7.3. References

[1] Jalalvand M, Czél G, Wisnom MR. Damage analysis of pseudo-ductile thin-ply UD hybrid composites – A new analytical method. Composites: Part A. 2015;69:83–93.
[2] Lim JC, Ozbakkaloglu T. Lateral Strain-to-Axial Strain Relationship of Confined Concrete. Journal of Structural Engineering. 2014;141(5).
[3] Lim JC, Ozbakkaloglu T. Unified Stress-Strain Model for FRP and Actively Confined Normal-Strength and High-Strength Concrete. Journal of Composites for Construction, ASCE, ISSN 1090-0268/04014072 (14). 2014.